UNIVERSITÄT ZU LÜBECK

Aus dem Institut für Virologie und Zellbiologie

Der Universität zu Lübeck

Direktor: Prof. Dr. Norbert Tautz

Host and Environmental Modulators of Norovirus Infection: Insights from Human Intestinal Enteroids and Complementary Model Systems

Inauguraldissertation

Zur Erlangung der Doktorwürde

der Universität zu Lübeck

Aus der Sektion der Naturwissenschaften

Vorgelegt von

Maryna Chaika

aus Kyiv, Ukraine

Lübeck 2025

1. Berichterstatter: Prof. Dr. rer. nat. Stefan Taube

2. Berichterstatter: Prof. Dr. Lars Redecke

Tag der mündlichen Prüfung: 10.02.2026

Zum Druck genehmigt. Lübeck, den 16.02.2026

Erklärung:

Ich versichere, dass ich die Dissertation ohne fremde Hilfe angefertigt und keine anderen als die angegebenen Hilfsmittel verwendet habe. Weder vorher noch gleichzeitig habe ich andernorts einen Zulassungsantrag gestellt oder diese Dissertation vorgelegt. Ich habe mich bisher noch keinem Promotionsverfahren unterzogen.

Abstract

Human noroviruses (HNoV) are the leading cause of non-bacterial gastroenteritis worldwide. Despite the significant disease and economic burden, currently no licensed vaccines or antivirals are available against norovirus infection. Progress in understanding norovirus biology has long been hindered by the inability to efficiently cultivate HNoV. This limitation was overcome with the development of the human intestinal enteroid (HIE) platform, which enables infection with clinical HNoV isolates in a physiologically relevant system that recapitulates the cellular diversity and the architecture of the human gut.

This dissertation investigates how host and environmental factors influence HNoV infection in the 3D-HIE. A robust and reproducible HNoV infection model in 3D-HIEs enabled detailed investigation of viral entry, replication, passaging, and virus-host interactions. From a laboratory owned biobank of diagnostic stool samples, four infectious HNoV isolates were identified, sequenced and genotyped. Through virological and biochemical approaches, glycans, divalent cations, bile acids, and polyamines were characterized as key host determinants that modulate HNoV infectivity, replication, and escape from antibody neutralization.

The 3D-HIE platform was extended to also study infection of a clinical human rotavirus (HRoV) isolate and an established human influenza A virus (IAV) laboratory strain. Active fucosylation in 3D-HIEs was identified as a critical determinant for infection by both HNoV GII.4 and HRoV G3.P[8]eq.-like strain but not IAV. However, use of fucosylated surface glycans differed between HNoV and HRoV as identified by lectin competition. Exogenous fucose supplementation enhanced HNoV replication rather than competing with infection.

Environmental ligands, specifically divalent cations and bile acids, were shown to shape norovirus infectivity and immune recognition. In both murine and human norovirus systems, magnesium ions and the bile glycochenodeoxycholic acid (GCDCA) were enhancing MNV and HNoV infections. Magnesium ions facilitated escape from neutralizing antibodies for two MNV strains and one GII.4 HNoV stool-isolate. For HNoV, magnesium was able to revert a loss in viral titers observed after storage of diluted stool isolates.

Host-derived polyamines were identified as broad host dependency factors for norovirus infection. Depletion of polyamines strongly suppressed MNV replication, inhibited capsid protein synthesis, and prevented virus-induced cytopathic effect (CPE), in a reversible manner. Mechanistic studies linked polyamine metabolism, norovirus replication, and virus-induced CPE with PI3K/Akt signaling and cholesterol metabolism as downstream targets. The dependency on polyamines for both MNV and HNoV infections suggests a broad relevance and a novel target for antiviral therapy suited to pharmacologically target chronic norovirus disease.

Collectively, this work advances understanding of the host and environmental determinants that promote norovirus infection by shaping viral entry, replication, infectivity, and neutralization escape. The identified host dependency factors, including fucosylated glycans and polyamines, emerge as critical regulators of infection and promising therapeutic targets, while the influence of environmental modulators on HNoV GII.4 infection and antibody escape provides important insights into norovirus biology and caveats for rational vaccine development.

Zusammenfassung

Humanen Noroviren (HNoV) sind weltweit die häufigste Ursache nicht-bakterieller Gastroenteritiden. Trotz der erheblichen Krankheits- und Wirtschaftsbelastung sind bisher weder zugelassene Impfstoffe noch antivirale Therapien gegen Norovirus-Erkrankungen verfügbar. Der Fortschritt im Verständnis der Norovirusbiologie wurde lange durch die fehlende Möglichkeit behindert, HNoV effizient in Zellkultur zu vermehren. Dieser Engpass wurde durch die Entwicklung des humanen intestinalen Enteroid-(HIE-) Systems überwunden, das Infektionen mit klinischen HNoV-Isolaten in einem physiologisch relevanten, miniaturisierten System ermöglicht, das dennoch die zelluläre Vielfalt und Architektur des menschlichen Darms abbildet.

Diese Dissertation untersucht, wie wirts- und umweltbedingte Faktoren die Infektion im 3D-HIE-Modell beeinflussen, mit Schwerpunkt auf HNoV. Ein robustes und reproduzierbares HNoV-Infektionsmodell in 3D-HIEs wurde mithilfe einer institutseigenen Biobank diagnostischer Stuhlproben etabliert, wodurch detaillierte Untersuchungen von viraler Eintrittsphase, Replikation, Passagierung und Virus-Wirt-Interaktionen ermöglicht wurden. Vier infektiöse HNoV-Isolate wurden identifiziert, sequenziert und genotypisiert. Mittels kombinierter virologischer und biochemischer Ansätze wurden Glykane, zweiwertige Kationen, Gallensäuren und Polyamine als zentrale Wirtsdeterminanten charakterisiert, die HNoV-Infektiosität, Replikation und Antikörperneutralisationsflucht modulieren.

Die Anwendung des 3D-HIE-Systems wurde erweitert, um auch die Infektion eines klinischen humanen Rotavirus-(HRoV-)Isolats sowie eines etablierten humanen Influenza-A-(IVA-)Laborstamms zu untersuchen. Eine aktive Fucosylierung in 3D-HIEs erwies sich als kritischer Faktor für die Infektion durch sowohl HNoV GII.4- als auch HRoV G3.P[8]eq.-ähnliche Stämme, jedoch nicht für IAV. Die Nutzung fucosylierter Oberflächenglykane unterschied sich jedoch zwischen HNoV und HRoV, wie durch Lektin- Kompetitionsassays gezeigt wurde. Eine exogene Supplementierung mit Fucose steigerte die HNoV-Replikation, anstatt mit der Infektion zu konkurrieren.

Umweltliganden, insbesondere zweiwertige Kationen und Gallensäuren, erwiesen sich als modulatorsiche Faktoren für Norovirus-Infektiosität und Immunerkennung. In sowohl murinen als auch humanen Norovirus-Systemen verstärkten Magnesium Ionen und die Gallensäure Glykochenodesoxycholsäure (GCDCA) die Infektion. Magnesium Ionen erleichterten zudem die Flucht vor neutralisierenden Antikörpern bei zwei MNV-Stämmen und einem GII.4-HNoV-Stuhlisolat. Bei HNoV konnte Magnesium zudem Titer Verluste kompensieren, die nach längerer Lagerung verdünnter Proben auftraten.

Wirtsabgeleitete Polyamine wurden als breit wirksame Wirtsfaktoren für Norovirus Infektionen identifiziert. Die Depletion von Polyaminen unterband die Virusreplikation stark, hemmte die Synthese des Capsidproteins und verhinderte reversibel den virusinduzierten zytopathischen Effekt (CPE). Mechanistische Analysen verknüpften den Polyaminstoffwechsel, Norovirus Replikation und CPE mit dem PI3K/Akt-Signalweg sowie dem Cholesterinstoffwechsel als nachgeschaltete Zielwege. Die Abhängigkeit sowohl von MNV- als auch HNoV-Infektionen von Polyaminen weist auf eine breite Relevanz und ein neuartiges antivirales Angriffsziel hin, das sich besonders für die Behandlung chronischer Norovirus Infektionen eignet.

Insgesamt erweitert diese Arbeit das Verständnis der wirts- und umweltbedingten Determinanten, die Norovirus Infektionen durch die Modulation von Viruseintritt, Replikation, Infektiosität und Neutralisationsflucht beeinflussen. Die identifizierten Wirtsfaktoren, darunter fucosylierte Glykane

und Polyamine, treten als wesentliche Regulatoren der Infektion und vielversprechende therapeutische Zielstrukturen hervor. Zudem liefern die Auswirkungen umweltbedingter Modulatoren auf HNoV-GII.4-Infektion und Antikörperflucht wichtige Impulse für die rationale Impfstoffentwicklung.

I. Table of contents

II. List of abbreviations

3D-HIE - 3-dimentional human intestinal enteroid
BME - Basement membrane extract
CI - confident interval
CPE - Cytopathic effect
CMGF– - Complete medium without growth factors
DC - Dendritic cell
DMEM - Dulbecco's Modified Eagle Medium
dpi - days post infection
dsRNA - double-stranded RNA
EDTA - Ethylenediaminetetraacetic acid
FBS - Fetal bovine serum
FITC - Fluorescein isothiocyanate
FUT - Fucosyltransferase
GCDCA - Glycochenodeoxycholic acid
GE - Genome equivalent
GI - Genogroup I
GII - Genogroup II
HBGA - Histo-blood group antigen
HCV - Hepatitis C virus
HRoV - Human rotavirus
HNoV - Human norovirus
hpi – hours post infection
HRP - Horseradish peroxidase
HSV-1 Human herpes virus 1
IgG - Immunoglobulin G
IFN - Interferon
kDa - kilo Dalton
Le^a/Le^b - Lewis antigen
LPS - Lipopolysaccharide
mAb - Monoclonal antibody
MNV - Murine norovirus
MOI - Multiplicity of infection
NEAA – Non-essential amino acids
mRNA - Messenger RNA
NS - Non-structural
PBS - Phosphate-buffered saline
PCR - Polymerase chain reaction
PI3K - Phosphoinositide 3-kinase
PS - Phosphatidylserine
RT - Reverse transcription
RT-qPCR - Reverse transcription quantitative polymerase chain reaction
SD - Standard deviation
SEM - Standard error of the mean
ssRNA - Single-stranded RNA
TMB - 3,3',5,5'-Tetramethylbenzidine
TCID50 - Tissue culture infectious dose 50
v/v - volume/volume
VLP - Virus-like particle
VP1 - Major capsid protein of norovirus

III. List of tables

IV. List of figures

1. Introduction

1.1. Noroviruses

1.1.1. Infection and disease

Noroviruses are non-enveloped, single-stranded, positive-sense RNA viruses ((+)ssRNA) belonging to the *Caliciviridae* family.

They are genetically diverse and are classified into ten genogroups (GI-GX) based on RNA-dependent RNA polymerase and major capsid proteins sequences (1). Noroviruses have a wide range of hosts, including humans, dogs, cats, mice, bats, cattle and more. Human infections are caused by human noroviruses (HNoVs) within genogroups GI, GII, GIV, GVIII, and GIX (2,3) (Figure 1).

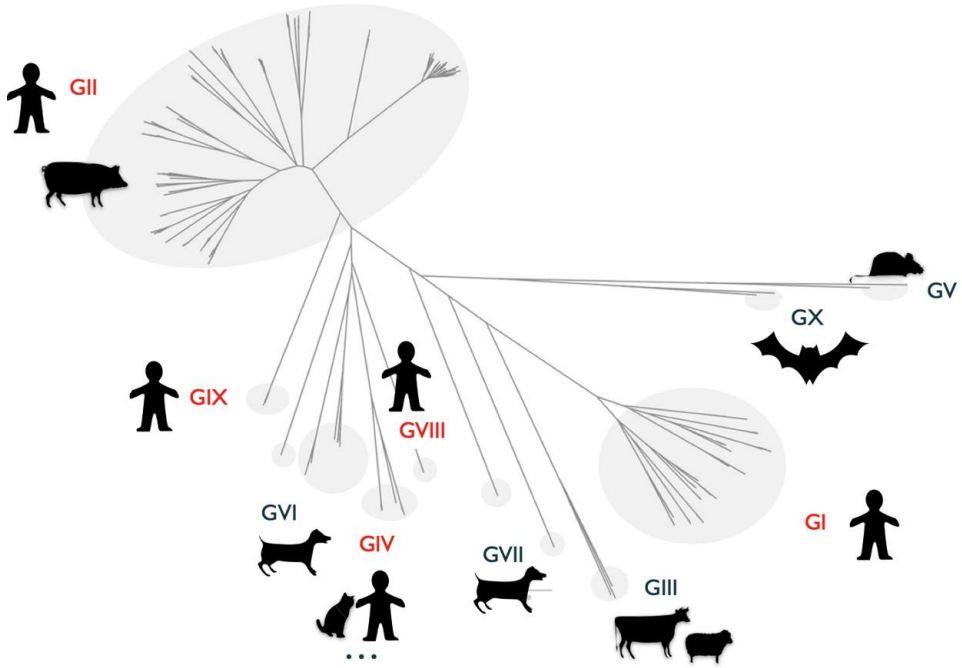

Figure 1. Phylogenetic classification of noroviruses. Phylogenetic analysis based on VP1 amino acid sequences into ten norovirus genogroups and their associated host species, including humans, pigs, cows, cats, mice and bats. Adapted with modification from (1).

HNoV is a leading cause of viral gastroenteritis globally (4,5). Transmission occurs predominantly via the fecal-oral route, contaminated food, water or surfaces, or direct person-to-person contact. HNoV is highly contagious, with as few as 20 particles being enough to cause infection (6,7). Noroviruses are also resistant to a broad range of common disinfectants and demonstrate high environmental stability (8,9). These features make HNoV a significant public health concern, particularly in semi-closed settings such as nursing homes, schools, and cruise ships.

In healthy individuals, HNoV infection is typically acute and self-limiting, with symptoms such as diarrhoea, vomiting, and low-grade fever (10). The highest burden of the HNoV disease is observed among children, the elderly, and immunocompromised individuals (11–13). In these populations, HNoV can establish chronic infection, characterized by prolonged viral shedding and severe, recurrent gastrointestinal symptoms (14).

Chronic HNoV infection presents a significant medical challenge, particularly in immunocompromised patients such as solid organ and hematopoietic stem cell transplant recipients. As in this cohort, HNoV are responsible for an approx. 22% of all diarrhea cases. Infections in this group are often difficult to manage, with half of patients requiring hospitalization for their symptoms and one-third needing intensive care (13). A complementary study reported that in around 22% of HNoV-positive stool samples collected from chronic patients, virus remain infectious *in vitro* (15), supporting concerns that chronic patients could be a reservoir for nosocomial norovirus transmission (14).

Cell tropism of HNoV remains an active area of investigation. Analysis of biopsy samples from infected patients consistently detected viral antigens in the small intestine, localized in the epithelial cells at or near the villus tips and within regions of gut-associated lymphoid tissue (GALT) (16,17). These findings suggest that intestinal epithelial cells serve as the primary target for HNoV, with both enteroendocrine cells (EEC) and enterocytes identified as permissive cell types (17). Whereas enterocytes are the most abundant cell population in the gut, EEC represent only 1% of the intestinal epithelium and are involved in sensory and hormonal signaling (18). Beyond epithelial lining, HNoV antigens have been detected in myeloid cells of the lamina propria, suggesting internalization by phagocytosis or through lysis-independent mechanism (16,17). These findings align with observations from *in vitro* models, where enterocytes (19) and immune cells, such as B cells (20,21) support HNoV infection. More recently, salivary gland cells have also been shown to support HNoV infection *in vitro*, although the relevance of these additional target cells remains to be established (22).

Despite the global health burden imposed by HNoV, no approved antivirals or vaccines exist to date (23). The failure of the HilleVax vaccine (Phase II trial) in 2024 (24) illustrates the immunological and antigenic challenges associated with generating broad, cross-genotype protection against noroviruses. The progress in antiviral and vaccine development has historically been constrained by the absence of reliable *in vitro* models capable of supporting efficient HNoV cultivation and propagation (25).

1.1.2. Classification and evolution

Based on the genetic diversity of major structural protein (VP1), the human-infecting norovirus genogroups GI, GII, GIV, GVIII, and GIX are further sub-divided into more than 30 genotypes, which differ by approx. 20-40% in amino acid sequence (26). Although humans can be infected by various HNoV (mainly GI and GII), GII.4 viruses have consistently represented the predominant cause of norovirus-associated outbreaks globally (23,27,28)(Figure 2). For over two decades, GII.4 viruses have accounted for more than 50% of identified HNoV strains (29–31). While other genotypes, such as GII.2 and GII.17, have occasionally emerged and predominated on the global scale, they have not persisted as GII.4 viruses (27).

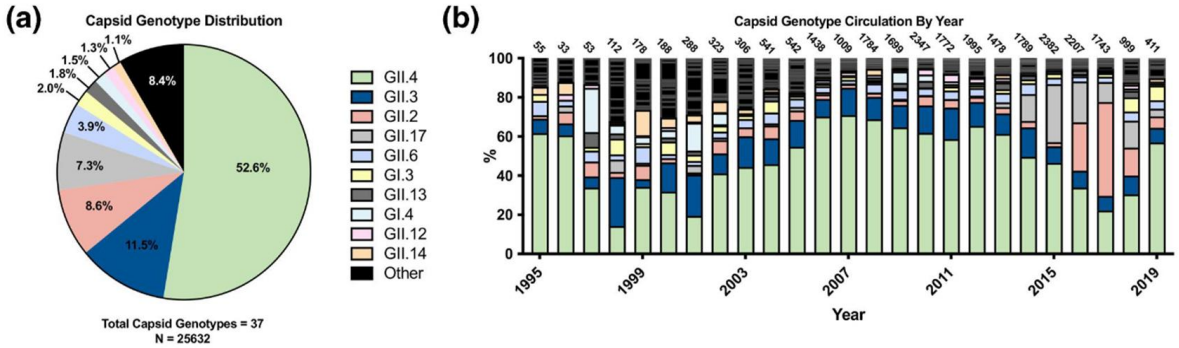

Figure 2. Temporal distribution of circulating human norovirus genotypes between 1995-2019. Genotype identification and quantification of the 25,632 norovirus sequences that sufficiently covered the capsid region. (a) The top 10 represented genotypes are displayed, with the remainder consolidated into another category. (b) Percentage breakdown of globally circulating capsid genotypes by year. Adapted from (28).

The emergence and sustained circulation of specific HNoV genotypes are influenced by multiple factors, including RNA-dependent RNA polymerase (RdRp) fidelity, binding to putative attachment factors, host population susceptibility and immunity. Norovirus replication is driven by the viral RdRp (NS7), which has low proofreading capacity. This low fidelity of RNA polymerase facilitates the accumulation of mutation in the viral genome, while selection pressure favors substitutions beneficial for replication, transmission and immune escape (32–34).

Among non-GII.4 strains, most nucleotide changes are synonymous, leading to minimal changes in the capsid protein sequence. By contrast, GII.4 strains accumulate non-synonymous mutations, particularly in antigenic regions of VP1, potentially facilitating immune escape and the emergence of new variants (35). Over the past three decades, at least nine distinct GII.4 strains have been identified, with the most recent addition being the San Francisco strain (36) .

Six major global epidemics have been associated with the emergence of GII.4 variants (28,37) (Figure 3). The first global outbreak was linked to the emergence and circulation of the Grimsby 1995 virus, the second to the Farmington Hills 2002 virus, and the third to the Hunter 2004 virus. In 2006, two distinct variants emerged, Yerseke 2006a and Den Haag 2006b, with the latter one causing global outbreaks (29). These variants were both outcompeted by the New Orleans 2009 strain. In 2012, the Sydney 2012 variant emerged with a distinct set of non-structural proteins, not previously observed in GII.4 variants. This strain replaced all others and has been circulating for more than a decade in the human population. In 2015, this variant was detected with a new RdRp (38). Other GII.4 variants have been detected (e.g., Sakai 2003, Yerseke 2006a, Osaka 2007, Apeldoorn 2007, and HongKong 2019); however, their impact on gastroenteritis outbreaks was limited to specific geographical regions (29). Since 2017, an emergence of the new GII.4 variant San Francisco has been observed and detected globally (36).

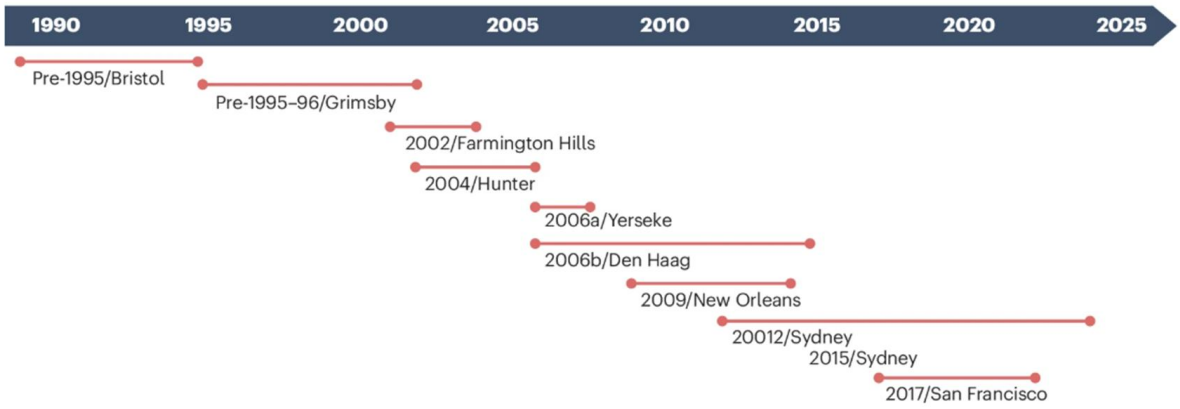

Figure 3. Epochal evolution and emergency of GII.4 variants are shown by their time of circulation. Evolution of GII.4 strains from 1990 to 2025 with duration of strain circulation showed. Adapted from (23).

Murine norovirus (MNV), first identified in 2003, remains the only norovirus that can be efficiently and reliably cultivated *in vitro* (39). MNV belongs to genogroup GV and consists of a single genotype, within which strains diverge by approx. 13% at the nucleotide level (40). Despite this relative low genomic sequence variability, MNV strains exhibit considered biological diversity in their ability to grow *in vitro* and infect or persist in wild-type mice.

Infection with acute MNV strains in mice typically initiates in the salivary glands and distal part of the small intestine and subsequently spreads to other segments of gastrointestinal tract, mesenteric lymph nodes and spleen (41,42) . In immunocompetent mice, acute MNV infection is self-limiting and typically resolves within seven days post-infection (40), while immunocompromised mice (STAT1-/-, lacking interferon response) unable to control infection and succumb to it (39). In contrast, chronic strains of MNV establish prolonged, asymptomatic infection with sustained viral shedding in feces (40,43).

MNV displays dual tropism infecting specialized epithelial cells called tuft cells and immune cells, such as B-cells, dendritic cells and macrophages in cell culture and *in vivo* (20,44,45). Persistent strains such as CR6 and CR3 establish long-term infection *in vivo* by targeting short-lived population of tuft cells (46,47). Tuft cells provide a reservoir that supports sustained viral replication, enabling viral shedding in feces up to 8 weeks post-infection (48). This persistence is enabled by the ability of chronic strains to suppress the host antiviral responses (48) and to exploit tuft cells as an immunoprivileged niche, where chronic MNV strains evade immune clearance by cytotoxic T lymphocytes (CD8+ T cells) (49).

The chronic and acute MNV strains productively replicate in myeloid-derived cells, inducing lysis of susceptible cells, including RAW264.7 macrophages (44), BV-2 microglial cells (50), murine B cells (20), as well as primary monocyte-derived cells particularly macrophages and dendritic cells (39).

MNV shares numerous molecular, structural, and biological characteristics with HNoV, making it a valuable surrogate model for studying HNoV biology (42). A key distinction, however, is MNV's use of the murine CD300lf/ld protein as a *bona fide* entry receptor (51,52), which currently has no known functional homolog in human HNoV infection (53).

1.1.3. Genome organization and replication

The HNoV genome is approx. 7.5 kb in length and comprises three open reading frames (ORFs) (Figure 4a). In addition to the ORFs, the genome contains conserved features at both termini: a genome-linked protein VPg covalently attached to the 5' end, and a poly(A) motif at the 3' end, both flanked by untranslated regions (UTRs) critical for replication and translation (23).

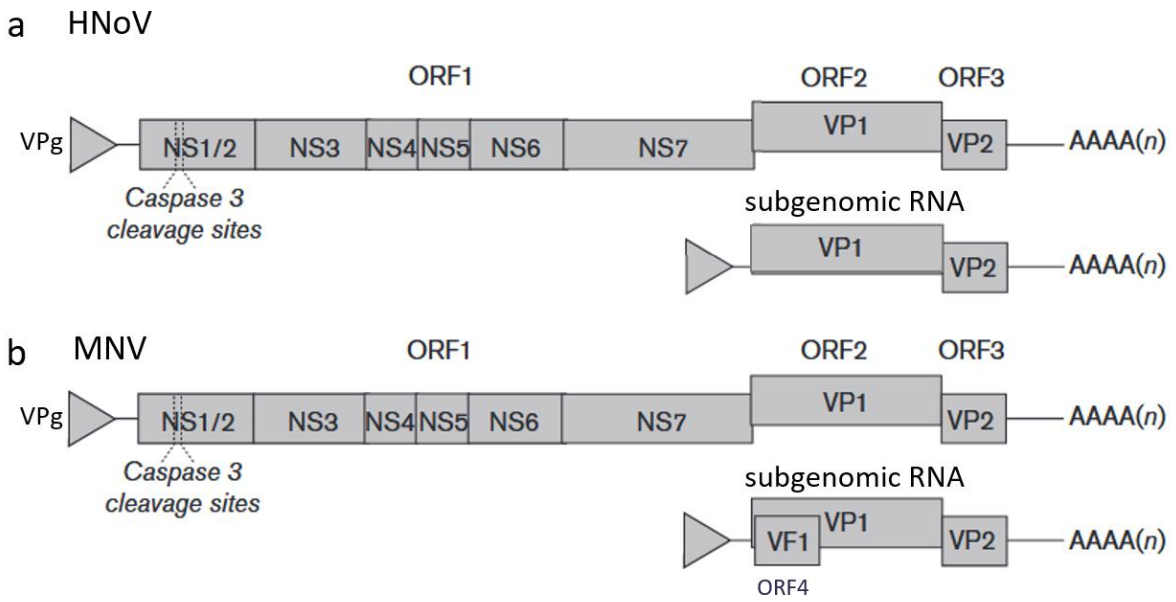

Figure 4. Norovirus genome structure.

(a) Shown for HNoV and (b) for MNV. Three ORFs and the encoded structural (VP1 and VP2) and non-structural proteins (NS1-7 with VF1 protein for MNV) are shown. Adapted with modification from (54).

For all noroviruses, ORF1 is translated as a large polyprotein, which is co- and post-translationally cleaved by the virus encoding protease (non-structural protein 6, NS6) to release six mature NS proteins, including the RNA-dependent RNA polymerase (NS7, RdRp), a viral protease (NS6), helicase (NS3), VPg (NS5), and regulatory proteins NS1/2 and NS4 proteins, which is implicated in formation of replication complexes (RC). HNoV and MNV NS1/2 is further processed by cellular caspases (54,55). ORF2 encodes the major capsid protein VP1, which forms the capsid of virion and is responsible for antigenic diversity and host immune evasion. Minor structural protein VP2 is expressed from ORF3 through ribosomal termination-reinitiation mechanism, where the ribosome upon finishing of ORF-2 translation remains associated with RNA and reinitiates at the start codon of ORF3 (23). VP2 stabilizes the virion (56) and is essential for genome replication (57).

The MNV-1 genome shares a similar organization in terms of length with ORFs 1-3 corresponding to homologous viral proteins (Figure 4b). However, it also encodes an additional ORF4, from which a virulence factor known as VF1 is expressed via ribosomal leaky scanning (58). VF1 protein is implicated in promoting viral persistence by modulating apoptosis and inhibiting host immune responses (59). This additional ORF has not been observed in HNoV and represents a key difference in genome content and function. Despite such differences, the structural and non-structural proteins are highly conserved in noroviruses, making MNV a valuable model system for investigating fundamental mechanisms of norovirus infections.

While HNoV and MNV share similar genome structures and replication strategies, their entry mechanisms differ significantly due to host-specific receptor usage. For MNV, the entry receptor has been identified as murine CD300lf (mCD300), a phospholipid-binding, immunoglobulin-like protein (51,52) expressed on the surface of murine myeloid cells and certain epithelial cells, like tuft cells in the intestinal epithelium (47) and in salivary gland cells (22). Out of eight CD300 family proteins in mice, CD300ld and CD300lf are used by MNV as receptor molecule (53). Direct interaction between

mCD300lf and MNV capsid protein VP1 mediates viral attachment and internalization via endocytosis. Ectopic expression of mCD300lf protein in otherwise non-permissive cell lines confers susceptibility to MNV infection, thereby confirming mCD300lf as a *bona fide* entry receptor (51,60). Additionally, TMEM30a protein, an essential subunit of lipid flippases, that mediates cell membrane fluidity, has been identified as a critical co-factor mediating binding of MNV to cells both *in vitro* and *in vivo* (61). Engagement of mCD300lf receptor by MNV leads to pH-, clathrin- and caveolin-independent endocytosis that requires cholesterol, lipid rafts and microtubules (62,63).

In contrast, the entry mechanism of HNoV remains incompletely understood and continues to be the focus of active investigation. One well-established determinant of host susceptibility to HNoV infection is the activity of fucosyltransferase 2 (FUT2) (64), an enzyme that catalyzes the fucosylation of histo blood group antigens (HBGA). HBGAs are carbohydrates on surface of cells (Figure 5) but can also be secreted into buidily fluids, such as intestinal fluids, saliva, and breast milk. They derive their name from their presence on the surface of red blood cells (RBCs), where they are the antigenic determinants for the ABO blood groups. They are abundantly present on mucosal tissues particularly in the gut HBGA are synthesized through the stepwise addition of monosaccharides to precursor glycans (Figure 5). The predominant precursor in the gut is the type 1 N-acetyllactosamine (LacNAc; Galβ1-3GlcNAc) antigen. In secretor-positive individuals, type 1 LacNAc is α1,2-fucosylated at the galactose position by FUT2, forming the H type 1 antigen (also called O type 1) (65). The type 2 precursor (Galβ1-4GlcNAc), the only precursor expressed on RBCs, can also be present in mucosal tissues but to a much lesser extent (66). Contrary to type 1, the type 2 precursor is fucosylated by FUT1 independently of the secretor phenotype generating the H type 2 antigen (Figure 5). The A and B glycosyltransferases then can extend both H type 1 or H type 2 by adding N-acetylgalactosamine (A enzyme) or galactose (B enzyme), producing A and B antigens. When expressed, FUT3 generates the Lewis antigen series adding a fucose to the the N-acetylglucosamine position. Le^a and Le^b are generated form the type 1 precursor and the most relevant Lewis antigens for HNoV.

Lewis antigens can serve as precursor for A and B antigens, synthesized by ABO transferases or Lewis antigens (Le^b and Le^y) synthesized by fucosyltransferase 3 (FUT3). All of the mentioned glycans belong to histo-blood group antigens (HBGAs) and can be found on the mucosal surfaces and secreted fluids, like saliva, of individuals with an active FUT2 gene (the secretor phenotype) (67). Around 80% of the human population are secretors and are significantly more susceptible to HNoV infection, especially by GII.4 strains (64,68,69). Conversely, non-secretors (FUT2-inactive individuals) are largely, but not completely, resistant to common HNoV genotypes (70–73).

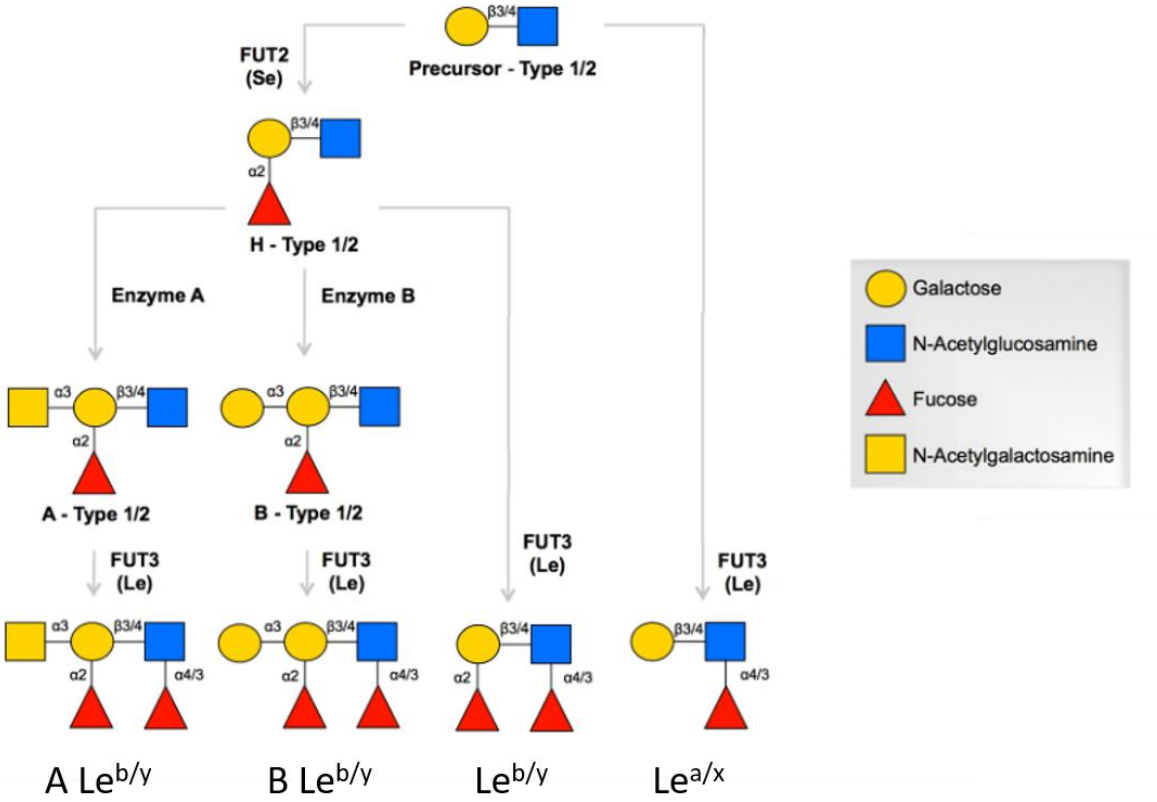

Figure 5. Biosynthesis pathways of type 1 and type 2 HBGAs. Fucosyltransferases generate the H type antigens by adding fucose in an α1,2-linkage to type-1 or type-2 precursor chains at the galactose position of the precursor. FUT2 is the predominant transferase in mucosal tissues and fucosylates the type 1 precursor, while FUT1 is predominantly expressed on RBC and fucosylates the type 2 precursor. Focosylation by FUT3, which introduces α1,3- or α1,4-linked fucose to the GlcNAc residue, produces the Lewis antigen series. On type 1 chains, FUT3 action results in Le^a in non-secretors or Le^b in secretors, whereas on type 2 chains it produces Le^x in non-secretors or Le^y in secretors. FUT3 and FUT2/FUT1 compete for the same precursors: if FUT3 acts first, its α1,4-fucosylation of type 1 or α1,3-fucosylation of type 2 blocks α1,2-fucosylation and leads to formation of Le^a or Le^x, whereas if FUT2 or FUT1 acts first to generate H type 1 or H type 2, these products can then be secondarily fucosylated by FUT3 to yield the bifucosylated Lewis antigens Le^b and Le^y, which then could be further glycosylated to A Leb/y and B Leb/. Adapted with modification from (67).

Saliva and *in vitro* oligosaccharide binding assays have demonstrated HNoV GI and GII variants preferentially bind to H type 1, ABO antigens (Table 1) compared to Lewis antigens but there are strain specific exceptions (23,74–76). For predominant GII.4 variants such as Hunter 2004, Den Haag 2006b, New Orleans 2009 and Sydney 2012 broad specificities have been observed including ABO and Lewis antigens (77,78), predominantly interacting with the secretor fucose (79).

Structural studies have identified that HBGA-binding pockets are located within the hypervariable P2 subdomain of VP1 on the apical side of the viral capsid (80,81). Notably, the HBGA binding sites in GI and GII genegroups are distinct. In GI viruses, each monomer of the VP1 dimer has an HBGA binding site (80,82), while in GII viruses, residues from both monomers form the two HBGA binding sites per dimer at the interface (81,83). Consequently, GII viruses require VP1 dimers for efficient HBGA binding. HNoV GI variants tend to have more restricted HBGA binding profiles predominantly interacting with the terminal galactose of HBGAs rather than the secretor fucose (84).

Emerging GII.4 variants (after 2002) show a broader binding profile, especially to di-fucose Lewis HBGAs, when compared to epochal variants (75,85). This increased binding to di-fucose Lewis HBGAs correlates with less evolutionary conservation of the Lewis fucose-binding site, compared to more conserved the secretor fucose-binding site (86), possibly contributing to the evolution of GII.4 variants (77).

Table 1. HBGA binding of selected norovirus VLPs to oligosaccharides. Adapted from (23).

			HBGA			Lewis	
Strain	Genogroup	Year	H	A	B	Le^a	Le^b
Norwalk	I.1	1968	X	X			X
SoV	I.2	1999				X	
DSV	I.3	1999		X		X	
Chiba	I.4	2000				X	
SMV	II.2	1976					
TV	II.3	1999		X			
GII.4.1997	II.4	1997		X	X		
Farmington Hills	II.4	2002	X		X		
Hunter	II.4	2004	X	X	X		X
Den Haag	II.4	2006	X	X	X		X
New Orleans	II.4	2009	X	X	X	X	X
Sydney	II.4	2012	X	X	X	X	X
GII.6	II.6	2021	X	X			
GII.7	II.7	1995			X	X	X
MNV	V	2004					

Despite of their importance in attachment, expression of native HBGAs (87–91) or knock-in of the FUT2 gene (87,91) to immortalized human cell lines failed to confer susceptibility to HNoV infection. These findings support the notion that HBGAs are insufficient as standalone entry receptors, and that additional, unidentified host factors are required to permit productive infection.

More recent studies suggested that the HNoV entry involves a complex process, initiated by interaction of VP1 protein with HBGA on the host cell membrane. This interaction promotes virus particles clustering at the cell membrane and is followed by recruitment of host factors such as galectin-3, ALG-2-interacting protein (ALIX) and lysosomal associated membrane protein 1 (LAMP-1). Notably, these early entry events are observed only in presence of HBGA, highlighting the importance of secretor phenotype for HNoV infection (92).

Following initial attachment, virus uptake is associated with membrane-wounding mechanism and supported by clathrin-independent carriers (CLIC pathway) (92). Outbreak-associated variants of GII.4,

such as Den Haag2006b and Sydney 2012, exhibit enhanced efficiency in induction of viral particles clustering and membrane wounding compared to other genotypes, such as GII.3, GII.17 and GI.1 and even earlier GII.4 variants Farmington Hill 2002 and Grimsby 1995. These observations suggest that epidemic GII.4 strains may have evolved a more efficient entry mechanism, potentially contributing to their transmissibility and global persistence (93).

The precise mechanism of uncoating and genome release of noroviruses remains poorly understood. In HNoV, endosome acidification appears to be a critical step (92), while for MNV entry appears to be pH independent (62). For other *Caliciviruses*, such as feline calicivirus, VP2 has been shown to mediate pore formation in host membranes, facilitating the genome delivery into the cytoplasm (94). It is plausible that a similar VP2-dependent mechanism could operate in noroviruses.

The translation and replication of norovirus occurs in the cytoplasm of the host cell (Figure 6). The viral protein VPg (NS5), covalently attached to the 5' end of the RNA genome, mimics the 5' cap structure of host mRNA and recruits the host translation initiation machinery by engaging the cap-binding eukaryotic initiation factor 4 gamma-complex (eIF4G). This allows the viral RNA to function directly, as messenger RNA (mRNA) in the initial steps of the infectious cycle leading to nonstructural polyprotein (NS1/2-NS7) synthesis (54).

Viral genome replication of noroviruses takes place within membrane-bound replication complexes (RC) (95), formed by the coordinated activity of regulatory NS1/2, NS3 and NS4 proteins and NS7 polymerase. NS4 protein plays a central role in formation of RC vesicles, as exogenous expression of NS4 alone is sufficient to induce the formation of intracellular vesicles (96,97). NS1/2 and NS3 individually can cause only re-modeling of pre-existing cellular membranes in the ER compartment, while their interaction with NS4 facilitates the generation of distinct vesicle structures (96). Additionally, norovirus NS7 RdRp has been shown to form the liquid-interphase phase-separated replication compartments, which segregate the viral genome synthesis from the host cytoplasm (98). Within these membrane complexes, NS7 RNA polymerase synthesizes a negative-sense RNA intermediate, which subsequently serves as the template for the production of positive-sense genomic RNA. Initiation of negative-strand synthesis requires NS7 to utilize the viral protein VPg (NS5) as a primer (54). This double-stranded RNA (dsRNA) intermediate is essential for replication and constitutes a pathogen-associated molecular pattern (PAMP), capable of triggering the host innate immune sensors (54).

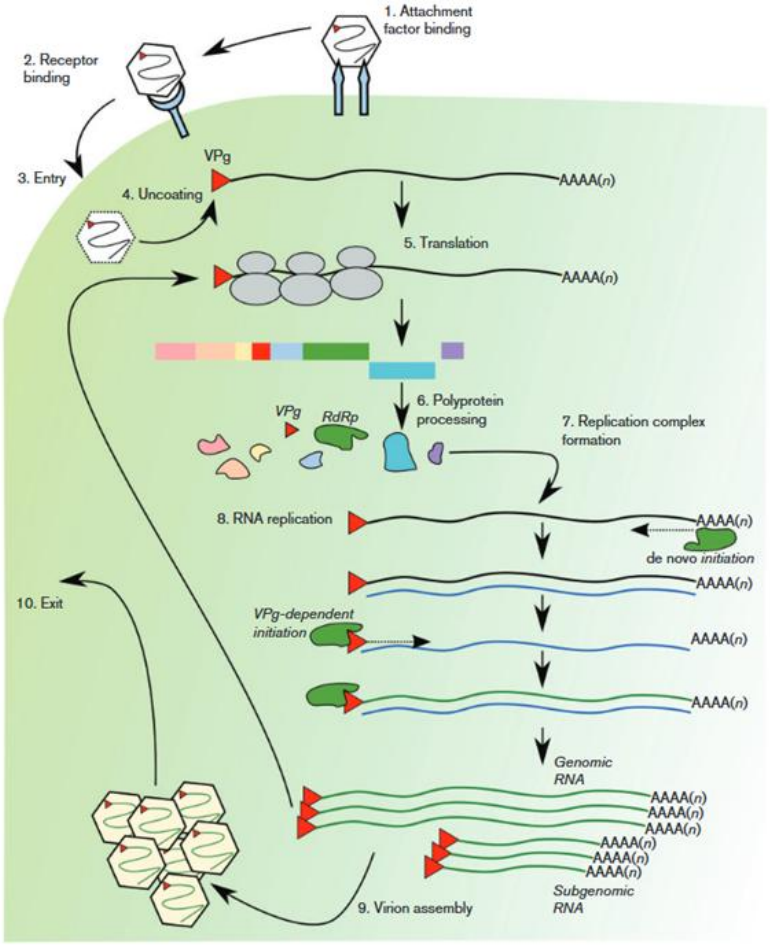

Figure 6. Schematic representation of the norovirus life cycle. Both HNoV and MNV initiate infection through the attachment to the cell surface using various carbohydrate attachment factors (1), followed by engagement with proteinaceous receptor mCD300 for MNV and yet an unknown postulated receptor for HNoV (2). These interactions initiate viral entry (3) and uncoating (4). The incoming viral genome is translated (5), through interactions with VPg (red triangle) and the cellular translation machinery. The ORF1 polyprotein is co- and post-translationally cleaved (6) by the viral protease NS6. The replication complex is formed by recruitment of cellular membranes to the perinuclear region of the cell (7), through interactions in part with NS1/2, NS3 and NS4. Genome replication occurs via a negative-strand intermediate, and genomic and subgenomic RNA are generated by the viral RdRp (8). The replicated genomes are translated (within the replication complex) and subgenomic translation of ORF-2 produces sufficient VP1 for the capsid assembly (9). Genome is packaged and infectious virion are released (10). Adapted from (54).

The structural proteins VP1 and VP2 are translated from subgenomic RNA (sgRNA), generated via premature and/or internal initiation (Figure 6). Two non-mutually exclusive models have been proposed for synthesis of sgRNA. One model suggests that sgRNA is generated via unidentified termination signal in the negative-sense RNA (-ssRNA), leading to the synthesis of a truncated positive-sense strand (+ssRNA) ((54)). The alternative model proposes that sgRNA originates via internal initiation at a highly conserved stem-loop structure located upstream of the subgenomic start site within -ssRNA, which serves as a promoter for RdRp (99). Both mechanisms lead to an increased pool of positive-sense sgRNA, thereby enhancing the translation efficiency of structural proteins required in high abundance for assembly of viral capsids (54,99,100).

When the viral replication is complete, the genomic RNA is packaged into icosahedral particles consisting of 180 copies of VP1 and estimated 9-12 copies of VP2 (54). The resulting capsid usually exhibits T = 3 icosahedral symmetry, structured as 90 dimers of VP1. Each VP1 subunit has a domain organization consisting of an internal N-terminal arm (NTA), a shell(S)-domain and protruding(P)-domain, divided into P1 and P2 subdomains (Figure 7). S- and P-domains are linked via a flexible hinge region. The P1 subdomain, located closer to the S domain is formed by the N- and C-terminal regions of the P domain, whereas the P2 subdomain is formed by the central portion of P-domain and is the most surfaced-exposed and hypervariable region of the capsid. The P2 subdomain mediates host entry molecule interactions, such as mCD300lf for MNV and HBGAs for HNoV (23).

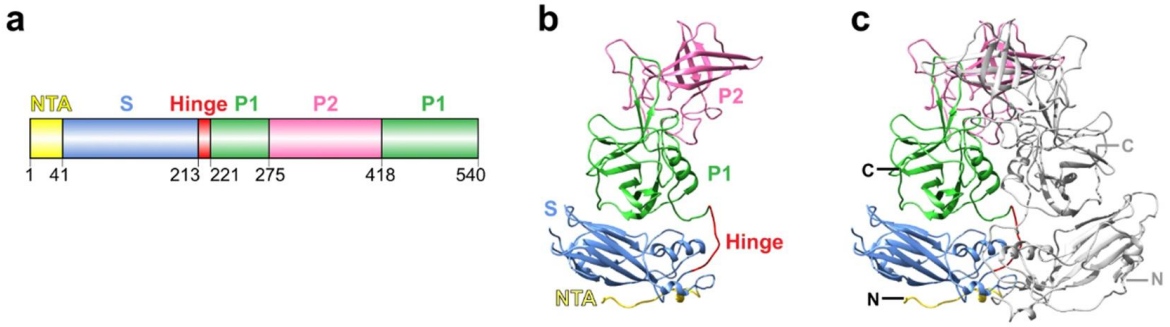

Figure 7. Structure of norovirus capsid protein. (a) Schematic of HNoV VP1 structure colored by domains. (b) Ribbon representation of VP1 monomer. The NTA, S domain, hinge, P1 subdomain, and P2 subdomain are colored corresponding to the schematic. (c) The VP1 dimeric formation. One subunit is colored as in B, and the other subunit is shown in gray. The N- and C- termini of the structure are labeled. Adapter from (101).

Although VP1 alone is sufficient to mediate the assembly of virus capsid, e.g. virus-like particles (102), VP2 supports capsid assembly and stability (56,103) and is essential for virus infectivity (57). Its interaction with viral VPg (NS5) protein is thought to mediate viral genome packaging into viral particles (104).

Norovirus release has been associated with apoptosis, a non-immunogenic form of programmed cell death (PCD) (105,106). Apoptosis is characterized by the orderly disassembly of cells into membrane-bound fragments known as apoptotic bodies (107). Hallmark features of apoptosis include activation of caspases, cleavage of DNA repair enzymes such as Poly (ADP-ribose) polymerase (PARP), downregulation of pro-survival Bcl-2 family proteins, like Mcl-1, and the externalization of phosphatidylserine (PS) to the outer leaflet of the plasma membrane (107). While many viruses have evolved mechanisms to inhibit apoptosis and prolong host cell survival (108), noroviruses strategically modulate the intrinsic apoptotic pathway to facilitate their replication and dissemination (109).

In early stages of infection, MNV suppresses apoptosis through the activation of the phosphoinositide 3-kinase (PI3K)/Akt signaling pathway (109), which further facilitated by the viral protein VF-1 (59). The inhibition of apoptosis at early time-points allows sufficient time for viral replication and assembly, affecting the balance between intracellular retention and release of virions (109). As infection progresses, MNV egress becomes associated with virus-induced apoptosis, mediated by host proteases such as caspases and cathepsins , and disrupt the pro-survival Bcl-2 proteins, like survivin or Mcl-1 (105,106,110,111).

Exogenous expression of MNV ORF-1 polyproteins or individual NS3 protein from both MNV and HNoV is sufficient to induce apoptosis via dysregulation of host pro-survival apoptotic proteins and initiation of host translation shut-off program (106,111–113). Host halting of translation (translation shut-off program) represents a cellular defense mechanism that can be activated by either virus or the host in response to infection. Since viruses lack their own translational machinery, they are dependent on the host to translate their proteins. As such, manipulation of host translation is critical to suppress antiviral responses and prioritize the synthesis of virus proteins (114).

MNV and HNoV NS3 protein encodes mitochondrial localization signal and domain homologous to the membrane disruption domain of the pseudokinase mixed lineage kinase domain-like (MLKL), a key effector of necroptosis. This allows NS3 localization to mitochondria and subsequent mitochondria membrane permeabilization, resulting in organelle dysfunction (115). In MNV infection, damage to both mitochondria and nuclear membrane has been observed, as evidenced by the release of DNA into cytoplasm. However, these effects have been attributed to the activity of NS4 (116). Still, deletion of MLKL-domain in MNV NS3 protein abolished mortality in immunodeficient mice model, underscoring the essential role of NS3 in virus-induced apoptosis and spread (115).

Apoptosis also plays a key role in tissue tropism and persistence of chronic MNV strains. In the persistent strain CR6, host caspases-mediated cleavage of NS1/2 enhances apoptosis activity, compared to acute MNV strains, and enabling the infection of the intestinal epithelial cell. This cleavage is essential for establishing persisting infection and sustained shedding in stool in the mouse model (45). In contrast, acute MNV strains lack the caspase cleavage site in the NS1/2 protein, which suggests that utilization of apoptosis mechanism was adopted specifically by persistent MNV strains (117). For HNoV, direct evidence of virus-induced apoptosis in cell culture remains limited. Nevertheless, HNoV NS3 protein has been shown to trigger caspase activation and PARP cleavage (111,113). Like MNV, HNoV NS1/2 and NS4 interact with NS3 and enhance its pro-apoptotic activity (113), indicating that regulated induction of apoptosis may be a conserved feature of noroviruses.

Importantly, apoptosis also facilitates norovirus dissemination and immune evasion. Virions released in apoptotic bodies, membrane-bound vesicles enriched in PS, can mimic dying cells and evade immune detection and antibody neutralization. Both HNoV and MNV, alongside other enteric viruses, such as rotaviruses, have been found within such vesicles *in vitro* and in stool samples. This mode of release enhances infection efficiency, as vesicles often contain multiple virions, resulting in a higher multiplicity of infection per cell and, consequently, elevated viral titers and more severe clinical outcomes in animal model (118).

1.1.4. Capsid plasticity

As initially observed first for MNV, and more recently for HNoV, the major capsid protein VP1, which comprises a P-domain and S-domain, can adopt two distinct conformations (Figure 8). In the “raised” state of the viral capsid, the P-domain is lifted off the S-domain, whereas in the “contracted” state, the P-domain is rotated over the S-domain and collapses right onto the S-domain (101,101,119–123). This is mediated by the flexible hinge region allowing the P domain to move independently of the S-domain. This conformational flexibility is the best characterized in MNV, where transition from the raised to the contracted state involves a collapse of P-domain onto S-domain, P-domain clockwise rotation by

40°, closure of A'B' and E'F' loops and an upward movement of C'D' loop (124), enhancing mCD300lf receptor engagement (125).

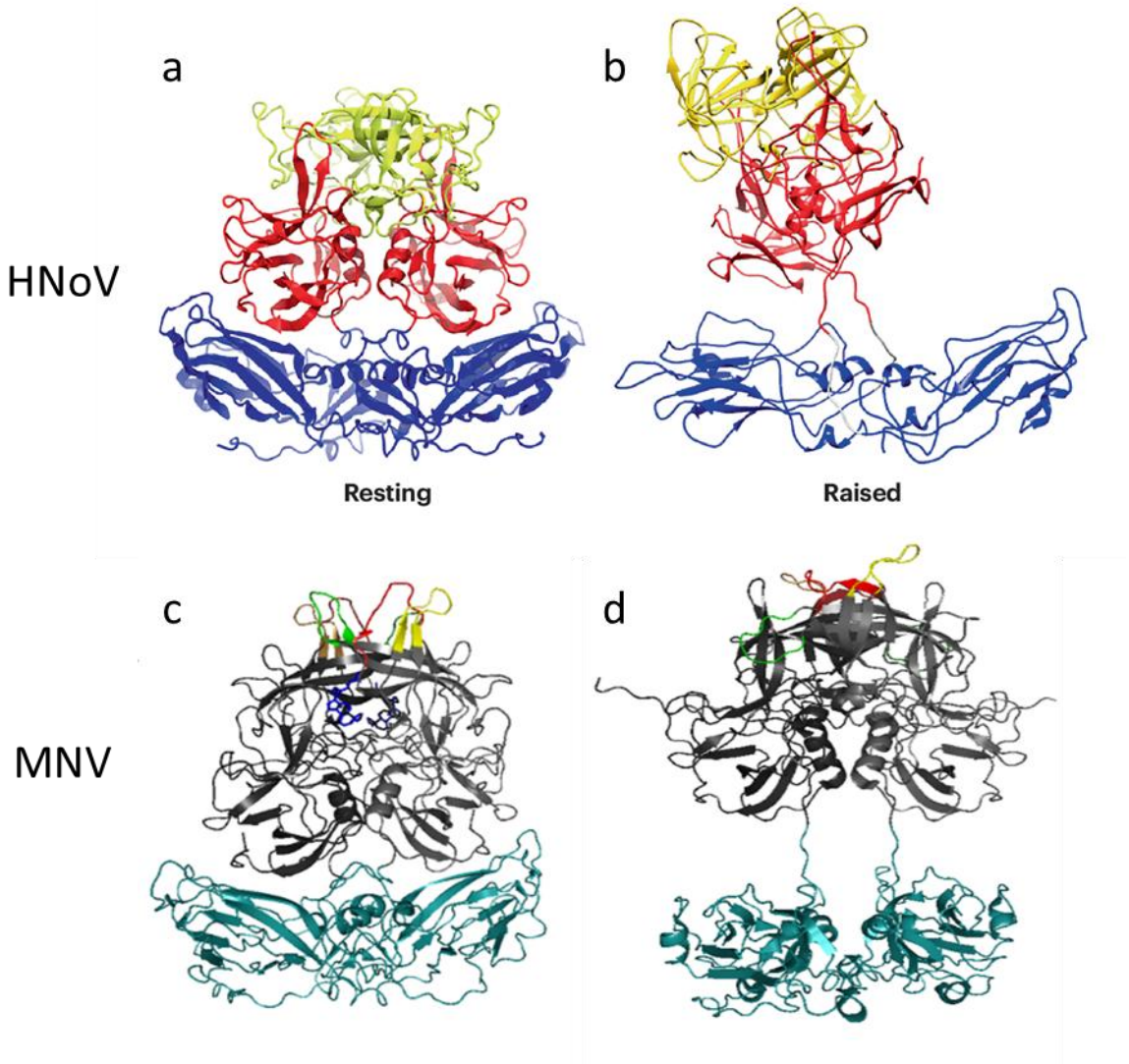

Figure 8. Resting and raised conformations of the capsid dimer of noroviruses. (a, b) The S-, P1-, and P2-subdomains of HNoV are shown in blue, red, and yellow, respectively. (c, d) The S- and P-domains of MNV are shown in grey and cyan, with the A'B', C'D', and E'F' loops highlighted in yellow, green, and red, respectively. The transition from a raised to a collapsed capsid conformation is induced upon binding of environmental factors, such as divalent cations or bile acids, and is associated with altered accessibility of surface-exposed epitopes. Adapted from (a, b) (23), (c) PDB 6P4J, and (d) combined models from PDB entries 3LQ6 and 6CRJ.

In MNV, this conformation changes are induced by environmental factors such as divalent cations, acidic pH and bile acids (126), which directly interact with MNV VP1 and promote the contracted state (120,125). This contracted state conceals the A'B' and E'F' loop immune epitopes, which are otherwise exposed and serve as binding sites for a broad panel of neutralizing monoclonal antibodies, such as A6.2, 2D3 and 4F9 (127). Notably, antibody escape mutants V339I and D348E (C'D' loop VP1, P-domain), selected under the pressure of 2D3 and 4F9 antibody (127), adopt the partially contracted state, even in absence of environmental factors, thus enabling immune evasion (124).

Furthermore, recent work has demonstrated that both bile acid GCDCA and divalent cations can pre-organize the conformational state of MNV VP1, facilitating the binding of the either ligand and enabling synergistic activity (124,128). These interactions are mediated via the bile acid-binding pocket at the dimer interface (W245, A392, and A437, main interacting residues) and three divalent cation-bindings site N364-D366, D410, D440 located within or adjacent to receptor binding pocket or in close proximity to bile acid binding pocket (125). Magnesium and calcium have been identified as principal ligands for the metal ion binding sites (128), whereas bile acid GCDCA serves as the primary ligand for bile acid pocket (125).

The functional implications of the VP1 conformational changes for MNV infectivity are still not completely understood. Comparative structural analysis between acute and chronic MNV strains have demonstrated that the persistent MNV CR6 strain requires stronger environmental stimuli to undergo detectable capsid changes in cryo-EM study. Specifically, while acidic pH alone (pH 5.0) was sufficient to induce the collapse of the P-domain onto S-domain in acute MNV-1, the CR6 strain required a combination of acidic pH and bile acid GCDCA to trigger a comparable conformation transition (119).

Functional experiments further supported these structural observations. In cell culture, acute MNV-1 and WU23 strains exhibited enhanced infectivity following mild medium acidification (pH 6.7), supplementation of fetal bovine serum or bile acid GCDCA, whereas CR6 required stronger acidification (pH 5.6) to achieve a similar increase in infectivity and were less responsive to other stimuli. These findings highlight distinct phenotypic properties of CR6 strain, including its lower infectivity under environmental factors and attenuated pathogenicity in murine model (119).

The role of bile acid GCDCA in promoting both MNV infectivity and immune escape has also been functional validated in cell culture experiments, particularly in the context of neutralization escape from monoclonal antibodies that targets A'B' and E'F' loops in VP1 protein (129). In contrast, the functional contribution of divalent cations to infectivity and immune escape of MNV remains less well characterized. Current evidence is mostly indirect, derived from an ELISA-based binding assay, where supplementation with calcium ions led to reduced antibody recognition of MNV virions (121).

While the conformational plasticity of capsid protein is well characterized for MNV, similar evidence for HNoV is only beginning to emerge. Structural studies of HNoV GII.4 and GII.3 (VLPs), a self-assembled virus capsid containing no genome, have demonstrated that HNoV VP1 can also undergo a raised-to-contracted transition, particularly under condition of depletion of stabilizing divalent cations (101,123). Complementary biophysical studies further revealed that removal of divalent cation enhances the VLP recognition by nanobodies (101), suggesting that divalent cation-dependent conformational changes may contribute to HNoV immune evasion.

The fact that environmental factors such as pH, divalent cations and bile acids alter the virus capsid and modulate the capsid's engagement with host factors underlines their importance in norovirus infection. It is interesting to note that , divalent cation- and bile acid-binding sites are not conserved between MNV and HNoV, neither in sequence nor in structural localization (Figure 9). For HNoV GII, putative metal ion binding sites have been proposed at three different positions: H293, close to the HBGA binding pocket, H460 at monomer interface, and H501 close to the to N-terminus (101,123,128). Additionally, NMR spectroscopy has confirmed binding of zinc, cadmium and other divalent metal ions to those residues (128). A distinct bile acid binding pocket has been suggested for HNoV GII variants,

comprising L486, F487 and L507-I509 residues. However, the interactions of HNoV VP1 with bile acids occur at much lower affinity than those observed for MNV (130).

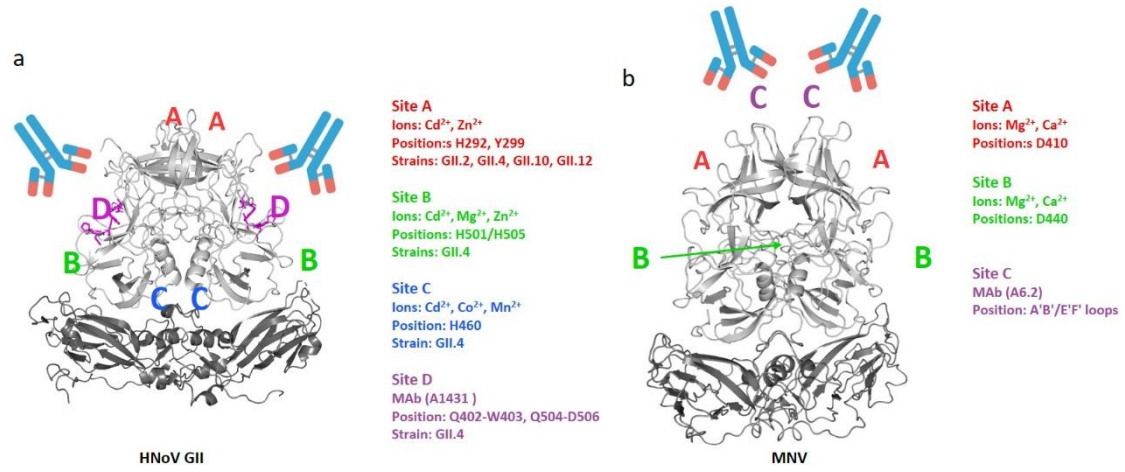

Figure 9. Divalent cations and monoclonal antibody binding sites in noroviruses VP1 protein. (a) The S- , P-domains showed in dark and light grey, respectively, for HNoV. Metal ion binding sites for HNoV is shown in red (site A, (128)), green (site B,(128)) and blue (site C, (101,128)), while mAb binding site is shown in magenta (site D, (131)). (b) The S- and P- domains shown in dark and light grey, respectively for MNV. Metal ion binding sites for MNV shown in red (site A, (121,128)) and green (site B, (121,128)), while mAb binding site is shown in magenta (site C, (127,132)). Adapted from PDB 7K6V (HNoV) and 6P4J (MNV).

1.1.5. HNoV cell culture and animal models

A key challenge in HNoV research has been the long-standing difficulty to cultivate the virus (23,133). Several *in vivo* models have been developed to facilitate the research, including mouse (134), gnotobiotic pigs (135), zebrafish (*Danio rerio*) ((136)) and non-human primate (NHPs) models (2,133).

BALB/c mice deficient in recombination-activation genes (RAG 1 or 2) and common gamma chain (γc-RAG), collectively referred as Rag/γc-/- mice, have been shown to support HNoV replication, with or without transplantation of human CD34+ hematopoietic stem cells (134). HNoV GI and GII replication was detected in multiple tissues, including intestinal tract, stomach, mesenteric lymph nodes and liver of infected mice. However, this model presents several limitations. Firstly, only combined oral and intraperitoneal inoculation of virus led to increase in viral titers in feces e.g. viral shedding, whereas inoculation by either route alone did not result in elevated fecal titers above the input level. Secondly, the majority of mice did not develop gastrointestinal symptoms, limiting the model's utility for pathogenesis studies (134). A subsequent study confirmed that HNoV replication in this model could be effectively inhibited by a broad RNA polymerase inhibitor 2'-C-methylcytidine (2-CMC) (137). Nevertheless, this study provided insights into the role of adaptive immunity for HNoV infection, as only RAG/γc-/- (lacking T- and B-lymphocytes) mice supported productive replication of HNoV, whereas wild-type mice remained resistant.

Gnotobiotic pigs, raised germ-free and lacking colonization by commensal bacteria, represent a more permissive model for HNoV. These animals are susceptible to HNoV infection via oral inoculation, develop diarrhea and exhibit robust viral shedding in feces (135,138,139). HNoV infection in gnotobiotic pigs can be significantly enhanced and prolonged by either supplementation of human gut microbiota (140) or disruption of RAG2/IL2RG gene, which mimics severe combined immunodeficiency

(SCID) in humans, characterized by absence of T- and B-lymphocytes, and natural killer (NK) cells (138). These findings once again highlight the importance of host immune status in modulating HNoV infection.

NHPs, specifically chimpanzees and macaques, have been evaluated as model for HNoV infection (141–143). Interestingly, while some animals were susceptible to infection and shed virus in stool, others were resistant and showed no evidence of viral replication or virus shedding. Infected chimpanzees developed an immune response resembling those observed in humans, and had gut pathology similar to ones in HNoV-infected patients (143). The use of the NHPs and gnotobiotic pigs remains limited due to associated costs and labour-intense maintenance.

Over the years, numerous attempts have been made to establish an *in vitro* cultivation system for HNoV. However, none of the commonly used immortalized cell lines, even those engineered to exogenously express FUT2, have successfully supported viral replication (87,91,133).

One of the earliest *in vitro* models that demonstrated HNoV replication was based on immortalized human B cells. In this system, replication efficiency was low and dependent on the presence of exogenous HBGA ligands, either as oligosaccharides or provided indirectly via commensal gut bacteria (20). However, replication of HNoV in B cells proved inconsistent and difficult to reproduce. A later study further characterized replication of HNoV in primary human B cells derived from whole-blood PBMCs, spleen or lymph node, as abortive and suggested that only certain subsets of B cells may be susceptible and permissive to HNoV infection (55).

Subsequently, the zebrafish (*Danio rerio*) emerged as a valuable model for HNoV research. Zebrafish were shown to robustly and consistently support the replication of HNoV from stool samples (144,145). Viral replication has been detected in hematopoietic cells, macrophages, intestinal enterocytes, as well as in hepatocytes and gallbladder epithelial cells (144,146). Although *Danio rerio* lacks FUT2-dependent α1,2-fucosylation, it expresses enzymes that catalyze α1,3-fucose addition (analogous to FUT3 in human), making it functionally comparable to non-secretors human (FUT2-negative, FUT3-positive). Inhibition of fucosyltransferase activity in *Danio rerio* impairs HNoV infection, underscoring the essential role of glycans for HNoV infection in this model (136).

As continuous passaging of HNoV remains a significant challenge in this model, HNoV research is performed with stool-isolates. One study reported successful continuous passaging of HNoV in the zebrafish model (147), while another study reported limited passaging (144).

A major breakthrough in HNoV research came with the development of human intestinal enteroid/organoid (HIE/O) cultures (19,148). Derived from induced pluripotent stem cells (HIO) or intestinal stem cells (HIE) obtained from human biopsies, these cultures recapitulate many features of human gut epithelium, including diverse cell types, including enterocytes, goblet cells, Paneth cells, and EECs, apical-basal polarity of cell membrane, tight junction's formation and a representative glycan repertoire (19,21,148). When derived from FUT2-positive donors, HIE/O express complex glycans, including HBGAs, that support HNoV infection (19,148). Conversely, cultures with FUT2 knock-out (149) or established from FUT2-negative donors (19,148) are not permissive to HNoV, whereas FUT2 knock-in restores susceptibility (149). This confirms the critical role of FUT2 activity and glycan expression for HNoV infection.

Historically, efforts to establish continuous HNoV passaging in HIE were largely unsuccessful (19,21). One early study using HIO reported sustained passaging of the GII.4 variant (148). However, subsequent study failed to reproduce this result but was successful in establishing passaging for the GII.17 strain (150). More recent, HIE-based experiments demonstrated that inhibition of chemokine receptors CXCR3/CCR5/CCR2 using the antagonist TAK-779, allowed continuous and robust passaging of GI.1 and GII.17 variants, but not the predominant GII.4 variants (151).

HIE and HIO models can be utilized either as 2D monolayers or as 3D spheroids for HNoV infection (19,21). Notably, upon differentiation, 3D-HIE adopt an apical-out polarity, exposing HBGAs that are restricted to the apical surface of intestinal epithelial cells (21,148). In the native human intestine, luminal apical membrane is enriched in digestive enzymes, transporters, and glycoconjugates, while the basolateral membrane is interfaced with the underlying stroma. Conventional 3D enteroids exhibit a basal-out orientation, with the apical surface enclosed within the lumen, thereby limiting direct access of pathogens to apically expressed receptors or ligands. The differentiation-induced apical-out configuration therefore provides physiological accessibility to HBGAs and other apical ligands, permitting norovirus infection without mechanical disruption, microinjection, or manipulation of epithelial polarity.

HIE support replication of the broad range HNoV strains from both GI and GII genogroups and represent state-of-the-art model to propagate HNoV in cell culture (152–154).

More recently, epithelial cells derived from human salivary glands have been explored as a novel model for HNoV. Immortalized salivary cells efficiently supported replication of HNoV GII.4 stool-isolates. The success of this model raises a question whether salivary glands might serve as an additional site of viral replication and whether transmission through saliva could represent alternative infection routes. Remarkably, the salivary cell model supported robust and continuous passaging of the HNoV GII.4 variant from stool sample (22). Reproducibility of HNoV replication in this platform by other laboratories remains to determined.

Although noroviruses represent the primary focus of this research, two additional RNA viruses, human rotavirus (HRoV) and influenza A virus H1N1 (IAV H1N1), were employed as complementary models. Despite differences in genomic organization, polarity of viral RNA and the disease pathogenesis, all three viruses, HNoV, HRoV and human IAV H1N1, share the reliance on host glycans, as essential factors, as well as their ability to replicate in the gut. These shared features rendered HRoV and IAV H1N1 suitable comparative models for investigating glycan-mediated virus-host interaction, particularly for HBGAs.

1.2. Human rotavirus (HRoV)

Rotaviruses are non-enveloped double-stranded RNA (dsRNA) viruses that have a complex triple-layer capsid architecture that encloses the genome of 11 dsRNA segments (155). The RNA segments encode six structural viral proteins (VP1-4, VP6 and VP7) and six non-structural proteins (NSP1-6) (Figure 10).

Rotavirus disease is primarily transmitted via person-to-person and fecal-oral route. Clinical manifestations of disease include diarrhea, vomiting, malaise and fever, with children, elderly and immunocompromised individuals being the most susceptible to severe disease. Importantly, vomiting is a hallmark of rotavirus disease, contributing to dehydration and complicating therapeutic interventions, such as oral rehydration therapy (155).

Live attenuated oral vaccines against rotavirus were licensed for global use in 2006 and are currently used in >100 countries (155). Before the introduction of vaccines, rotavirus-associated gastroenteritis caused >500,000 deaths in children <5 years of age annually (156). Although the introduction of vaccines has reduced the number of rotavirus-associated deaths, the efficacy of licensed vaccines is suboptimal in low-income countries, where rotavirus still results in >200,000 deaths annually (157).

Rotavirus structural proteins in the mature virus particle determine host specificity, cell entry and contain epitopes that generate immune responses. The non-structural proteins are involved in genome replication and antagonism of the innate immune response, specifically NSP1, while NSP4 acts as viral enterotoxin (155).

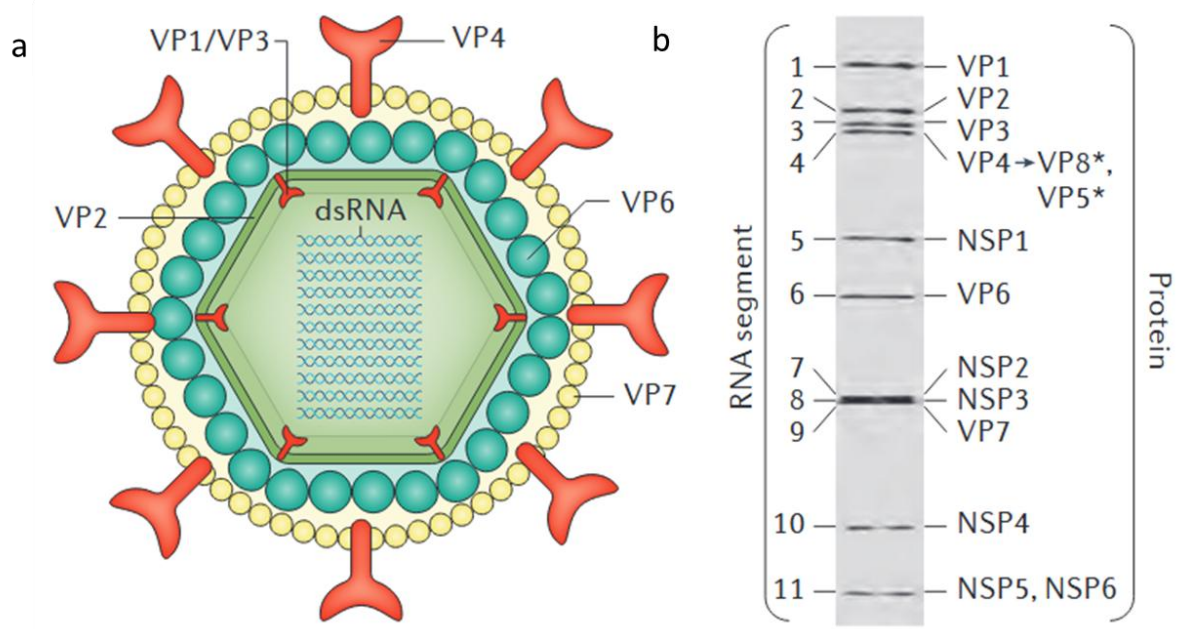

Figure 10. Rotavirus capsid structure. (a) Cross-sectional schematic of the rotavirus triple-layered particle (TLP). This structure consists of the inner capsid layer (viral protein (VP)2), the middle capsid layer (VP6) and the outer capsid layer (VP7 and the spike protein VP4). VP4 is proteolytically cleaved into VP8 and VP5*. The structural protein VP2, the enzymes VP1 and VP3 and the viral genome compose the virion core. The middle capsid layer protein (VP6) determines species, group and subgroup specificities. The outer capsid layer is composed of two proteins, VP7 and VP4, which elicit an immune response in infected hosts, leading to the production of rotavirus-specific antibodies. (b) Electrophoretic migration profile of the 11 segments of rotavirus double-stranded RNA (dsRNA) and the encoded proteins for simian rotavirus SA11 strain. NSP, non-structural protein. Adapted from (155).*

Rotaviruses are classified in species A-J, based on sequence and antigenic variation in VP6 protein (Figure 11). Among these, species A rotaviruses are the most prevalent in the pediatric population. Further genotyping of species A rotaviruses is based on RNA segments encoding VP7 (G types) and VP4 (P types), forming the basis for the dual nomenclature system. To date, 32 G genotypes and 47 P genotypes of species A rotavirus have been identified. However, a limited number of strain combinations account for the vast majority of global infections, with G1.P[8], G2.P[4], G3.P[8], G4.P[8], G9.P[8] and G12.P[8], accounting for >90% of globally circulating species of rotavirus A (158–162). Lately, an emerging G3.P[8] equine-like (eq.-like) strain, presumed to be of zoonotic origin, has gained attention due its increasing detection and geographic spread in recent years, now representing a significant proportion of infections (163,164).

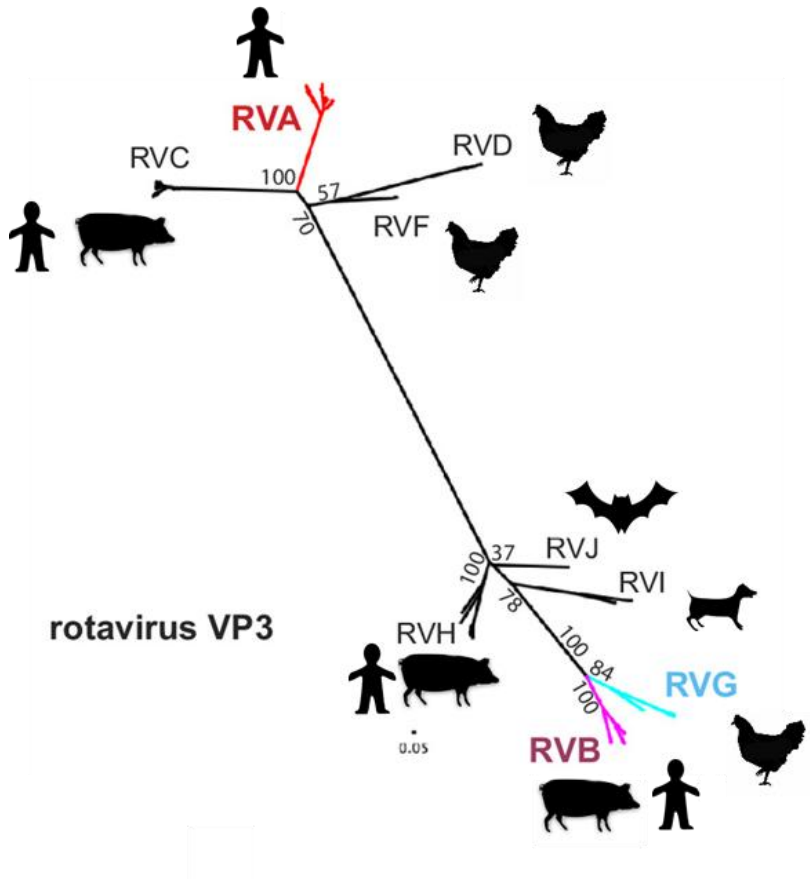

Figure 11. Phylogenetic classification of rotaviruses. Rotavirus phylogeny is based on VP3 amino acid sequences into nine genogroups and their associated host species, including humans, pigs, chickens, cats, mice and bats. Adapted with modifications from (165).

HRoV infects and replicates in the mature, non-dividing enterocytes located in the middle and tip of the intestinal villi, as well as in EEC in the small intestine. Compared to HNoV, a variety of immortalized cell lines models are available for HRoV cultivation, including MA104 (green monkey kidney cells), HT-29 (human colon cancer cells), Caco-2 (human colorectal adenocarcinoma cells), as well as primary cell models such as HIE (166) and HIO (167). The susceptibility of both enterocytes and EEC to rotavirus infection has been shown in a mouse model, in transformed human enteroendocrine cell line and in HIE cultures (155).

Rotavirus attachment is mediated by the outer capsid protein VP4 (through its VP8 domain), which binds to HBGAs on the host cell surface. Rotavirus-HBGA interactions are P genotype-dependent and provides insights into host range restriction and interspecies transmission of different rotavirus strains. Emerging evidence indicates that HBGA binding and activity of fucosyltransferases (FUT2/FUT3) shape population susceptibility to HRoV (168).

In oligosaccharides binding assays, HRoV have demonstrated strain-specific recognition of HBGAs, as P[4] and P[8] strains were binding Le^b, H type 1, A-type HBGAs and mucin core antigen (67,169–173), whereas P[6] strains primarily recognizing precursor of H type 1 antigen or binding weakly to Le^b (67,174).

Some cell culture-adapted strains, such as HAL1166 P[8] and K8 P[8], demonstrated exclusive binding to A-type antigen, although without engaging α1,2-fucose moiety. Furthermore, A-type antigen has

been shown to outcompete binding of these strains to MA104 cell, thereby reducing infection (171). For other adapted strains, such as Wa P[8], the reported glycan binding profiles are inconsistent, with studies both supporting and refuting binding to Le^b and H type 1 HBGAs (67,171).

Saliva binding assays have confirmed the importance of FUT2 status for HRoV attachment, as binding of common P[4], P[6] and P[8] strains were observed only to saliva samples of secretor (FUT2+) donors (169,170,174). Recently, the necessity of FUT3 activity for HRoV binding has also been identified, as P[8] strains failed to bind to the saliva of FUT2+FUT3- donors. This finding aligns well with prior observations of difucosylated Le^b HBGA binding by P[4] and P[8] strains (67), as in order to have difucosylated HBGAs individuals have to be both FUT2 and FUT3 positive.

Following the attachment to the host cell, rotaviruses are internalized via endocytosis. Upon trafficking to the endosomes, low calcium concentration triggers the loss of the VP4-VP7 outer layer. This results in the release of transcriptionally active double layer particles (DLPs) into the cytoplasm (175).

From each of the 11 dsRNA segments, capped (+)ssRNAs are transcribed. These transcripts either undergo translation, or serve as templates for the synthesis of -ssRNA during replication of the viral genome (176).

In the cytoplasm, virus-encoded NSP2 and NSP5 proteins interact to form inclusions, known as viroplasms, which concentrate the viral components required for genome assortment and replication, and the assembly of infectious subviral particles (ISVPs), thus acting as viral factories. Within these factories, interactions between several viral proteins (VP1, VP3, VP2, VP6, and NSP2) with the pre-genomic +ssRNA, result in their co-packaging into early assembly intermediates. Inside these intermediates, VP1/VP2 interactions initiate dsRNA synthesis from +ssRNA template. Subsequently, intermediate capsid protein VP6 assembles onto the core to form the DLPs, which bud from viroplasms into ER-membranes, where NSP4 is inserted, acting as an intracellular receptor for DLPs. Later, DLPs acquire the membrane-resident outer-capsid proteins, VP7, and the spike protein, VP4, forming a temporary enveloped particle. The envelope is lost during the formation of the infectious triple layer particle (175,176).

Seroconversion and protective status to HRoV has been demonstrated to correlate with FUT2 and FUT3 status in several epidemiological studies (67,177–179). The role of HBGAs in modulating the host susceptibility to attenuated rotavirus vaccine, and their subsequent influence on vaccine efficacy has emerged as areas of public health research. This is particularly relevant in low- and middle-income countries, where the genetic diversity of ABO, FUT2 and FUT3 alleles and their population frequencies, differ compared to European or North American populations (180,181), and may account for the reduced efficacy of rotavirus vaccines (155). The dependency of HRoV infection *in vitro* and *in vivo* on FUT2/3-mediated glycan expression is less well defined compared to HNoV.

1.3. Influenza A virus

Influenza viruses are enveloped -ssRNA viruses with a segmented genome. Among the four genera - influenza A, B, C and D, only influenza A and B are known to cause infectious respiratory disease in humans. Both influenza A and influenza B viruses contain eight RNA segments, which encode the RNA dependent RNA polymerase (RdRp), viral nucleoprotein (NP), matrix protein (M1), membrane protein (M2), the nonstructural protein NS1 and nuclear export protein (NEP), as well as two major surface glycoproteins, namely, hemagglutinin (HA) and neuraminidase (NA) (Figure 12). HA is composed of

globular ‘head’ and ‘stalk’ domains, which facilitate viral entry, while NA facilitates viral release. These two viral glycoproteins are located at the surface of the virus particle and are the main targets for protective antibodies induced by influenza virus infection and vaccination (182).

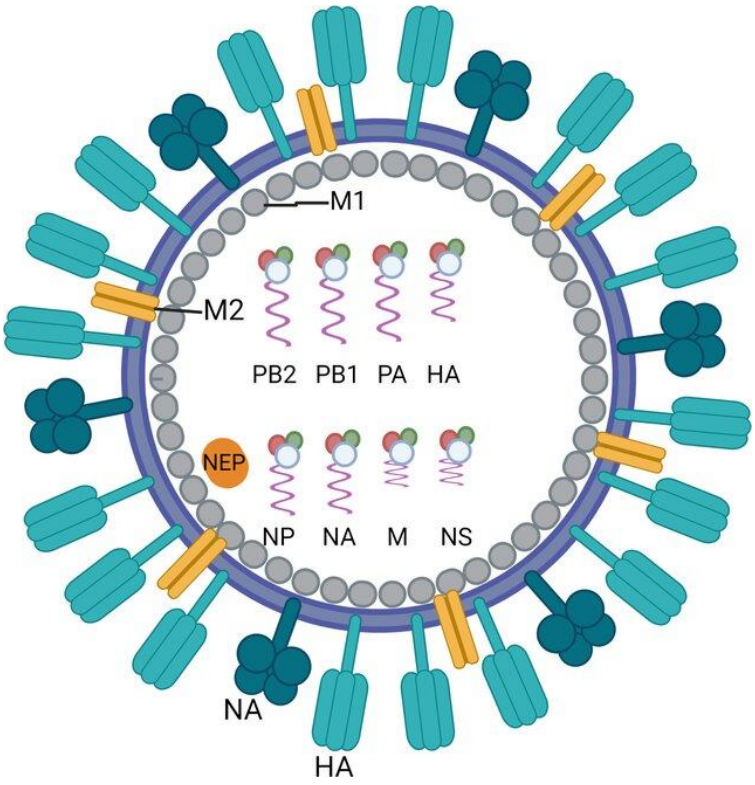

Figure 12. Schematic of an influenza A virus particle. Influenza A virus encodes the RNA polymerase complex (PB1, PB2, PA), surface glycoproteins hemagglutinin (HA) and neuraminidase (NA), nucleoprotein (NP), matrix protein (M1), ion channel (M2), and nonstructural proteins (NS1, NEP). HA mediates cell entry, while NA facilitates viral release. Additional accessory proteins (e.g., PB1-F2, PA-X in influenza A) modulate host responses. Adapted from (183).

The segmented nature of the influenza genome enables genetic reassortment, wherein genomic RNA segments may be exchanged when two viruses of the same type (two influenza A viruses or two influenza B viruses) infect the same cell. This capacity for reassortment, particularly in influenza A viruses, contributes to their remarkable antigenic diversity. Influenza A viruses circulate not only in humans but also in domestic animals, pigs, horses and poultry and in wild migratory birds. A total of 16 antigenically different HA and 9 antigenically different NA subtypes have been identified among the avian strains of influenza A virus, providing a vast genetic and potential for emergence of novel strains (184).

Transmission of human influenza viruses occurs through the respiratory route, targeting epithelial cells of upper and low respiratory tract. In contrast, avian influenza viruses are typically transmitted through the faecal-faecal, faecal-oral or faecal-respiratory routes, with replication primarily occurring in the intestinal tract of birds. In humans, severe disease is associated with viral replication in the lower respiratory tract and resulting inflammation due to immune cell infiltration (182,184).

The viral replication cycle is initiated by the binding of the HA to the host cell surface sialylated glycans. Human-adapted influenza viruses preferentially bind to α2,6-linked sialic acids, which are abundant in the human respiratory tract, whereas avian influenza viruses favour binding to α2,3-linked sialic acids,

which are more abundant in the epithelial cells of the human lower respiratory tract and of the avian intestinal tract, respectively (182,184).

After binding, the virus is internalized via endocytosis. As the endosome matures and acidifies, HA undergoes a conformational change that enables fusion of viral and endosomal membranes. As the endosomal pH varies between host species, the pH stability of HA is one of the determinants of viral tropism. The fusions of membranes results in the release of virus genetic material in the form of eight viral ribonucleoproteins (vRNPs), into the cytoplasm. The vRNPs are subsequently transported into the nucleus of the infected cells, where transcription and replication of the viral RNA takes place. The viral polymerases (PB1, PB2 and PA) and viral NP are also transported to the nucleus to facilitate the viral RNA synthesis (185).

At the same time, virus transmembrane proteins HA, NA and M2 are trafficked to the plasma membrane. Budding of new virions happens via the incorporation of the vRNPs into new virus particles composed of M1 viral protein with a membrane derived from the host plasma membrane and containing the viral transmembrane proteins. The NA activity prevents non-productive binding of new virions HAs to sialic acids in the membrane of the infected cells, facilitating viral spread. Viral replication results in cell death via apoptosis and contributes to tissue damage and disease symptoms (185).

Although influenza is classically regarded as a respiratory virus, certain seasonal and novel IAV may also replicate within human gastrointestinal tissue (186). This is supported by clinical observations, such as detection of viral RNA and virus isolation from stool or rectal swab specimens, and histopathological findings in autopsy cases (187,188). Additionally, *in vitro* and *in vivo* studies have demonstrated replication of IAV in human intestinal epithelial cells (189–192) and in gastrointestinal tract of animals inoculated with IAV intranasally (193,194). Possibility of IAV replication in the gut is also supported by the widespread distribution of α2,3- and α2,6-linked sialic residues in the human and animal intestine, which may serve as functional receptors for virus entry (186).

IAV infectious models include diverse *in vitro* primary and immortalized cell systems. Conventional immortalized cell models such as MDCK, A549, and HEK293T support viral entry and replication but require supplementation with exogenous trypsin to cleave the HA precursor (HA0) into HA1/HA2, a modification required for productive infection and viral spread (195). More advanced primary models, including primary human airway epithelial cells, air-liquid interface (ALI) cultures, and lung organoids, providing differentiated and polarized epithelial lining that closely mimic *in vivo* cellular composition, innate immune responses, and tissue physiology (196). Together, these *in vitro* systems enable investigating of IAV replication, host-pathogen interactions, and preclinical assessment of antivirals.

The capacity of IAV to utilize non-fucosylated glycans for cellular entry, along with its gastrointestinal tropism, highlights its utility as a model for investigating glycan-mediated mechanisms of viral infection.

1.4. Polyamines

One of the objectives of this study are polyamines, a class of small, positively charged carbon-chain molecules that are present in all cells. The three major biogenic polyamines are putrescine, spermidine, and spermine (Figure 13). These molecules are synthesized through a tightly regulated metabolic pathway starting from ornithine. Ornithine is converted to putrescine by ornithine decarboxylase 1

(ODC1), which subsequently converted into spermidine by the spermidine synthase (SRM), and further into spermine by the spermine synthase (SMS). In addition to endogenous biosynthesis, commensal gut bacteria can produce PAs, which are absorbed by the host and contribute to systemic polyamine levels (197).

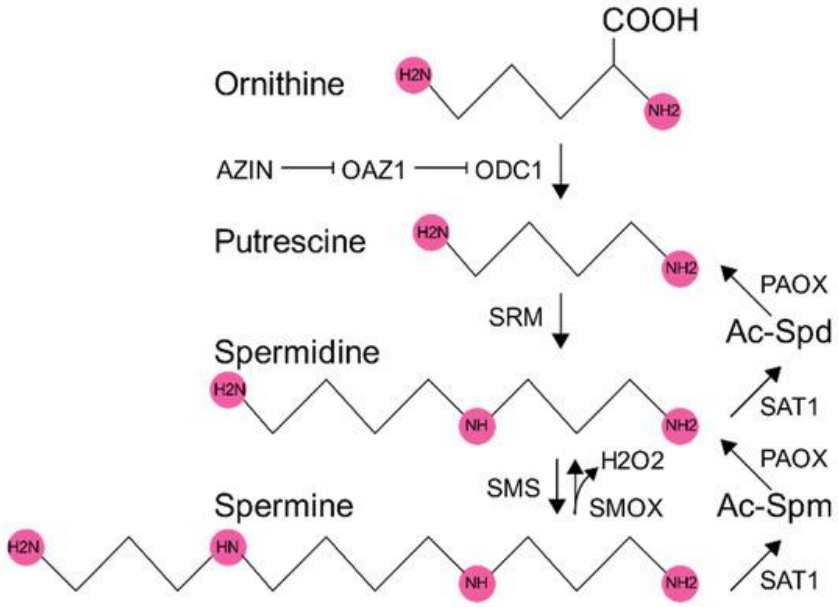

Figure 13. Schematic of the polyamine pathway in mammalian cells. An ornithine precursor is deacetylated by ornithine decarboxylase (ODC1) to form putrescine. Subsequently, putrescine is converted to spermidine by spermidine synthase (SRM), and spermidine is further converted to spermine by spermine synthase (SMS). ODC1 antizyme (OAZ1) inhibits ODC1 enzyme, while antizyme in turn can be inhibited by antizyme inhibitor (AZIN). The conversion of spermine to spermidine produces hydrogen peroxide (H_2O_2) byproduct. Spermine and spermidine are acetylated by spermidine-spermine acetyltransferase (SAT1) to form acetylated moieties (Ac-Spm and Ac-Spd). Acetylated spermidine or spermine can be converted to putrescine or spermidine through the action of polyamine oxidase (PAOX). Adapted from (197).

Polyamine participates in a wide range of cellular processes, including DNA stabilization, transcription regulation, protein translation, chromatin remodeling, and modulation of membrane fluidity. In the context of this study, the role of polyamines in nucleic acid stabilization and protein translation are particularly relevant (197,198).

Firstly, polyamine stabilizes nucleic acids by electrostatically binding the negatively charged phosphate backbone of RNA and DNA. This interaction supports nucleic acid conformation and influences host ability to sense cytoplasmic DNA (Figure 14). Spermine and spermidine facilitate the transition from B- to Z-DNA conformation that is not recognized by DNA cytoplasmic sensor cyclic GMP-AMP synthase (cGAS). cGAS can detect cytosolic DNA and initiate downstream signaling that results in activating type I interferon and interferon-stimulated genes (199). While cGAS can sense viral DNA from DNA viruses, it can also detect leaked host mitochondrial and nuclear DNA in cytoplasm during RNA virus infection, including noroviruses. Such leakage acts as a danger signal, triggering activation of innate immune response (116). The polyamine-induced Z-conformation masks this signal from cGAS, thereby suppressing the interferon response and serves pro-viral function. For instance, supplementation with

spermine and spermidine during herpes simplex virus (HSV-1, DNA virus) infection facilitates infection both in vivo and in vitro via inhibition of interferon production (199).

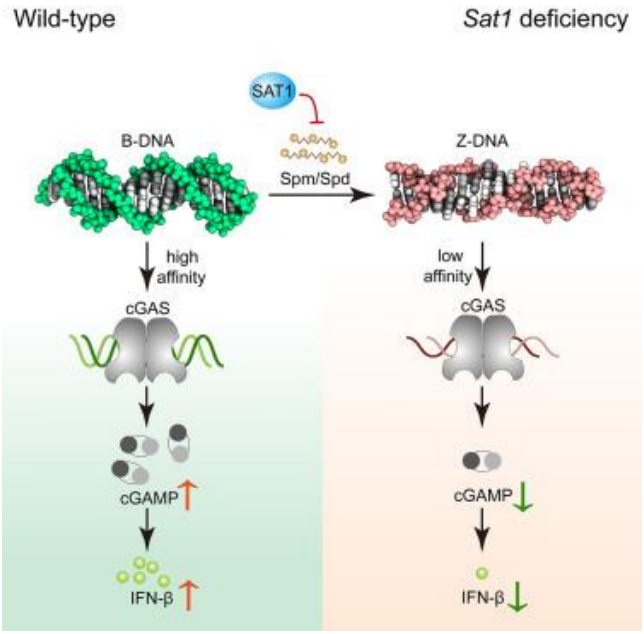

Figure 14. Schematic representation of the polyamines role in interferon production. Spermine and spermidine induce a B-to-Z DNA transition to reduce B-DNA concentrations in the cytoplasm. This conformational shift limits DNA binding by cGAS, leading to reduced cGAS activation and downstream inhibition of interferon-β (IFN-β) synthesis. Adapted from (199).

Secondly, spermidine plays a critical role in the post-translational regulation known as hypusination, which involves the covalent attachment of spermidine to the eukaryotic translation initiation factor 5A (eIF5A) (Figure 15). This modification is required for functional activation of eIF5A and subsequent protein translation (197). The synthesis of SREBP2, a master regulator of lipid synthesis pathways, is dependent on hypusinated eIF5A activity, which leads to the essential role of polyamine in cell lipid synthesis. SREBP2-regulated proteins are particularly relevant for RNA viruses, as they require overproduction of lipids for generation of viral replication factors and for proper binding of viral particles to cellular membranes (200).

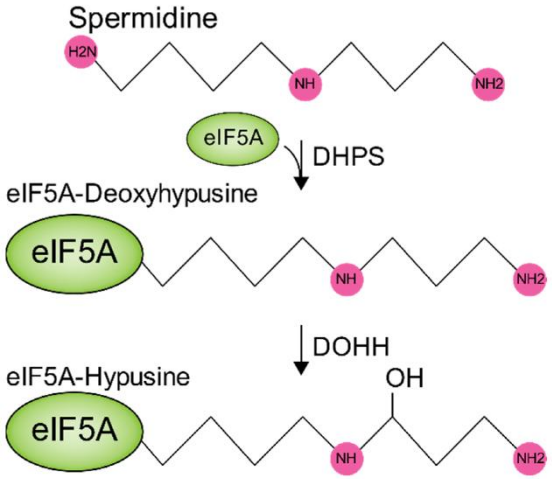

Figure 15. The mammalian eIF5A hypusination pathway. Spermidine is conjugated to eIF5A by the deoxyhypusine synthase (DHPS) to form eIF5A-deoxyhypusine, which is deacetylated by deoxyhypusine hydroxylase (DOHH) to form eIF5A-hypusine. Adapted from (197).

Third, polyamine takes part in modulating programmed cell death. Depletion of polyamine has been shown to protect cells from apoptosis induction across multiple cell types, including epithelial (201) and immune cell (202). Although the precise mechanism remains unknown, the PI3-kinase-Akt pathway has been identified as key modulation. Polyamine depletion reduces abundance of cell death regulation proteins, such as caspases (203), prevents externalization of PS to the outer membrane leaflet (204) and reduces the cellular response to extrinsic cell death signals such as tissue necrosis factor alpha (TNF-α) (201,205).

Polyamines have been identified as host factors important for the replication of numerous DNA and RNA viruses. Polyamines support critical steps in the viral infection, such as virus binding, genome replication, transcription, and translation of viral proteins and virion assembly (197,206). For example, Coxsackievirus B3 (CVB3) (200), a picornavirus, and SARS-CoV-2 (207) requires polyamine for cell binding and entry, while Zika virus (ZV) and other Flaviviruses require polyamines for genome replication (208). Bunyaviruses, like Rift Valley Fever Virus (RVFV), incorporate polyamines into virions and rely on polyamines for production of infectious particles (209,210). Some RNA viruses like Ebola virus and Hepatitis B require polyamines for hypusination for synthesis of viral proteins (211,212).

Additionally, polyamine metabolism represents a validated therapeutic target in the treatment of trypanosomosis. The irreversible ornithine decarboxylase (ODC) inhibitor difluoromethylornithine (DFMO, eflornithine) is an approved drug for the treatment of African trypanosomiasis and is widely used in clinical practice (213–215).

1.5. Aim of the thesis

The aim of this thesis was to investigate the role of host and environmental factors in enteric virus infection using a physiologically relevant 3D-HIE model that recapitulates key features of the human intestinal epithelium, such as cell polarity and differentiated epithelial cells.

This thesis is divided into four sections addressing two main objectives:

First, a 3D-HIE was adapted to support infection with enteric viruses from clinical isolates, enabling the study of glycan-dependent viruses as potential targets for inhibition.

Second, the effects of host and environmental factors, including polyamines, bile acids, and divalent cations, on norovirus infection were examined, using MNV as a tractable surrogate for functional studies and HNoV infections in 3D-HIEs as a relevant model.

Section 1. Adapting the 3D-HIE system to support enteric virus infections from clinical isolates

- Identify a panel of infectious stool samples from a lab internal biobank using the 3D-HIEs model
- Evaluate and optimize reproducibility of HNoV infections from stool samples
- Establish molecular tools to visualize HNoV infection in 3D-HIEs
- Expand the 3D-HIE platform to include additional glycan-dependent viruses

Section 2. Targeting cell-surface glycans in a 3D-HIE model to block viral Infection

- Investigate the importance of fucosylation in 3D-HIEs for HNoV, HRoV, and IAV infections
- Assessing cell-surface glycans as therapeutic targets for blocking HNoV, HRoV, and IAV infections through lectin competition
- Evaluate natural glycans and glycomimetics as competitive inhibitors to target HNoV infection

Section 3. Investigating the role of environmental factors in norovirus infection

- Investigate the impact and synergy of divalent cations and bile acid GCDCA on MNV infection and antibody escape in immortalized cell culture
- Investigate the impact and synergy of divalent cations and bile acids GCDCA on HNoV infection and antibody escape in 3D-HIEs

Section 4. Investigating the role of polyamines in norovirus infection

- Examine the relevance and underlying mechanism of polyamines effect on MNV infection in immortalized cell culture
- Investigate the relevance of polyamines for HNoV infections in 3D-HIEs

2. Materials

Table 2. Chemicals and kits

Chemical, reagent, kit	Manufacturer/Vendor
2'-C-methylcytidine (2-CMC)	Sigma/Merck
2-fucosyllactose (2-FL)	Laura Hartmann, Uni Düsseldorf
Acrylamide:Bisacrylamide (29:1)	Ro Carl Roth GmbH + Co. KGth
Advanced Dulbecco's Modified Eagle Medium/F12 (DMEM/F12)	Gibco
Ammonium persulfate (APS)	Carl Roth GmbH + Co. KG
Ammonium sulfate	Carl Roth GmbH + Co. KG
AS1842856 (AS184), FOXO inhibitor	AdooQ BioScience
Avicell	IMCD
B27 Supplement (B27)	Thermo Fisher Scientific
Bio-Rad iTaq Universal Probe kit	Bio-Rad
Bovine Serum Albumin (BSA)	BioMol
Bromophenol blue	Carl Roth GmbH + Co. KG
Difluoromethylornithine (DFMO)	Tebu-Bio
Dimethyl sulfoxide (DMSO)	Carl Roth GmbH + Co. KG
Direct-zol™ RNA Prep Kit (RNA Prep Kit)	Zymo Research
ECL reagent (Pierce™ ECL Western Blotting Substrate)	Thermo Fisher Scientific
Erythrosine B	Sigma/Merck
Fetal Bovine Serum (FBS)	Capricorn Scientific
Fucoidan from *Fucus vesiculosus*	Sigma/Merck
GFP-CERTIFIED® Apoptosis/Necrosis kit	Enzo Life Sciences GmbH
Glycerin	Carl Roth GmbH + Co. KG
Glycine	Carl Roth GmbH + Co. KG
Glycochenodeoxycholic acid (GCDCA)	Sigma/Merck
HEPES (4-(2-hydroxyethyl)-1-piperazineethanesulfonic acid)	C-C-Pro
Hoechst 33321 dye	Thermo Fisher Scientific
LumiKine™ Xpress mIFN-β 2.0	Invivogen
KCl (Potassium chloride)	Carl Roth GmbH + Co. KG
L-Fucose	Thermo Fisher Scientific or Sigma-Aldrich
L-Galactose	Merck-Millipore
L-Glucose	Carl Roth GmbH + Co. KG
L-Glutamine	C-C-Pro
Lacto-N-Fucopentaose I (LNFP I)	by Laura Hartmann; Uni Düsseldorf
LDH Cytotoxicity Assay Kit	Cayman Chemical
Leu15-Gastrin	Sigma-Aldrich
Luna Universal Probe One-Step RT-qPCR Kit	New England Biolabs, NEB
LY294002	Tebu-Bio

Magnesium chloride hexahydrate (MgCl2·6H2O)	Carl Roth GmbH + Co. KG
Magnesium sulfate heptahydrate (MgSO4·7H2O)	Carl Roth GmbH + Co. KG
Matrigel (Basal Membrane Matrix)	Corning
MEM (Minimum Essential Medium)	Thermo Fisher Scientific
Methanol p.a.	Carl Roth GmbH + Co. KG
Milk powder	Carl Roth GmbH + Co. KG
Mouse Epidermal Growth Factor (mEGF)	Invitrogen
N-acetylcysteine	Sigma/Merck
N1,N11-Diethylnorspermine tetrahydrochloride (DENSpm)	Bio-Teche
Nitrocellulose membrane (0.2 µm)	VWR or Sartorius Stedim Biotech
Noggin/R-spondin Conditioned Medium	Produced in Taube Lab
Paraformaldehyde	Carl Roth GmbH + Co. KG
Prestained protein ladder (Cat. 26616)	Thermo Fisher Scientific
Ruxolitinib	Sigma/Merck
Sodium dodecyl sulphate (SDS)	Carl Roth GmbH + Co. KG
Tetramethylethylenediamine (TEMED)	Carl Roth GmbH + Co. KG
Tricin	Carl Roth GmbH + Co. KG
Tris (Tris(hydroxymethyl)aminomethane)	Carl Roth GmbH + Co. KG
Triton X-100	Sigma/Merck
Trypsin/ EDTA (T/E)	Sigma/Merck
TPCK-treated trypsin	Sigma/Merck
Tween 20	Sigma/Merck
Western Lightning Plus-ECL	Perkin Elmer
α-Spd ELISA kit (GENLISA™)	Biozol

Table 3. General buffers

Buffer	Composition
PBS (Phosphate-buffered saline)	137 mM NaCl; 10 mM Na_2HPO_4; 2.7 mM KCl; 1.8 mM KH_2PO_4 [pH 7.4]
Sodium phosphate buffer	78 mM Na_2HPO_4; 22 mM NaH_2PO_4 [pH 7.4]

Table 4. Microscopy analysis buffers

Buffer	Composition
PBS-Triton	0.1 % (v/v) Triton X-100 in 1× PBS
Blocking buffer	5 % (w/v) Bovine Serum Albumin (BSA) in 0.1 % PBS-Triton

Table 5. SDS-PAGE buffers

Buffer	Composition
Jagow buffer	0.3 M Tris; 0.3 % (w/v) Sodium dodecyl sulfate (SDS) in ddH_2O [pH 8.45]
Anode buffer (1×)	0.2 M Tris-HCl in ddH_2O [pH 8.9]
Cathode buffer	0.1 M Tris-HCl; 0.1 M Tricin; 0.1 % (w/v) SDS in ddH_2O [pH 8.25]
Denaturation buffer	62.5 mM Tris-HCl; 10 % (v/v) Glycerol; 5 % (v/v) β-Mercaptoethanol; 2 % (w/v) SDS; 0.1 % (w/v) bromophenol blue in ddH_2O [pH 6.8]

Table 6. Western Blot buffers

Buffer	Composition
Transfer buffer	25 mM Tris; 193 mM Glycine; 20 % (v/v) Methanol in ddH_2O
PBS-Tween	0.05 % (v/v) Tween 20 in 1× PBS
Blocking buffer	5 % (w/v) powdered milk in PBS-Tween

Table 7. Cell culture media

Medium	**Composition**
Plaque overlay medium	5 % (v/v) FBS; 1 % (v/v) Penicillin/Streptomycin (P/S); 1 % (v/v) L-Glutamine; 50 % (v/v) 2.4 % Avicel added to 2× MEM
CMGF−	1 % (v/v) HEPES; 1 % (v/v) Penicillin/Streptomycin (P/S); in Advanced Dulbecco's Modified Eagle Medium/F12 (DMEM/F12)
Differentiation Medium	2 % (v/v) B27; 1 % (v/v) N2; 1 mM N-acetylcysteine; 50 ng/mL Mouse Epidermal Growth Factor (mEGF); 10 nM Leu15-Gastrin;

	500 nM A83-01; 5 % (v/v) Noggin/R-spondin Medium; in CMGF−
DMEM10	10 % (v/v) FBS; 1 % (v/v) P/S; 1 % (v/v) L-Glutamine; 1 % (v/v) NEAA; in DMEM
DMEM5	5 % (v/v) FBS; 1 % (v/v) P/S; 1 % (v/v) L-Glutamine; 1 % (v/v) NEAA; in DMEM
Intesticult	Stem Cell Technologies medium (ready-to-use)
2x MEM (Minimal Essential Medium)	9.53 g MEM powder; 29 mL 7.5 % $NaHCO_3$; top up with ddH_2O to 500 mL; sterile filtered; [pH 7.3-7.4]
Polyamine-free Differentiation Medium	1 mM N-acetylcysteine; 50 ng/mL mEGF; 10 nM Leu15-Gastrin; 500 nM A83-01; 5 % (v/v) Noggin/R-spondin Medium; in CMGF−

Table 8. Antibodies

Name	Host	Used for	Notes, working dilution	Supplier (Cat. No.)
anti-Caspase-3	Rabbit	Western Blot	Monoclonal 1:1000	Cell Signaling Technologies (9662S)
anti-chromogranin A (CHGA)	Rabbit	Immunofluorescence	Polyclonal, 0.5 µg/mL	Sigma-Aldrich (HPA017369)
anti-dsRNA (clone rJ2)	Mouse	Immunofluorescence	Monoclonal, 1:25-50	Merck-Millipore (MABE1134)
anti-GII.1 ORF-2 (HV-18)	Mouse	Neutralization assay	Monoclonal, 90-180 µg/mL	Kind gift of Peter Sander, R-Biopharm
anti-GII.10 ORF-2	alpaca	Neutralization assay	Nanobody, 60 µg/mL	Kind gift of Dr. Florian Schmidt (University of Bonn)
anti-GII.2 ORF-2 (SMV)	Mouse	Neutralization assay	Monoclonal, 2 µg/mL	Kind gift of Peter Sander, R-Biopharm

anti-GII.4 P domain (A1431)	Mouse	Neutralization assay	Monoclonal, 4 µg/mL	Absolute Antibody (Ab02974-1.1)
anti-GII.7 ORF-2 (serum)	Rabbit	Neutralization assay	Polyclonal, 1:10	Kind gift of Dr. Christiane Wobus, University of Michigan
anti-MNV ORF-2 (A6.2)	Mouse	Neutralization assay	Monoclonal, 2 µg/mL	inhouse from hybridomas
anti-MNV ORF-2	Rabbit	Immunofluorescence	polyclonal serum, 1:100	Kind gift of Dr. Christiane Wobus, University of Michigan
anti-rabbit IgG-AF488	Goat	Immunofluorescence	Secondary, 1:1000-1500	Thermo Fisher Scientific (A-11008)
anti-mouse IgG-AF594	Donkey	Immunofluorescence	Secondary, 1:1000-1500	Jackson ImmunoResearch (715-587-003)
anti-mouse IgG-HRP	Goat	Western Blot	Secondary, 1:1000	Dianova (115-035-003)
anti-PARP	Rabbit	Western Blot	Monoclonal, 1:1000	Cell Signaling Technologies (9542T)
anti-mouse IgG-Cy3	Goat	Immunofluorescence	Secondary, 1:1000-1500	Jackson ImmunoResearch (115-165-003)
anti-rabbit IgG-HRP	Goat	Western Blot	Secondary, 1:1000	Dianova (111-045-003)
anti-GII.3 ORF-2 (TV19)	Mouse	Western Blot	Monoclonal, 2-5 µg/mL	Kind gift of Peter Sander, R-Biopharm
anti-β-Actin	Mouse	Western Blot	Monoclonal, 0.01 µg/mL	Bio-Techne (MAB8929-SP)

Table 9. Cells and viruses

Cells / Viruses	Notes
BV-2	Murine brain microglial cells; a kind gift from Ian Goodfellow; University of Cambridge

HIE HT-124 cell line (21)	Fetal human intetsinal enteroids derived from illeal tissue; a kind gift from Dr. Christiane Wobus; University of Michigan
HNoV	Stool-isolates from internal laboratory collection, obtained from Christian-Albrechts-University of Kiel (CAU) and The University Hospital Schleswig-Holstein (UKSH) Lübeck
HRoV	Stool-isolate obtained from Sonja Jacobson, Robert Koch Institute
Huh7^{naïve}	Human hepatocarcinoma cells; a kind gift from Norbert Tautz; University of Lübeck
Huh7^{mCD300lfb}	Genetically modified human hepatocarcinoma Huh7^{naive} cells expressing murine CD300lf receptor and reporter system for MNV
Influenza A virus A/WSN/1933 (H1N1)	A kind gift from Dr. Gülsah Gabriel; Leibniz Institute of Virology
MDCK (Madin-Darby Canine Kidney cells)	Canine kidney cells; A kind gift from Dr. Paul Becher; University of Hannover
MNV.CR3	a kind gift from Dr. Christiane Wobus; University of Michigan
MNV-1	Recombinant MNV-1.CW1; a kind gift from Dr. Christiane Wobus; University of Michigan
RAW264.7	Murine macrophages; a kind gift from Dr. Christiane Wobus; University of Michigan

Table 10. List of HNoV and HRoV clinical isolates

Isolate strain	Stool number	Ct value	GEs/mL	Source
GII.4 Sydney	153	18.57	4×10^6	CAU
GII.4 Den Haag #1	805929	17.93	$9{,}3\times10^6$	UKSH
GII.4 Den Haag #2	602064	18	5×10^6	UKSH

GII.4 Yerseke	560252	14.71	$5,2\times10^{7}$	UKSH
GII.4	20942	18	-	University of Michigan
G3.P[8]eq.-like	-		$1,06\times10^{10}$	Robert Koch Institute

Table 11. Realtime PCR primers and probes

Name	Sequence type	Sequence
HNoV GII	Forward	AGCCAATGTTCAGATGGATG
	Probe	[6-FAM]-TGGGAGGGCGATCGCAATCTGGC-[BHQ-1]
	Reverse	TCGACGCCATCTTCATTCAC
HRoV	Forward	ACTCAATGTGTAGTTGAGGTCGG
	Probe	[VIC]-ATCTTTCCGCACGC-[MGB]
	Reverse	CTTTTAAAAGTTCTGTTCCGAG
MNV	Forward	GTGCGCAACACAGAGAAACG
	Probe	[6-FAM]-CTAGTGTCTCCTTTGGAGCACCCTA-[BHQ-1]
	Reverse	CGGGCTGAGCTTCCTGC

Table 12. Equipment/Software

Equipment / Software	Notes
Confocal Microscopy	Carl Zeiss
Fluorescence Microscopy	Carl Zeiss (Axio Observed Z1)
2-photon Microscopy	W Plan-Apochromat; Carl Zeiss
GraphPad Prism 10	GraphPad Software
ImageJ	National Institutes of Health (NIH)
Imaris Viewer 10.2.0	Oxford Instruments

3. Methods

3.1. Virus stock preparation and purification

Production and purification of MNV-1 virus stock

MNV-1 virus stock was generated to perform infectivity assays with defined MOIs. BV-2 cells were cultured in 150 cm² flasks to 70-80% confluency and infected with MNV-1.CW1 passage 3 or MNV CR3 passage 4 at an MOI of 0.1 in 30 mL DMEM5. Cultures were incubated at 37 °C, 5% CO_2, and 90% RH for 24 h. Virus was harvested once >80% of cells displayed CPE. To release intracellular virus, cultures were frozen at -80 °C and thawed, resulting in complete cell lysis.

Lysates were clarified by centrifugation at 3,000×g for 10 min at 4 °C to remove cell debris. Ammonium sulfate was added to the supernatant to achieve 40% saturation., incubated overnight at 4 °C with rotation, and centrifuged at 10,000×g for 15 min at 4 °C. The resulting pellet was resuspended in 5 mL of sodium phosphate buffer (100 mM, pH 7.4) per five 150 cm² flasks, clarified at 5,000×g for 5 min to remove aggregates, and sterile-filtered through a 0.22 µm membrane. Virus stocks were aliquoted in 150 µL portions and stored at -80 °C. Viral titers were determined by $TCID_{50}$ assay.

Preparing of HNoV, HRoV and HAstV infectious stool filtrates

Virus-containing stool samples were thawed at RT. A 100 µL aliquot of stool was diluted in 900 µL Opti-MEM in a sterile screw-cap tube and homogenized by pipetting. Suspensions were centrifuged at 14,000×g for 3 min to pellet debris, and the supernatant was transferred into 9 mL Opti-MEM in a sterile 15mL tube. The mixture was sterile-filtered through a 0.22 µm membrane. Stool filtrates were aliquoted in 500 µL portions and stored at -80°C.

HNoV GII.4 isolates were sequenced at the Robert Koch Institute by Dr. Sandra Niendorf. Strain assignment was performed based on the VP1 nucleotide sequence using the Norovirus Typing Tool version 2.0 (216).

Production of IAV H1N1 virus stock

IAV H1N1 stocks were produced in MDCK cells. Cells were cultured in 150 cm² flasks to 70-80% confluency and infected with IAV A/WSN/1933 (H1N1) at an MOI of 1 in 30 mL DMEM10 containing 4 µg/mL of TPCK-treated trypsin. Cultures were incubated at 37 °C, 5% CO_2, and 90% RH for 48-72 h. Virus was harvested once >80% of cells exhibited CPE. Intracellular virus was released by one freeze-thaw cycle (-80 °C). Lysates were clarified at 5,000×g for 10 min at 4 °C to remove cell debris. Virus stocks were aliquoted in 500 µL portions and stored at -80 °C. Viral titers were determined by plaque assay.

3.2. Immortalized cell culture

RAW264.7 macrophages

RAW264.7 cells were maintained at 37 °C in a humidified incubator with 5% CO_2 and 90% RH. Cultures were propagated in 150 cm² flasks containing 30 mL DMEM10. Once confluency exceeded 80%, the medium was aspirated, and cells were detached using a cell scraper in 10 mL of fresh DMEM10. Cells

were split at a ratio of 1:15 to 1:20 into flasks containing 30 mL fresh medium. Cultures typically reached confluency within 2-3 days and were used up to passages 30-35.

BV-2 microglial cells

BV-2 cells were maintained at 37 °C in a humidified incubator with 5% CO_2 and 90% RH. Cultures were propagated in 150 cm² flasks containing 40 mL DMEM5. Once confluency exceeded 80%, the medium was aspirated and cells were detached using a cell scraper in 10 mL of fresh DMEM5. Cells were split at a ratio of 1:25 to 1:30 into flasks containing 40 mL fresh medium. Cultures typically reached confluency within 2-3 days and were used up to passage 30-35.

Huh7naive and Huh7-mCD300lf-sec61b cells

$Huh7^{naive}$ and $Huh7^{mCD300lf}$ cells were maintained at 37 °C in a humidified incubator with 5% CO_2 and 90% RH in 150 cm² flasks containing 25 mL DMEM10. Cultures were passaged at 80-100% confluency. To passage, the medium was aspirated, cells were washed once with 20 mL PBS, and detached with 2 mL Trypsin/EDTA for 2 min at 37 °C. Cells were split at a ratio of 1:8 to 1:12 and the culture volume was replenished with DMEM10 up to 25 mL. Cultures typically reached confluency within 3-4 days and were maintained up to the early 30s pa ssages.

MDCK cells

MDCK cells were maintained at 37 °C in a humidified incubator with 5% CO_2 and 90% RH in 150 cm² flasks containing 30 mL DMEM10. Cultures were passaged at 80-100% confluency. To passage, the medium was aspirated, cells were washed once with 40 mL PBS, and detached with 2 mL Trypsin/EDTA for 5-7 min at 37 °C. Cells were split at a ratio of 1:30 to 1:40, and the culture volume was replenished with DMEM10 up to 25 mL. Cultures typically reached confluency within 3-4 days and were maintained up to the early 30s passages.

Cell counting using the Neubauer counting chamber

For plating purposes, cell density and viability were determined using a Neubauer hemocytometer. Cells were detached from flasks as described above. A 20 µL aliquot of the suspension was mixed 1:1 with 1 mg/mL Erythrosine B in PBS, yielding a final volume of 40 µL. A mixture of 10 µL was loaded into a Neubauer chamber and examined under the light microscopy.

Cells were counted in the four large quadrants. Viable cells appeared bright and unstained, whereas non-viable cells appeared red. The number of viable cells per mL was calculated according to the manufacturer's instruction:

$$avarage\ number\ of\ cells\ per\ one\ quadrant\ \times\ 10{,}000\ \times\ dilution\ factor$$

Treatment of mammalian cell culture prior infection

To assess the influence of polyamine on MNV-1 infection, polyamine depletion and degradation were induced in RAW264.7, $Huh7^{mCD300lf}$, and BV-2 cells using DFMO and DENSpm, respectively. Cells were sub-cultured from confluent flasks at a 1:8 ratio for RAW264.7 and BV-2 cells, and at a 1:4 ratio for Huh7 cells. The following day, cells were treated with 500 µM DFMO and incubated at 37 °C, 5% CO_2,

and 90% RH. After 72 hours of treatment, cells were harvested by scraping (RAW264.7 and BV-2) or trypsinization (Huh7), counted, and re-plated into 24-well flat-bottom plates at a density of 6×10^5 cells/well for RAW264.7, 4×10^5 cells/well for BV-2 and 2×10^5 cells/well for Huh7 in 500 µL DMEM5 or DMEM10. To maintain polyamine depletion, DFMO was replenished at a final concentration of 500 µM for the remaining 24 hours prior to infection. For polyamine degradation, RAW264.7 cells were seeded at a density of 4×10^5 cells/well, and BV-2 and Huh7 cells at 2×10^5 cells/well. Cells were treated immediately after plating with 100 µM DENSpm for 24 hours prior to infection under standard culture conditions.

3.3. Primary cell culture

Maintenance of HIEs

For splitting of HIEs, the culture medium was removed and replaced with fresh ice cold CMGF− media. For 6-well plates, 1 mL of medium per well was used. The matrigel domes containing the HIEs were carefully detached using a sterile cell scraper. The suspension was pipetted two times up and down with a 1 mL pipette to disrupt the matrigel. To further dissociate the spheres, the suspension was passed twice through a sterile insulin syringe fitted with a 26G/27G needle. Dissociated spheres were combined with 9 mL of ice cold CMGF- in sterile 15-mL tube. The cell suspension was centrifuged at 80-90×g for 4 minutes at 4 C° to selectively pellet dissociated spheres while excluding matrigel debris. After centrifugation, the supernatant was discarded, and the pellet was resuspended in 200 µL of matrigel per well. The suspension was gently pipetted to ensure a homogeneous distribution without introducing air bubbles. A 1:2 split ratio was used to maintain spheroid density.

The HIE matrigel suspension was plated onto pre-warmed tissue culture 6-well flat-bottom plates in 12 µL droplets, with 20-25 droplets per well. The plates were incubated at 37 °C for 10 minutes to allow matrigel to polymerize. Following solidification, 2 mL of intesticult medium was added to each well. The cultures were maintained at 37 °C, 5% CO_2, and 90% RH in a humidified incubator. Medium changes were performed every 2-3 days. Passaging was conducted on a 7-day schedule.

Differentiation of HIEs

HIEs were cultivated in differentiation medium for 7 days, with the medium being refreshed every 2 days. Cultures were incubated at 37 °C, 5% CO_2, and 90% RH in a humidified incubator. For polyamine -free HIE differentiation, the differentiation medium formulation without the B2 and N27 supplement was used.

Treatment of HIEs cells prior infection

To increase the number of EECs in 3D-HIE cultures, spheres were treated with AS184 at a concentration of 100 nM. Treatment was initiated 2 days after splitting and continued throughout stem sphere growth and HIE differentiation. AS184 was also supplemented post-infection to maintain EEC induction during viral replication.

For inhibition of fucosyltransferases, 3D-HIEs were treated with 500 µM 2-FPF inhibitor during the final 2 days of differentiation. In addition, 2-FPF was supplemented during viral inoculation and throughout the infection period to maintain inhibition.

For lectin competition assays, native lectins (dissolved in PBS) were applied at the indicated concentrations and used to pre-treat 3D-HIEs for 1 h at 37 °C prior to infection. Virus inocula were added directly without removing lectins, thereby maintaining competitive binding conditions.

For sugar and magnesium pre-treatments, 3D-HIEs were incubated with either 50 mM fucose (dissolved in ddH_2O) or 50 mM $MgCl_2$ (dissolved in ddH_2O) in differentiation medium for 1 h at 37 °C. Following incubation, HIEs were washed three times with 1 mL $CMGF^-$ in Eppendorf tubes to remove residual compounds.

For polyamine degradation, HIEs were treated with 100 µM DENSpm during the final 2 days of differentiation and incubated at 37 °C, 5% CO_2, and 90% RH. For infectivity assays conducted under polyamine-depleted conditions, all medium changes included 100 µM DENSpm to maintain polyamine depletion throughout the experiment.

3.4. Infection of immortalized and primary cell culture

Infection with MNV-1

One day prior to infection, cells were seeded at defined densities depending on the downstream application. For infectivity assays, RAW264.7 cells were plated at 4×10^5 cells/well and BV-2 and Huh7 cells at 2×10^5 cells/well in 24-well tissue culture plates. For confocal microscopy, 4×10^5 RAW264.7 cells were seeded per well in 8-well chambered glass slides. For Western blot (WB) analysis, 5×10^6 RAW264.7 cells were seeded per well in 6-well plates.

On the day of infection, MNV was added at the indicated multiplicity of infection (MOI) in 150 µL cold PBS per well (24-well or 8-chamber format) or 500 µL per well (6-well format). The MOI was calculated using the formula:

$$MOI = \frac{number\ of\ viruses}{number\ of\ target\ cells}$$

Cells were incubated for 1 h at 4 °C to allow viral attachment. Following incubation, the inoculum was aspirated, and cells were washed three times with ice-cold PBS (for polyamine assays) or sodium phosphate buffer (for magnesium assays). Fresh cell culture medium was added, and cultures were incubated at 37 °C, 5% CO_2, and 90% RH for the indicated times post infection. For polyamine assays, DFMO, DENSpm, spermine, spermidine or PI3-kinase inhibitor LY294002 were supplemented at indicated concentrations.

Harvesting of lysate or supernatant for titration

For supernatants, culture media from infected wells were collected, clarified by centrifugation at 500×g for 5 min to remove debris, and stored at -80 °C. For cell lysates, entire plates were frozen at -80°C. Upon thawing, cells were resuspended by pipetting to ensure complete lysis. Viral titers were determined by $TCID_{50}$ or plaque assay.

Infection of 3D-HIEs with HNoV, HRoV, HAstV and IAV H1N1

One confluent well of a 6-well plate (20-25 domes, ~15-20 spheroids per dome) was used for four infection conditions, including day 0 and 2 time points. HIE-containing matrigel domes were

mechanically disrupted by scraping, and spheroids were gently pipetted to be release from matrigel. Suspensions from 1-2 wells were pooled in 15 mL tubes on ice, adjusted to 10 mL with CMGF−, and centrifuged at 80-90×g for 4 min at 4°C. Supernatants were aspirated, leaving ~1 mL above the pellet, and residual Matrigel debris was carefully removed.

For infection, 100 µL spheroid suspension (~15-20 spheroids) was combined with 50 µL stool-derived virus filtrate and 20 µL GCDCA (final concentration 500 µM), adjusted to 200 µL with differentiation medium. This corresponded to an estimated MOI of 1, based on GE titers determined from 1% stool filtrates. The mixture was incubated for 1-2 h at 37 °C, 5% CO_2, and 90% RH. Following infection, HIEs were washed three times with CMGF− medium, each followed by centrifugation at 100×g for 3 min. During the third wash, pellets were resuspended in 1 mL CMGF− and split into two 500 µL aliquots. After a final centrifugation step, pellets were embedded in matrigel (30 µL per sample) and plated as 3-4 domes per well of a pre-warmed 24-well plate. Plates were incubated for 10 min to allow polymerization before overlaying with 500 µL differentiation medium containing 500 µM GCDCA, 2 µM Ruxolitinib, and other compounds. Samples from day 0 were harvested immediately in 400 µL TRIzol®. Cultures were incubated for 2 days before harvest, unless indicated otherwise. The same infection protocol was applied for HRoV and HAstV stool filtrates, with the additional step of virus activation by incubation with 10 µg/mL TPCK-treated trypsin for 30 minutes at 37 °C prior to infection.

IAV H1N1 infections were conducted using a similar protocol, but without bile acid supplementation. Instead, 4 µg/mL TPCK-treated trypsin was added to the culture medium and maintained throughout the 2-day incubation period.

Harvesting of lysate or supernatant for titration

For total lysates, matrigel domes containing HIEs were scraped and transferred into microcentrifuge tubes, followed by addition of 400 µL TRIzol®. Samples were stored at -20 °C. For separate analysis of supernatant and cells, culture media were collected into fresh tubes, supplemented with TRIzol®, and stored at -20 °C, while HIE domes were harvested directly into 400 µL TRIzol®.

3.5. Determination of viral titers

Tissue culture infectious dose 50 ($TCID_{50}$) assay

To quantify infectious MNV particles, $TCID_{50}$ assays were performed. For the assay, 1×10^4 BV-2 cells in 180 µL of DMEM5 were seeded per well in flat-bottom 96-well tissue culture plates. After cell adherence, 12-step 10-fold serial dilutions of virus samples were prepared directly on the plate. In brief, 20 µL of the viral sample was added to the wells in the first column, mixed thoroughly, and 20 µL was transferred to the next column, continuing up to the final dilution step. The last 20 µL was discarded to maintain equal volumes across wells. At least four technical replicates were performed for each condition. Plates were incubated for 3-4 days at 37 °C, 5% CO_2, and 90% RH. After incubation, wells were examined for signs of infection by light microscopy, assessing both the presence of CPE and medium color change due to pH shift. Viral titers were calculated as $TCID_{50}$/mL using the Reed-Muench method (Reed & Muench, 1938; reviewed in Ramakrishnan, 2016).

Plaque assay for MNV

For plaque titration of MNV, 2×10^5 Huh7-mCD300lf cells or 5×10^6 RAW264.7 cells were seeded per well in 6-well plates in 2 mL DMEM10 and incubated for 24 h at 37 °C, 5% CO_2, and 90% RH. Confluency was verified by brightfield microscopy and ranged between 60-80%. Six consecutive 10-fold serial dilutions (e.g., 10^{-1} to 10^{-6}) of viral samples were prepared in PBS. Briefly, 125 µL of sample was mixed with 1125 µL PBS (1:10), and 125 µL was transferred stepwise to subsequent dilutions. Duplicate 6-well plates were used per condition. The culture medium was aspirated, and 500 µL of each virus dilution was added to wells in sequence from highest to lowest dilution. Plates were incubated for 1 h at 37 °C, 5% CO_2, and 90% RH. The inoculum was then removed, and cells were overlaid with an Avicel medium. After 48 h incubation under the same conditions, an overlay medium was aspirated, cells were washed with 2 mL PBS per well, and stained with 1 mL of 1 mg/mL Erythrosine B for 5-10 min. The staining solution was aspirated, plates were air-dried, and plaques were enumerated to determine viral titers.

Plaque assay for IAV H1N1 virus

For plaque titration of IAV H1N1, 4×10^5 MDCK cells were seeded per well in 12-well plates in 2 mL DMEM10 and incubated for 24 h at 37 °C, 5% CO_2, and 90% RH. Confluency was verified by brightfield microscopy and ranged between 80-90%. Six consecutive 10-fold serial dilutions of viral samples were prepared as described for MNV. Technical duplicates were performed for each condition. Following the aspiration of culture medium, 500 µL of each dilution was added per well and incubated for 1 h at 37 °C, 5% CO_2, and 90% RH. After incubation, inoculum was aspirated and cells were overlaid with Avicel medium containing 4 µg/mL TPCK-treated trypsin. Plates were incubated for 72 hunder the same conditions. The overlay medium was aspirated, cells were washed with 2 mL PBS, fixed with 70% ethanol in ddH2O, and stained with 0.5 mL of 1 mg/mL Erythrosine B for 5 min. After aspirating the staining solution and drying the plates, plaques were counted, and titers were determined.

Genome titers quantifications of HNoV

For RNA extraction, an equal volume of 100% ethanol was added to the TRIzol®-containing sample and mixed by shaking for 5 seconds. From here the Direct-zol™ RNA P=Extraction kit was used. Up to 800 µL of the mixture was transferred to a spin column and centrifuged for 30 seconds at 11,000×g. This step was repeated until the entire sample was processed. The flow-through was discarded after each centrifugation. Next, 400 µL of RNA Pre-Wash Buffer was added to the column, followed by centrifugation for 30 seconds at 11,000×g. The column was washed with 650 µL RNA Wash Buffer and centrifuged for 2 minutes at 11,000×g. For RNA elution, 50 µL of DNase/RNase-free water was added directly to the column matrix. The column was placed into a new RNase-free collection tube and centrifuged for 1 minute at 11,000×g.

For quantification by RT-qPCR, a synthetic Gene Block (GB) a double-stranded DNA with sequence identical to the PCR amplicon was used as a standard. To generate a standard dilution series, seven RNase-free tubes were each filled with 45 µL of RNase-/DNase-free water. 5 µL of the GB was added to the first tube and mixed thoroughly. A 10-fold serial dilution was performed by transferring 5 µL from one tube to the next. Dilution was performed from 10^8 to 10^2 GE per sample. Lower volumes were avoided to minimize pipetting errors. RT-qPCR reactions were prepared using the Luna One-Step Kit in a total volume of 20 µL per reaction. The reaction mix included 10 µL 2× Master Mix, 0.24 µL forward primer (stock 25 µM), 0.24 µL reverse primer (stock 25 µM), 0.08 µL probe (stock 25 µM), 1 µL reverse transcriptase, 3.92 µL RNase-free water, and 5 µL RNA template.

Aliquots of 15 µL were loaded into the wells of a 96-well PCR plate. 5 µL of RNA sample or standard was added to each well. The NTC received 5 µL of RNase-free water instead of RNA. The thermal cycling program was as follows 55 °C for 10 minutes (reverse transcription), 95 °C for 5 minutes (initial denaturation), 40 cycles of: 94 °C for 10 seconds and 60 °C for 30 seconds.

Genome titers quantifications of HRoV

For RNA extraction, an equal volume of 100% ethanol was added to the TRIzol®-containing sample and mixed by shaking for 5 seconds. From here the Direct-zol™ RNA P=Extraction kit was used. Up to 800 µL of the mixture was transferred to a spin column and centrifuged for 30 seconds at 11,000×g. This step was repeated until the entire sample was processed. The flow-through was discarded after each centrifugation. Next, 400 µL of RNA Pre-Wash Buffer was added to the column, followed by centrifugation for 30 seconds at 11,000×g. The column was washed with 650 µL RNA Wash Buffer and centrifuged for 2 minutes at 11,000×g. For RNA elution, 50 µL of DNase/RNase-free water was added directly to the column matrix. The column was placed into a new RNase-free collection tube and centrifuged for 1 minute at 11,000×g.

RNA samples were subsequently sent to the Robert Koch Institute for determination of GE/mL by RT-qPCR (Japhet 2017).

Genome titers quantification of MNV

For MNV, RNA was extracted using the same Direct-zol™ RNA Extraction Kit under the same procedure. Briefly, clarified lysates were mixed with ethanol and processed according to the manufacturer's instructions, with final elution in 50 µL of RNase-free water.

RT-qPCR quantification was performed similar to HNoV, using a synthetic Gene Block standard corresponding to the MNV target amplicon. A 10-fold dilution series (up to 10^2 GE) was prepared for calibration. Reactions were prepared with the Bio-Rad iTaq Universal Probe Kit or NEB Luna One-Step Kit in 20 µL total volume, containing 10 µL 2× Master Mix, 0.24 µL forward primer (25 µM), 0.24 µL reverse primer (25 µM), 0.1 µL probe (25 µM), 1 µL reverse transcriptase, 3.92 µL RNase-free water, and 5 µL RNA template.

Samples, standards, and NTCs were run in 96-well plates under the same thermal cycling program as HNoV: 55 °C for 25 min or 10 min, respectively of kit used, 95 °C for 5 min, followed by 40 cycles of 94 °C for 10 s and 60 °C for 30s.

Attachment assay for MNV

BV-2 (5×10^5 cells/well), RAW264.7 (5×10^6 cells/well), and Huh7-mCD300lf (2×10^5 cells/well) cells were seeded in 6-well tissue culture plates one day prior to the assay. For polyamine depletion assays, cells were pre-treated with 500 µM DFMO for 3 days prior to seeding and supplemented with DFMO again post-seeding.

On the day of inoculation, the virus inoculum was prepared by diluting MNV-1 to a MOI of 5 in either PBS (for polyamine assays) or sodium phosphate buffer (for magnesium assays). The inoculum was supplemented with spermine and/or DFMO or with increasing concentrations of $MgCl_2$ and bile acid GCDCA (magnesium assays). A total of 500 µL of virus solution was added to each well and incubated on ice for 1 h to allow viral attachment.

Following incubation, the inoculum was aspirated, and cells were washed three times with ice-cold PBS or sodium phosphate buffer, as appropriate, to remove unbound virus. After the final wash, residual liquid was completely aspirated, and cells were lysed directly in 500 µL TRIzol® reagent (Zymo Research). Total RNA was extracted using the Direct-zol™ RNA Extraction Kit according to the manufacturer's instructions. MNV genome equivalents (GEs) were quantified as previously described. In polyamine assays, quantified GEs were normalized to the total RNA yield obtained from each cell lysate.

3.6. Cell viability assays for MNV-1 infections

WST-1 metabolic activity assay

To evaluate the metabolic activity of cells under the different conditions, a colorimetric WST-1 assay was performed. At different time points, WST-1 reagent was added directly to the wells at a ratio of 1:10 (50 µL WST-1 in 500 µL culture medium per well). Following addition, cells were incubated at 37 °C, 5% CO_2, and 90% RH. Absorbance at 450 nm was measured at 10-minute intervals using a Tecan microplate reader, with 660 nm serving as the reference wavelength. The assay was terminated once the control reached an optical density (OD) of 1.0-1.2, ensuring comparability across experiments.

Trypan blue exclusion assay

Cell viability under the different conditions was additionally assessed by trypan blue exclusion. Cells were harvested and transferred to microcentrifuge tubes. Cell suspension in 10 µL volume and mixed 1:1 with 0.4% trypan blue solution in PBS. The mixture was gently homogenized by pipetting and immediately loaded into a Neubauer hemocytometer. Viable cells remained unstained, whereas non-viable cells exhibited blue staining. At least 100-200 cells per sample were counted manually under a light microscope. Cell viability was calculated as the percentage of unstained cells relative to the total number of cells.

LDH release assay

To assess plasma membrane integrity, an lactate dehydrogenase (LDH) release assay was performed under the different conditions. Culture supernatants were collected at 8 hpi and 24 hpi for LDH quantification. LDH activity was measured using a commercial LDH Cytotoxicity Assay Kit following the manufacturer's instructions. Absorbance at 490 nm was measured at 10-minute intervals using a Tecan microplate reader. The percentage of LDH release was calculated using the formula:

$$\%\, LDH\ Released\ = \frac{(OD\ Maximal\ Release - OD\ Spontaneous\ Release)}{(OD\ Experimental\ Release - OD\ Spontaneous\ Release)} \times 100$$

where spontaneous LDH release corresponds to uninfected control cultures and maximal LDH release was induced in uninfected cells by treatment with 1% Triton X-100 for 30 min at 37 °C. For additional control, maximal LDH release was also determined for DFMO-treated cells by exposing uninfected DFMO-treated cultures to 1% Triton X-100 under the same conditions.

3.7. Immunostaining of viral proteins and replicating RNA

To visualize viral replication and protein expression, indirect immunofluorescence staining was performed. For MNV, the VP1 protein was stained, while double-stranded RNA (dsRNA), a marker of viral replication, was assessed for both MNV and HNoV infection.

Cells or 3D-HIEs at selected time points post-infection were washed with PBS and fixed in 4% paraformaldehyde in PBS (0.5 mL per well of a 24-well plate, or equivalent volumes for chamber glass slide and enteroid preparations) for 20 min at RT. Following fixation, samples were washed three times with PBS and incubated for 1 h at RT with a blocking buffer to reduce nonspecific binding and permeabilize membranes. Primary antibodies, diluted in blocking buffer, were applied for 1 h at RT under gentle agitation. Alternatively, FITC-conjugated lectins (50 µg/mL) were used for glycan staining of 3D-HIEs. After three washes with PBS-Triton (5 min each), samples were incubated for 1 h at RT with fluorophore-conjugated secondary antibodies in blocking buffer, followed by three 10-min washes with PBS-Triton. Nuclear counterstaining was performed with Hoechst 33321 (10 µg/mL in PBS-Triton, 10 min, RT), after which samples were washed three times with PBS-Triton and stored in PBS-Triton at 4 °C until imaging. For 2-photon microscopy spheres were plated in matrigel in 60×15 mm cell culture dishes to immobilize spheres and overlaid with CMGF- medium.

Epifluorescence microscopy was employed to visualize co-stained MNV-infected cells, confocal microscopy was used to assess co-localization of MNV VP1 and dsRNA, and two-photon microscopy was applied to 3D-HIEs to allow full-sphere imaging within a single field of view.

Quantification of externalized phosphatidylserine (PS)

Phosphatidylserine (PS) externalization on the outer plasma membrane leaflet, a hallmark of early apoptosis, was quantified using the GFP CERTIFIED® Apoptosis/Necrosis Detection Kit (Enzo Life Sciences). Annexin V conjugated to a fluorescent probe (Annexin V-EnzoGold) was used to enable visualization.

Cells were harvested into the binding buffer provided in the kit. Annexin V-EnzoGold reagent was added to the binding buffer at a final concentration of 1% (v/v), according to the manufacturer's instructions. Samples were incubated with the staining solution for 15 min at RT in the dark. Nuclei were counterstained with Hoechst 33321 (10 ng/mL in PBS, 10 min, RT, protected from light), followed by three PBS washes. After which the solution was removed and replaced with a binding buffer to prevent desiccation. Cells treated with 2 µM staurosporine served as positive controls for apoptosis induction, while untreated uninfected cells served as negative controls.

Samples were analyzed on a Zeiss (Axio Observed Z1) fluorescence microscope using DsRed and DAPI filter channels. The number of Annexin-positive cells was quantified by determining the proportion of Annexin V-positive cells relative to the total number of Hoechst-stained nuclei per field of view.

3.8. Viral and host protein detection using Western Blot

RAW264.7 macrophages (5×10^6 cells/well in 6-well format) or 3D-HIEs (10-20 spheres, comparable to infection assay sample size) were prepared as described for infectivity assays. Following infection, treatment, and incubation, cells were lysed in 200 µL (RAW264.7) or 20 µL (3D-HIEs) of ice-cold lysis buffer. To ensure complete lysis, samples were incubated on ice for 10-15 min, then centrifuged at

16,000×g for 20 min at 4 °C. Supernatants were transferred to fresh tubes, mixed with 6× SDS denaturation buffer at a 1:3 ratio (sample:buffer) and boiled for 10 min at 99°C.

Proteins were separated by SDS-polyacrylamide gel electrophoresis (SDS-PAGE) following the protocol of Schägger and von Jagow (1987). Depending on protein size, 10% or 12% Jagow gels were prepared. For each sample, 10-15 µL of protein preparation were loaded per lane. Electrophoresis was performed at 80 V for 10 min, followed by 120 V for 65 min (12% gels) or 50 min (10% gels). A PageRuler prestained protein ladder (10-180 kDa) was included as a molecular weight marker.

Table 13. Recipe for the resolving layer of SDS gel

	For 4 small 10% SDS gels	For 4 small 12% SDS gels
Acrylamide	5 mL	6 mL
Jagow-buffer	6.6 mL	6.6 mL
ddH_2O	7.2 mL	6.2 mL
Glycerin	1 mL	1 mL
10x APS	100 µL	100 µL
TEMED	20 µL	20 µL

Table 14. Recipe for the stacking layer of SDS gel.

	For 4 small SDS gels
Acrylamide	1 mL
Jagow-buffer	2.5 mL
ddH_2O	6.4 mL
Glycerin	1 mL
Bromphenol blue	200 µL
10x APS	80 µL
TEMED	20 µL

After electrophoresis, proteins were transferred to 0.2 µm nitrocellulose membranes in a transfer buffer at 100 V for 90 min (12% gels) or 60 min (10% gels). Membranes were blocked overnight at 4 °C in a blocking buffer to minimize nonspecific binding. Primary antibody incubations (α-PARP, α-Casp3, TV19) were performed for 1 h at room temperature (RT) in the blocking buffer. Following three 10 min washes in PBS-T, membranes were incubated with HRP-conjugated secondary antibodies for 1 h at RT, followed by washing as above. Signals were detected using Enhanced Chemiluminescence (ECL) substrate reagents, and chemiluminescence was visualized on an Amersham ImageQuant 800 system.

All membranes probed with α-PARP, α-Casp3, and TV19 antibodies were additionally analyzed with α-β-actin antibody as a loading control following a similar staining protocol.

3.9. Indirect spermidine ELISA

Intracellular spermidine levels in RAW264.7 macrophages were quantified following treatments with DENSpm, DFMO, or spermidine, according to the conditions used for infectivity assays (without viral infection). After incubation, cells were washed three times with PBS, scraped, and counted. For each

condition, 5×10^5 cells were transferred to fresh tubes and pelleted by centrifugation (4 min, 500×g). The supernatant was aspirated, and cell pellets were resuspended in 200 µL PBS. To release intracellular contents, including spermidine, cells were subjected to three freeze-thaw cycles. Cellular debris was removed by centrifugation (10 min, 835×g), and the resulting supernatant was collected for spermidine quantification.

Spermidine concentrations were determined using the Human Spd GENLISA™ ELISA Kit. The microtiter plate provided with the kit was pre-coated with anti-spermidine antibodies. A total of 100 µL of either standard dilutions, blanks, FBS, DMEM10, or cell samples was added to the respective wells and incubated for 80 min at 37 °C. After incubation, wells were aspirated and washed four times with a wash buffer. Subsequently, 100 µL of biotinylated anti-spermidine antibody solution was added, and samples were incubated for 50 min at 37 °C. Wells were washed as described above, followed by incubation with 100 µL streptavidin-HRP conjugate solution for 50 min at 37 °C. After an additional wash step, 100 µL TMB substrate was added and incubated for 10 min at 37 °C. The reaction was terminated by adding 100 µL stop solution. Absorbance was measured at 450 nm using a Tecan microplate reader. Spermidine concentrations were calculated from a standard curve ranging from 0.79 to 50 ng/mL, according to the manufacturer's instructions

3.10 Statistical analysis

All statistical analyses were performed using GraphPad Prism version 10. Data were first evaluated for normality using multiple tests, including the D'Agostino-Pearson omnibus, Anderson-Darling, Shapiro-Wilk, and Kolmogorov-Smirnov (distance) tests. When datasets met the assumptions of normal distribution and homogeneity of variance, statistical significance was assessed using one-way or two-way ANOVA. If normality criteria were not satisfied, or when sample sizes were too small for reliable parametric testing, the Kruskal-Wallis test was applied.

4. Results

4.1. Adapting the 3D-HIE system to support enteric virus infections from clinical isolates

Given the need for a physiologically relevant platform to model enteric infection, the first section of this project addresses the adaption of the 3D-HIE system to support enteric virus infections from clinical isolates focusing on HNoV, HRoV and IAV H1N1 infections.

At the onset of this study, limited information was available regarding screening of clinical stool samples, the reproducibility of HNoV infection and the impact of storage conditions on the stability of HNoV stool filtrates. Employing clinical isolates for infection studies requires building a validated panel of isolates and the implementation of reliable protocols for managing infectious stool specimens. To assemble a panel of infectious stool samples, lab's internal biobank of HNoV stool isolates was screened and evaluated for infection efficiency and reproducibility in 3D-HIE model. In addition, HNoV replication and capsid protein synthesis in 3D-HIEs were characterized using 2-photon microscopy and Western Blot analysis.

4.1.1. Biobank Screening of clinical stool isolates for HIE infection

To identify HNoV GII-positive stool samples suitable for *in vitro* infection of 3D-HIEs, 10 samples were used to infect differentiated 3D-HIEs at an estimated MOI of 1 (based of GEs per cell). The cell number per infectious sample was determined by quantifying cells from dissociated spheres from one well of a 6-well plate. The number of cells used for MOI quantification represented the mean of three independent quantification experiments.

Infections were then compared to the reference stool isolate #20942 obtained from the Dr. Christiane Wobus (University of Michigan). All infections with HNoV GII isolates were performed using 1% (w/v) stool filtrated prepared in Opti-MEM and supplemented with interferon inhibitor Ruxolitinib and bile acid GCDCA post-infection, unless indicated otherwise. Among the 10 tested samples, 3 stools showed >100-fold increase in GEs at day two compared to day zero post-infection and were designated as potent replicating isolates (21). Three additional samples showed a 10- to 100-fold increase in GEs and were designated as modest replicating isolates. The remaining 4 samples exhibited <10-fold increase in GEs and were characterized as non-replicating isolates (Figure 16). None of the tested isolates demonstrated replication levels similar to the provided reference stool sample (>1000-fold increase in GEs).

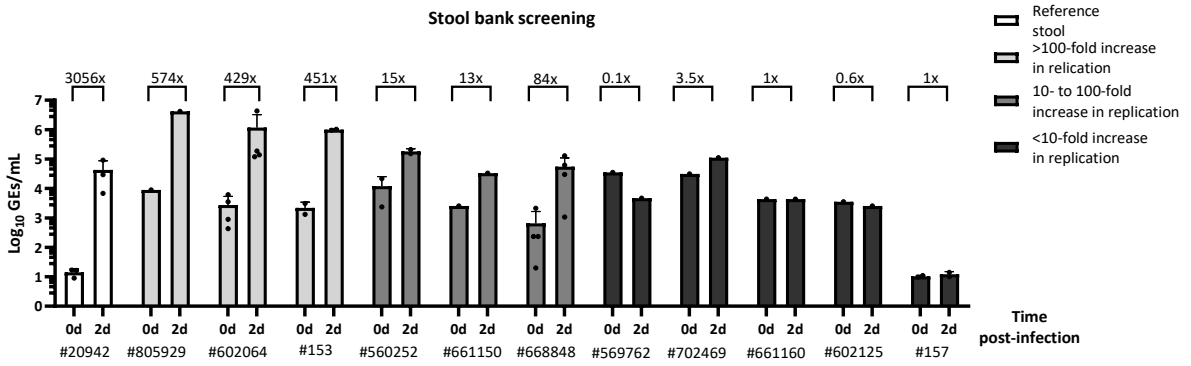

Figure 16. Screening of stool biobank samples in 3D-HIEs.Differentiated 3D-HIEs were infected with HNoV GII stool filtrates at an estimated MOI of 1. Samples were harvested day 0 and 2 post-infection

for viral GEs quantification by RT-qPCR. Values above the bars indicate the mean fold increase of GE titers at day 2 relative to 0. Data represent means ± standard deviation (SD) of at least one independent biological assay. Individual data points are shown.

4.1.2. Evaluation and optimization reproducibility of HNoV infections from stool

Following the identification of 6 replicating HNoV GII stool-isolates, 3 potent (>100 fold increase) isolates were selected (#805929, #602064, #153) and 1 modest replicating isolate (#560252) (10-100 fold increase) for further studies. To assess the robustness and reproducibility of HNoV infections in 3D-HIEs, infections were performed using 4 above-mentioned isolates over a 12-week period to evaluate the impact of 1% stool filtrate aging under the storage conditions (-80°C). Isolates #805929 and #153 demonstrated robust and consistent replication in HIEs, with mean increase of 574- and 979-fold in GEs titers, respectively and with minimal variation observed in GEs at both day 0 and 2 post-infection (Figure 17a). Isolate #602064 also showed robust replication, however, it exhibited substantial variation in GEs at day 0 post-infection, resulting in variability in the calculated fold increase of GE titers (Figure 17b). The modest replicating isolate #560252 produced a smaller increase in GEs titers (64-fold), consistent with observations during the biobank screening, and showed variability at both day 0 and 2 post-infection (Figure 17b). No notable loss of infectivity was detected within the 12-week period.

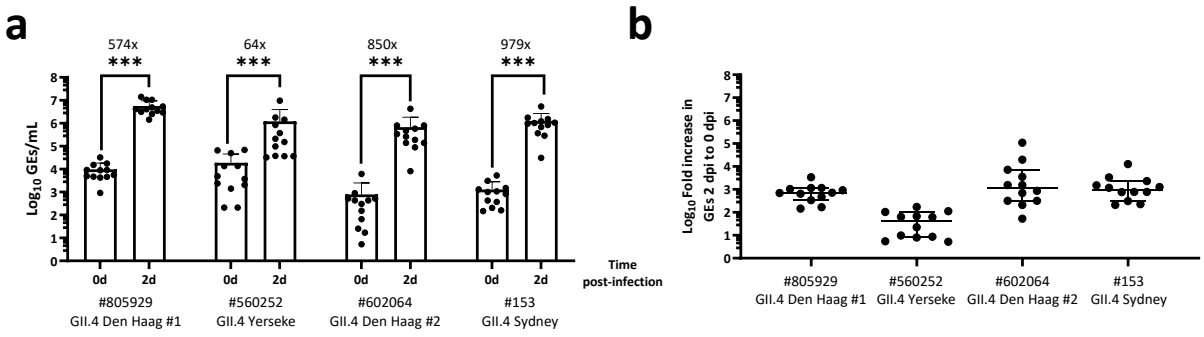

*Figure 17. Reproducibility of HNoV GII infections in 3D-HIEs. (a) Differentiated 3D-HIEs were infected with four selected HNoV GII stool filtrates at an estimated MOI of 1. Samples were harvested at 0 d and 2 d post infection for RNA extraction and viral GEs quantification by RT-qPCR. (b) Fold increase in GEs titers at day 2 compared to day 0 for each stool-isolated was quantified to investigate the reproducibility of infection. Values above the bars indicate the mean fold increase of GE titers at day 2 relative to day 0. Experiments were performed with biological replicates collected over a 12-week period. Data represent (a) means ± standard deviation (SD) or (b) median with 95% confident interval (CI) of twelve independent biological assays. Individual data points are shown. Statistical significance was assessed using the two-way ANOVA test (a) to compare day 2 to day 0: *** p≤0.001.*

To evaluate if prolonged storage (-80 °C) of stool filtrates would affect virus stability, 1% stool filtrates (preparations) were stored for over 6 months and then tested in 3D-HIEs. When infectivity of aged stool preparations (stored for >6 months) were compared to fresh preparations (stored for <6 months), a clear decline in infectivity were observed for HNoV GII isolates #560252, #602064 and #153. The fold increase in GEs dropped from 20-fold to 2-fold for isolate #560252, from 885-fold to 113-fold for isolate #602064 and from 1458-fold to 50-fold for isolate #153 (Figure 18). Correspondingly, GE titers at day 2 post-infection were significantly lower in aged preparations versus fresh preparations. Notably, isolate #805929 maintained stable infectivity across all storage durations tested.

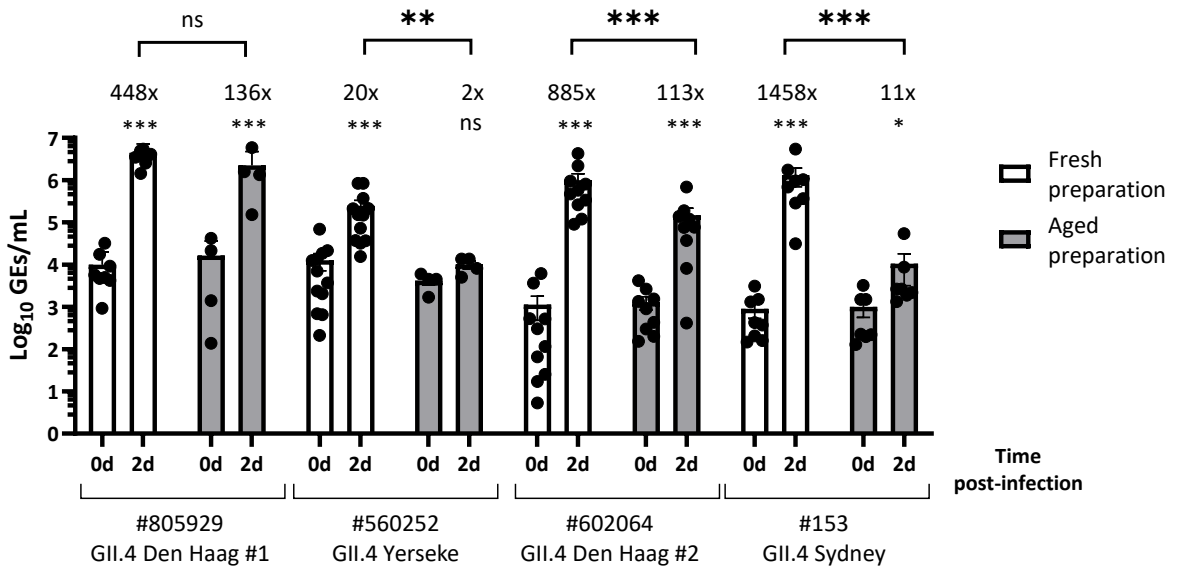

*Figure 18. Aging of HNoV GII stool-isolates under storage conditions. Differentiated 3D-HIEs were infected with HNoV GII. #560252, #602064 and #153 stool filtrates from fresh preparation (stored for <6 months) and aged preparation (stored for >6 months) at an estimated MOI of 1. Samples were harvested at day 0 and day 2 post-infection for viral GEs quantification by RT-qPCR. Values above the bars indicate the mean fold increase of GE titers at day 2 relative to day 0. Data represent means ± standard deviation (SD) of at least three independent biological assays. Individual data points are shown. Statistical significance was assessed using the two-way ANOVA test to compare day 2 to day 0 and between fresh and aged preparations at day 2: ns, not significant; *p≤0.05; ** p≤0.01; *** p≤0.001.*

All 4 HNoV GII stool-isolates were genotype and fully sequenced by Dr. Sandra Niendorf at the Robert Koch-Institute. All stool-isolates were identified as GII.4 strains based on their capsid sequence, consistent with the strain distribution during the sampling period (2015-2017). Stool-isolates #805929 and #602064 were classified as Den Haag 2006b [P4], and will hereafter be referred to as Den Haag #1 and Den Haag #2. Isolate #153 was identified as Sydney [P4 New Orleans], and isolate #560252 was identified as Yerseke 2006a [P4]. Typing was confirmed using the norovirus typing tool from RIVM, Netherlands (216).

In summary, among 10 tested HNoV GII-positive stool samples, 6 (60%) were infectious, as indicated by >10-fold increase in GEs titers at day 2 compared to day 0 post-infection. No correlation was observed between the GE/mL concentration of the stool filtrate and the robustness of viral replication. Stool filtrates exhibited shelf-life of approx. 6 months when stored at -80°C, with decline in infectivity occurring gradually. Genotyping and sequencing confirmed that the stool-isolates represented commonly circulating strains during the collection period.

4.1.3. HNoV release in infected HIEs

Following the identification of infectious stool isolates, strategies to improve HNoV yields in 3D-HIEs were explored. Prolonged incubation of infected HIEs with HNoV GII.4 Den Haag #1 stool-isolate was tested to determine whether extended culture time could increase genome titers. No increase in GEs was observed at day 3 post-infection compared to day 2 (Figure 19a). This finding prompted us to examine the release of HNoV GEs into the supernatant. A similar number of HNoV GEs was detected in supernatant compared to cell-associated fraction (Figure 19b), indicating that HNoV GEs were partially released from infected cells.

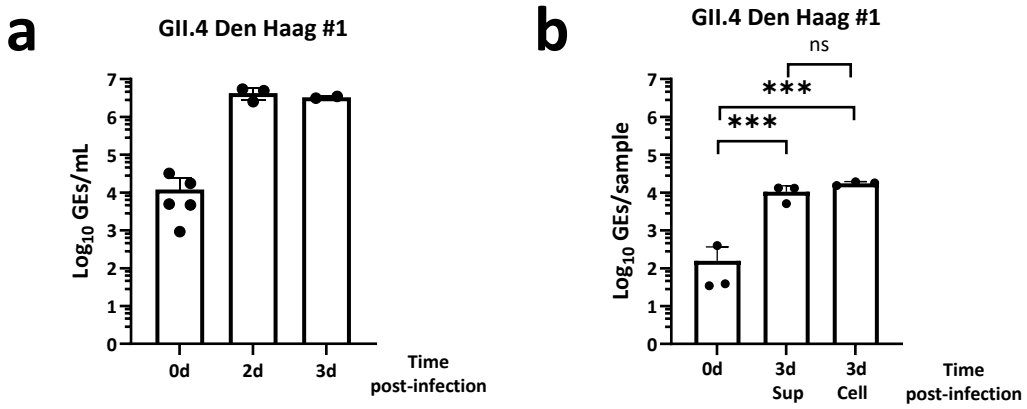

*Figure 19. Release of HNoV GII.4 Den Haag #1 into the supernatant of 3D-HIEs. Differentiated 3D-HIEs were infected with HNoV GII.4 Den Haag #1 stool-isolate at an estimated MOI of 1. (a) Samples were harvested at day 0 ,2 and 3 post-infection for viral GEs quantification by RT-qPCR. (b) HIE supernatant and cell fraction were harvested separately for viral GEs quantification at day 0 and 3 post-infection. Data represent means ± standard deviation (SD) of at least two independent biological assays. Individual data points are shown. Statistical significance was assessed using the one-way ANOVA test to compare day 3 to day 0 samples: ns, not significant; *** p≤0.001.*

4.1.4. Molecular detection of HNoV infection in HIEs

The next objective was to develop additional molecular detection methods to monitor HNoV infection in 3D-HIEs, focusing on the detection of intermediate replication product dsRNA and viral protein expression.

To estimate the number of infected spheres and infected cells per sphere, an immunofluorescence assay targeting dsRNA, a replication intermediate product of +ssRNA viruses, was established. Infections of 3D-HIEs were performed at an estimated MOI of 1 using GII.4 stool-isolates of Den Haag #1, Sydney and Yerseke. At MOI of 1 detection of dsRNA-positive cells were inconsistent, with rare positive single cells observed for Den Haag #1 and Sydney isolates, and no detectable signal for Yerseke isolate. However, increasing the inoculum to an estimated MOI of 5, resulted in consistent detection of cell clusters positive for dsRNA (Figure 20i) for GII.4 Sydney stool-isolate, although the total number of dsRNA-positive cells per sphere remained low.

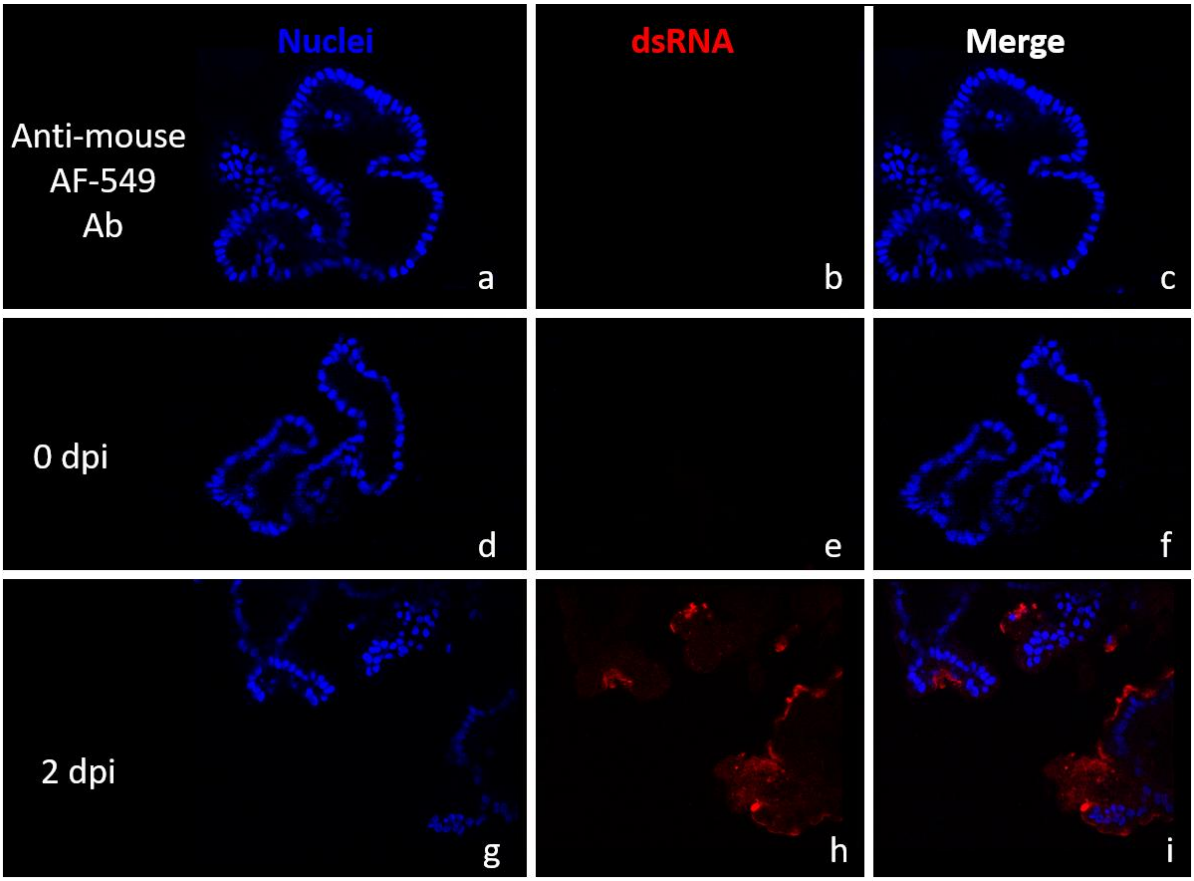

Figure 20. Detection of dsRNA in HNoV GII.4 infected 3D-HIEs. Differentiated 3D-HIEs were infected with HNoV GII.4 Sydney at an estimated MOI of 5. Samples were harvested at day 0 and 2 post-infection, fixed with 4 % PFA, and stained with anti-dsRNA mAb. (a-c) The top horizontal pane shows day 2 post-infection 3D-HIEs stained with secondary anti-mouse AF594 antibodies only. The horizontal panels in (d-f) the middle and (g-i) at the bottom shows day 0 and day 2 post-infection, where HIEs were stained with both primary anti-dsRNA mAb and secondary antibodies. Images are representative of three independent experiments.

To assess the polarity of HNoV infected dsRNA-positive sphere, GII.4 Sydney-infected 3D-HIEs were co-stained with anti-dsRNA mAb and FITC-UEA-I lectin, which binds to fucosylated glycans, which are present exclusively on the apical membrane of intestine. As expected, dsRNA-positive cells were only found in apical-out spheres (Figure 21). Furthermore, dsRNA-positive cells lacking UEA-I staining were observed, indicating a loss of fucosylated glycans from cellular membrane.

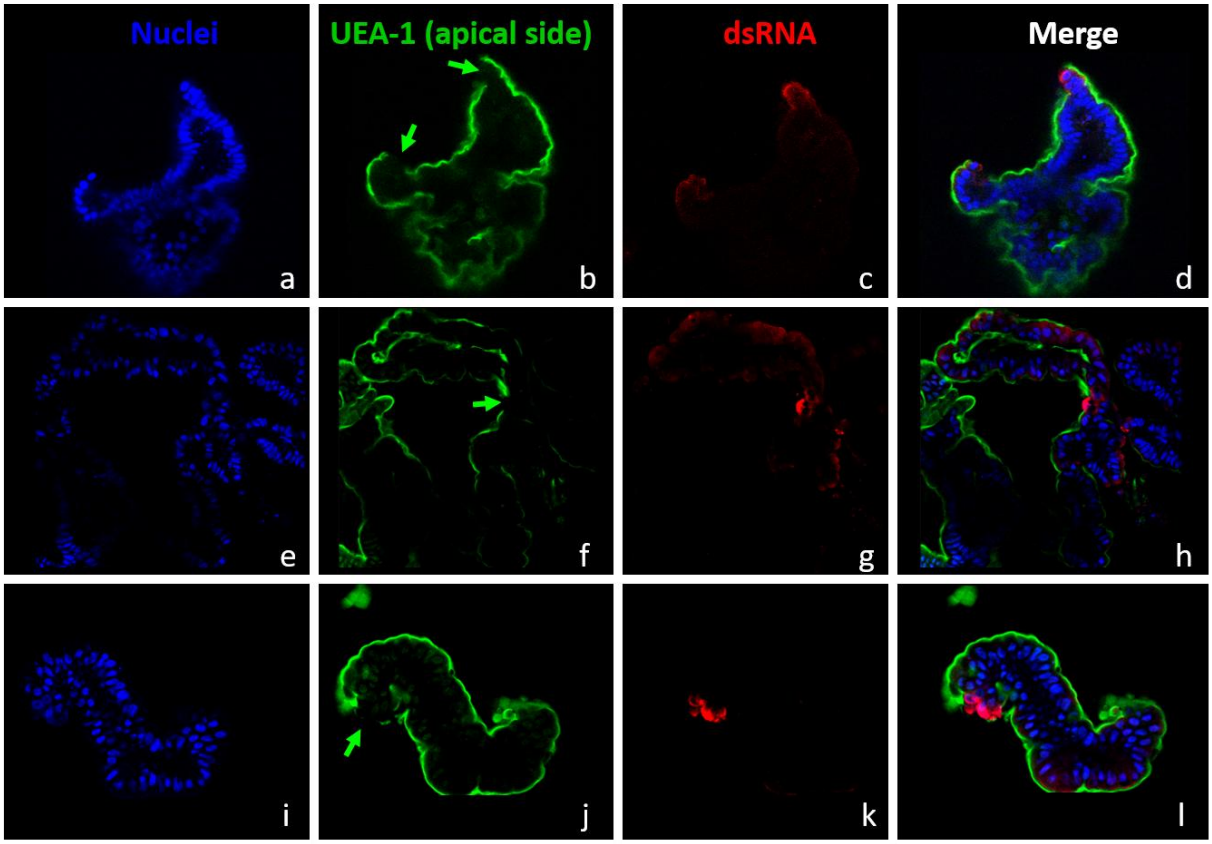

Figure 21. Loss of surface fucosylated glycans in HNoV GII.4-infected HIEs. Differentiated 3D-HIEs were infected with HNoV (a-d and i-l) GII.4 Sydney and (e-h) Den Haag #1 stool filtrate at an estimated MOI of 5. Samples were harvested at day 2 post-infection, fixed with 4% PFA, and stained with anti-dsRNA mAb and FITC-UEA-I. (a-d) The top, (e-h) middle and (i-l) bottom horizontal panels present day 2 post-infection samples from three independent experiments. Green arrows indicate loss of fucosylated glycans at the cell membrane.

To assess production of HNoV major structure protein VP1, a Western Blot detection method was established using the anti-VP1 mAb TV19, which targets the S-domain of the VP1. HNoV VP1 was detected in the undiluted stool sample, as well as in the day 2 post-infection samples. Based on the respective amino acid sequence, the expected size of monomeric VP1 is 58 kDa. Yet, VP1 from the GII.4 Sydney stool-isolate contained a double band, with prominent top band (~58 kDa size) and weaker lower band (~55 kDa size) (Figure 22), while newly synthesized VP1 at day 2 post-infection was observed as only lower band (~55 kDa size).

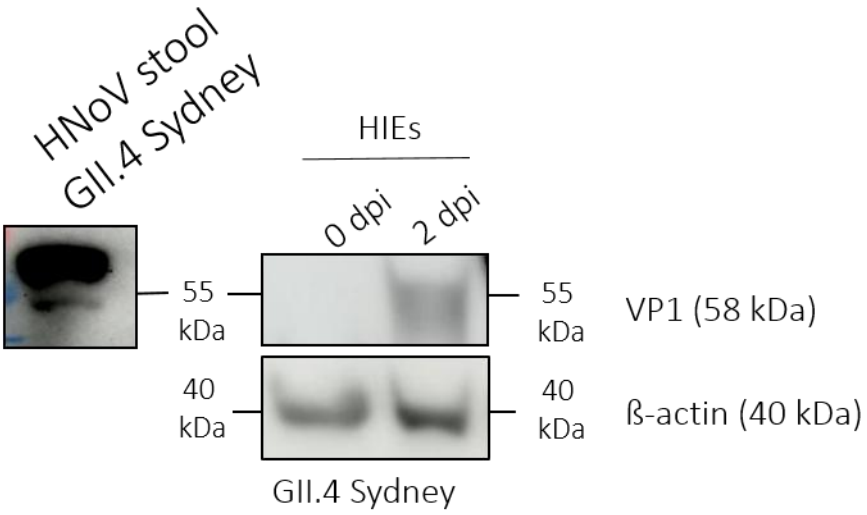

Figure 22. Western Blot analysis of HNoV GII.4 VP1 in infected 3D-HIEs. Differentiated 3D-HIEs were infected with HNoV GII.4 Sydney at an estimated MOI of 1. Samples were harvested at day 0 and 2 post-infection in 30 uL of lysis buffer for protein extraction and analysis by western blot. The HNoV stool sample was prepared by harvesting ~30 µL of stool and combining with an equal part of the lysis buffer. β-actin was used as internal loading control. Data shown are representative of one independent biological assay.

In summary, active replication of HNoV GII.4 stool isolates in 3D-HIEs was detected using anti-dsRNA monoclonal antibodies under high-MOI conditions. However, the proportion of dsRNA-positive spheres, as well as the number of positive cells within individual spheres, remained low, indicating that HNoV replication is restricted. Notably, dsRNA-positive cells coincided with regions lacking fucosylated glycans, suggesting that these glycans may be internalized during HNoV entry. Analysis of VP1 revealed a distinct double-band pattern in stool-derived virus, whereas de novo synthesized VP1 matched the lower-molecular-weight band, indicating potential differences in post-translational processing or maturation of capsid protein.

4.1.5. Enrichment of entero-endocrine cells (EEC) in 3D-HIEs

EECs constitute a unique and highly specialized subtype of intestinal epithelial cells responsible for production of hormones, amines and signal molecules which collectively regulate gastrointestinal digestion, motility and mucosal immunity. Less than 1% of the total epithelial cell population are estimated to be EECs in the intestine, making them a rare cell type (18). Multiple subtypes of EECs exist, each dedicated to the production of distinct hormonal factors (18). In histopathological samples of HNoV-infected patients, EECs were identified as permissive cell type for HNoV infection (17). Therefore, whether an increase in EEC in HIEs would enhance HNoV infection in HIEs.

To increase the abundance of EECs in HIEs, a small-molecule inhibitor of Forkhead box O1 protein (FOXO) called AS184 (18) was employed.

In non-treated 3D-HIEs, only few EECs are observed, with an estimated distribution of approx. 1-2 EEC per sphere (Figure 23b-c). The FOXO inhibitor AS184 was administered starting from day 2 post-splitting and maintained until 7 days post-differentiation. AS184-treated HIEs (Figure 23d) displayed distinct morphological changes compared to non-treated (Figure 23a), consistent with the original report. Immunofluorescent staining using chromogranin A (CHGA) as a marker for EECs, confirmed an

increased number of EECs per sphere following AS184 treatment, with an estimate distribution of minimum 5-7 EEC per sphere (Figure 23e-f).

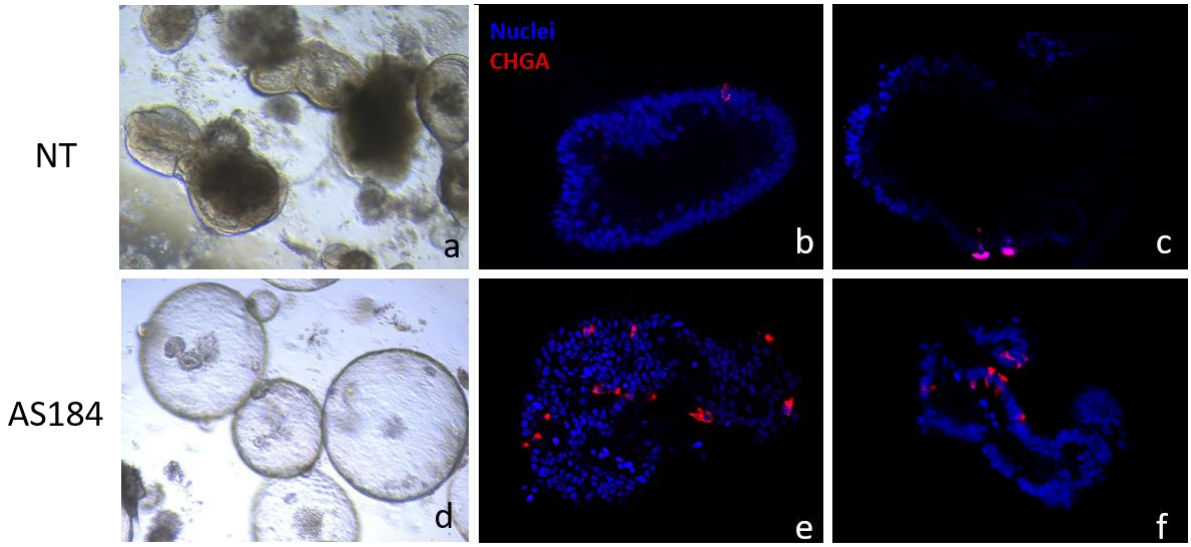

Figure 23. Detection of EECs in differentiated 3D-HIEs. Non- or AS184-treated differentiated 3D-HIEs were fixed with 4% PFA at day 7 post-differentiation and stained with anti-CHGA mAb. The top horizontal panel shows (a) bright field and (b-c) 2-photon photos of NT 3D-HIEs. The bottom horizontal panel shows (d) bright field and (e-f) 2-photon photos of AS184-treated HIEs. Images are representative of three independent biological assays.

To determine whether this enrichment of EECs in HIEs affect HNoV infection, differentiated AS184-treated 3D-HIEs were infected with 5 available GII.4 stool-isolates. Interestingly, a reduction in HNoV GII.4 replication was observed in AS184-treated 3D-HIEs compared to non-treated culture (Figure 24), which did not correspond to our hypothesis.

This result suggests that expansion of the AS184-responsive EEC subset in HIEs in fact exert detrimental effect on HNoV infection in HIEs.

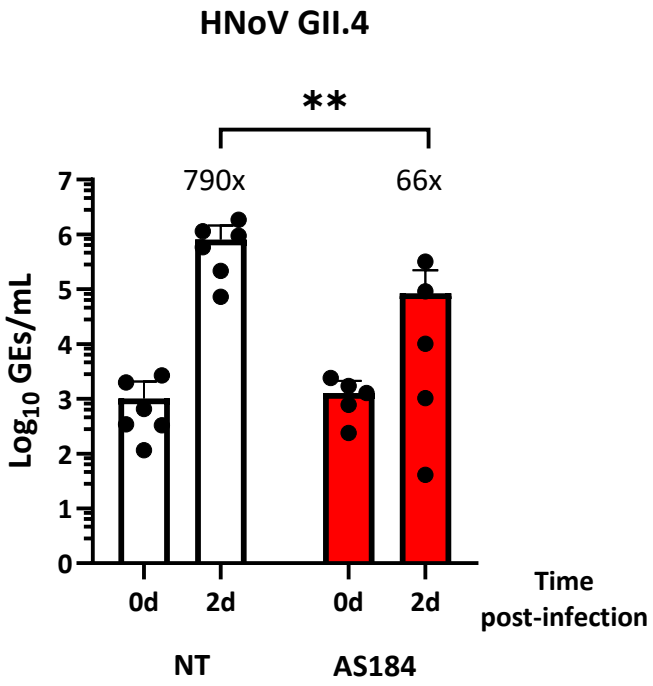

*Figure 24. AS184-mediated enrichment of EECs reduces HNoV GII.4 replication in 3D-HIEs.NT- or AS184-treated differentiated 3D-HIEs were infected with five HNoV GII.4 stool-isolates (Sydney, Den Haag #1 and #2, Yerseke and #20942) at an estimated MOI of 1. Samples were harvested at day 0 and 2 post-infection for viral GEs quantification by RT-qPCR. Values above the bars indicate the mean fold increase of GE titers at day 2 relative to day 0. Data represent means ± standard deviation (SD) of pooled results for five GII.4 isolates. Individual data points are shown. Statistical significance was assessed using the two-way ANOVA test to compare results from NT- and AS184-treated HIEs at day 2: ** p≤0.01.*

4.1.6. HIEs support infection of other enteric viruses

To expand the repertoire of model organisms available for the future studies, 3D-HIEs infections were also established for glycan-binding viruses infecting the gut, such as HRoV and IAV H1N1.

HRoV G3.P[8]eq.-like stool samples were obtained from Dr. Sonja Jacobson from Robert Koch Institute. Infections with HRoV were performed at an estimated MOI of 1 in 3D-HIEs using 1% (w/v) stool filtrates prepared similarly to HNoV infection. Additionally, prior to inoculation, viral preparations were treated with TPCK-treated trypsin to allow for proteolytic cleavage of HRoV spike VP4 protein (217,218), and Ruxolitinib was added during infection, as described for HNoV (21). HRoV replicated in 3D-HIEs with a mean GEs titer increase of 65-fold at day 2 compared to day 0 post-infection (Figure 25).

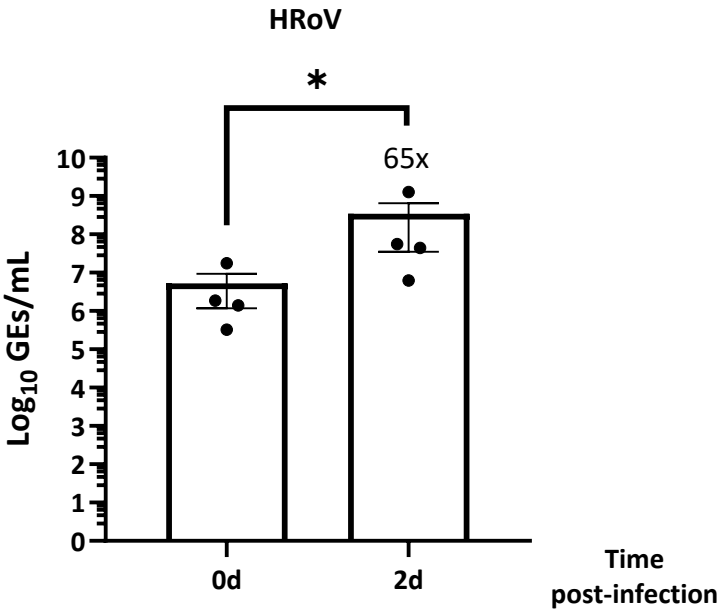

*Figure 25. Replication of HRoV in 3D-HIEs. Differentiated 3D-HIEs were infected with HRoV G3.P[8]eq.-like stool-isolates at an estimated MOI of 1. HRoV was activated with 10 µg/mL TPCK-treated trypsin for 30 min at 37°C prior to infection. Samples were harvested at day 0 and 2 post-infection for viral GEs quantification by RT-qPCR. Values above the bars indicate the mean fold increase of GE titers at day 2 relative to day 0. Data represent means ± standard deviation (SD) of four independent biological assays. Individual data points are shown. Statistical significance was assessed using the two-way ANOVA test to compare day 2 to 0: ns, not significant; * p≤0.05.*

To establish IAV infection in 3D-HIEs, stocks of influenza A/WSN/1933 (H1N1) virus were produced and titrated in MDCK cells by plaque assay. 3D-HIEs were infected with IAV H1N1 strain at an MOI of 0.1, supplemented with TPCK-treated trypsin to facilitate the HA cleavage and spread of virus in cell culture (219,220) and interferon inhibitor Ruxolitinib, both added post-infection. At defined time points, HIEs were harvested together with cell culture medium and frozen at -80℃ prior to analysis. Viral titers were determined from lysates via plaque assay on MDCK cells. A marked increase in PFU was observed at both day 2 and 4 compared to day 0 post-infection (Figure 26). Replication inhibitor 2-CMC, a nucleoside analogue, which targets the viral RNA polymerase and interferes with genome replication (221), potently suppressed IAV infection in HIEs diminishing virus titers (Figure 26).

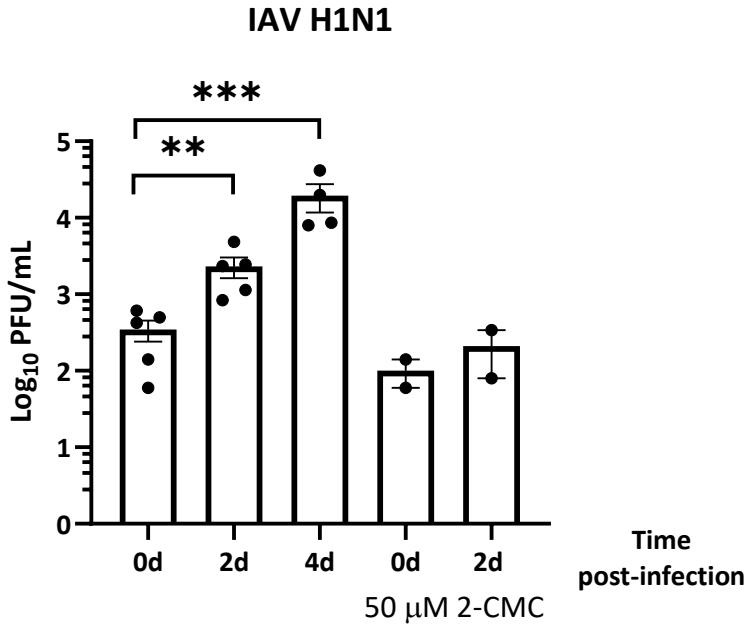

*Figure 26. Replication of IAV H1N1 in 3D-HIEs. Differentiated 3D-HIEs were infected with IAV H1N1 at an MOI of 0.1. Following infection, HIEs were washed three times with CMGF-, re-seeded in BME and maintained in differentiation medium supplemented with 2 µM Ruxolitinib, 4 µg/ml of TPCK-treated trypsin and 50 µM 2-CMC. Samples were harvested at day 0, 2 and 4 post-infection for PFU quantification by plaque assay. Data represent means ± standard deviation (SD) of at least two independent biological assays with two technical repeats. Individual data points are shown. Statistical significance was assessed using the one-way ANOVA test to compare day 2 and 4 to 0: ** p≤0.01; *** p≤0.001.*

In summary of this section:

- Screening of an internal biobank using 3D-HIEs identified a panel of infectious HNoV GII.4 stool isolates, with 6 out of 10 samples showing genome replication.
- HNoV infection in 3D-HIEs was robust and reproducible, however loss of infectivity in stool preparation was observed upon long-term (> 6 months) storage.
- Active HNoV replication in 3D-HIEs was visualized using anti-dsRNA staining and VP1 analysis, enabling detection of infected cells and newly synthesized capsid protein.
- The 3D-HIE platform was successfully extended to HRoV G3.P[8]eq-like and IAV H1N1.

4.2. HNoV and HRoV requirements for glycans in HIEs

The second section of this thesis focuses on the role of HBGAs in HNoV and HRoV infection. Central to HBGA biosynthesis are the fucosyltransferases FUT2 and FUT3, which are both expressed and functional in the gut. Although HBGA expression alone does not confer susceptibility to HNoV or HRoV *in vitro*, epidemiological data indicate that infection with common HNoV (GII.4) and HRoV (P[8]) variants depends on FUT2- and FUT3-mediated fucosylation (64,67).

Functional studies using genetically modified HIEs have demonstrated that only FUT2-expressing HIEs were susceptible to HNoV infection and knock-down of FUT2 abolished susceptibility, aligning closely with epidemiology data (149).

The glycan dependency of HRoV *in vitro* is less well understood, with notable discrepancies between clinical isolates and cell culture-adapted strains in terms of glycan requirement. For instance, data shows that Rotarix vaccine strains G1.[P8] and Ito G3.[P8] infect HIEs regardless of FUT2 status, diverging strongly from epidemiological data. Also, cell culture adapted HRoV Wa [P8], Rotarix vaccine [P8], DS-1 [P4] strains infected immortalized cell lines independent of fucosyltransferases activity (67). Subsequent studies reported that cell culture-adapted HRoV strains replicated less efficiently in primary HIEs (222). However, the mechanisms and implications of these adaptations remain unclear. Overall, leaving the requirement for glycans in HRoV infection an open question.

To advance our understanding in virus-glycan interaction, the glycan requirements for HRoV and HNoV infection in 3D-HIEs were investigated. Epidemic HNoV GII.4 Sydney and epochal Den Haag clinical isolates, along with emerging HRoV G3[P8]eq.-like isolated were employed. HBGA biosynthesis was modulated using 2-fluoro-peracetyl-fucose (2-FPF) (223), a broad-spectrum fucosyltransferase inhibitor that provides a practical alternative to genetic manipulation of HIEs.

To determine which sugar moieties in HBGAs, such as terminal fucose or galactose, contribute to HNoV, HroV and IAV H1N1 attachment and infection, a panel of glycan-binding lectins was applied to compete for these residues during infection. In addition, the antiviral potential of fucose-rich glycans and HMOs was assessed, as these molecules have previously been reported to reduce HNoV binding to HBGAs.

4.2.1. Inhibition of fucosyltransferases activity abrogates HNoV and HRoV infection in HIEs, but has no effect on IAV H1N1

To investigate the role of HBGAs in enteric virus infection, the glycan repertoire of differentiated 3D-HIEs was first characterized. A FITC-coupled lectin panel targeting distinct glycan moieties was established. The panel included Concanavalin A (ConA), a mannose-binding lectin from *Canavalia ensiformis*; Sambucus nigra agglutinin (SNA), an α2,6-sialic-acid-binding lectin from *Sambucus nigra*; wheat germ agglutinin (WGA), an N-acetyl-galactosamine/glucosamine- and sialic-acid-binding lectin from *Triticum aestivum*; and Ulex europaeus agglutinin I (UEA-I), a monofucose-binding lectin from *Ulex europaeus.*

Staining of 3D-HIEs with FITC-coupled lectin panel confirmed the presence of mannose, sialic acids, acetyl-galactosamine/glucosamines (present in A antigens) and fucose-containing (including H type 1 and 2 antigens) residues on the cellular membrane of HIEs (Figure 27a-d). Among these, sialic acid binding lectin showed the weakest binding (Figure27b). As mannose is a major component of N-linked

glycoproteins, it is therefore abundantly expressed on all intestinal epithelial cells (Figure 27a). All other lectins, except for ConA appeared non-homogenous, suggesting differential surface presence.

Given our focus on fucose-containing glycans and their role in HNoV and HRoV infection, a model system to modulate cellular fucosylation activity was next established. To achieve this, 2-fluoro-peracetyl-fucose (2-FPF), a cell-permeable broad-spectrum fucosyltransferases inhibitor was employed. Treatment of 3D-HIEs for 2 days with 500 µM of 2-FPF resulted in loss of FITC-UEA-I binding, indicating depletion of fucosylated glycans (Figure 27g). Importantly, the presence of mannose-, sialic- or acetyl-galactose/glucosamine-containing glycans were not affected (Figure 27 a compared to e, b compared to f, c compared to g), confirming selective inhibition of fucosylation with 2-FPF treatment.

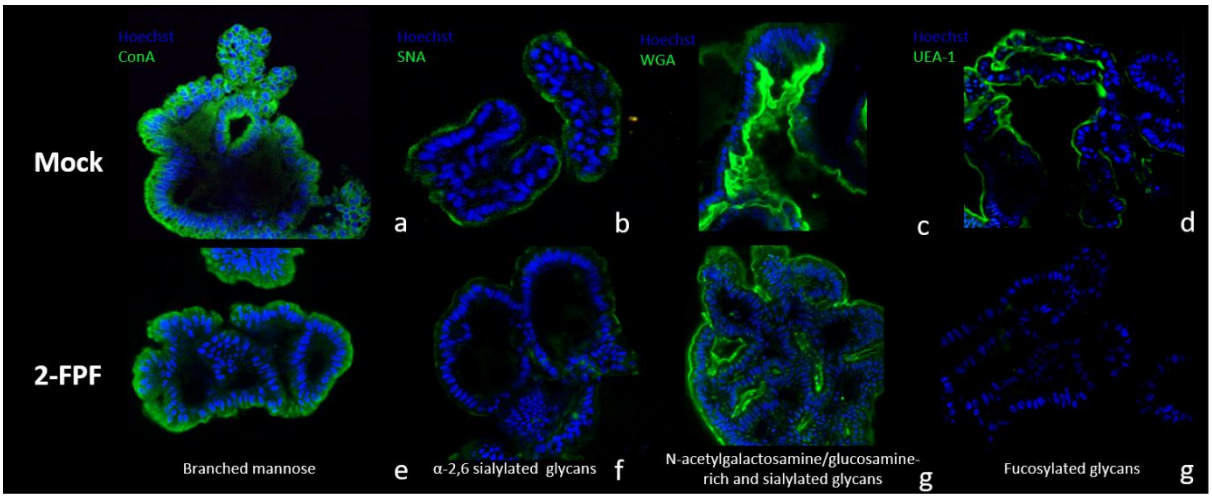

Figure 27. 2-FPF reduces surface fucosylated glycan presentation in 3D-HIEs. Differentiated 3D-HIEs (a-d) mock-treated or (e-g) 2-FPF-treated were stained with FITC-ConA, FITC-SNA, FITC-WGA and FITC-UAE-I. HIEs were visualized using 2-photon microscopy. Images shown are representative fields from multiple spheres within a single staining experiment.

To determine the functional importance of fucosylation in enteric virus infection, 2-FPF-treated (Figure 28a) 3D-HIEs were infected with HNoV GII.4 Sydney and HRoV G3.[P8]eq-like stool-isolates. To verify the specificity of the drug treatment, IAV H1N1 infection was also performed as it should not be fucose dependent.

Inhibition of fucosylation by 2-FPF completely abrogated infection by both HNoV GII.4 and HroV (Figure 28b-c), indicating that fucosylation is essential for both viruses infection in 3D-HIEs. As anticipated, IAV H1N1 infection was unaffected by 2-FPF treatment (Figure 28d). A modest increase in IAV infection under 2-FPF treatment at day 2 post-infection relative to untreated control, suggests that inhibition of fucosylation does not impair overall cell viability or non-fucose-dependent entry pathways.

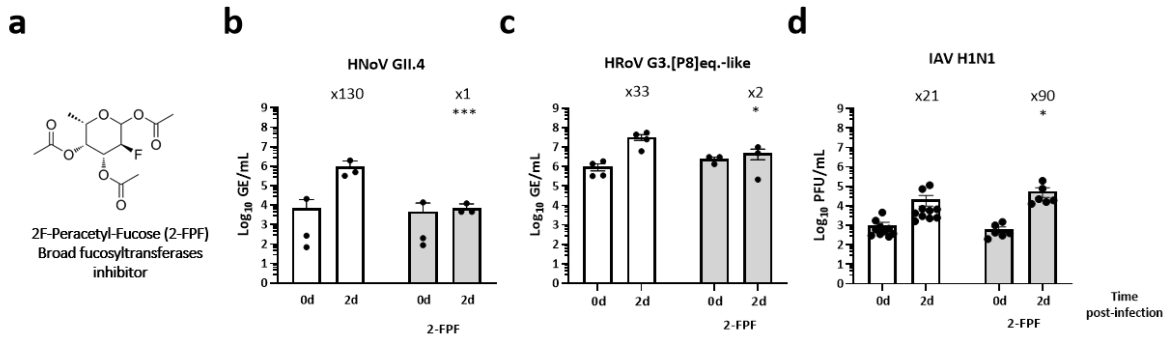

*Figure 28. 2-FPF reduces HNoV GII.4 and HRoV G3.[P8]eq-like replication in 3D-HIEs. (a) Molecular structure of 2-FPF inhibitor. Differentiated 3D-HIEs were pre-treated with 500 µM 2-FPF for 2 last days of differentiation. HIEs were infected with (b) HNoV GII.4 Sydney and (c) HRoV G3.[P8]eq-like stool-isolates at an estimated MOI of 1 and with (d) IAV H1N1 at an MOI of 0.1. Following infection, HIEs were washed three times with CMGF-, re-seeded in BME and maintained in differentiation medium supplemented with 500 µM 2-FPF, 2 µM Ruxolitinib, 500 µM GCDCA or 4 µg/mL of TPCK-treated trypsin for IAV H1N1 infection only. Samples were harvested at day 0 and 2 post-infection for viral GEs quantification by RT-qPCR or for viral titers quantification by plaque assay. Values above the bars indicate the mean fold increase of GE titers at day 2 relative to 0. Data represent means ± standard deviation (SD) of three independent (b and c) biological assays with (d) two technical repeats. Individual data points are shown. Statistical significance was assessed using the one-way ANOVA test to compare mock- and 2-FPF-treated conditions at day 2: ns, not significant; * p≤0.05; *** p≤0.001.*

Together, the 2-photon microscopy data confirm that 3D-HIEs express respective of glycans on their apical surface. Moreover, it was demonstrated that fucosylation is an active process, a targetable pathway in 3D-HIEs and can be efficiently inhibited using 2-FPF. Our data establish that fucosylation is indispensable for HNoV GII.4 Sydney and HRoV G3.[P8]eq-like stool-isolates infection, but dispensable for IAV H1N1 and thereby a druggable target for viruses that require fucylated glycans for infection.

4.2.2. Fucose- and acetylgalactosamine/glucosamine-binding lectins inhibit HNoV GII.4, but not HRoV G3.P[8]eq.-like infection in HIEs

To investigate the role of specific sugar moieties in glycans for HNoV GII.4, HRoV P[8] and IAV H1N1 infection, a lectin competition assay in 3D-HIEs was established, using previously described lectin panel. Differentiated 3D-HIEs were pre-incubated with each lectin for 1 hour at 37℃ prior to viral challenge, allowing lectins to block access to the corresponding sugar moieties in glycans.

Pre-treatment with mannose-binding ConA or α2,6-sialic acid-binding SNA lectins had no measurable effect on infection by either of tested HNoV GII.4 strains (Figure 29 a,e,b,f). Fucose-binding UEA-I lectin inhibited both GII.4 Sydney and GII.4 Den Haag #2 infection in dose-dependent manner (Figure 29 d and h), with 10 µM nearly abolishing infection. Acetyl-galactosamine/glucosamine-binding WGA lectin completely inhibited GII.4 Den Haag #2 infection and partially inhibited GII.4 Sydney infection (Figure 29 c and g).

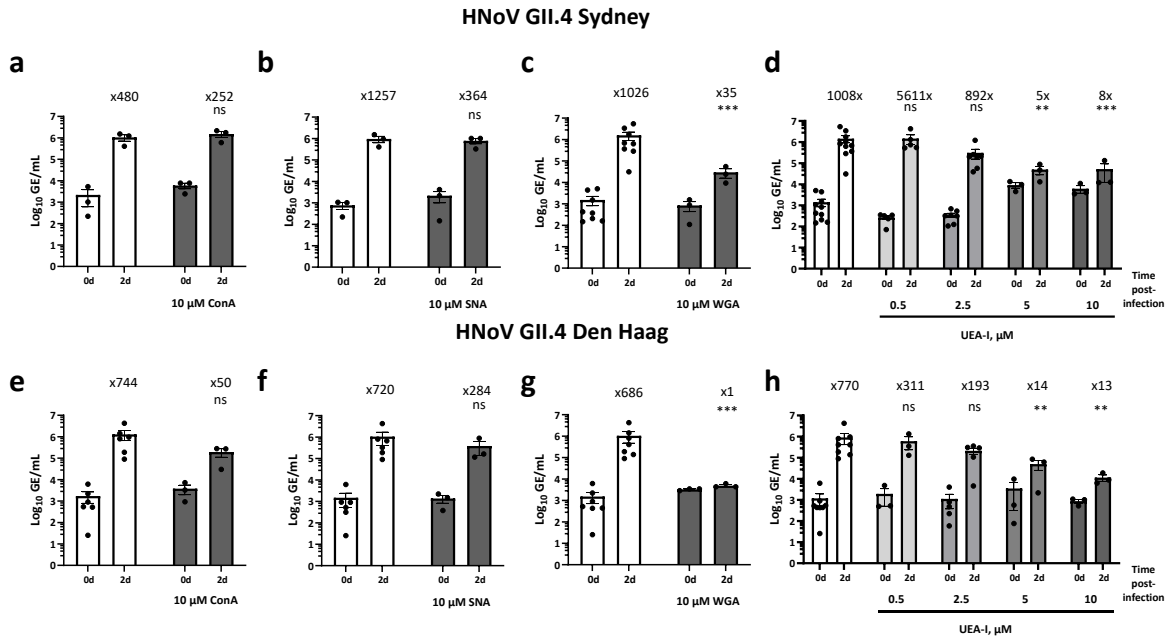

*Figure 29. Fucose- and N-acetylgalactosamine/glucosamine-binding lectins inhibit HNoV GII.4 infection in 3D-HIEs. Differentiated HIEs were pretreated with the indicated concentrations of (a, e) ConA, (b, f) SNA, (c, g) WGA and (d, h) UAE-I for 1 hat 37℃ prior to infection. (a-d) HNoV GII.4 Sydney and (e-h) Den Haag #2 stool-isolates were used for infection at an estimated MOI of 1. Samples were harvested at day 0 and 2 post-infection for viral GEs quantification by RT-qPCR. Values above the bars indicate the mean fold increase of GE titers at day 2 relative to 0. Data represent means ± standard deviation (SD) of three independent biological assays. Individual data points are shown. Statistical significance was assessed using the one-way ANOVA test to compare mock- and lectin-treated conditions at day 2: ns, not significant; ** p≤0.01; *** p≤0.001.*

The same lectin panel was then evaluated against HRoV G3.[P8]eq-like stool-isolate. None of the lectins, including UEA-I, reduced HRoV infection in 3D-HIEs (Figure 30), suggesting that glycans blocked by lectin panel are not the major entry factors for HRoV entry in 3D-HIEs.

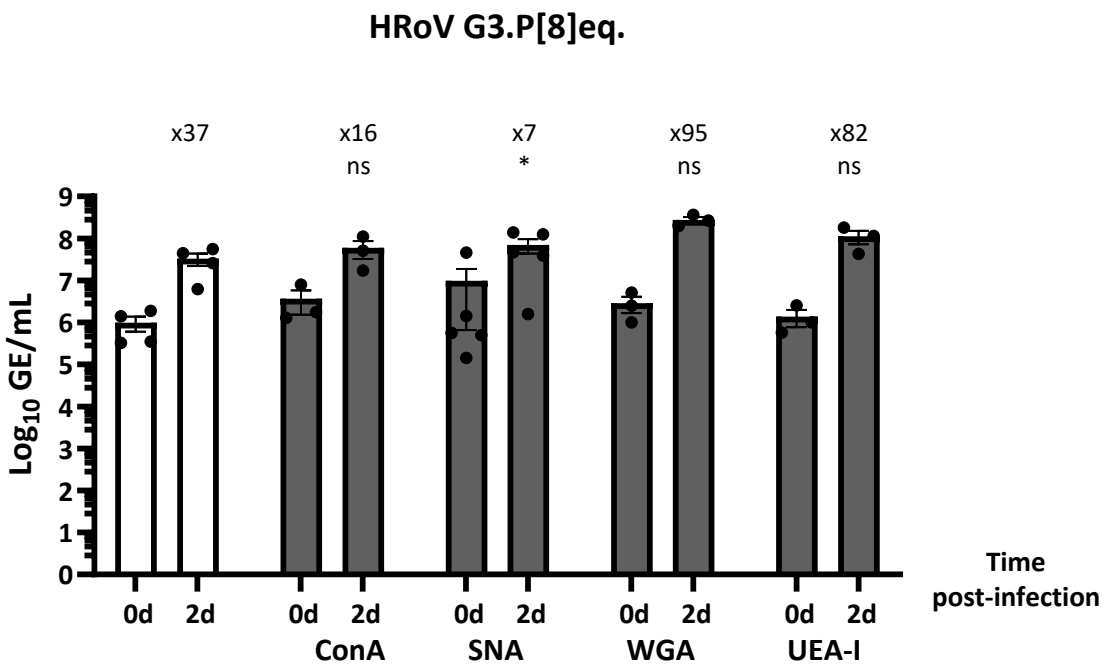

*Figure 30. Fucose- and sialic-binding lectins did not inhibit HRoV G3[P8]eq.-like infection in 3D-HIEs. Differentiated HIEs were pretreated with 10 µM of ConA, SNA, WGA and UEA-I for 1 hat 37℃ before infection. While HRoV was activated with 10 µg/mL TPCK trypsin for 30 min at 37°C prior to inoculation. HRoV G3[P8]eq.-like stool-isolate was used for a subsequent infection at an estimated MOI of 1. Samples were harvested at day 0 and 2 post infection for viral GEs quantification by RT-qPCR. Values above the bars indicate the mean fold increase of GE titers at day 2 relative to 0. Data represent means ± standard deviation (SD) of three independent biological assays. Individual data points are shown. Statistical significance was assessed using the Kruskal-Wallis test to compare mock- and lectin-treated conditions at day 2: ns, not significant; * p≤0.05*

To investigate the glycan requirement for IAV H1N1 in 3D-HIE infection, the lectin panel was again employed. As expected, sialic acid-binding lectins SNA and WGA (low affinity sialic acid binder) lectin completely inhibited H1N1 infection in HIEs (Figure 31), confirming the requirement for exposed sialic acids in 3D-HIEs. Moreover, mannose-binding ConA lectin also completely blocked IAV H1N1 infection in HIEs.

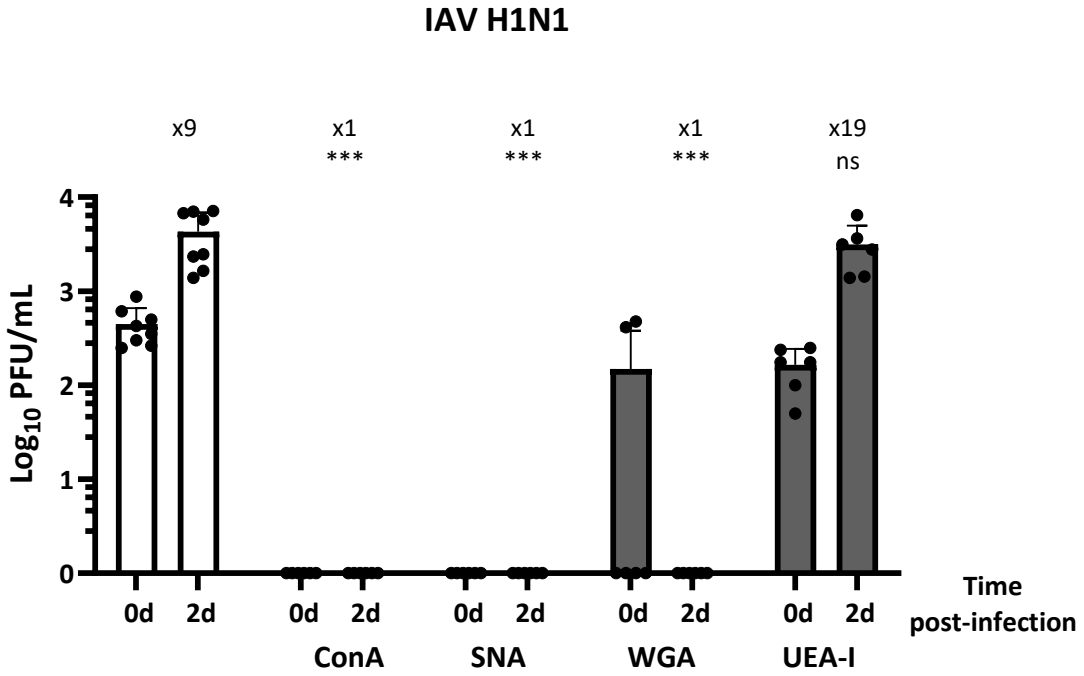

*Figure 31. Mannose- and sialic-binding lectins inhibit IAV H1N1 infection in 3D-HIEs. Differentiated HIEs were pretreated with 10 µM of ConA, SNA, WGA and UEA-I for 1 hat 37℃ prior to infection. IAV H1N1 was used for a subsequent infection at an MOI of 0.1. Samples were harvested at day 0 and 2 post-infection for viral titers quantification by plaque assay. Values above the bars indicate the mean fold increase of GE titers at day 2 relative to 0. Data represent means ± standard deviation (SD) of at least three independent biological assays with two technical repeats. Individual data points are shown. Statistical significance was assessed using the Kruskal-Wallis test to compare mock- and lectin-treated conditions at day 2: ns, not significant; *** p≤0.001.*

In summary, lectin competition experiments revealed virus-specific requirements for sugar moieties in 3D-HIEs. HNoV GII.4 stool-isolates require exposed fucose and acetyl-galactosamine/glucosaminamine residues for efficient infection in HIEs, as evident from potent inhibition of HNoV GII.4 infection by UEA-I and WGA lectin (Figure 29 c,d, g and h). HRoV G3.P[8]eq.-like isolate infection was not inhibited by any of test lectins, while IAV H1N1 relied on exposed sialic acids for successful infection, and unexpectedly also on exposed mannose residues (Figure 31). However, since HRoV G3.[P8]eq-like responded to 2FPF inhibition, this suggests that this non-cell culture adapted HRoV stool-isolate requires fucosylated glycans distinct from those recognized by UEA-I and distinct from those used by HNoV GII.4 strains. Our findings underscore the heterogeneity of glycan usage among enteric viruses and reinforce the importance of fucose and acetyl-galactosamine/glucoseamine residues for HNoV infection, sialic and mannose residues for IAV H1N1 infection and distinct sugar moieties requirement for HRoV.

4.2.3. Fucose supplementation enhances HNoV GII.4 infection in HIEs

Given the observed requirement for exposed fucose residues on the 3D-HIEs membrane for successful HNoV GII.4 infection and binding of exogenous fucose to HNoV GII capsid protein (224), the ability of an excess of exogenous fucose to outcompete infection in 3D-HIEs was next evaluated.

Contrary to the expectation, supplementation of 50 mM fucose did not inhibit HNoV GII.4 infection, but reproducibly enhanced GII.4 infection (Figure 32a-c). In case of the GII.4 Yerseke stool-isolate,

fucose presence during inoculation rescued the infection of non-replicative stool. (Figure 32d). Overall, the increase in mean GEs titers at 2 day post-infection was observed for all tested variants between 2- and 10-fold.

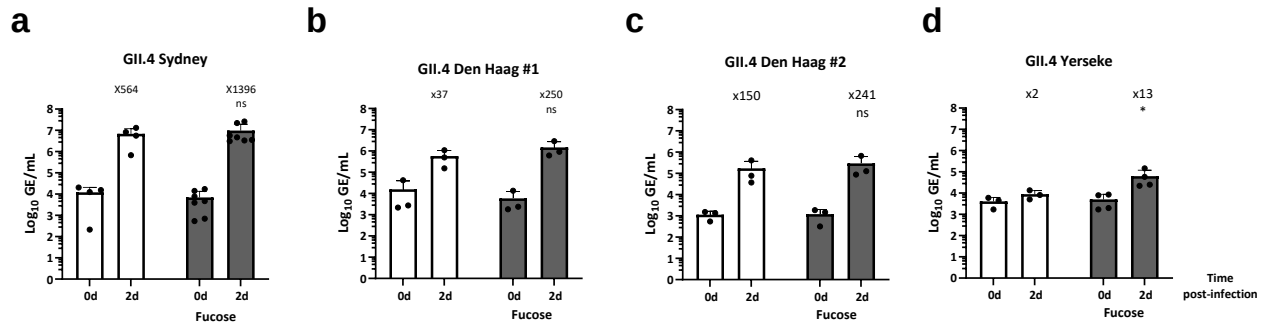

*Figure 32. Fucose enhances HNoV GII.4 infection in 3D-HIEs. Differentiated 3D-HIEs were infected with HNoV (a) GII.4 Sydney, (b) Den Haag #1 and (c) #2, (d) Yerseke stool-isolates at an estimated MOI of 1 in presence of 50 mM fucose. Samples were harvested at day 0 and 2 post-infection for viral GEs quantification by RT-qPCR. Values above the bars indicate the mean fold increase of GE titers at day 2 relative to 0. Data represent means ± standard deviation (SD) of three independent biological assays. Individual data points are shown. Statistical significance was assessed using the one-way ANOVA test to compare mock- and fucose-supplemented conditions at day 2: ns, not significant; * p≤0.05.*

As exogenous fucose was shown to rescue replication of the non-replicating preparation of GII.4 Yerseke, its ability to restore infectivity of an aged GII.4 Sydney preparation was also examined. Fucose supplementation resulted in a robust recovery of GII.4 Sydney replication (Figure 33). To determine whether this enhancement was virus- or host-mediated, an additional condition in which cells were pre-treated with fucose (pre-treatment) and then removed was compared with untreated control and with co-treatment, in which HNoV and fucose were present together during inoculation (similar to conditions in Figure 32). Replication enhancement was observed exclusively under the co-treatment condition, indicating that the effect is virus-directed. Replication of the aged GII.4 Sydney preparation was increased to 209-fold upon fucose supplementation.

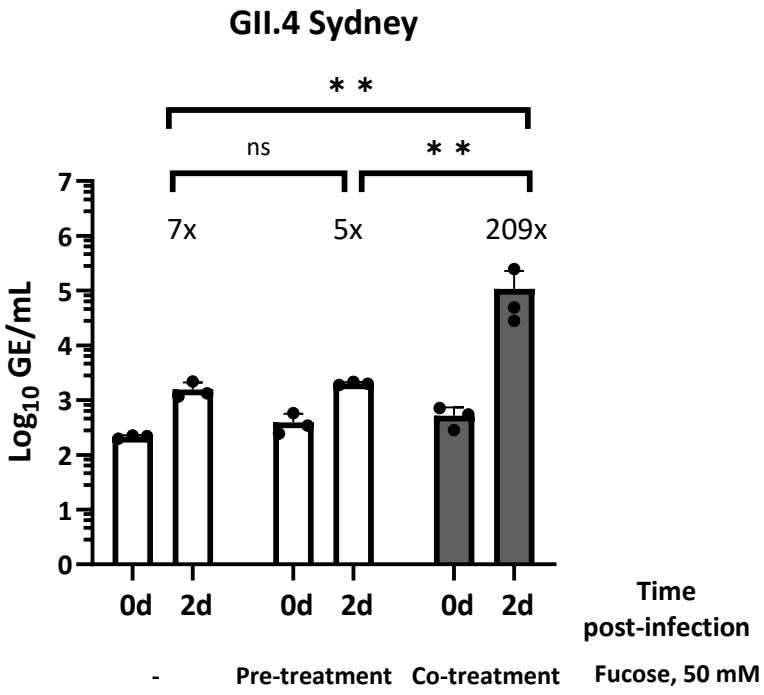

*Figure 33. Fucose enhances HNoV GII.4 Sydney infection by acting on the virus rather than on cells. Differentiated 3D-HIEs were infected with HNoV GII.4 Sydney stool isolate at an estimated MOI of 1. Experimental conditions included infection in the absences of fucose (non-treatment); pre-treatment of cells with 50 mM fucose for 1 hat 37℃ followed by fucose removal and infection (Pre-treatment); pre-incubation of HNoV with 50 mM fucose for 1 hat 37℃ followed by infection in the presence of fucose (Co-treatment). Samples were harvested at day 0 and 2 post-infection for viral GEs quantification by RT-qPCR. Values above the bars indicate the mean fold increase of GE titers at day 2 relative to 0. Data represent means ± standard deviation (SD) of three independent biological assays. Individual data points are shown. Statistical significance was assessed using the one-way ANOVA test to compare mock- and fucose-supplemented conditions at day 2: ns, not significant; ** p≤0.01. Data were contributed by Iqra Kashif, M.Sc.*

Given the ability of fucose to enhance replication of multiple HNoV GII.4 stool-isolates, it was tested whether fucose supplementation could extend serial passaging of GII.4 Sydney in 3D-HIEs. In presence of fucose, significant GII.4 Sydney replication was maintained up to passage 1 (Figure 34), whereas replication in untreated culture was lost after passage 0. However, by the passage 2, infectivity of GII.4 Sydney was lost in both conditions, indicating that while fucose may temporarily support GII.4 replication, it cannot fully overcome host restrictions on sustained passaging.

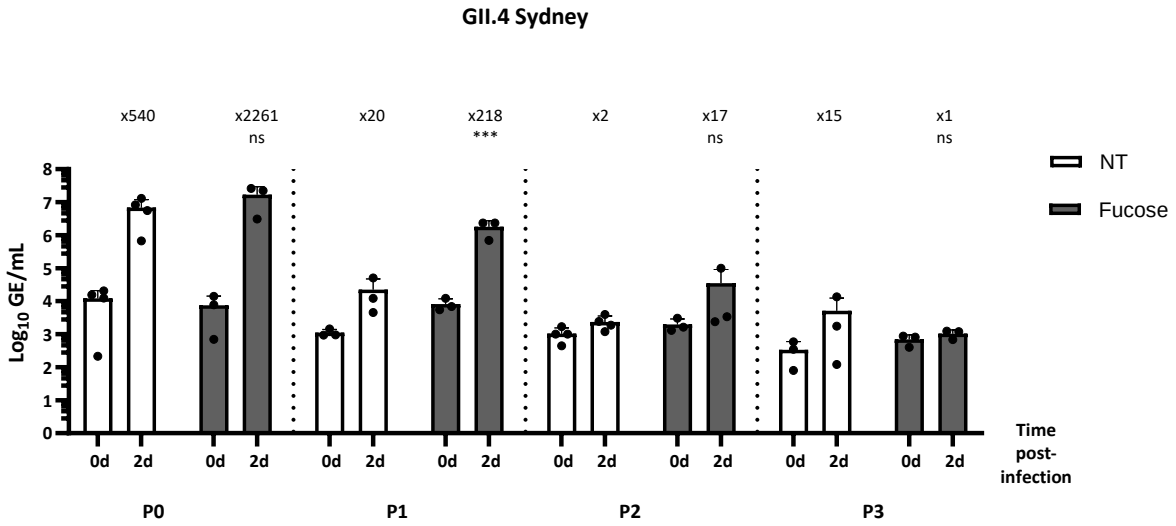

*Figure 34. Fucose prolongs serial passaging of HNoV GII.4 Sydney in 3D-HIEs. Differentiated 3D-HIEs were infected with HNoV GII.4 Sydney at an estimated MOI of 1 in the presence of 50 mM fucose. At day 2 post-infection, cells and supernatant were divided into two equal samples: one portion was harvested by freezing at -80°C, and the other portion was harvested for RNA extraction into TRIzol®. For the next passage, one fifth of the infectious sample was used, with or without supplementation of 50 mM fucose, to initiate the next infection. For each passage, samples were harvested at day 0 and 2 post-infection for viral GEs quantification by RT-qPCR. Values above the bars indicate the mean fold increase of GE titers at day 2 relative to 0. Data represent means ± standard deviation (SD) of three independent biological assays. Individual data points are shown. Statistical significance was assessed using the one-way ANOVA test to compare mock- and fucose-supplemented conditions at day 2: ns, not significant; *** p≤0.001.*

In summary, fucose supplementation enhanced infection of all HNoV GII.4 stool-isolates tested, restored infectivity in aged non-replicative GII.4 preparation, and prolonged HNoV replication during serial passaging in 3D-HIEs. Fucose effect was mediated directly on the virus.

4.2.4. Exogenous fucose did not rescue HNoV GII.4 infection in 3D-HIE after surface depletion of fucosylated glycans

Since supplementation of exogenous fucose mimics the secretor phenotype, it was investigated whether fucose supplementation could compensate for the loss of membrane-bound fucosylated glycans. To test this, 3D-HIEs were treated with fucosyltransferase inhibitor 2-FPF and infected with GII.4 Sydney in the presence of 50 mM fucose. Fucosylation inhibition abrogated GII.4 Sydney infection, and this phenotype was not rescued by fucose supplementation (Figure 35). This finding confirms that fucosylated glycans must be present on the cell surface to support HNoV infection and free fucose cannot substitute for their function.

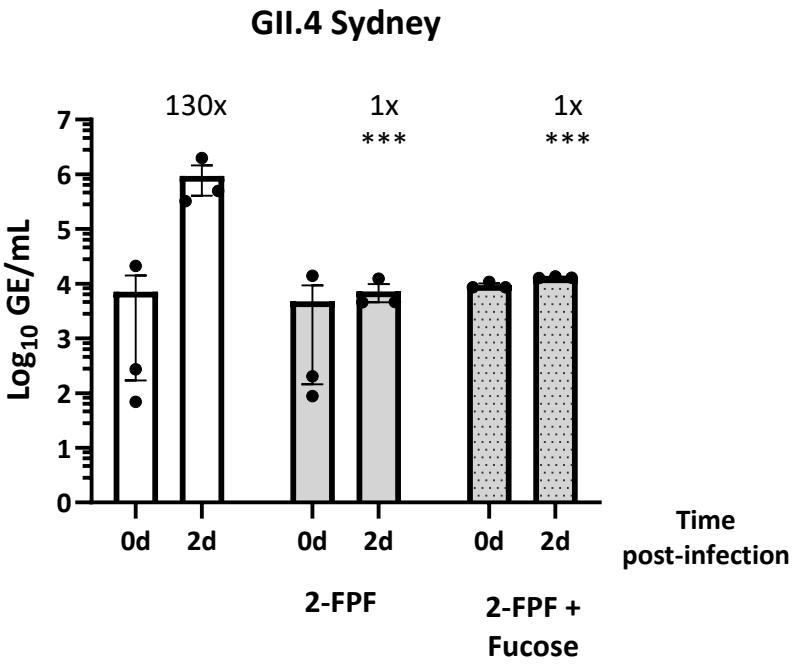

*Figure 35. Supplemented free fucose does not compensate for the absence of fucosylated glycans in 3D-HIEs for HNoV GII.4 Sydney infection. Differentiated HIEs were treated with 500 µM 2-FPF for 2 last days of differentiation. HIEs were infected with HNoV GII.4 Sydney at an estimated MOI of 1 in presence or absence of 50 mM fucose. Samples were harvested at day 0 and 2 post-infection for viral GEs quantification by RT-qPCR. Values above the bars indicate the mean fold increase of GE titers at day 2 relative to 0. Data represent means ± standard deviation (SD) of three independent biological assays. Individual data points are shown. Statistical significance was assessed using the one-way ANOVA test to compare mock- and 2FPF-treated conditions at day 2: ns, not significant; *** p≤0.001.*

4.2.5. HMOs do not effect HNoV GII.4 infection in HIEs

Like fucose, HMOs have been shown to bind to HNoV capsid proteins via the HBGA-binding pocket and are hypothesized to interfere with HNoV attachment to cells (225). The effect of two representative fucose-containing HMOs: 2'-fucosyllactose (2-FL) and lacto-N-fucopentaose I (LFNP I) (Figure 36a) was evaluated on HNoV GII.4 Sydney and Den Haag #2 infections in HIEs. Consistent with the observation for fucose, neither 2-FL nor LNFP I inhibited HNoV GII.4 stool-isolates replication in HIEs (Figure 36b-c). Furthermore, supplementation of 50 mM 2-FL resulted in a modest increase in replication in both stool-isolates compared with untreated controls.

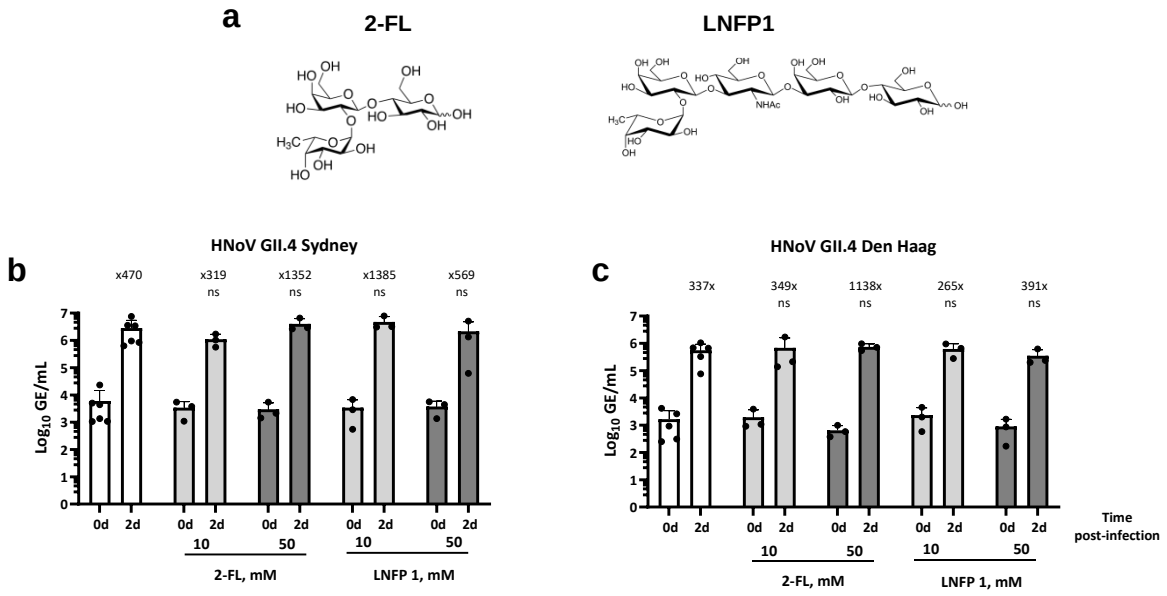

Figure 36. 2-FL and LNFP I do not affect HNoV GII.4 Den Haag #2 and Sydney infection in 3D-HIEs. (a) Schematic of 2-FL and LNFP I. c Differentiated 3D-HIEs were infected with HNoV (b) GII.4 Sydney and (c) Den Haag #2 stool-isolates at an estimated MOI of 1 in presence of increasing concentrations of 2-FL and LNFP I. Samples were harvested at day 0 and 2 post-infection for viral GEs quantification by RT-qPCR. Values above the bars indicate the mean fold increase of GE titers at day 2 relative to 0. Data represent means ± standard deviation (SD) of three independent biological assays. Individual data points are shown. Statistical significance was assessed using the one-way ANOVA test to compare mock- and glycan-supplemented conditions at day 2: ns, not significant.

4.2.6. Fucose-containing glycomimetics inhibits HNoV GII.4 and IAV H1N1 infection in HIEs

A common characteristic of previously tested sugars was the presence of a single fucose moieties per molecule. While these compounds demonstrated strong HNoV-binding in surrogate assays (225), they failed to inhibit HNoV GII.4 infection in 3D-HIEs (Figure 32, 33 and 36). It was therefore evaluated whether compounds with higher affinity or avidity could function as competitors for HNoV GII.4 infection.

To address this hypothesis, fucoidan, a naturally occurring fucopyranose-based polymer extracted from brown algae *Fucus vesiculous*, was examined for its anti-viral activity (Figure 37a). Fucoidan has previously demonstrated anti-HNoV activity in the zebra fish model, where it potently inhibited HNoV GII.4 infection (226–228). In our assay, fucoidan treatment inhibited replication of both HNoV GII.4 Sydney and IAV H1N1 infection (Figure 37b-c) in 3D-HIEs at concentration of 50 mg/mL (estimated 500 µM).

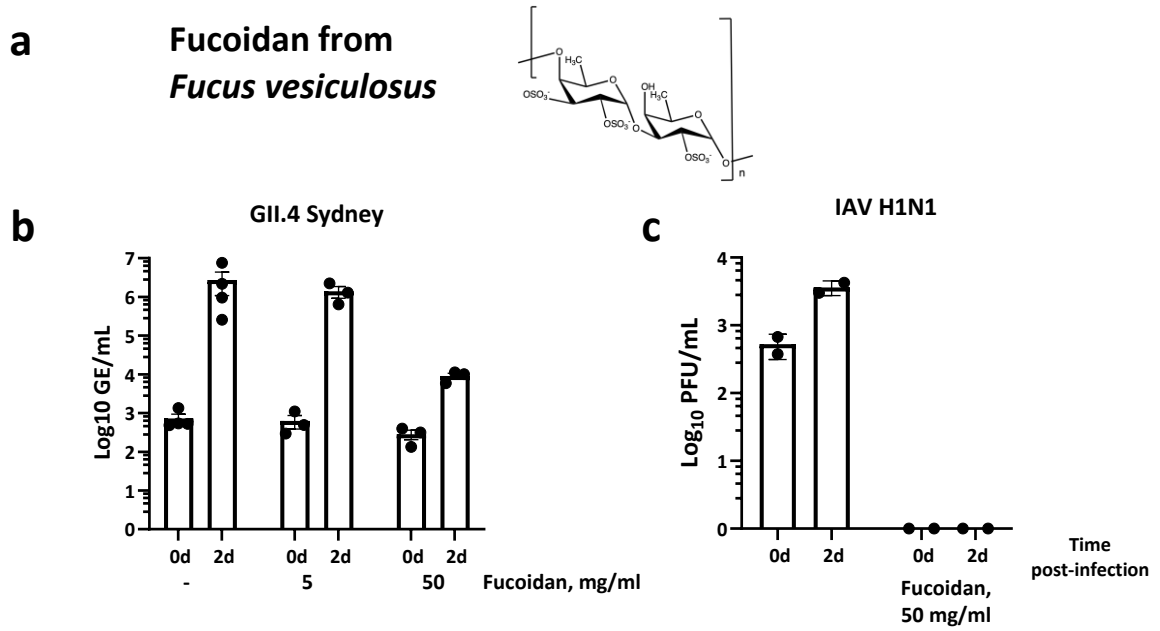

Figure 37. Fucose-rich polymeric compound fucoidan inhibits HNoV GII.4 Sydney and IAV H1N1 infection in 3D-HIEs. (a) Schematic of fucoidan from Fucus vesiculosus. Differentiated 3D-HIEs were infected with (b) HNoV GII.4 Sydney stool-isolate at an estimated MOI of 1 and (c) IAV H1N1 at an MOI 0.1 in presence of increasing concentrations of fucoidan. Samples were harvested at day 0 and 2 post-infection for viral GEs quantification by RT-qPCR or for viral titers quantification by plaque assay. Values above the bars indicate the mean fold increase of GE titers at day 2 relative to 0. Data represent means ± standard deviation (SD) of at least two independent biological assays. Individual data points are shown.

Next, an optimized synthetic glycomimetic compound Ugi-78-bi was investigated against HNoV GII.4 stool-isolates in 3D-HIEs. Compound Ugi-78-bi was designed by incorporating fucose and fluorine modifications into the core structure, which is linked at both termini by a linker molecule (Figure 38a). This approach improved its binding affinity to HNoV VP1 capsid protein, as measured by NMR spectroscopy (Prof. Dr. Thomas Peters, Institute of Chemistry and Metabolomics, University of Lübeck, unpublished data). The highest tested concentration of Ugi-78-bi of 10 mM was determined based on binding constant obtained for HNoV GII.4 VP1 capsid protein in NMR binding assays (229). In the 3D-HIE model, Ugi-78-bi exhibited potent inhibition of GII.4 Den Haag #2 and Sydney stool-isolates at 10 mM concentration (Figure 38b).

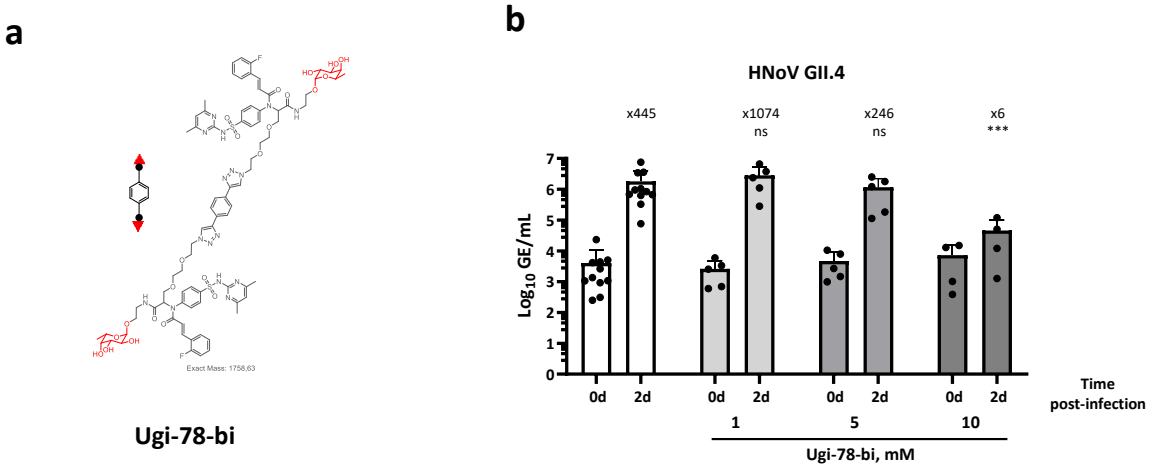

*Figure 38. Ugi-78-bi glycomimetic compound inhibits HNoV GII.4 infection in 3D-HIEs. (a) Schematic of Ugi-78-bi compound. Differentiated 3D-HIEs were infected with (b) HNoV GII.4 Sydney and Den Haag #2 stool isolates at an estimated MOI of 1 in presence of increasing concentrations of Ugi-78-short. Samples were harvested at day 0 and 2 post-infection for viral GEs quantification by RT-qPCR. Values above the bars indicate the mean fold increase of GE titers at day 2 relative to 0. Data represent means ± standard deviation (SD) of pooled results from two HNoV GII.4 stool-isolates with minimum four independent biological assays. Individual data points are shown. Statistical significance was assessed using the one-way ANOVA test to compare mock- and glycan-supplemented conditions at day 2: ns, not significant; *** p≤0.001.*

Fucoidan and Ugi-78-bi compound significantly inhibited HNoV GII.4 infection compared to monofucosylated HMO. The inhibition of IAV H1N1 by fucoidan was unexpected, as IAV entry does not depend on fucosylated glycans and does not require exposed fucose residues. A possible explanation might be that the strong negative charge of the sulfate groups would allow fucoidan to interact not only with the virus but also with cellular surface molecules. Together these findings provide evidence that multifucosylated glycans can serve as effective entry inhibitors of norovirus.

In summary of this section:

- Fucosylation is an active, targetable host pathway that is essential for HNoV GII.4 and HRoV G3.[P8]eq-like stool isolate infection in 3D-HIEs, but is dispensable for IAV H1N1 infection
- HNoV GII.4 infection depends on exposed fucose and acetyl-galactosamine/glucosamine residues in 3D-HIEs, while HRoV G3.[P8]eq-like infection requires distinct exposed glycans to HNoV. IAV H1N1 infection requires sialic acid and mannose residues in 3D-HIEs
- Exogenous fucose enhances HNoV GII.4 infection by acting on virus, prolongs GII.4 Syndey passaging in 3D-HIEs, but cannot substitute membrane-bound fucosylates glycans
- Monofucosylated HMOs did not inhibit HNoV GII.4 infection, whereas multifucosylated glycans and glycomimetics (Ugi-78-bi) efficiently blocked HNoV GII.4 infection

4.3. Bivalent cations and bile acid enhancement of norovirus infectivity and mediation of antibody escape

The third section of this thesis focuses on the role of norovirus capsid ligands, specifically divalent cations and bile acids in modulating entry and immune evasion of HNoV and MNV. Divalent cations, acidic pH, and bile acids are abundant and co-occurring environmental factors within the intestine, the primary site of norovirus infection. For MNV, binding of these environmental factors to the capsid protein induces transitions from a "raised" to a "contracted" capsid conformation, resulting in increased receptor affinity and masking of previously exposed immune epitopes (120,121). For HNoV, the concept of conformational plasticity is only beginning to emerge, however initial evidence supports the ability of HNoV to undergo comparable "raised" to a "contracted" transition, and as a consequence, escape from antibody recognition (101).

To date, much of the knowledge regarding norovirus capsid plasticity has been derived from structural or biophysical studies (101,120,121,124). The functional relevance of these ligand-induced structural changes in the context of viral infection and escape from immune neutralization remains poorly understood. Here, the effect of physiological concentrations of divalent cations and bile acids on MNV and HNoV infectivity *in vitro* was investigated.

Naturally susceptible murine microglial cells BV2 and genetically modified human Huh7 cells expressing the MNV receptor mCD300lf (Huh7^{mCD300lf} cells) were utilized as MNV infectious model, as well as 3D-HIE model for HNoV, to examine the divalent cation and bile acid GCDCA effect on noroviruses. To determine whether these environmental factors can individually or synergistically modulate immune neutralization of both viruses, cell culture neutralization assays using monoclonal antibodies was performed in presence of magnesium and bile acid GCDCA.

Through this approach, it is evaluated whether the functional outcomes inferred from structural studies of norovirus capsid dynamics are reproduced under physiologically relevant infection conditions.

4.3.1. Magnesium, but not bile acid GCDCA enhances MNV-1 binding to cells

To investigate whether divalent cation, e.g. magnesium, and bile acid GCDCA impact the MNV-1 attachment to the susceptible cells, an RT-qPCR-based attachment assay was adapted (230), using murine microglial BV- 2, recombinant Huh7^{mCD300lf} and non-susceptible Huh7^{naïve}. Particularly, cells were inoculated with MNV-1 at an MOI of 5 in the presence of an increasing concentration of magnesium and/or bile acid GCDCA. The inoculum was removed after a 1 hour of incubation on ice, after which cells were harvested for total RNA extraction and RT-qPCR quantification of GEs titers. Importantly, all MNV experiments in this section were performed in divalent cation-reduced conditions, as MNV stocks were reconstituted in sodium phosphate buffer prepared with ultrapure (Milli-Q) water to reduce the divalent cation background. The same sodium phosphate buffer, prepared in a similar manner, was used throughout all cell culture experiments, with magnesium and/or bile acid GCDCA supplemented where indicated.

The concentration range of magnesium was selected based on physiological levels in the small intestine under normal (1-25 mM) and diarrheal conditions (up to 120-130 mM) (231,232). For bile

acids, physiological levels in the small intestine vary between 1 to 10 mM depending on fasted or fed state (233), here a lower concentration was chosen due to bile cytotoxic effect.

A dose-dependent enhancement of MNV-1 attachment to Huh7^{mCD300lf} cells in the presence of magnesium, but not bile acid GCDCA was observed (Figure 39). Synergistic action of magnesium and bile acid GCDCA did not enhance MNV-1 attachment to Huh7^{mCD300lf} beyond levels observed in just magnesium supplemented condition. MNV-1 attachment to naturally susceptible BV-2 cells were also increased by magnesium supplementation. While in non-susceptible Huh7^{naïve} magnesium supplementation failed to enhance viral attachment, suggesting that magnesium-mediated enhancement is receptor-dependent.

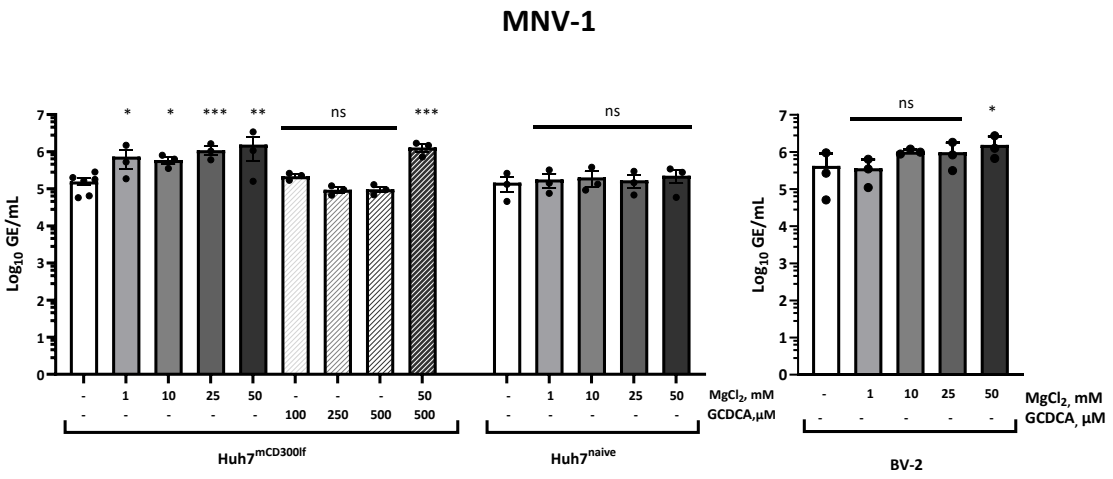

*Figure 39. Dose-dependent enhancement of MNV-1 binding to murine microglial BV-2 and human recombinant or naive Huh7 cells by magnesium. Huh7^{mCD300lf}, Huh7^{naïve} and BV-2 cells were inoculated with MNV-1 at an MOI of 5 and incubated on ice for 1 hour with increasing concentration of $MgCl_2$ and bile acid GCDCA. Cells were washed three times with ice cold sodium phosphate buffer and harvested in TRIzol® for total RNA extraction. MNV-1 viral genome equivalents were determined via RT-qPCR. Data represent means ± standard deviation (SD) of three independent biological assays. Individual data points are shown. Statistical significance was assessed using the one-way ANOVA test compared to non-treated: ns, not significant; * p≤0.05; ** p≤0.01; *** p≤0.001.*

4.3.2. Magnesium increases MNV-1 infectivity and mediates antibody escape

To investigate if the magnesium-induced increase in MNV-1 cellular attachment results in increased infectivity, a single-round MNV-1 infection assay was performed in Huh7^{mCD300lf} cells at MOI of 5. In addition, to determine whether magnesium exerts its effect on the virus or on the host cells, MNV-1 infection in absence of any supplemented divalent cation (mock) and infection in presence of magnesium (co-treatment) were compared to pre-treatment of cells with magnesium before infection and post-treatment after infection. Samples were harvested 8 hpi to allow only one infectious cycle and titrated using plaque assay. A significant 10-fold infectivity increase in MNV-1 infection was observed when magnesium ions were present only during infection (co-treatment) (Figure 40), but not when cells were pre- or post-treated with $MgCl_2$. Our findings confirm that magnesium enhances MNV-1 infectivity *in vitro* by acting on the virus.

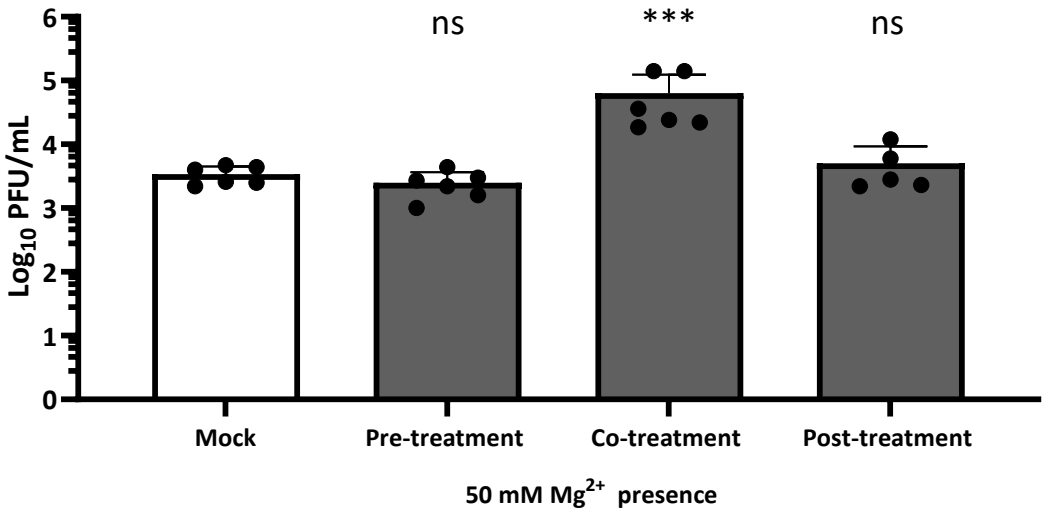

*Figure 40. Magnesium increases MNV-1 infection by acting on the virus rather than on cells.Huh7^{mCD300lf} cells were infected with MNV-1 MOI of 5 in presence or absence of 50 mM $MgCl_2$. The experimental conditions included infection in absences of magnesium (mock); pre-treatment of cells prior to infection; infection in the presence of 50 mM $MgCl_2$; and infection in the absence of divalent cations followed by post-infection treatment with 50 mM $MgCl_2$. At 8 hpi samples were harvested, MNV-1 titers were quantified by plaque assay. Data represent means ± standard deviation (SD) of three independent biological assays with two technical repeats each. Individual data points are shown. Statistical significance was assessed using the one-way ANOVA test compared to non-treated: ns, not significant; *** p≤0.001.*

Next a plaque-based MNV-1 neutralization assay was performed in the presence of monoclonal neutralizing antibody A6.2, together with increasing concentrations of $MgCl_2$ to investigate magnesium-induced escape from antibody binding. A dose-dependent increase in infectivity and escape from neutralization of MNV-1 was observed (Figure 41), where 50 mM of $MgCl_2$ led to a 10-fold increase in MNV-1 titer and complete escape from neutralization.

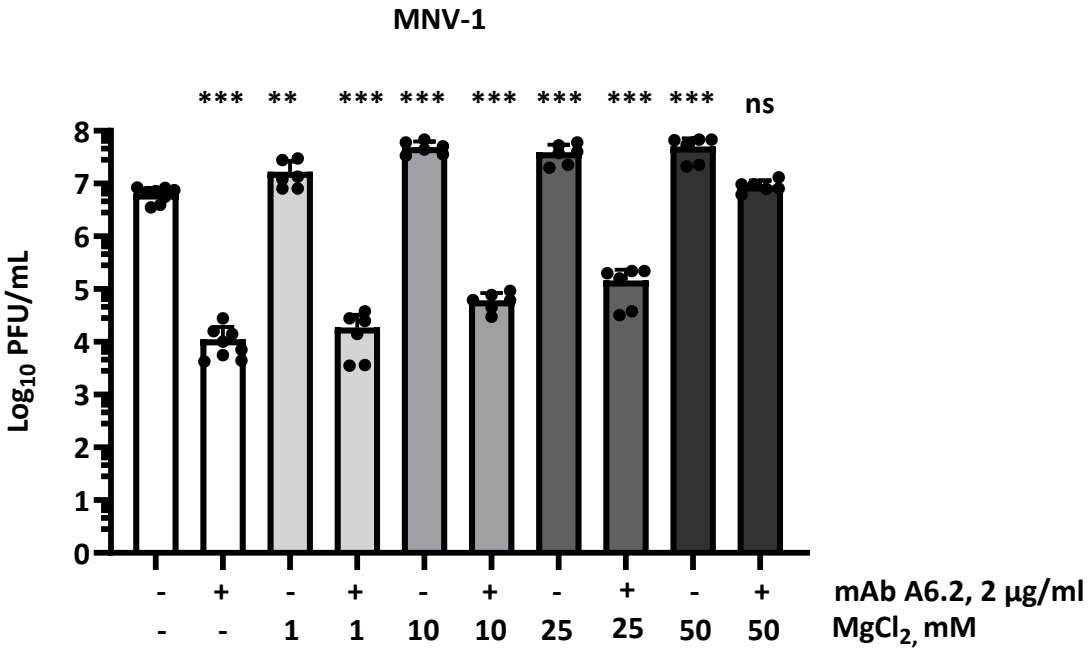

*Figure 41. Magnesium increases MNV-1 infectivity and mediates neutralizing antibody escape. MNV-1 plaque-based neutralization assays were performed in Huh7^{mCD300lf} cells in the presence of increasing concentrations of $MgCl_2$ and 2 µg/mL IgG A6.2 monoclonal antibodies. Data represent means ± standard deviation (SD) of three independent biological assays with two technical repeats each. Individual data points are shown. Statistical significance was assessed using the one-way ANOVA test compared to non-treated: ns, not significant; ** p≤0.01; *** p≤0.001.*

Our findings support predictions from structural studies (124), showing that divalent cation, specifically magnesium, at physiologically relevant concentrations, enhance MNV-1 infectivity and mediating escape from neutralizing antibodies.

4.3.3. Magnesium acts synergistically with bile acid GCDCA and induces neutralizing antibody escape of MNV

Divalent cations were postulated to work synergistically with GCDCA via pre-organizing MNV VP1 conformational state and facilitating the binding of the other ligand (124,128). To determine whether magnesium and bile acid GCDCA can act synergistically to enhance MNV infection and facilitate antibody escape *in vitro*, a plaque-based MNV-1 neutralization assays was performed using monoclonal neutralizing A6.2 antibodies in the presence of 500 µM GCDCA, low-dose (1 mM) or high-dose (50 mM) $MgCl_2$.

To our surprise, under divalent cation-free conditions, GCDCA alone did not induce antibody escape of MNV-1. Low-dose magnesium was similarly not inducing antibody escape, however, combination of low-dose magnesium and GCDCA resulted in partial antibody escape, supporting the hypothesis that magnesium and GCDCA act synergistically (Figure 42a). Furthermore, these findings indicate that GCDCA-induced MNV-1 antibody escape is magnesium-dependent.

To determine whether the effect of magnesium and bile acid GCDCA on MNV escape from neutralizing antibodies is conserved across viral strains, a chronic strain CR3 ability to evade neutralization under the above-mentioned conditions was investigated. As expected, neither low-dose $MgCl_2$ nor GCDCA

alone induced CR3 escape from monoclonal antibodies. However, the combination of low-dose or high-dose $MgCl_2$ with GCDCA induced partial to complete neutralization escape of CR3 (Figure 42b). Our observations confirm that magnesium-induced escape from neutralization is conserved in the chronic CR3 strain.

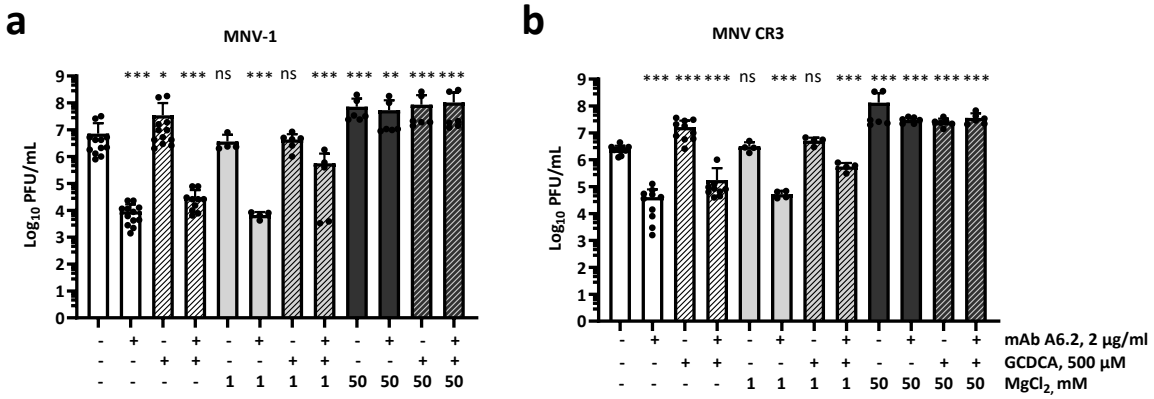

*Figure 42. Magnesium induces neutralizing antibody escape of MNV and acts synergistically with bile acid GCDCA. (a) MNV-1 and (b) MNV CR3 plaque-based neutralization assays were performed on Huh7^{mCD300lf} in the presence of low (1 mM) or high (50 mM) concentrations of $MgCl_2$, 500 µM GCDCA, or a combination of $MgCl_2$ with GCDCA. Viral neutralization was assessed using 2 µg/mL IgG A6.2 monoclonal antibodies. Data represent means ± standard deviation (SD) of three independent biological assays with two technical repeats each. Individual data points are shown. Statistical significance was assessed using the one-way ANOVA test compared to non-treated: ns, not significant; * p≤0.05; ** p≤0.01; *** p≤0.001.*

To explore the effect of magnesium on HNoV infectivity, magnesium supplementation assay was performed in 3D-HIEs. Three conditions were compared: infection under standard conditions (non-treated, approx. 3 mM combined calcium and magnesium present in infection medium); pre-treatment of cells with 50 mM $MgCl_2$ before infection and HNoV GII.4 infection in presence of magnesium (co-treatment). In the pre-treatment condition, magnesium was removed from cells prior to infection to distinguish whether magnesium exerts its effect on the virus or on the host cells. Four available HNoV GII.4 stool-isolates from the panel were tested, including GII.4 epochal Yerseke, Den Haag #1 and #2 and epidemic Sydney. Of note, all conditions were supplemented with bile acid GCDCA, as component of infectious medium.

A significant 30- to 60-fold increase in replication was observed for all GII.4 epochal stool-isolates when magnesium was present during infection, but not in non- or pre-treated conditions (Figure 43). These findings indicate that magnesium acts directly on HNoV rather than on the host cells to enhance the infectivity.

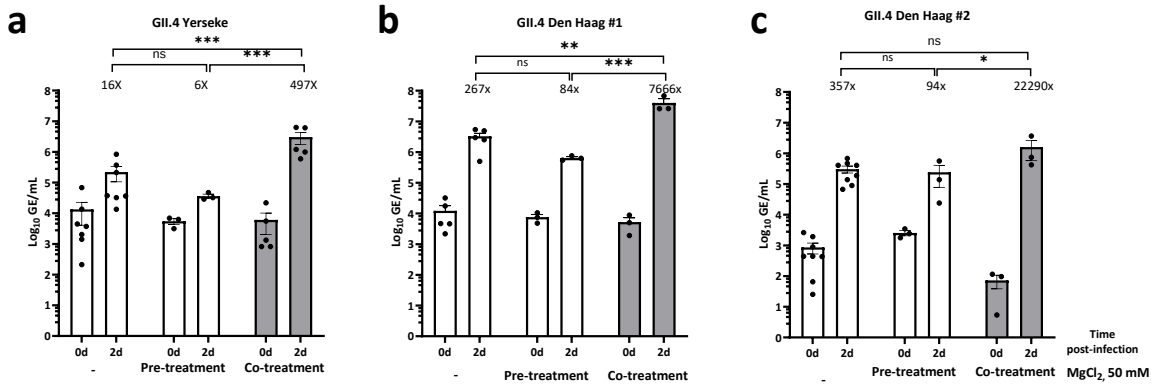

*Figure 43. Magnesium enhances HNoV GII.4 infection by acting on the virus rather than on cells. Differentiated 3D-HIEs were infected with HNoV (a) GII.4 Yerseke, (b) Den Haag #1 and (c) #2 stool-isolates at an estimated MOI of 1. The experimental conditions included infection in absences of magnesium ("-", non-treated); pre-treatment of cells with 50 mM $MgCl_2$ for 1 hat 37°C, followed by three washes with CMGF- and infection in presence of 500 µM GCDCA (co-treatment); pre-incubation of HNoV with 50 mM $MgCl_2$ prior to infection n in the presence of 500 µM GCDCA (pre-treatment). Samples were harvested at day 0 and 2 post-infection for viral GEs quantification by RT-qPCR. Values above the bars indicate the mean fold increase of GE titers at day 2 relative to 0. Data represent means ± standard deviation (SD) of at least three independent biological assays. Individual data points are shown. Statistical significance was assessed using the one-way ANOVA test compared to day 2 of non-treated: ns, not significant; * p≤0.05; ** p≤0.01; *** p≤0.001.*

As for GII.4 Sydney, when using a fresh stool preparation, no significant increase in GEs titers following magnesium supplementation was observed (Figure 44). The observed decrease in replication of the aged GII.4 Sydney preparation prompted us to test whether magnesium could rescue viral infectivity, given that divalent cations have been proposed to stabilize the HNoV GII capsid. (Jung 2019). A significant rescue of GII.4 Sydney infectivity was observed following magnesium supplementation in recently degraded preparations (<1 months after the onset degradation) (Figure 44). This effect, however, was time-dependent, as prolonged storage of degraded preparations (>1 months after the onset degradation) abolished the rescue capacity of magnesium.

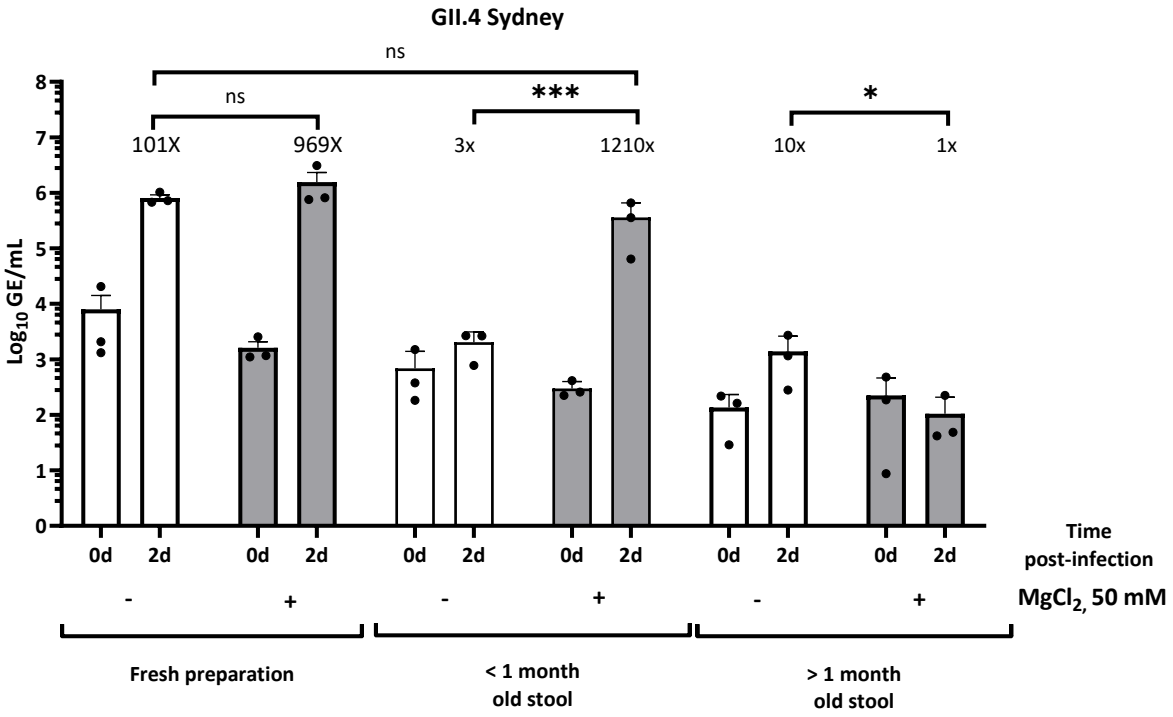

*Figure 44. Magnesium restores HNoV GII.4 Sydney infectivity in aged preparation. Differentiated 3D-HIEs were infected with HNoV GII.4 Sydney stool-isolates from fresh and aged preparation at an estimated MOI of 1. The experimental conditions included infection in absences of magnesium ("-", non-treated) and pre-incubation of HNoV with 50 mM $MgCl_2$ prior to infection in the presence of 500 µM GCDCA ("+", co-treated). Samples were harvested at day 0 and 2 post-infection for viral GEs quantification by RT-qPCR. Values above the bars indicate the mean fold increase of GE titers at day 2 relative to 0. Data represent means ± standard deviation (SD) of three independent biological assays. Individual data points are shown. Statistical significance was assessed using the one-way ANOVA test compared to non-treated at day 2: ns, not significant; * p≤0.05; *** p≤0.001. Data for aged preparation was provided by Iqra Kashif, M.Sc (TaubeLab).*

Taken together, these results demonstrate that magnesium in combination with GCDCA enhances HNoV GII.4 stool-isolates infectivity and exert stabilizing effect HNoV GII.4 stool preparations, consistent with similar observations reported for MNV.

4.3.4. Identification of neutralizing antibodies against HNoV GII.4 stool-isolates

Having confirmed that divalent cations, such as magnesium, enhance HNoV GII.4 infectivity in 3D-HIEs, the potential of magnesium to mediate neutralizing antibody escape in HNoV GII.4 variants was next investigated. To address this, potent neutralizing anti-HNoV GII.4 antibodies suitable for functional studies in the HIE model were first identified.

Neutralization assays were performed using HNoV GII.4 Den Haag #1 stool-isolate and a panel of antibodies available in the laboratory, including monoclonal antibodies against GII.2, GII.1, and GII.4 variants, polyclonal serum against GII.7 variant, and a nanobody against GII.10. Among all tested antibodies, only the anti-GII.4 monoclonal antibody (A1431) (Figure 45a) effectively neutralized GII.4 Den Haag #1 stool-isolate, with an inhibitory concentration of 4 µg/mL (Figure 45b). None of other antibodies displayed a cross-reactivity towards GII.4 Den Haag #1 stool-isolate.

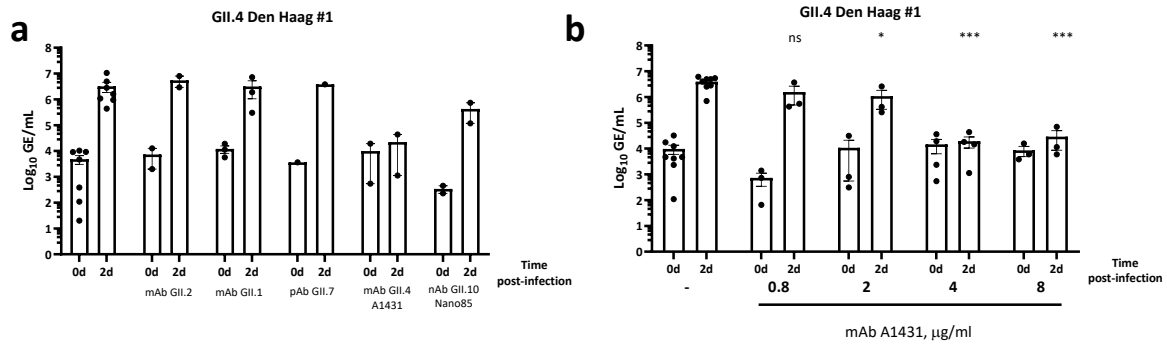

*Figure 45. Neutralization of HNoV GII.4 Den Haag #1 infection in 3D-HIEs. Differentiated 3D-HIEs were infected with HNoV GII.4 Den Haag #1 stool-isolate at an estimated MOI of 1 in presence of 500 µM GCDCA and (a) one of the following antibodies: 2 µg/mL GII.2 monoclonal antibody, 90 µg/mL GII.1 monoclonal antibody, 4 µg/mL GII.4 A1431 monoclonal antibody, 1:10 dilution of GII.7 polyclonal serum and 60 µg/mL GII.10 nanobody 85 or (b) with increasing concentration of GII.4 A1431 monoclonal antibody. Antibody concentrations were selected based on published literature or, when unavailable, on the highest achievable concentration compatible with the experimental setup. Samples were harvested at day 0 and 2 post-infection for viral GEs quantification by RT-qPCR. Data represent means ± standard deviation (SD) of at least one independent biological assays. Individual data points are shown. Statistical significance was assessed using the one-way ANOVA test compared to non-treated day 2: ns, not significant; * p≤0.05; *** p≤0.001.*

To further characterize A1413 monoclonal antibody, its neutralization potency was testes both prior to viral attachment (pre-treatment) and after viral attachment to host cells (post-treatment). In both conditions, A1431 antibody significantly reduced viral GE titers at day 2 post-infection compared to untreated condition (Figure 46). These observations confirm A1431 monoclonal antibody as a potent neutralizing antibody against HNoV GII.4 Den Haag #1 stool-isolate and suggest that it interferes with viral replication beyond the first infection cycle, likely across multiple cycles of infection.

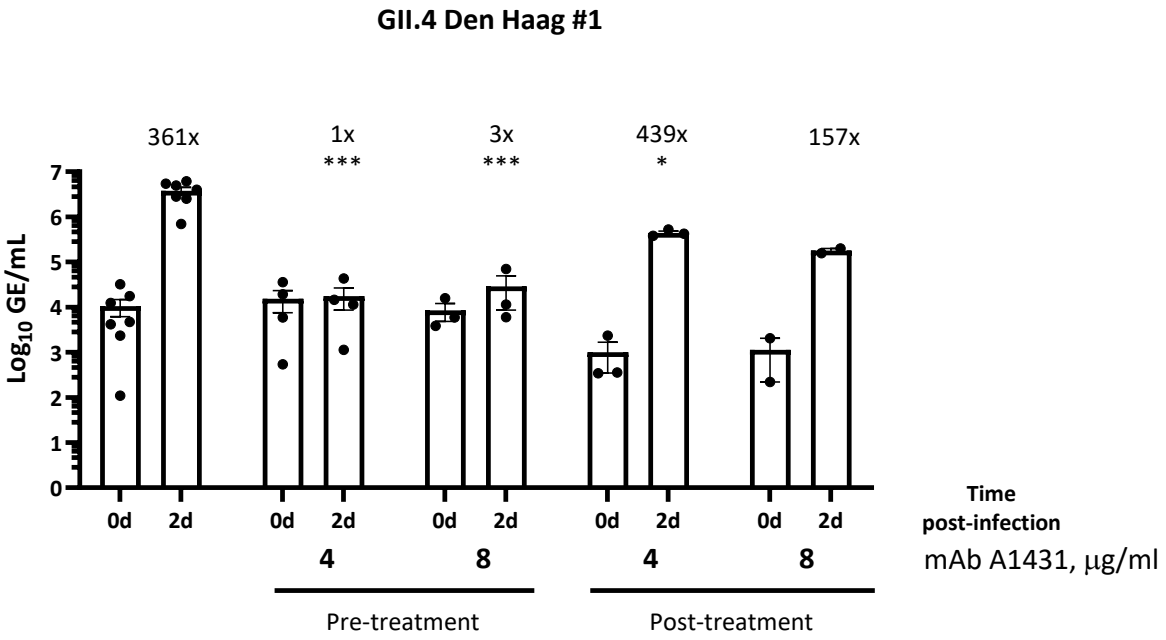

*Figure 46. Neutralization of HNoV GII.4 Den Haag #1 infection by A1431 monoclonal antibody in 3D-HIEs. Differentiated 3D-HIEs were infected with HNoV GII.4 Den Haag #1 stool-isolate at an estimated MOI of 1 in presence of 500 µM GCDCA and increasing concentration of A1431 monoclonal antibody. Following infection, HIEs were washed three times with CMGF-, re-seeded in BME and maintained in differentiation medium supplemented with 2 µM Ruxolitinib, 500 µM GCDCA and A1431 monoclonal antibody in post-treatment condition. Samples were harvested at day 0 and 2 post-infection for viral GEs quantification by RT-qPCR. Data represent means ± standard deviation (SD) of at least two independent biological assays. Individual data points are shown. Statistical significance was assessed using the one-way ANOVA test compared to non-treated day 2: ns, not significant; * p≤0.05; *** p≤0.001.*

4.3.5. Magnesium induces HNoV GII.4 to escape from neutralizing antibodies

To determine whether magnesium facilitates HNoV GII.4 antibody neutralization escape, a neutralization assays in the 3D-HIE model was performed in the presence of 50 mM $MgCl_2$, 500 µM GCDCA, and 4 µg/mL monoclonal antibody A1431 using HNoV GII.4 Den Haag #1, Den Haag #2, and Yerseke stool-isolates.

None of the three tested stool-isolates exhibited GCDCA sensitivity, as they replicated efficiently without bile acid supplementation (Figure 47). Magnesium supplementation enhanced replication of Den Haag #1 and Yerseke isolates (Figure 47a and c), but had no effect on the Den Haag #2 isolate (Figure 47b). As expected, bile acid GCDCA alone did not induce HNoV GII.4 escape from antibody neutralization, whereas magnesium supplementation led to modest neutralization escape for the Den Haag #1 isolate (Figure 47a), as indicated by increased viral GE titers at day 2 post-infection compared to antibody-treated conditions without magnesium. The combination of magnesium and GCDCA significantly enhanced the replication of Den Haag #1 and Yerseke stool-isolated. The synergistic effect of magnesium and bile acid GCDCA led to partial escape from neutralization for Den Haag #1 isolate (Figure 47a), but not for the Yerseke or Den Haag #2 isolates.

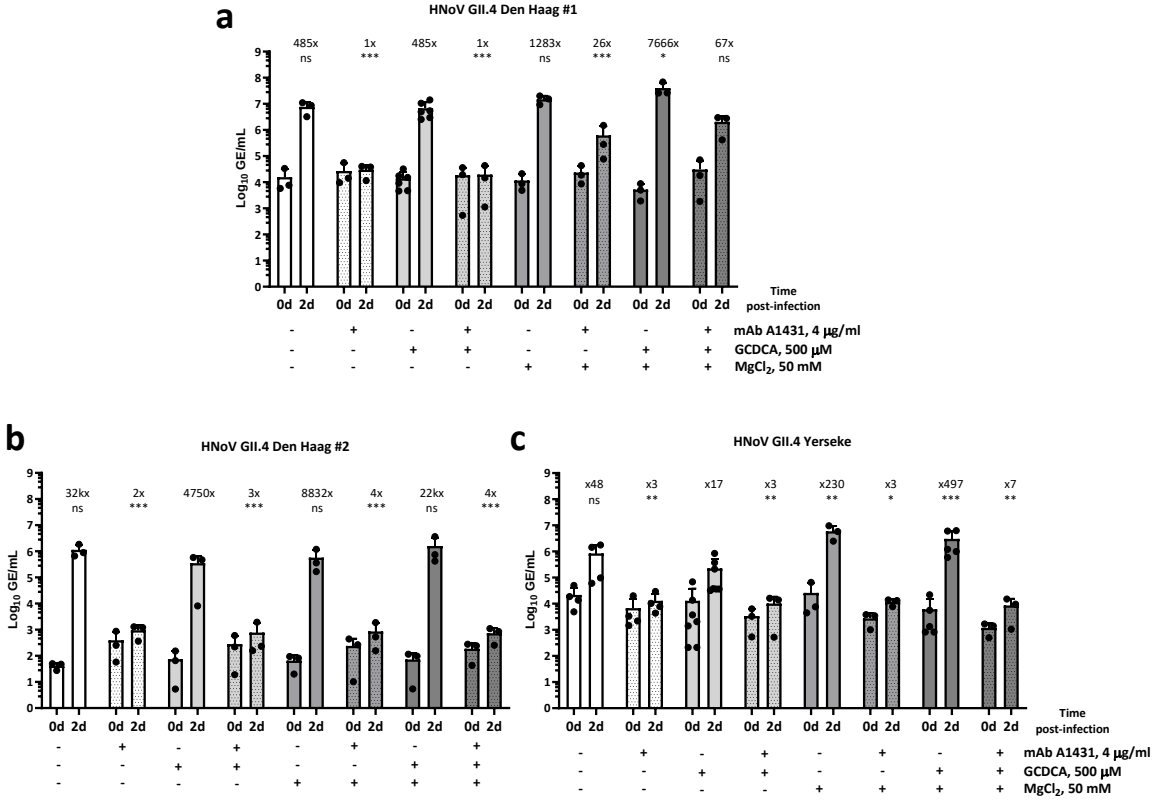

*Figure 47. Magnesium acts synergistically with bile acid GCDCA to enhance HNoV replication in HIEs and induce neutralizing monoclonal antibody escape in a stool-isolate dependent manner. Differentiated 3D-HIEs were infected with HNoV (a) GII.4 Den Haag #1, (b) Den Haag #2 and (c) Yerseke stool-isolates at an estimated MOI of 1 in presence of 500 µM GCDCA, 50 mM $MgCl_2$, or a combination of both, with and without 4 µg/mL A1431 monoclonal antibody. Following infection, HIEs were washed three times with CMGF-, re-seeded in BME and maintained in differentiation medium supplemented with 2 µM of Ruxolitinib, 500 µM GCDCA, 50 mM $MgCl_2$, or a combination of both. Samples were harvested at day 0 and 2 post-infection for viral genome copies quantification by RT-qPCR. Values above the bars indicate the mean fold increase of GE titers at day relative to 0. Data represent means ± standard deviation (SD) of at least three independent biological assays. Individual data points are shown. Statistical significance was assessed using the one-way ANOVA test compared to GCDCA-treated condition at day 2: ns, not significant; * p≤0.05; ** p≤0.01; *** p≤0.001.*

The synergistic effect of magnesium and bile acid GCDCA enhanced the replication of HNoV GII.4 Den Haag #1 and Yerseke stool-isolates and induced the escape from neutralization for the Den Haag #1 isolate. These findings support the role of magnesium and bile acid GCDCA in modulating HNoV GII.4 infectivity and neutralization escape, similar to the observations in MNV, although the effect appears to be not uniformly conserved across stool-isolates.

In summary of this section:

- Magnesium alone, and in synergy with the bile acid GCDCA, induces escape of MNV from neutralizing antibodies.
- In the absence of antibodies, GCDCA and magnesium can enhance MNV infectivity.
- Magnesium in combination with GCDCA enhances and prolongs the infectivity of HNoV GII.4 of stool preparations, and promotes isolate-dependent escape from neutralizing antibodies.

4.4. Polyamine depletion restricts norovirus infection

The fourth section of this thesis focuses on the role of polyamines, host-produced small aliphatic molecules, in norovirus infection. Polyamines serve multiple functions in host metabolism, including the regulating of protein translation, host cholesterol synthesis, apoptosis induction and interferon production (197,199–201).

Polyamines are also involved in the replication of the wide range of both DNA and RNA viruses (197). In RNA viruses, polyamines have been shown to facilitate viral attachment, genome replication or they are directly incorporated into viral particles (197,207,208). DNA viruses primarily depend on polyamines to support viral and host protein synthesis and can also be incorporated in viral particles (234). DNA viruses, such as HSV-1, require polyamines to modulate production of host restriction factors, such as interferon (199).

Preliminary research conducted by Dr. Carmen Mirabelli in collaboration with the laboratory of Dr. Christiane Wobus (University of Michigan) identified in an unbiased metabolomic approach that HNoV VLPs can inhibit the production of polyamines, specifically spermidine, from commensal gut bacteria such as *Enterobacter cloacae*. This observation prompted us to investigate, whether polyamines are required for norovirus infection in host cells.

To address this question, two well-characterized pharmacological inhibitors of polyamine biosynthesis were utilized: difluoromethylornithine (DFMO) and N^1,N^{11}-diethylnorspermine (DENSpm), which are widely employed to deplete cellular polyamine pools in both cellular and virological studies (Figure 48a). DFMO, also known as eflornithine, is an inhibitor of ODC1, which by blocking the conversion of ornithine to putrescine effectively reduces the subsequent synthesis of spermidine and spermine. DENSpm is a synthetic spermine analog that exerts its effects by inducing the expression of spermidine/spermine N^1-acetyltransferase 1 (SAT1). SAT1 acetylates spermidine and spermine, targeting them for either export from the cell or oxidative degradation by polyamine oxidases. This mechanism leads to a more rapid depletion of intracellular polyamines compared to DFMO. Both DFMO and DENSpm have been extensively utilized in viral research due to their established efficacy and tolerability in *in vitro* and *in vivo* models (199,208).

To elucidate the role of polyamines in MNV infection, the effects of DFMO and DENSpm treatment on viral replication were examined across multiple susceptible cell culture models. The specific stage of the viral life cycle impacted by polyamine depletion was then assessed. Finally, to determine whether polyamine dependence is conserved among noroviruses, the analysis was extended to the 3D-HIE model to evaluate the impact of polyamine depletion on HNoV infection.

4.4.1. MNV-1 is sensitive to polyamine depletion

To examine the role of polyamines in norovirus infection, MNVs sensitivity to polyamine depletion was determined using well established polyamine inhibitors, DFMO and DENSpm. Dose-response assays were performed in naturally susceptible murine macrophage cell line RAW264.7 to determine effective compound concentration (Figure 48b-c). Following established protocols, RAW264.7 macrophages were pre-treated with DENSpm for 24 hours prior to infection, whereas DFMO pre-treatment was extended to 96 h to allow for substantial polyamine depletion. Consistently with published literature, treatment with 100 µM of DENSpm and 500 µM for DFMO effectively inhibited of the MNV-1 infection (Figure 48b–c), confirming the suitability of these concentrations for subsequent studies.

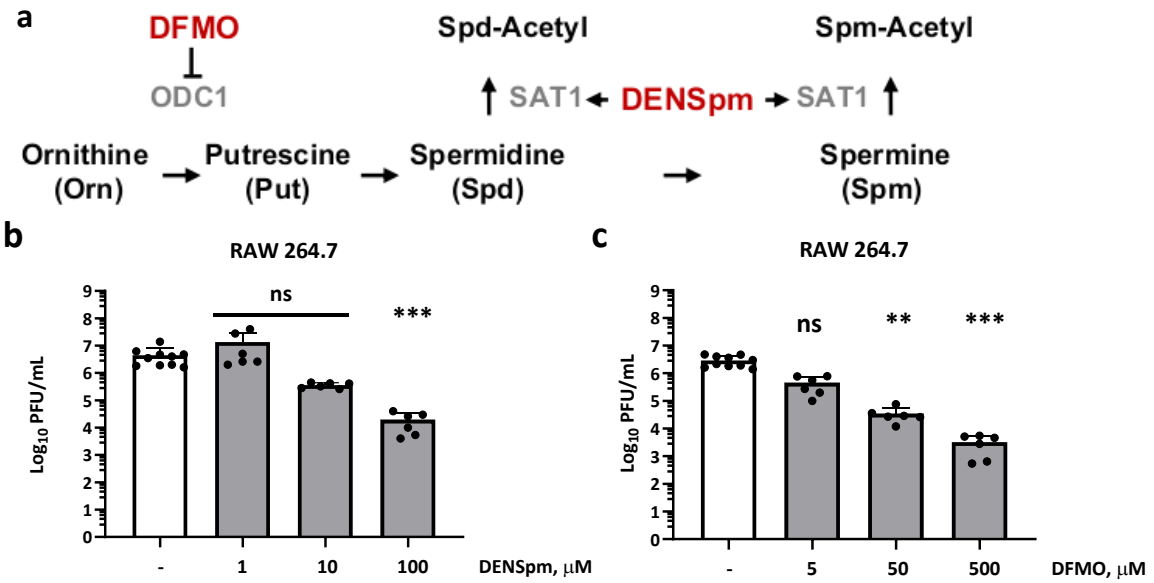

*Figure 48. Dose-dependent inhibition of MNV-1 infection by DENSpm and DFMO. (a) Polyamines biosynthesis and catabolic pathway. RAW264.7cells were pretreated with increasing concentration of (b) DENSpm for 24 h or (c) DFMO for 96 h. Cells were inoculated with MNV-1 at MOI 0.1 and for 1 h at 4°C. The inoculum was removed and replaced with culture medium (-) or medium supplemented with DENSpm or DFMO. Virus titers were determined 24 hpi by plaque assay. Data represent means ± standard deviation (SD) of three independent biological assays with two technical repeats each. Individual data points are shown. Statistical significance was assessed using the Kruskal-Wallis test compared to non-treated/infected: ns, not significant; ** p≤0.01; *** p≤0.001.*

The effect of polyamine depletion and spermine and spermidine re-supplementation on MNV-1 infection was investigated in three distinct cell lines: recombinant human Huh7^{mCD300lf} epithelial cells, murine BV-2 microglial cells, and murine RAW264.7 macrophages.

To deplete polyamines cell lines were pretreated with 100 µM DENSpm for 24 h prior to infection, as indicated (Figure 49 a–c). Following pretreatment, cells were infected with MNV-1 at MOI 0.1 for 1 hour on ice, then shifted to 37 °C in the continued presence of DENSpm, with and without supplemented spermine or spermidine. Viral titers were then quantified by plaque assay 24 hpi. The data showed that DENSpm treatment significantly impaired MNV-1 infection across all tested cell lines, with significant reductions of 2-3 logs in BV-2 and RAW264.7 cells, and up to 5 logs in Huh7mCD300lf cells. Supplementation with 100 µM spermine or spermidine restored viral titers comparable to untreated controls.

Next, Huh7^{mCD300lf}, BV-2, and RAW264.7 cells were treated with 500 µM DFMO for 4 days prior to infection (Figure 49 d–f). Cells were inoculated with MNV-1 at a MOI of 0.1 for 1 h on ice, followed by an incubation for 24 h at 37 °C in the continued presence of DFMO, with or without supplementation of spermine or spermidine. Similar to DENSpm, DFMO treatment led to significant inhibition of MNV infection across all tested cell lines by 24 hpi, highlighting the role of polyamines as critical host factors for MNV infection in both immune and epithelial cell types.

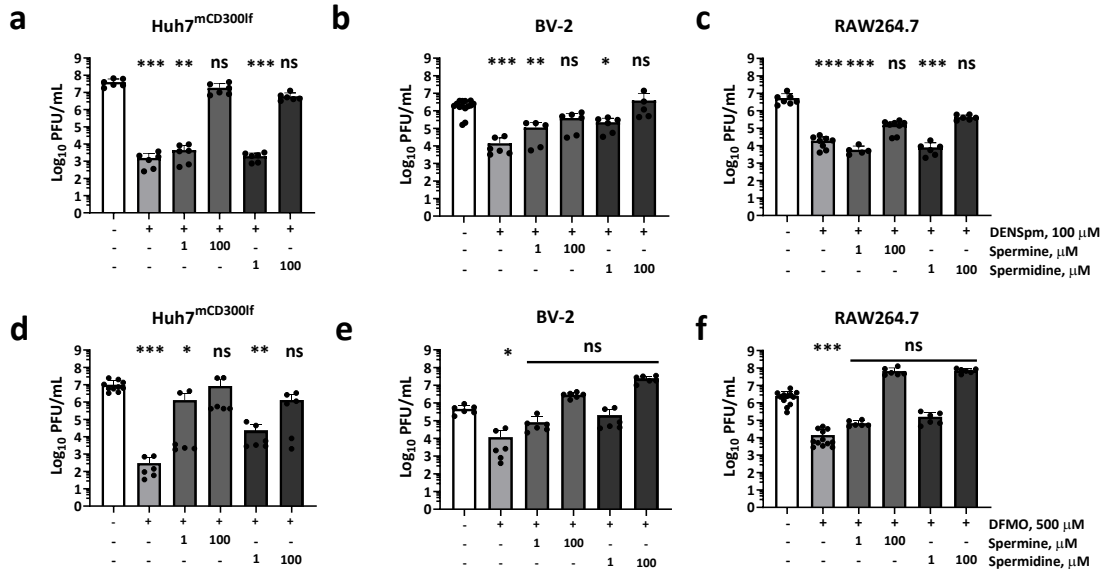

*Figure 49. Polyamine depletion restricts MNV-1 infection in immune and epithelial cells. (a, d) Huh7^{mCD300lf}, (b, e) BV-2 and (c, f) RAW264.7 were pretreated with (a-c) 100 µM DENSpm for 24 h or (d-f) 500 µM DFMO for 96 h. Cells were inoculated with MNV-1 at MOI 0.1 and for 1 h at 4°C. The inoculum was removed and replaced with culture medium (-) or culture medium supplemented with DENSpm, DFMO with or without 1 or 100 µM of spermine or spermidine. Samples were lysed 24 hours post infection (hpi) and virus titers were determined by plaque assay. Data represent means ± standard deviation (SD) of three independent biological assays with two technical repeats each. Individual data points are shown. Statistical significance was assessed using the Kruskal-Wallis test compared to non-treated/infected: ns, not significant; * p≤0.05; ** p≤0.01; *** p≤0.001.*

Notably, the addition of spermine or spermidine to untreated (polyamine-intact) cells did not alter MNV-1 titers (Figure 50a–c). This suggests that baseline polyamines levels in standard culture conditions are adequate to support infection.

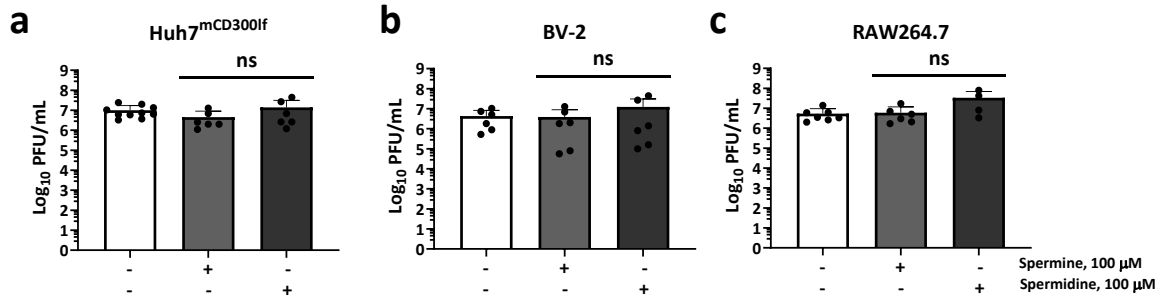

Figure 50. Polyamine supplementation is not affecting MNV-1 infection in immune and epithelial cells. (a) Huh7^{mCD300lf}, (b) BV-2 and (c) RAW264.7 cells were infected with MNV-1 at a MOI of 0.1 for 1 h on ice. The inoculum was removed and medium containing 100 µM spermine or 100 µM spermidine were supplemented to cells. At 24 hpi, samples were harvested for titer quantification via plaque assay. Data represent means ± standard deviation (SD) of three independent biological assays with two technical repeats each. Individual data points are shown. Statistical significance was assessed using Kruskal-Wallis test compared to non-treated/infected: ns, not significant.

To determine whether polyamine requirements were conserved across MNV strains, polyamine-depleted Huh7^{mCD300lf} cells was infected with chronic CR3 strain. Here DFMO treatment led to an almost 5-log reduction in infection (Figure 51). Supplementation of spermidine and spermine did not enhance viral replication beyond baseline in the polyamine intact samples but restored infection in the DFMO treated conditions.

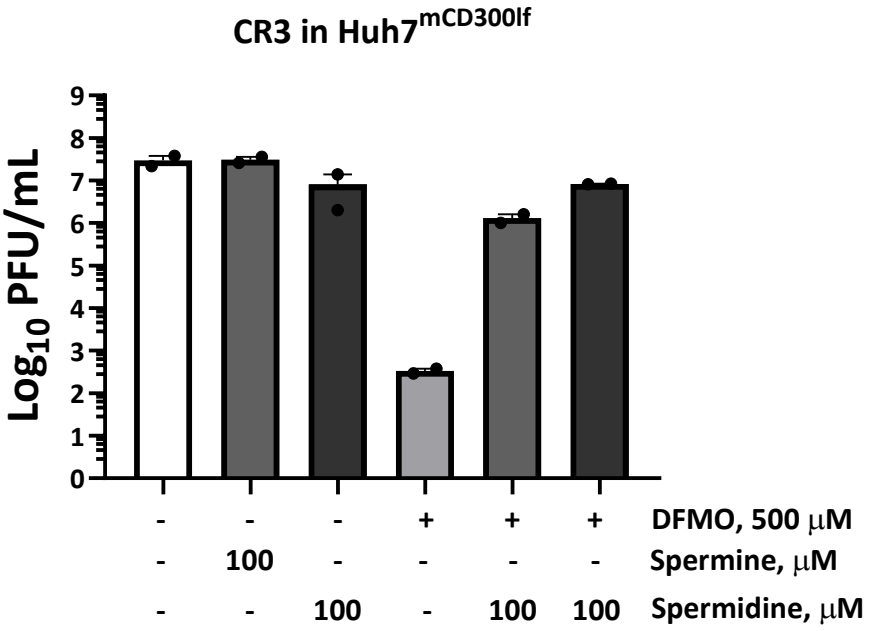

Figure 51. Polyamine depletion inhibits MNV CR3 infection in epithelial cells.Huh7^{mCD300lf} were pretreated with 500 μM DFMO for 96 h. Cells were inoculated with MNV CR3 at MOI 0.1 for 1 h at 4°C. The inoculum was removed and replaced with culture medium (-) or supplemented with DFMO and/or 100 μM of spermine or spermidine. Virus titers were determined 24 hpi by plaque assay. Data represent means ± range of two independent biological assays. Individual data points are shown.

To assess for any potential cytotoxicity associated with polyamine depletion or supplementation, metabolic activity and cell viability of RAW264.7 cells was assessed using a WST-1 and a trypan blue exclusion assay (Figure 52). No negative effect on cell health during polyamine depletion was observed (Figure 52a–b). However, a significant increase in metabolic activity of DFMO-treated and spermine or spermidine supplemented cells was observed in the WST-1 assay.

These data show that the reduced infection titers were specific for polyamine depletion and not due to reduced cell viability. Interestingly an increased metabolic activity beyond baseline in the rescued samples (DFMO plus spermine/spermidine) could explain a similar effect on infection, where the infectious titers also exceeded base line levels.

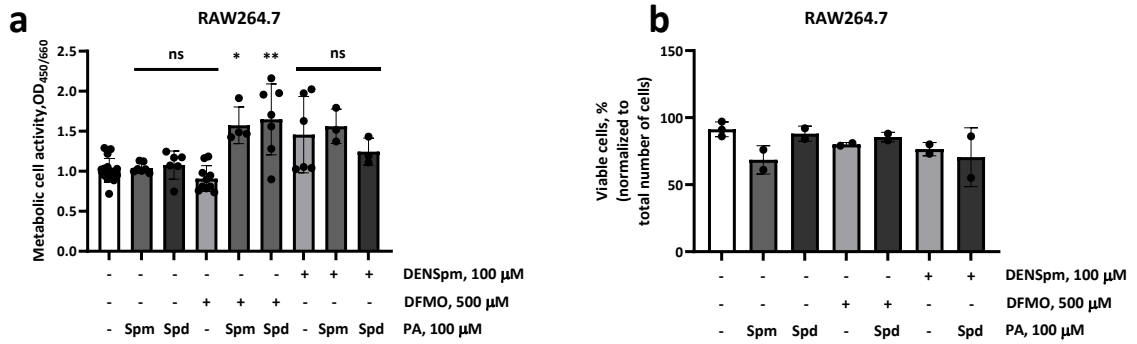

*Figure 52. Polyamines and polyamine-modulating drugs do not affect RAW264.7 macrophage viability or metabolic activity. RAW264.7 cells were pretreated with 100 µM DENSpm for 24 hours or 500 µM DFMO for 96 hours . Following pretreatment, the medium was replaced with either control (mock) or supplemented with DENSpm, DFMO, 100 µM Spd, or 100 µM Spm. After 24 hours of Spm or Spd supplementation, metabolic activity was assessed using a (a) WST-1 assay, and (b) cell viability was determined by trypan blue exclusion. Data represent means ± standard deviation (SD) of minimum two independent biological assays. Individual data points are shown. Statistical significance was assessed using the Kruskal-Wallis test compared to non-treated/infected: ns, not significant; * p≤0.05; ** p≤0.01. Based on data from Marina Pekelis, M.Sc. (235).*

Although the specificity and working concentrations of DENSpm and DFMO is well established (208), a decrease in intracellular spermidine upon DFMO and DENSpm treatment of RAW264.7 cells was examined (Figure 53). The restoration of intracellular spermidine levels upon its supplementation to the cell culture medium was also observed (Figure 53a), indicating no negative impact on exogenous supplemented polyamine in presence of serum. While bovine serum was postulated to contain polyamines and polyamine-catabolizing enzymes (236), no spermidine was detected in FCS (Figure 53b).

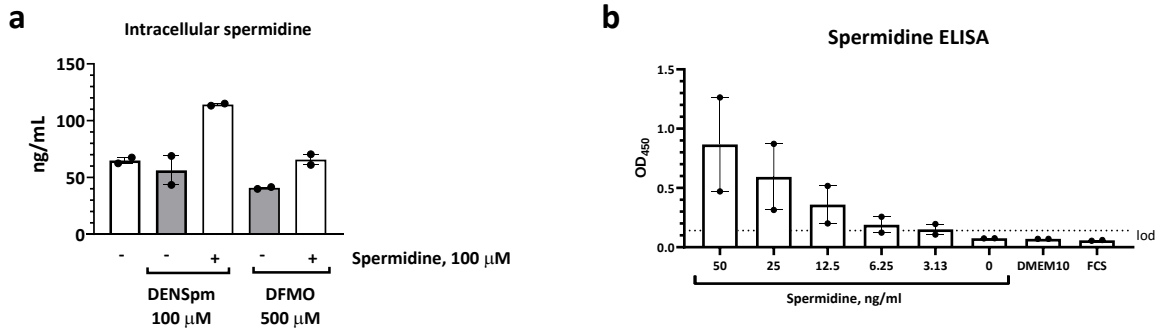

Figure 53. Polyamine degradation and depletion reduce intracellular spermidine concentration in RAW264.7 macrophages. RAW264.7 were pretreated with 100 µM DENSpm for 24 h or 500 µM DFMO for 96 h. Spermidine were supplemented to cells 6 h prior to harvesting samples by freezing. (a) Efficacy of polyamine restriction drugs was assessed by measuring intracellular spermidine via indirect ELISA assay and normalizing to mock treated condition. (b) Spermidine content of cell medium components was also measured via indirect ELISA assay. Data represent means ± range of two independent

biological assays. Individual data points are shown. Data were generated in collaboration with Marina Pekelis, M.Sc. (235).

In conclusion, our data demonstrates that polyamine depletion significantly inhibits MNV-1 infection across multiple cell types and that this is reversible. A dose dependent rescue of viral infection was shown for supplemented polyamine.

4.4.2. MNV-1 attachment to cells is not affected by polyamine depletion

Previous studies have shown that other enteric RNA viruses depend on polyamines for efficient binding and entry (237). Because polyamines regulate the transcription factor SREBP2, which controls intracellular cholesterol biosynthesis (200), their depletion reduces cellular cholesterol levels and may impair viral entry. Since MNV entry is cholesterol-dependent (62,63), the polyamine depletion effect on MNV-1 attachment to host cells was investigated. Huh7^{mCD300lf}, BV-2 cells, and RAW264.7 cells were cultured in the presence of 500 µM DFMO for 4 days to deplete polyamines (Figure 54). Cells were then inoculated with MNV-1 at MOI 5 and incubated on ice for 1 hour to allow viral binding without internalization. The unbound virus was removed by washing, and cells were harvested in TRIzol® for total RNA extraction. Viral genome equivalents were quantified by RT-qPCR.

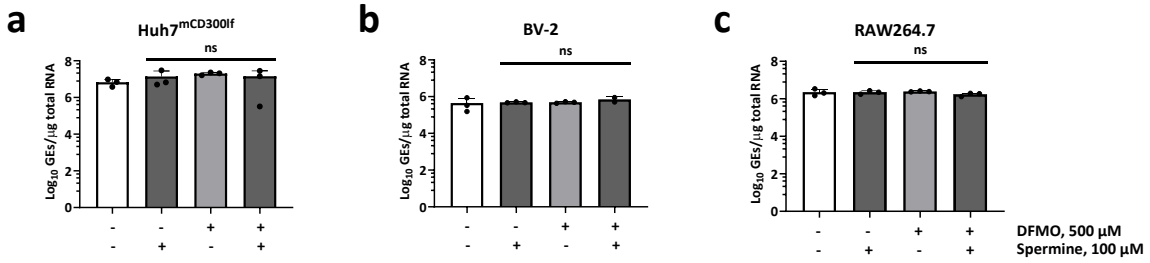

Figure 54. Polyamine depletion does not alter MNV-1 attachment to cells. (a) Huh7^{mCD300lf}, (b) BV-2, and (c) RAW264.7 were pretreated with 500 µM DFMO for 4 days. Cells were inoculated with MNV-1 at an MOI of 5 on ice in the presence of DFMO and 100 µM spermine. After 1 h incubation to allow for virus attachment, cells were washed and harvested for total RNA extraction. MNV titers were quantified by RT-qPCR and normalized to 1 µg of total extracted RNA. Data represent means ± standard deviation (SD) of three independent biological assays with two technical repeats each. Individual data points are shown. Statistical significance was assessed using the Kruskal-Wallis test compared to non-treated/infected: ns, not significant.

In summary, polyamine depletion did not impair MNV-1 attachment to any of the tested cell lines and the addition of spermine had no effect on viral binding to host cells (Figure 54).

4.4.3. Polyamine depletion modestly impacts MNV-1 genome replication

For several flaviviruses and bunyaviruses, polyamines are important for RNA genome replication and packaging (208,234). To investigate the effect of polyamines on MNV-1 genome replication, RAW264.7 cells were pre-treated for 4 days with DFMO and infected cells with MNV-1 at an MOI of 5 (Figure 55). Lysates were harvested at 16 hpi, with genome equivalents being quantified by RT-qPCR and infectious units by plaque assay from the same sample.

Modest inhibition of MNV-1 replication (26-fold, Figure 55a) was observed under polyamine depletion, while a comparatively bigger reduction was observed in respective infectious units (248-fold, Figure

55b). The genome to PFU ratio in polyamine-depleted cells was slightly increased (Figure 55c), suggesting that decline in genomes is insufficient to account for the decline in viral titers.

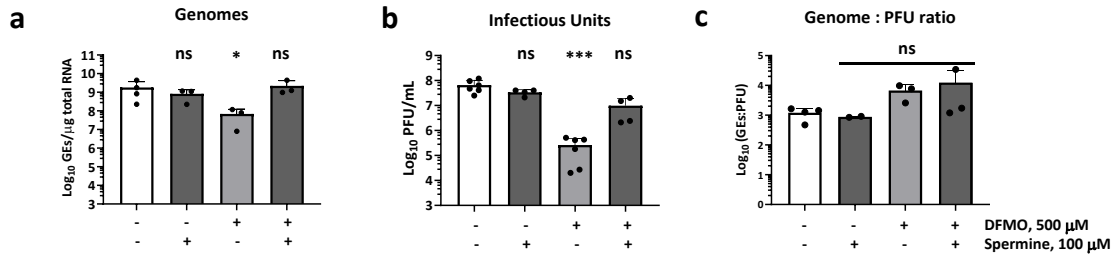

*Figure 55. Impact of polyamine depletion on genome equivalents versus infectious units in RAW264.7 cells. RAW264.7 cells were treated with 500 µM DFMO for 4 days to deplete polyamines, then infected with MNV-1 at an MOI of 5. Inoculated cells were supplemented with DFMO and/or 100 µM Spm. Cells were harvested by freezing at 16 hpi for quantification of (a) viral genome via RT-qPCR and (b) infectious particles via plaque assay. (c) The genome to PFU ratio is depicted. Data represent means ± standard deviation (SD) of at least three independent biological assays with two technical repeats for the plaque assay. Individual data points are shown. Statistical significance was assessed using the Kruskal-Wallis test and shown compared to non-treated/infected: ns, not significant; * p≤0.05; *** p≤0.001.*

This suggests that polyamines may impact other steps in the infectious cycle, after genome replication, to explain the overall decline in viral titers.

4.4.4. Modulation of interferon response by polyamines does not impact MNV-1 replication

Since polyamines were dispensable for MNV attachment and genome replication, cellular processes known to be regulated by polyamines were next investigated. Prior work on HSV-1 showed that polyamines suppress virus-induced interferon response. By altering DNA conformation, spermine and spermidine reduce cGAS sensing of cytoplasmic DNA, while polyamine depletion enhances cGAS recognition of DNA and interferon production, thereby restricting infection (199).

MNV infection is similarly sensitive to interferon-mediated restriction (238), which involves the cGAS pathway. Here, activation of cGAS is triggered by mitochondrial and nuclear DNA leakage to cytoplasm and as a result induction of interferon production during MNV infection (116). Based on these observations, it was hypothesized that polyamine depletion restricts MNV-1 infection by boosting virus-induced interferon production.

To test this hypothesis, first MNV-induced interferon production was evaluated in two naturally susceptible models: murine RAW264.7 macrophages and microglia BV-2 cells (Figure 56). Cells were infected with MNV-1 at an MOI of 0.1 and 1, or stimulated with lipopolysaccharides (LPS, 2 ng/mL). Interferon levels were quantified at 1, 24 and 48 hours post-infection or stimulation. RAW264.7 cells displayed robust interferon production following both infection and LPS stimulation (Figure 56a). In contrast, BV-2 cells produced markedly lower quantities of interferon upon both infection and LPS stimulation (Figure 56b-c).

Next the kinetics of interferon production from both cell lines were characterized. In RAW264.7 macrophages, LPS-induced interferon production peaked at 16 hpi and declined thereafter (Figure

56d). In contrast, MNV-induced interferon production showed a delayed kinetic profile, with levels progressively increasing between 24 and 48 hpi and peaking at 48 hpi (Figure 56d). As anticipated, BV2 cells produced minimal interferon in response to either LPS or MNV infection (Figure 56d).

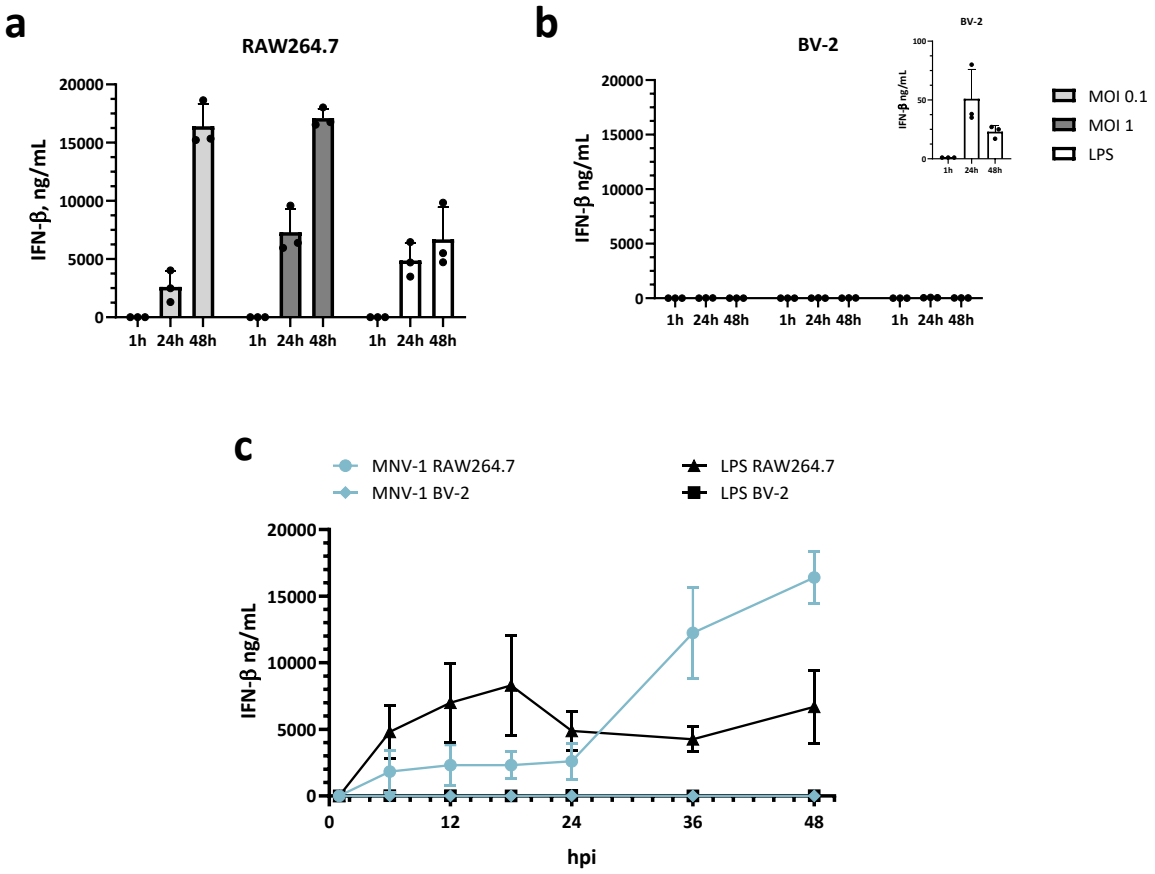

Figure 56. Kinetic of interferon-β production in microglial BV-2 and RAW264.7 macrophages infected with MNV-1. RAW264.7 and BV-2 cells were infected with MNV-1 at a MOI of 0.1 or 1, or stimulated with 2 ng/mL of LPS. Cell supernatants were collected over 48 hours period following infection or stimulation to compare (a-b) levels and (d) kinetics of interferon-β release. (c) Production of interferon-β by BV-2 upon stimulation with LPS (2 ng/mL). Data represent means ± standard deviation (SD) of three independent biological assays. Individual data points are shown. Based on data from Heike Laschin, M.Sc. (239).

To test whether interferon production restricts MNV infection in naturally susceptible and recombinant cells, the effect of Janus-kinase (JAK) inhibitor Ruxolitinib, a potent inhibitor of the interferon signaling pathway, was evaluated on MNV-1 replication. If interferon exerts an antiviral effect on MNV infection, inhibition of interferon signaling would be expected to enhance the infection.

Two concentrations (2 µM and 10 µM) and two treatment schemes were employed: pre-treatment, in which cells were exposed to the inhibitor for 24 hours prior to infection and maintained under supplementation post-infection, and post-treatment, in which the compound was added only after infection.

A significant enhancement of MNV-1 replication was observed following the pre-treatment of RAW264.7 cells with Ruxolitinib (Figure 57a). In BV2 cells, however, a comparable significant enhancement of infection was observed only at higher concentration of the Ruxolitinib (Figure 57b). MNV-1 infection of Huh7^{mCD300lf} cells remained unaffected by Ruxolitinib treatment (Figure 57c), which is consistent with inactive innate immune sensing pathway in those cells (240).

These data established RAW264.7 macrophages as the optimal model for subsequent mechanistic studies on polyamine-associated interferon restriction of MNV-1 infection.

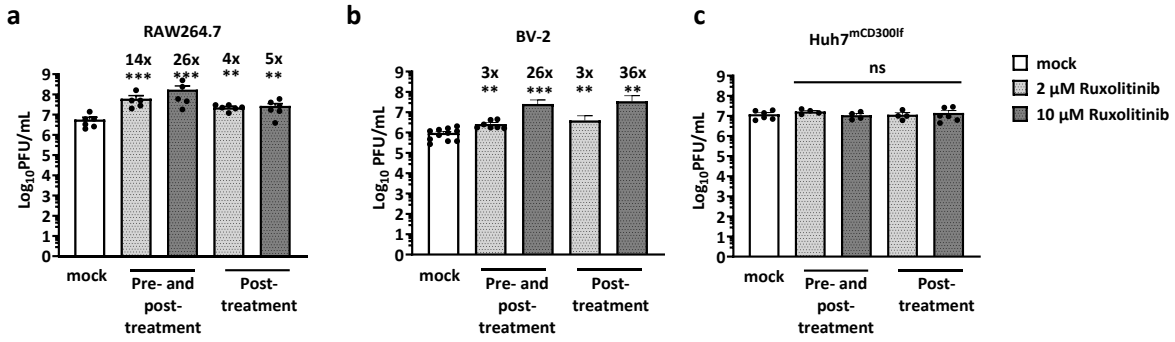

*Figure 57. JAK inhibitor Ruxolitinib enhances MNV-1 infection in naturally susceptible murine cell lines but not in the recombinant human cell line. (a) RAW264.7, (b) BV-2 and (c) Huh7^{mCD300lf} were pretreated with 2 µM and 10 µM of Ruxolitinib or mock-treated 24 hours prior to infection. Cells were inoculated with MNV-1 at MOI 0.1 and for 1 h at 4°C. The inoculum was removed and replaced with culture medium or culture medium supplemented 2 µM and 10 µM of Ruxolitinib. Samples were lysed 24 hpi and virus titers were determined by plaque assay. Data represent means ± standard deviation (SD) of three independent biological assays with two technical repeats each. Individual data points are shown. Statistical significance was assessed using the one-way ANOVA test compared to non-treated/infected: ns, not significant; ** p≤0.01; *** p≤0.001. Based on data from Heike Laschin, M.Sc. (239)*

To investigate the impact of polyamine modulation on interferon production during MNV infection, interferon levels in DENSpm-treated and re-supplemented with spermine RAW264.7 infected cells was measured (Figure 58). Cell culture supernatants were collected at multiple time points post-infection to assess the kinetics of interferon production. As anticipated, supplementation of spermine significantly reduced interferon production at 36 and 48 hpi, coinciding with the pick interferon production in mock-treated control. Unexpectedly, DENSpm treatment significantly suppressed interferon production in MNV-1-infected cells, with minimal to no rescue upon spermine supplementation.

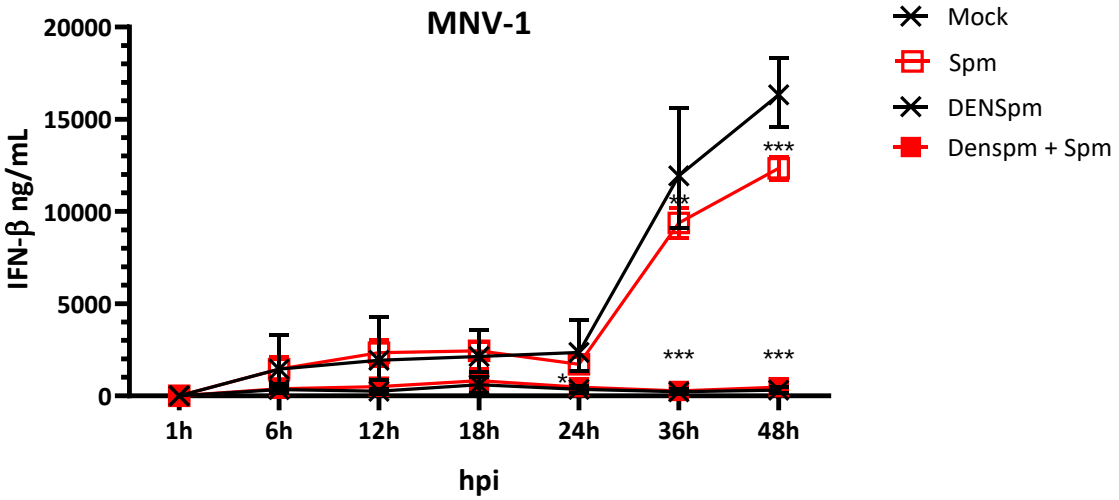

*Figure 58. Kinetics of interferon-β production in polyamine-degraded RAW264.7 macrophages infected with MNV-1.RAW264.7 were pretreated with 100 µM DENSpm for 24 h prior to infection. Cells were inoculated with MNV-1 at MOI 0.1 and for 1 h at 4°C. The inoculum was removed and replaced with culture medium (-) or culture medium supplemented with DENSpm, with or without 100 µM of spermine. Cell supernatants were collected up to 48 hpi and interferon-β levels were measured using indirect ELISA assay. Data represent means ± standard deviation (SD) of three independent biological assays with two technical repeats each. Statistical significance was assessed using the two-way ANOVA test and shown compared to non-treated/infected: ns, not significant; * p≤0.05; ** p≤0.01; *** p≤0.001.*

Based on data from Heike Laschin, M.Sc. (239).

Given the strong inhibition of interferon production observed with spermine supplementation, an effect of spermidine was assessed by pre-treating RAW264.7 macrophages with 100 µM spermidine for 24 hours prior to infection and maintaining them with either 100 µM or 500 µM post-infection to evaluate dose- and duration-dependent effects on interferon production and MNV-1 replication. Contrary to our expectations, no effect of spermidine supplementation on MNV-1 replication and interferon production was observed in murine macrophages (Figure 59a-b).

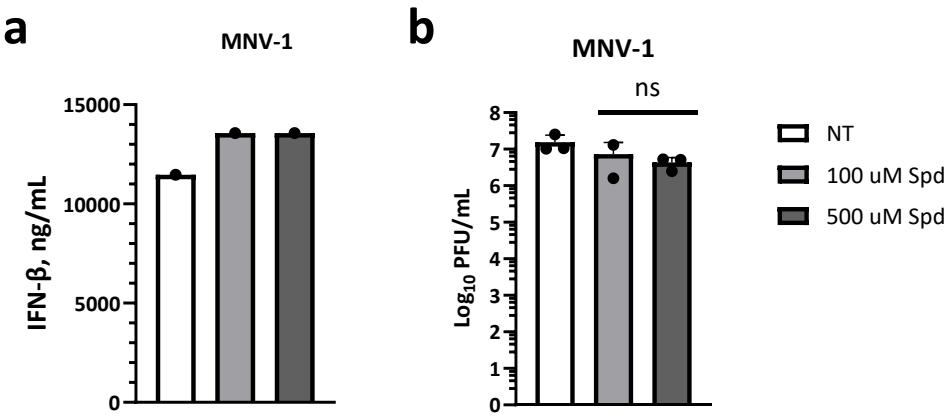

Figure 59. Spermidine supplementation does not affect interferon-β production and MNV-1 replication in RAW264.7 murine macrophages. RAW264.7 were pretreated with 100 µM spermidine for 24 h prior to infection. Cells were inoculated with MNV-1 at MOI 0.1 and for 1 h at 4°C. The inoculum was removed and replaced with culture medium or culture medium supplemented with 100 µM or 500 µM of spermine. (a) Cell supernatants were collected 48 hpi for interferon-β levels quantification and (b) total cell lysates were collected for plaque assay titration. Data represent means ± standard deviation (SD) of three independent biological assays for infectious titer quantification and one independent biological assays with two technical repeats for interferon-β quantification. Based on data from Heike Laschin, M.Sc. (239).

Contrary to our hypothesis, DENSpm treatment resulted in significant inhibition of interferon production upon MNV infection. However, the inhibition of interferon production did not correspond to an increase in viral replication. This suggests that interferon modulation by polyamine is not linked to viral replication

In summary, the interferon response and its restrictive effect on MNV-1 infection in naturally susceptible murine cell lines with or without polyamine depletion was examined. Consistent with our hypothesis, exogenous spermine, but not spermidine, significantly reduced interferon production following MNV-1 infection. Supplementation with neither spermine, nor spermidine increased viral replication in infectivity assay.

4.4.5. Polyamine restriction prevents MNV-induced death of bystander cells

During our work, another prominent phenotype was observed: a complete loss of the cytopathic effect (CPE) in MNV-infected but polyamine-depleted cells. Even at high MOI infection (MOI of 5), DFMO-treated cells showed no CPE (Figure 60a panel v) vs infected but non-treated (Figure 60a panel ii) at 48 hpi. This phenotype was again completely reverted by adding spermidine to infected and DFMO-treated (Figure 60a panel vi).

To quantify this effect on cell viability a WST-1 assay was performed showing that about 50% of the infected cells died 24 hpi and up to 70 % by 48 hpi (Figure 61b). However, no change in cell death was observed in infected and DFMO-treated cells. Here, the cell death was again completely restored when spermine was supplemented. These data suggest that polyamines are necessary for MNV-1 induced cell death.

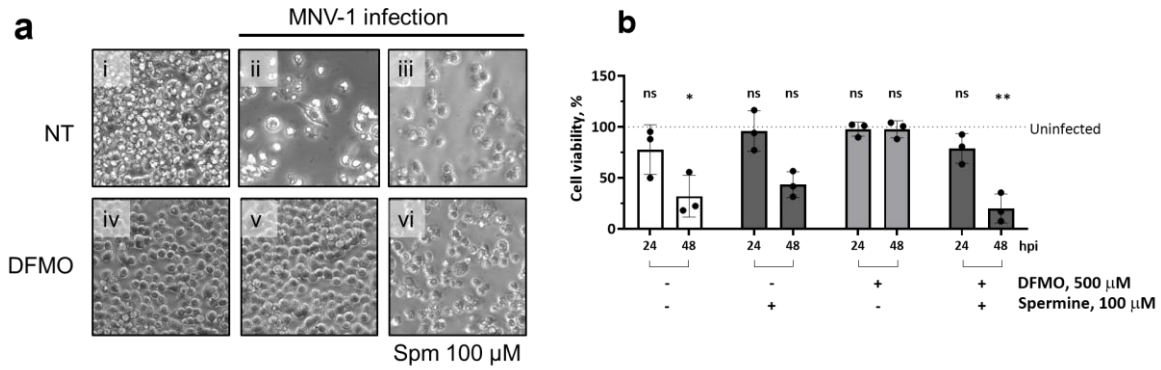

*Figure 60. Loss of virus-induced cytopathic effect in polyamine-depleted murine macrophages. RAW264.7 cells were pretreated with 500 µM DFMO for 4 days, and subsequently infected with MNV-1 at MOI of 5 on ice for 1h. After infection, the inoculum was removed, and cells were reconstituted with medium containing DFMO and/or 100 µM spermidine. (a) MNV-induced CPE was analyzed 48 hpi by bright-field microscopy and (b) cell viability was determined by WST-1 assay at 24 and 48 hpi and shown as percent viable compared to the respective uninfected control. Data are presented as means ± standard deviation (SD) from three independent biological experiments. Statistical significance was assessed using Kruskal-Wallis test and shown compared to the corresponding non-treated (NT)/non-infected sample: ns, not significant; * p≤0.05; ** p≤0.01. Based on data from Heike Laschin, M.Sc. (239).*

As apoptosis is a key step in the MNV life cycle and required for virus release (106,111), the effect of polyamine depletion on MNV egress was assessed by quantifying infectious units in total lysate (cells plus supernatant) and in clarified supernatants between 8 and 48 hpi (Figure 61a-b). RAW264.7 cells were pretreated with 500 µM DFMO for 4 days and infected with MNV-1 on ice at an MOI of 5. After infection, the inoculum was removed and cells were maintained in medium containing DFMO and/or 100 µM spermine for 8-48 h. To evaluate release, total lysates and supernatants were collected separately at each time point, and infectious units were quantified for both fractions.

Infectious units were significantly and consistently diminished upon DFMO treatment in both lysate, as early as 8 hpi, also not significantly, and in supernatant fractions, showing that polyamine depletion impacts MNV-1 infection early during infection. Supplementation with spermine fully restored infection at all-time points. In DFMO-treated lysates, titers increased between 8 and 24 hpi, which was not observed in the corresponding supernatants.

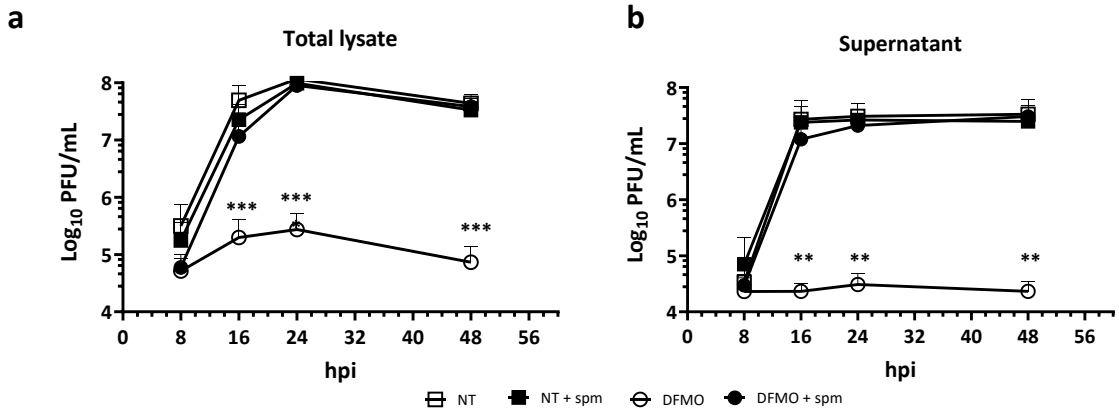

*Figure 61. Polyamine depletion impairs MNV-1 infection and release. RAW264.7 cells were pretreated with 500 µM DFMO for 4 days to deplete polyamines, then infected with MNV-1 at an MOI of 5. Infected cells were supplemented with/without DFMO and/or 100 µM spermine (Spm). (a) Total lysate and (b) supernatant was collected separately, and virus titers were determined by plaque assay. Data represent means ± standard deviation (SD) of three independent biological replicates and two technical repeats for each condition. Statistical significance was assessed using a one-way ANOVA test and shown compared to non-treated (NT): ns, non-significant (not shown for clarity); ** p≤0.01; *** p≤0.001. Based on data from Heike Laschin, M.Sc. (239).*

Collectively, these findings demonstrate that polyamine depletion inhibits both production of new viral progeny and release from infected cells.

Because polyamines are known to exert protective effects against apoptosis (201,204,241), it was hypothesized that the absence of CPE in polyamine-depleted infected cells may reflect an inability of the virus to induce apoptosis. As MNV infection has recently been shown to promote cleavage of caspase-3 and PARP, with apoptosis being required for efficient replication and viral release (106,111), PARP cleavage, a downstream marker of caspase-3 activation, was examined as an indicator of virus-induced apoptosis.

Cells were depleted for polyamines using DFMO and reconstituted at first using spermine supplementation. Similarly, to the reported observations (106), our data confirmed that MNV-1 infection led to a full loss of uncleaved PARP in polyamine-competent RAW264.7 cells (Figure 62a-c). In DFMO-treated and infected cells, no virus-induced loss of PARP and no accumulation of VP1 occurred 24 hpi (Figure 62a-b), suggesting that in polyamine-depleted cells PARP is not cleaved and apoptosis is inhibited.

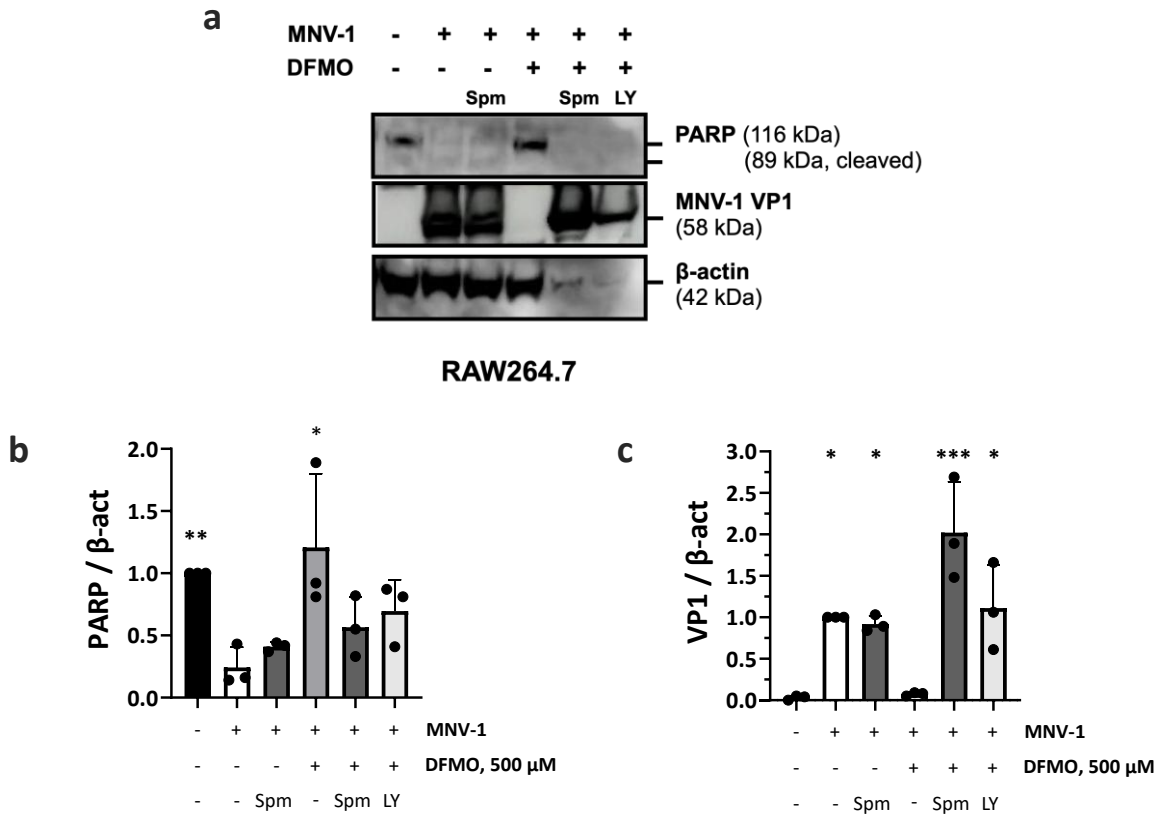

*Figure 62. Polyamine depletion prevents MNV-1 induced PARP cleavage and infection and can be rescued by spermine reconstitution and PI3K inhibition. RAW264.7 cells were pretreated with 500 µM DFMO treatment for 4 days. Cells were then infected with MNV-1 at MOI 1 on ice for 1 h. Following infection, the inoculum was removed, and the medium was supplemented with/without DFMO, 10 µM LY294002 (LY) or 100 µM spermine (Spm). (a) At 24 hpi, cell fractions were harvested for protein extraction and subsequently analyzed by western blotting to determine expression levels of MNV capsid protein VP1, PARP and β-actin (β-act). A representative western blot is shown. (b) A quantification of PARP and (c) VP1 was performed using ImageJ gel analysis and normalized to β-actin. Data represent means ± standard deviation (SD) of three independent biological assays (a-f). Individual data points are shown. For statistical analysis PARP expression was compared to the untreated and uninfected control, while VP1 was compared to untreated and infected samples. Statistical significance was assessed using the Kruskal-Wallis test: ns, not significant (omitted for clarity); * p≤0.05; ** p≤0.01. Data were generated in collaboration with Heike Laschin, M.Sc. (239).*

The protective effect of polyamine depletion on apoptosis induction is known to be reversible via inhibition of PI3K by LY294002 (LY), PI3K reversible inhibitor (201,205). Subsequently, LY was next tested in polyamine-depleted cells to determine whether MNV-1-induced apoptosis and PARP cleavage could be restored via PI3K inhibition. Indeed, in infected polyamine-depleted RAW264.7 cells, LY restored PARP cleavage and MNV-1 VP1 accumulation similarly to spermine (Figure 62). Under these conditions, a loss of β-actin was observed, potentially reflecting the increased cell death.

Importantly, in uninfected polyamine-intact and depleted cells, PARP cleavage occurred only in staurosporine-treated (Stau, protein kinase inhibitor, inducer of apoptosis) cells, but not LY- and spermine-treated cells (Figure 63), showing that PARP cleavage is a consequence of the infection and not of PI3K inhibition or polyamine reconstitution.

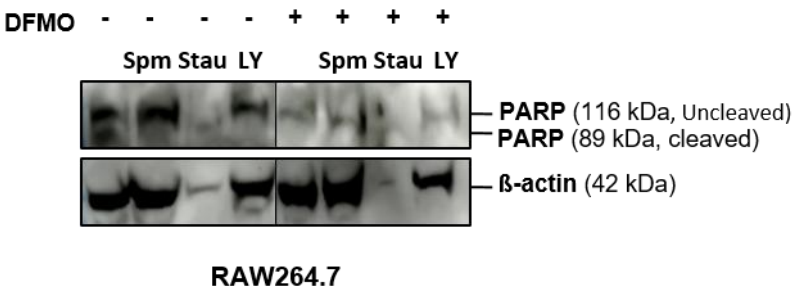

Figure 63. Effect of polyamines and polyamine modulation drugs on apoptosis induction. Uninfected murine macrophages RAW264.7 were pretreated with 500 µM DFMO for 4 days. Following treatment, the medium was replaced with a fresh medium containing DFMO, 20 µM LY, 100 µM Spm and 2 µM staurosporine. At 24 hours post treatment, cell fractions were harvested for protein extraction and subsequently analyzed by western blotting to determine expression levels of PARP. β-actin was used as a reference protein. Data were generated in collaboration with Heike Laschin, M.Sc. (239).

To address the polyamine depletion effect on late stages of MNV-induced apoptosis, the surface presentation of PS (via Annexin V staining) in MNV-1 infected macrophages was characterized.

RAW264.7 cells were treated with DFMO and subsequently infected at an MOI of 0.1. During the infection, cells were supplemented as indicated and stained with Annexin V at 24 hpi. MNV-1 infection induced PS externalization in approximately 17% of cells. In contrast, polyamine-depleted, MNV-infected macrophages showed PS externalization levels comparable to uninfected cells (~5% Annexin V-positive). Supplementation with spermine or LY restored PS externalization in polyamine-depleted,

infected cells to 14% and 20% (Figure 64), respectively, in line with our observations for loss of uncleaved PARP (Figure 62).

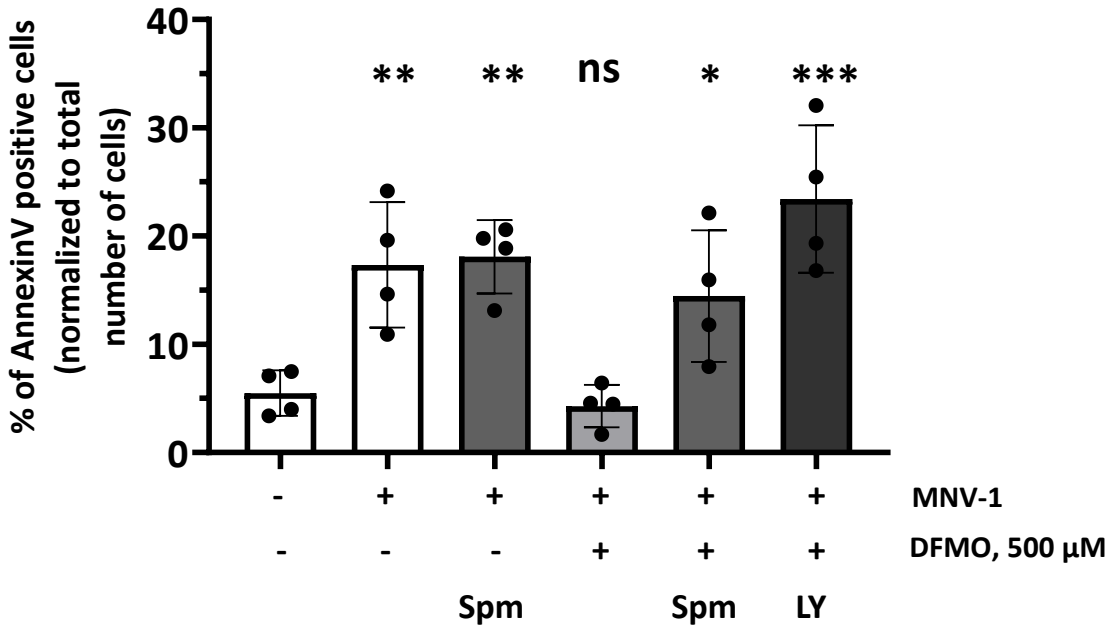

*Figure 64. PS externalization in MNV-infected macrophages depends on polyamine availability. RAW264.7 cells were treated with 500 µM DFMO treatment for 4 days, then cells were infected at an MOI of 0.1 for 1 hon ice. The inoculum was removed and replaced with a medium containing DFMO, 20 µM LY or 100 µM Spm. At 24 hpi, live cells were stained with AnnexinV to detect PS externalization and Hoechst for nuclei. PS-positive cells were quantified and normalized to total number of cells per field of view. Data represent mean ± standard deviation (SD) of at least two independent biological assays. Individual data points are shown. Statistical significance was assessed in comparison to uninfected and untreated using ANOVA: ns, not significant; * p≤0.05; ** p≤0.01; *** p≤0.001.*

Since a rescue of capsid protein accumulation was observed upon PI3K inhibition in Western Blot analysis (Figure 62), it was next investigated whether MNV-1 infection and release would likewise be restored. For this purpose, MNV-1 replication and viral release were assessed in the presence of spermine or LY under low (0.1) and high (5) MOI conditions. First, the ability of LY to rescue MNV-1 infection under polyamine depletion was assessed at 24 hpi, corresponding to the conditions used for the Western blot analysis. However, no differences were observed between DFMO-treated cells and those treated with LY (data not shown). This prompted an assessment at 48 hpi, as clear accumulation of VP1 is detectable by Western blot at 24 hpi. At this later time point, and under both MOI conditions, spermine and LY restored viral infection and release in RAW264.7 cells (Figure 65a-b). The proportion of released MNV-1 in supernatants was additionally quantified at MOIs of 0.1 and 5 (Figure 65c-d), revealing a significant decrease in virus release from polyamine-depleted cells, whereas supplementation with spermine or LY rescued this defect.

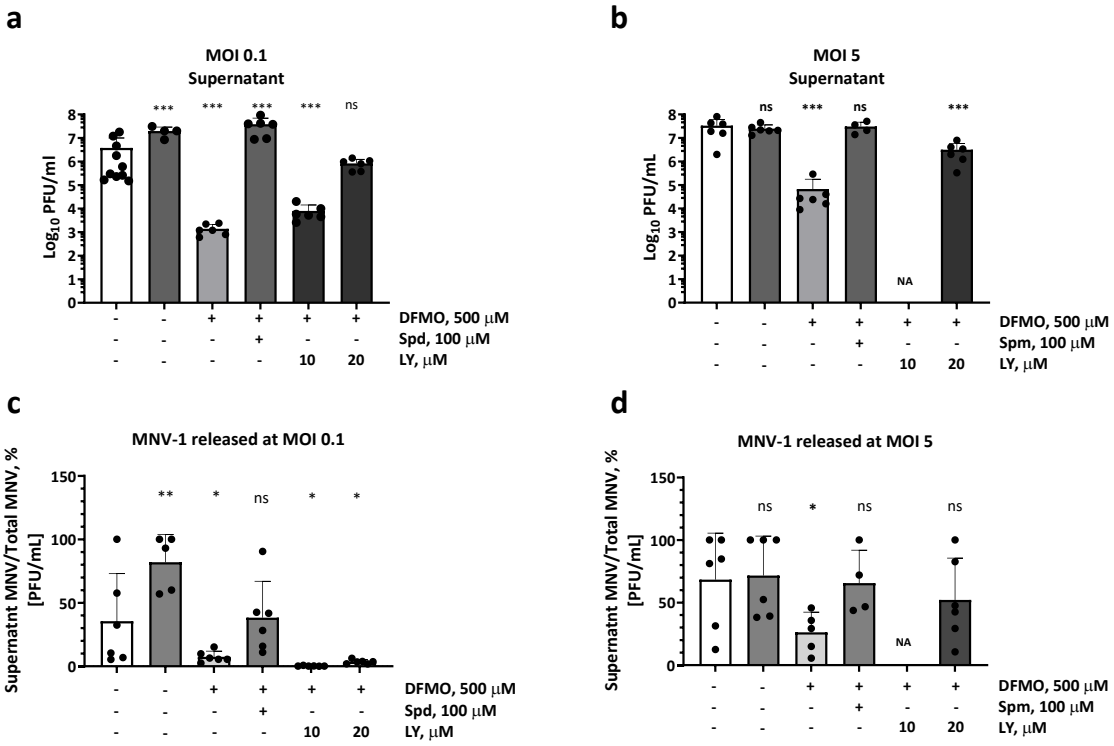

*Figure 65. PI3K inhibition rescues MNV-1 release in polyamine-depleted cells. RAW264.7 cells were pretreated with 500 μM DFMO for 4 days to deplete polyamines and infected with MNV-1 at an (a) MOI of 0.1 and (b) 5. Infected cells were supplemented with/without DFMO and/or 100 μM spermine (Spm), or 10 to 20 μM LY294002 (LY). Supernatant was harvested 48 hpi, and virus titers were determined by plaque assay. (c and d) The percentage of released MNV-1 was calculated as the ratio of infectious virus in the supernatant to that in the total cell lysate. Data are presented as means ± standard deviation (SD) from three independent biological repeats with two technical repeats. NA, data not available. Individual data points are shown. Statistical significance was assessed using the one-way ANOVA and shown as compared to non-treated: ns, not significant; * p≤0.05; ** p≤0.01; *** p≤0.001; NA, non-available.*

Having established that polyamine depletion reduces MNV infection and release, likely through altered apoptosis induction, the next objective was to determine whether this reduction resulted from impaired viral protein synthesis. To address this, the accumulation of the MNV-1 capsid protein VP1 and of dsRNA, an intermediate replication product, was examined by immunofluorescence microscopy, as VP1 expression was undetectable by Western blot in polyamine-depleted cells.

RAW264.7 macrophages treated with DFMO to deplete intracellular polyamines and subsequently infected at MOI 1 with MNV-1. Samples were harvested 24 and 48 hpi and stained with anti-VP1 rabbit polyclonal serum and anti-dsRNA monoclonal antibodies.

Immunofluorescence analysis revealed that only a small proportion (5%) of mock-treated infected cells exhibited VP1 or dsRNA signals at 24 hpi, with the number of positive cells increasing at 48 hours (Figure 66). Under polyamine-depleted conditions, no detectable signal was observed at 24 hpi, and only limited accumulation of dsRNA became apparent at 48 hpi.

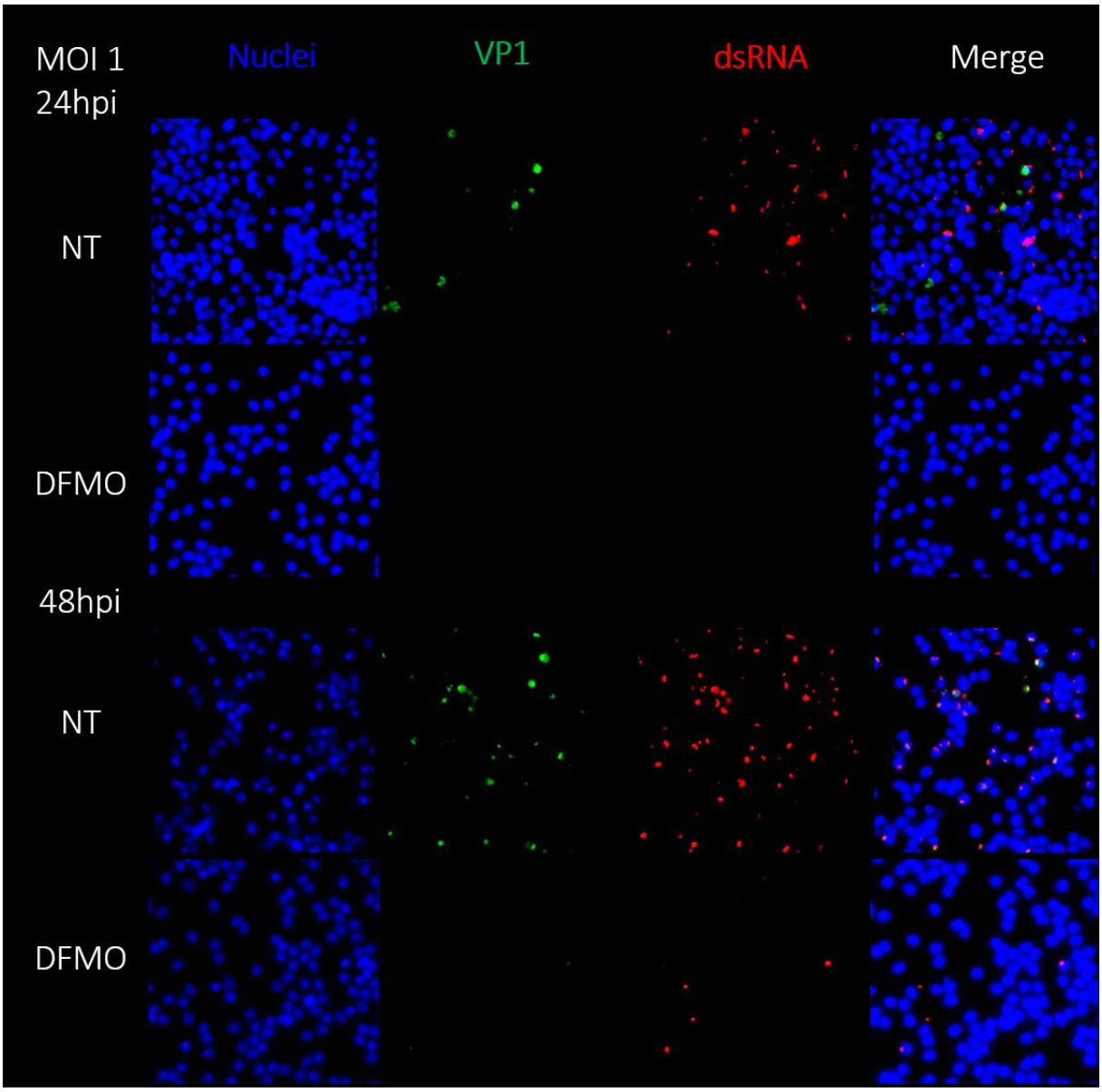

Figure 66. Polyamine depletion inhibits MNV-1 replication and capsid protein production. RAW264.7 cells were pretreated with 500 µM DFMO for 4 days to deplete polyamines, then infected with MNV-1 at an MOI of 1. Infected cells were supplemented with cell medium with or without DFMO. Samples were harvested at 24 and 48 hpi, fixed with 4% PFA, and stained with anti-dsRNA mAb and anti-VP1 rabbit serum for visualization in epifluorescence microscopy. Nuclei were visualized using Hoechst staining. Images shown are representative fields from a single staining experiment.

In summary, immunostaining revealed that only ~ 5% of RAW264.7 macrophages were positive for VP1 and/or dsRNA, an unexpectedly low proportion of cells given the MOI 1 infection and 24 hpi time point chosen for analysis. Despite the limited number of infected cells, cultures showed a complete loss of uncleaved PARP, an early marker of apoptosis, and 17% of cells exhibited PS externalization, indicative of late-stage apoptosis. These findings suggest that MNV infection induces apoptosis in bystander, non-infected cells. Polyamine depletion markedly reduced VP1 accumulation and prevented apoptosis initiation in these bystander populations, whereas PI3K inhibition restored capsid protein accumulation, both early and late apoptotic events and MNV-1 infection. Collectively, these results indicate that MNV-1 replication and apoptosis induction depend on polyamines and PI3K pathway activity.

4.4.6. Polyamine depletion restricts MNV-1 major capsid protein accumulation and intracellular localization

To enable more reliable assessment of viral protein accumulation and virus release under polyamine depletion, an infection model with a higher proportion of infected cells, preferably >50%, was required to ensure sufficient production of viral particles. For this purpose, RAW264.7 macrophages were infected with MNV-1 at an MOI of 50 following DFMO treatment. Viral titers were quantified at multiple time points in both total cell lysates (cells plus supernatant) and clarified supernatants.

In mock-treated and spermine-supplemented cells, MNV replication and release peaked at 24 hpi (Figure 67a-b), whereas in DFMO-treated cells, MNV-1 replication and release were markedly reduced, with maximal release occurring at 24 hpi (Figure 67b). A substantial reduction (2.5-logs) in released MNV-1 from polyamine-depleted cells was observed between 24 and 72 hpi (Figure 67b). Exogenous supplementation with spermine rescued MNV-1 replication and release as early as 8 hpi.

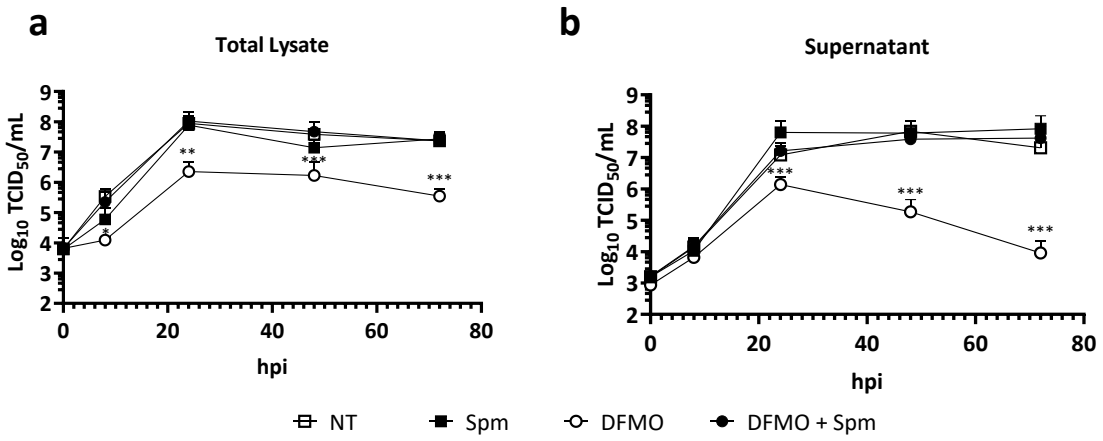

*Figure 67. Polyamine depletion inhibits MNV-1 replication and release at MOI of 50 infection. RAW264.7 cells were pretreated with 500 µM DFMO for 4 days to deplete polyamines, then infected with MNV-1 at an MOI of 50. Infected cells were supplemented with/without DFMO and/or 100 µM spermine (Spm). (a) Total cell lysate (supernatant and cells) and (b) clarified supernatant was collected separately, and virus titers were determined by $TCID_{50}$ assay. Data represent means ± standard deviation (SD) of three independent biological replicates. Statistical significance was assessed using a one-way ANOVA test and shown compared to non-treated (NT): ns, non-significant (not shown for clarity); ** p≤0.01; *** p≤0.001. Based on data from Alexander Müller, M.Sc. (242).*

At earlier time points, such as 8 and 10 hpi, corresponding to completed first replication cycle and early viral release, a consistent delay in MNV-1 replication and release was observed under polyamine-depleted conditions (Figure 68a-b).

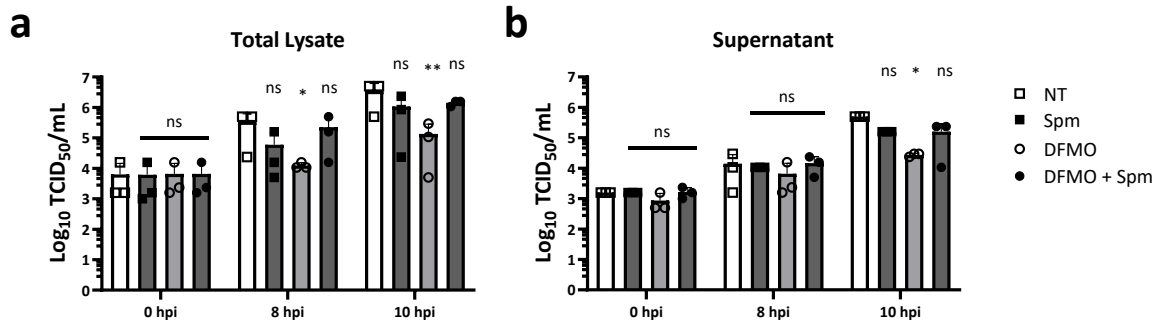

*Figure 68. Polyamine depletion inhibits MNV-1 infection at early time points. RAW264.7 cells were pretreated with 500 µM DFMO for 4 days to deplete polyamines, then infected with MNV-1 at an MOI of 50. Infected cells were supplemented with/without DFMO and/or 100 µM spermine (Spm). (a) Total cell lysate (supernatant and cells) and (b) clarified supernatant was collected separately, and virus titers were determined by $TCID_{50}$ assay. Data represent means ± standard deviation (SD) of three independent biological replicates. Statistical significance was assessed using a one-way ANOVA test and shown compared to non-treated (NT): ns, non-significant; * p≤0.05; ** p≤0.01. Based on data from Alexander Müller, M.Sc. (242).*

Consistently with our previous observations, no CPE was detected in polyamine-depleted cells following MOI of 50 MNV-1 infection up to 48 hpi (Figure 69a panel v), whereas in mock-treated (Figure 69a panel ii) and supplemented conditions (Figure 69a panel iii and vi), extensive decimation of monolayer was evident at 24 hpi.

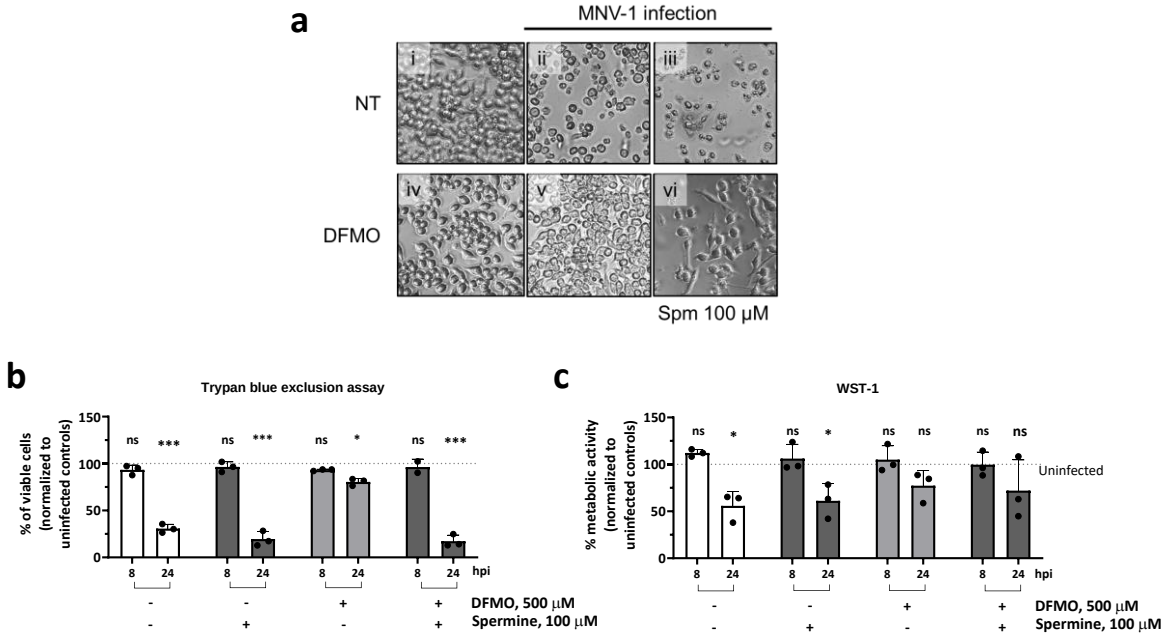

Figure 69. Inhibition of CPE and cell death in polyamine-depleted MNV-1 infected RAW264.7 macrophages. RAW264.7 cells were pretreated with 500 µM DFMO for 4 days, and subsequently infected with MNV-1 at MOI of 50 on ice for 1h. After infection, the inoculum was removed, and cells were reconstituted with medium containing DFMO and/or 100 µM spermine (Spm). (a) MNV-induced CPE was analyzed 48 hpi by bright-field microscopy, (b) cell viability was determined by trypan blue

*exclusion assay and (c) WST-1 assay at 8 and 24 hpi and shown as percent viable compared to the respective uninfected control. Data are presented as means ± standard deviation (SD) from three independent biological experiments. Statistical significance was assessed using a one-way ANOVA and shown compared to the corresponding non-treated (NT)/non-infected sample: ns, not significant; * p≤0.05. Based on data from Alexander Müller, M.Sc. (242).*

In earlier experiments, the absence of CPE was associated with reduced MNV release due to inhibition of virus-induced apoptosis. However, in the MOI of 50 infection model, an approx. 10^6 $TCID_{50}$/mL of MNV-1 was released into supernatant, a titer that under normal conditions is sufficient to induce visible CPE. This observation prompted us to quantify the cell viability and membrane integrity of infected cells.

To assess cellular viability, assessment of metabolic activity using a WST-1 assay and quantification of dead and live cells by trypan blue exclusion assay was performed. At 8 hpi, ~ 95% of cells were viable under all conditions. By 24 hpi, DFMO-treated cells retained around 80% viability, whereas only 25% of cells remained viable in all other conditions (Figure 69b). In the WST-1 assay, ~ 100% of cells were metabolically under all conditions. At 24 hpi, metabolic activity significantly declined (by 50%) in all conditions except for DFMO-treated cells, which retained approx 80% of their baseline activity (Figure 70c).

To further evaluate membrane integrity of the infected cells, a lactate dehydrogenase (LDH) release assay was used to measure the plasma membrane permeability. As a first step, maximal LDH content in untreated and polyamine-depleted cells was assessed by lysing them with Triton X-100 to establish baseline values. A slightly lower OD_{490} signals from polyamine-depleted cells was observed compared to non-treated, corresponding to ~15% reduction in total LDH content (Figure 70a). Additionally, non-treated MNV-1 infected cells released slightly higher levels of LDH than non-infected controls. This can be attributed to increased production of lactic acid (lactate) following MNV infection (243), which can artificially elevate LDH readings rather than reflecting genuine difference in enzyme abundance.

The LDH retention in polyamine-depleted and infected cells was then evaluated. At 8 hpi, no measurable LDH was detected in all conditions. By 24 hpi, significant LDH release was observed in all conditions except in DFMO-treated cells, where less than 15% leakage was detected (Figure 70b). These findings confirm that polyamine depletion preserves plasma membrane integrity and prevents virus-induced cell lysis.

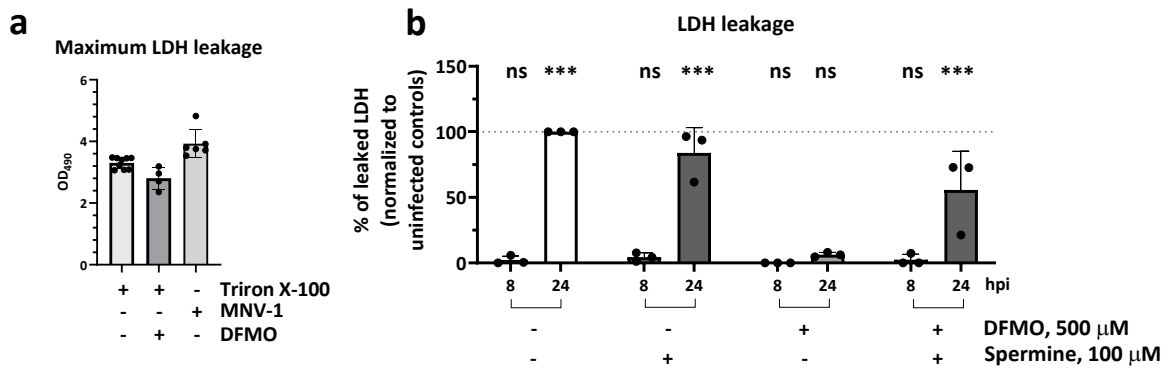

*Figure 70. Retention of membrane integrity in polyamine-depleted MNV1-infected RAW264.7 macrophages. RAW264.7 cells were pretreated with 500 µM DFMO for 4 days, and subsequently infected with MNV-1 at MOI of 50 on ice for 1h. After infection, the inoculum was removed, and cells were reconstituted with medium containing DFMO and/or 100 µM spermine (Spm). (a) Maximum LDH leakage was determined in infected and non-infected mock- and DFMO-treated cells to assess whether infection or polyamine modulation affected total LDH content. (b) MNV-induced membrane damage was analyzed by LDH assay at 8 and 24 hpi and shown as percent leakage compared to the respective uninfected control. Data are presented as means ± standard deviation (SD) from three independent biological experiments. Statistical significance was assessed using a one-way ANOVA and shown compared to the corresponding non-treated (NT)/non-infected sample: ns, not significant; * p≤0.05. Based on data from Alexander Müller, M.Sc. (242).*

In summary, the established MOI of 50 infection model in RAW264.7 macrophages, enabled determination that *de novo* progeny generation of MNV-1 is inhibited by polyamine depletion, but virus release is not entirely prevented. Despite of measurable quantities of infectious MNV-1 particles being released from DFMO-treated cells, the majority of these cells remained viable, metabolically active and exhibited minimal damage to the membrane. The observation that substantial viral titers are released from predominantly intact and viable cells raises the question whether MNV can exit host cells via a non-lytic release pathway under conditions of polyamine depletion.

To further assess MNV replication and capsid protein production under polyamine depletion, immunostaining of DFMO-treated and infected macrophages for dsRNA and VP1 was performed at 8, 24, and 48 hours post-infection. Monitoring infected cells over time would allow to correlate the proportion of infected cells with cell viability data. If the number of infected cells would exceed the proportion of non-viable cells, this would again suggest that MNV can be released via non-lytic mechanism.

At 8 hpi, dsRNA signals were detected in the perinuclear region across all experimental conditions, while only minimal VP1 staining was observed (Figure 71). As expected for this early stage of infection, no CPE was visible.

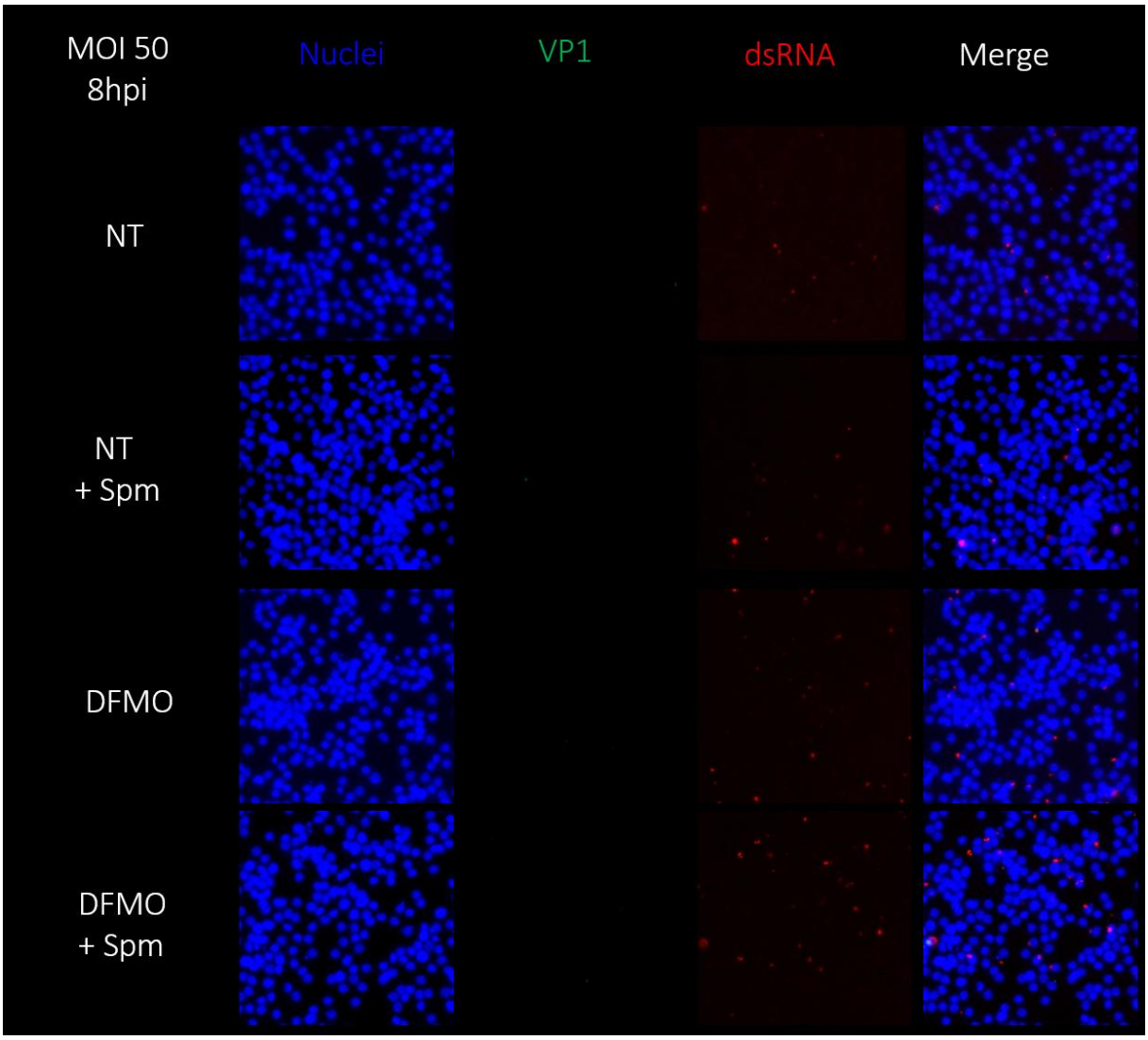

Figure 71. Accumulation of dsRNA intermediate in MNV-1 infected polyamine-depleted RAW264.7 macrophages at 8 hpi. RAW264.7 cells were pretreated with 500 µM DFMO for 4 days to deplete polyamines, then infected with MNV-1 at an MOI of 50. Infected cells were maintained with or without DFMO and supplemented, where indicated, with 100 µM spermine (Spm). Samples were harvested at 8 hpi, fixed with 4% PFA, and stained with anti-dsRNA mAb and anti-VP1 rabbit serum for visualization in epifluorescence microscopy. Nuclei were visualized using Hoechst staining. Images are representative of three independent experiments. Based on data from Alexander Müller, M.Sc. (242).

By 24 hpi, the majority of cells in mock-treated, spermine-supplemented and DFMO-treated and spermine-supplemented conditions exhibited both dsRNA and VP1 signals (double-positive), indicating active replication and viral protein synthesis (Figure 72). Occasional single-positive cells were observed across all samples. In contrast, most DFMO-treated cells remained negative for both VP1 and double-positive signal and displayed only condensed dsRNA foci. Consistent with these findings, CPE with partial monolayer loss was evident in all conditions except for DFMO-treated cells. The 48-hour post-infection samples displayed comparable signals to those observed at 24 hours (data not shown).

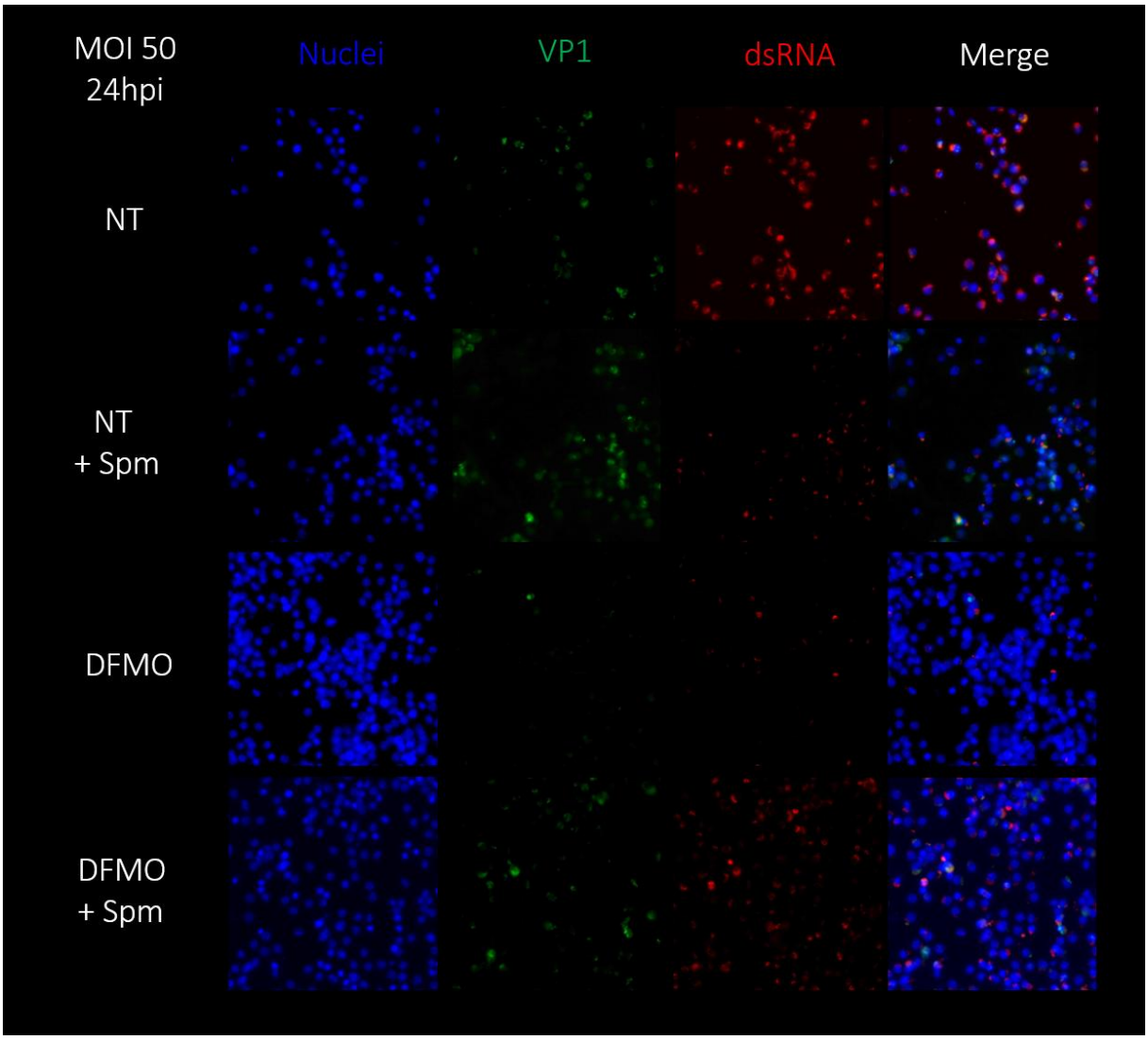

Figure 72. Loss of VP1 protein accumulation in MNV-1 infected polyamine-depleted RAW264.7 macrophages at 24 hpi. RAW264.7 cells were pretreated with 500 µM DFMO for 4 days to deplete polyamines, then infected with MNV-1 at an MOI of 50. Infected cells were maintained with or without DFMO and supplemented, where indicated, with 100 µM spermine (Spm). Samples were harvested at 24 hpi, fixed with 4% PFA, and stained with anti-dsRNA mAb and anti-VP1 rabbit serum for visualization in epifluorescence microscopy. Nuclei were visualized using Hoechst staining. Images are representative of three independent experiments. Based on data from Alexander Müller, M.Sc. (242).

Next the proportions of dsRNA-, VP1- and double-positive cells to all cells were quantified to evaluate the kinetics of viral replication and protein synthesis. At 8 hpi, no significant differences were observed among conditions in the number of dsRNA or VP1 positive cells (Figure 73). Between 5% to 7% of cells were positive for dsRNA signal, with 1% VP1-positive and 1% double-positive.

At 24 hpi, the proportion of VP1- and double-positive cells increased to 4-16% and 12-70%, respectively, in mock- and spermine-treated, and spermine-rescued conditions, whereas the proportion of dsRNA-positive cells remained similar (8-11%) to that at 8 hpi (Figure 73). In contrast, DFMO-treated cells showed no increase in VP1-positive cells and double-positive cells. Notably, both spermine-supplemented conditions displayed a higher proportion of VP1-positive cells compared to mock-treated at 24 and 48 hpi. The proportion of dsRNA-, VP1- and double-positive DFMO-treated cells remained constant between 8, 24 and 48 hpi time points. At 48 hpi, an increase in negative cells

in mock-treated and spermine-supplemented conditions was observed (Figure 73), like reflecting CPE progression.

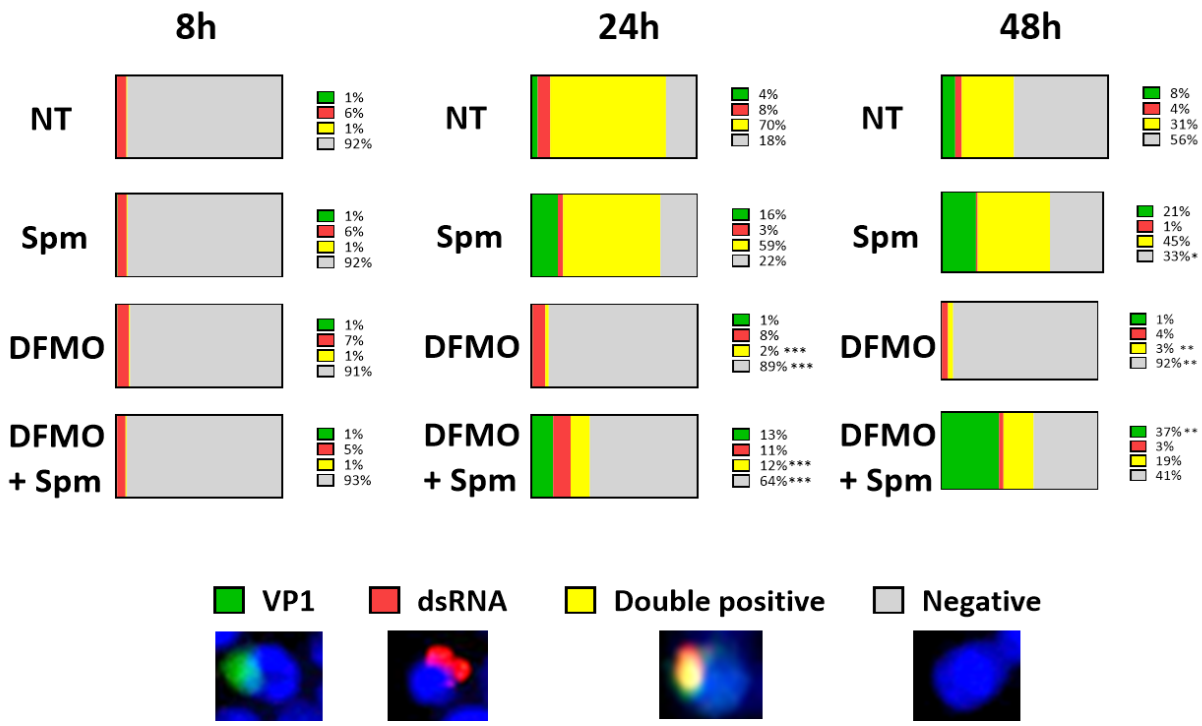

*Figure 73. Polyamine depletion inhibits RAW264.7 macrophages re-infection with MNV-1. Quantification of VP1-, dsRNA-, double-positive and negative cells was performed from epifluorescence microscopy images. One randomly selected field of view was analyzed per replicate from three independent biological experiments. Example of VP1-, dsRNA-, double-positive and negative cells are shown under the legend. Data are presented as means, and statistical significance was determined using a two-way ANOVA test relative to non-treated (NT) controls within each time point: ns, not significant (not shown for clarity); * $p \leq 0.05$; ** $p \leq 0.01$; *** $p \leq 0.001$. Based on data from Alexander Müller, M.Sc. (242).*

In summary, a restriction of VP1 protein accumulation was observed in polyamine-depleted RAW264.7 macrophages. VP1 accumulation could be rescued or even enhanced compared to mock condition by supplementation of the exogenous spermine. Moreover, no increase in numbers of virus-positive cells was detected under polyamine-depletion, as the fraction of infected cells remained consistently 8-11% throughout the experiment. This observation aligns with the plateau in viral titers after 24 hpi in infectivity assays, as well as the modest reduction of 10-20% in cell viability, metabolic activity and membrane integrity. Together, these results indicate the absence of the re-infection of DFMO-treated cells with *de novo* produced progeny.

Given the distinct dsRNA signal pattern observed in DFMO-treated cells compared with mock-treated cells, the intracellular distribution of dsRNA and VP1 signals was next investigated. Confocal microscopy was performed on infected polyamine-depleted RAW264.7 macrophages, and cells exhibiting both signals were selected to assess their localization and potential co-localization.

At 8 hpi, VP1 signals were undetectable in all conditions, whereas dsRNA signals observed as abundant, punctate clusters throughout the cytoplasm (Figure 74) of infected cells. In DFMO-treated cells, the

number of dsRNA puncta per cell appeared lower and the signal was shifted further away from the nucleus.

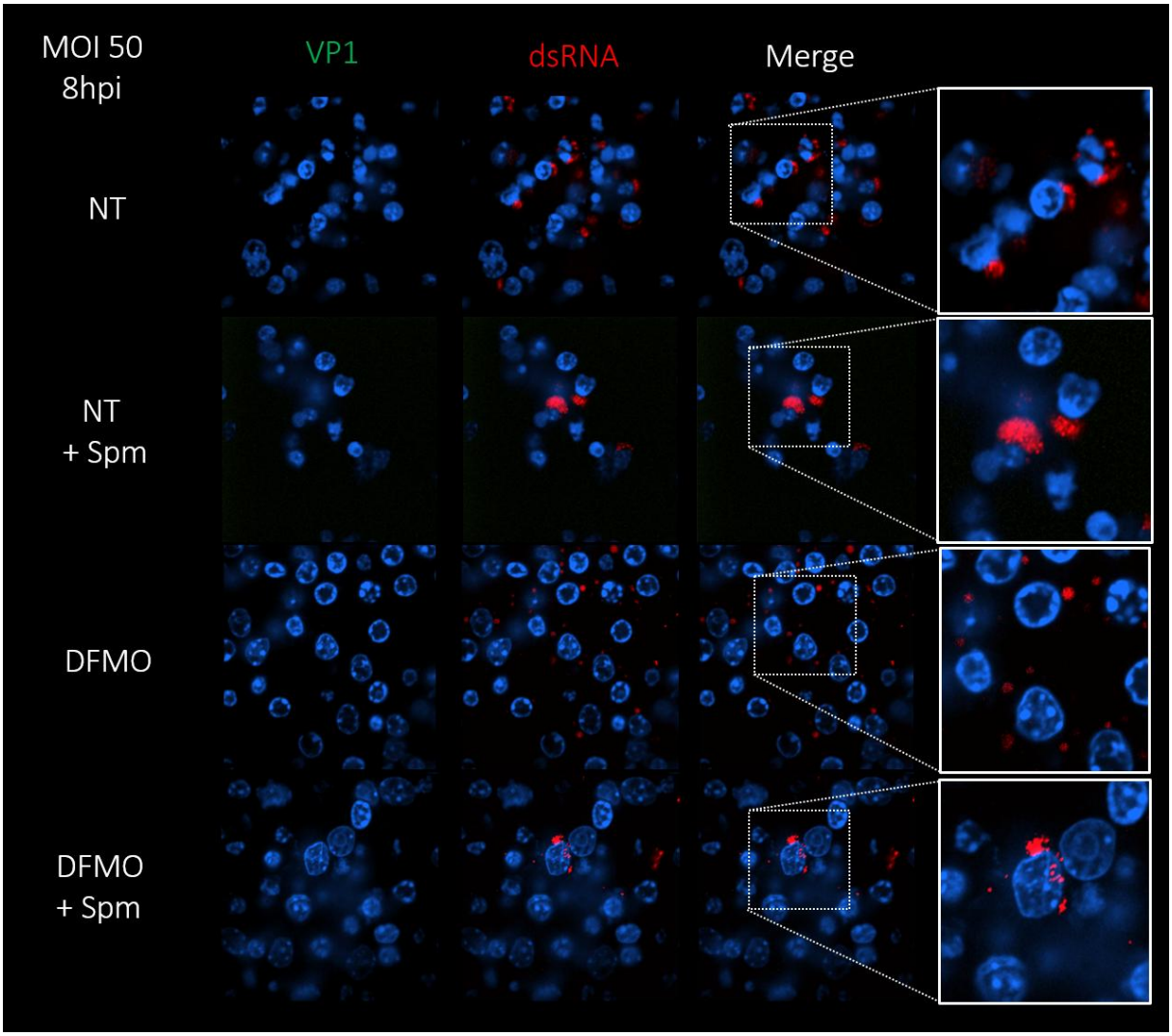

Figure 74. Polyamine depletion alters intracellular distribution of MNV-1 dsRNA at 8 hpi. RAW264.7 cells were pretreated with 500 µM DFMO for 4 days to deplete polyamines, then infected with MNV-1 at an MOI of 50. Infected cells were maintained with or without DFMO and supplemented, where indicated, with 100 µM spermine (Spm). Samples were harvested at 8 hpi, fixed with 4% PFA, and stained with anti-dsRNA mAb and anti-VP1 rabbit serum for visualization in confocal microscopy. Nuclei were visualized using Hoechst staining. Images are representative of one independent experiment. Based on data from Alexander Müller, M.Sc. (242).

At 24 hpi, dsRNA distribution appeared comparable among all conditions. However, the VP1 signal pattern differed between mock and polyamine-depleted cells. In mock and spermine supplemented cells, VP1 formed multiple perinuclear punctate clusters, occasionally forming dense foci that co-localized with dsRNA signal, indicative of replication complexes (Figure 75). In contrast, in DFMO-treated cells, both with and without spermine supplementation, less of VP1 punctate was observed. Nevertheless, in polyamine-depleted double-positive cells, partial co-localization of both dsRNA and VP1 signals was observed.

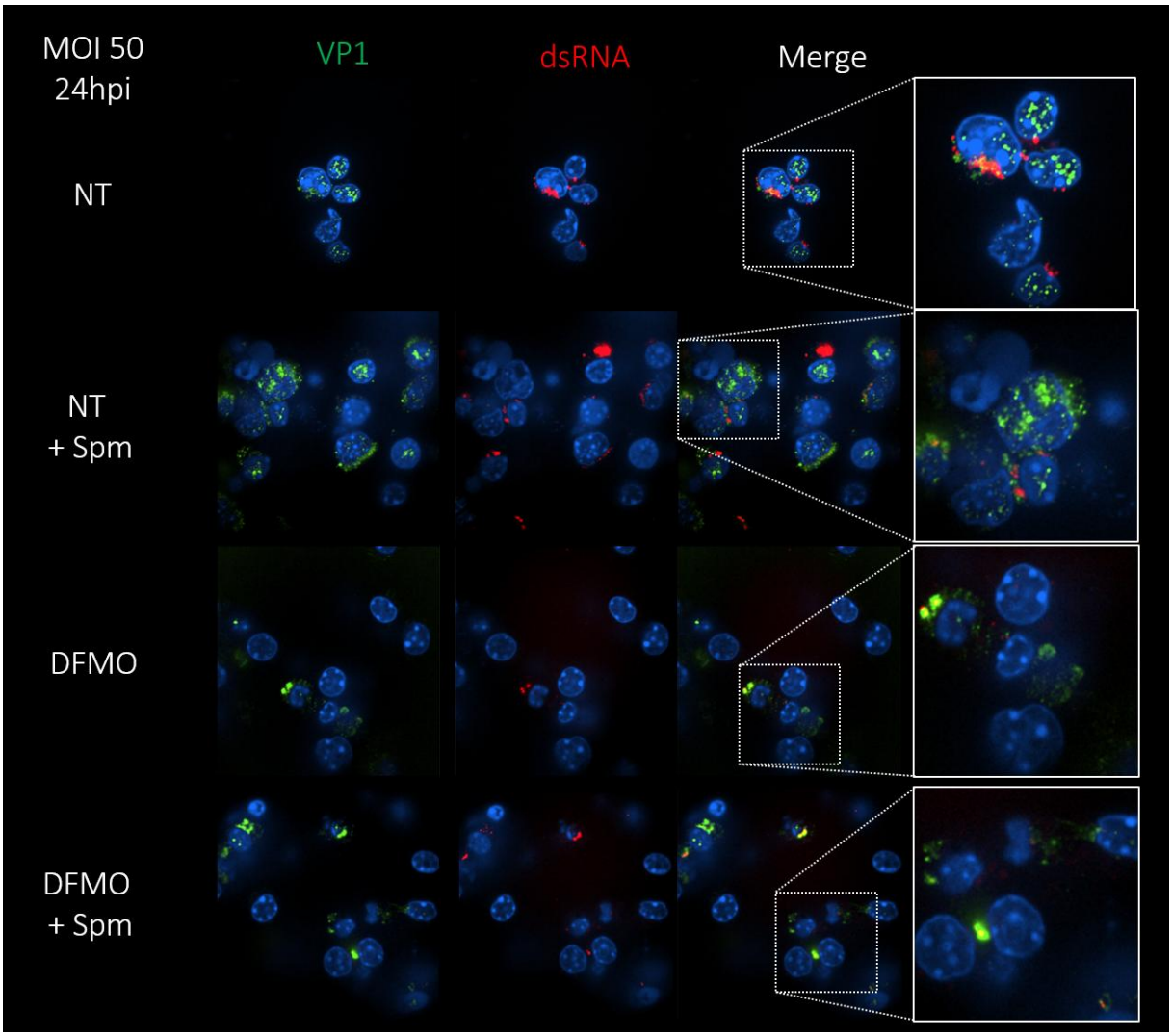

Figure 75. Polyamine depletion alters intracellular distribution of MNV-1 VP1 protein at 24 hpi. RAW264.7 cells were pretreated with 500 µM DFMO for 4 days to deplete polyamines, then infected with MNV-1 at an MOI of 50. Infected cells were maintained with or without DFMO and supplemented, where indicated, with 100 µM spermine (Spm). Samples were harvested at 24 hpi, fixed with 4% PFA, and stained with anti-dsRNA mAb and anti-VP1 rabbit serum for visualization in confocal microscopy. Nuclei were visualized using Hoechst staining. Images are representative of two independent experiments. Based on data from Alexander Müller, M.Sc. (242).

Although only a few polyamine-depleted cells were positive for VP1 staining, closer analysis of the signal pattern revealed that VP1 localized farther from the nucleus and was more broadly dispersed throughout the cytoplasm (Figure 76) in polyamine-depleted cells, lacking the defined punctate structures observed in mock-treated cells. This altered spatial distribution indicates a disrupted organization of viral protein accumulation under polyamine-depleted conditions.

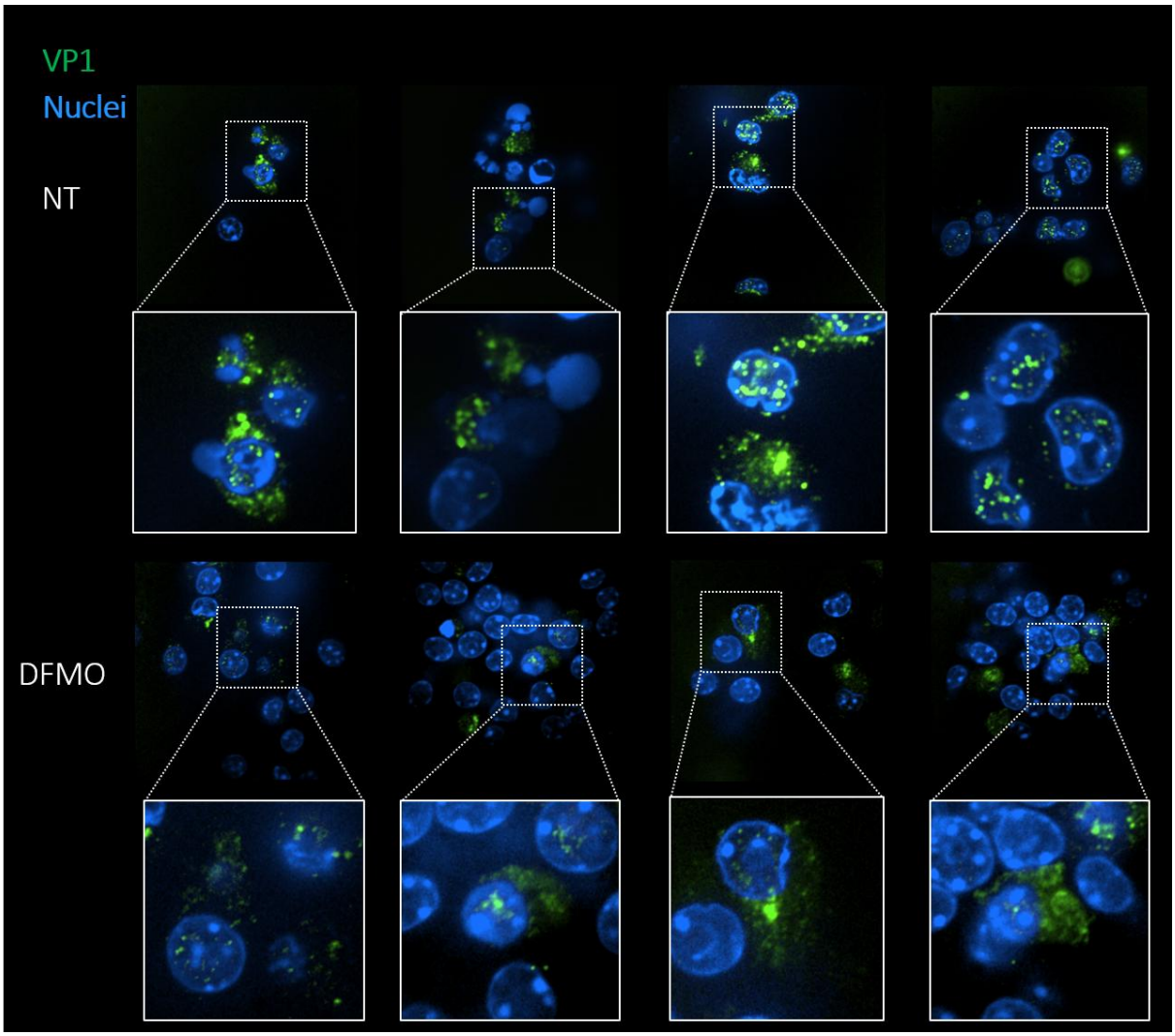

Figure 76. Polyamine depletion alters intracellular localization and distribution of MNV-1 VP1 protein. RAW264.7 cells were pretreated with 500 µM DFMO for 4 days to deplete polyamines, then infected with MNV-1 at an MOI of 50. Infected cells were maintained with or without DFMO and supplemented, where indicated, with 100 µM spermine (Spm) Samples were harvested at 24 hpi, fixed with 4% PFA, and stained with anti-dsRNA mAb and anti-VP1 rabbit serum for visualization in confocal microscopy. Nuclei were visualized using Hoechst staining. Images are representative of two independent experiments. Based on data from Alexander Müller, M.Sc. (242).

In summary, an altered intracellular distribution of VP1 and dsRNA signals was observed in DFMO-treated cells. The diffused cytoplasmic distribution of VP1 protein prompted us to question whether polyamine depletion disrupts the formation of viral replication complexes. These complexes are membranous webs derived from remodeled cellular membranes that separates viral replication from host immune sensors and restriction factors (244). The biogenesis of replication complexes depends heavily on host lipid metabolism, particularly on cholesterol and other membrane lipids (245,246).

Polyamines are known to regulate host cholesterol biosynthesis and reduced membrane cholesterol (200,247). However, MNV attachment was not affected by polyamine depletion, while nor genome replication, was modestly to not inhibited, as demonstrated by attachment assays and the presence of dsRNA in infected cells. It was therefore hypothesized that inhibition of cholesterol synthesis under polyamine depletion may affect the intracellular distribution of viral proteins and thereby inhibit MNV-

1 infection. To test this hypothesis, exogenous cholesterol was supplemented during MNV-1 infection of polyamine-depleted RAW264.7 macrophages, and its effect on viral replication was analyzed.

Upon cholesterol supplementation, restoration of CPE was observed in cholesterol-supplemented cells, as early as 24 hpi (data not shown), with even stronger effect at 48 hpi (Figure 77a). MNV-1 infection was assessed in the presence of spermine or 200 µM cholesterol under 0.1 and 50 MOI conditions. First, the ability of cholesterol to rescue MNV-1 infection under polyamine depletion was evaluated at 24 hpi, however, no differences were observed between DFMO-treated cells and those supplemented with cholesterol (data not shown). This prompted an assessment at 48 hpi, as rescue of CPE phenotype was observed at 24 hpi. At this later time point, and under both MOI conditions, spermine and cholesterol restored viral infection and release in RAW264.7 cells (Figure 77b-c).

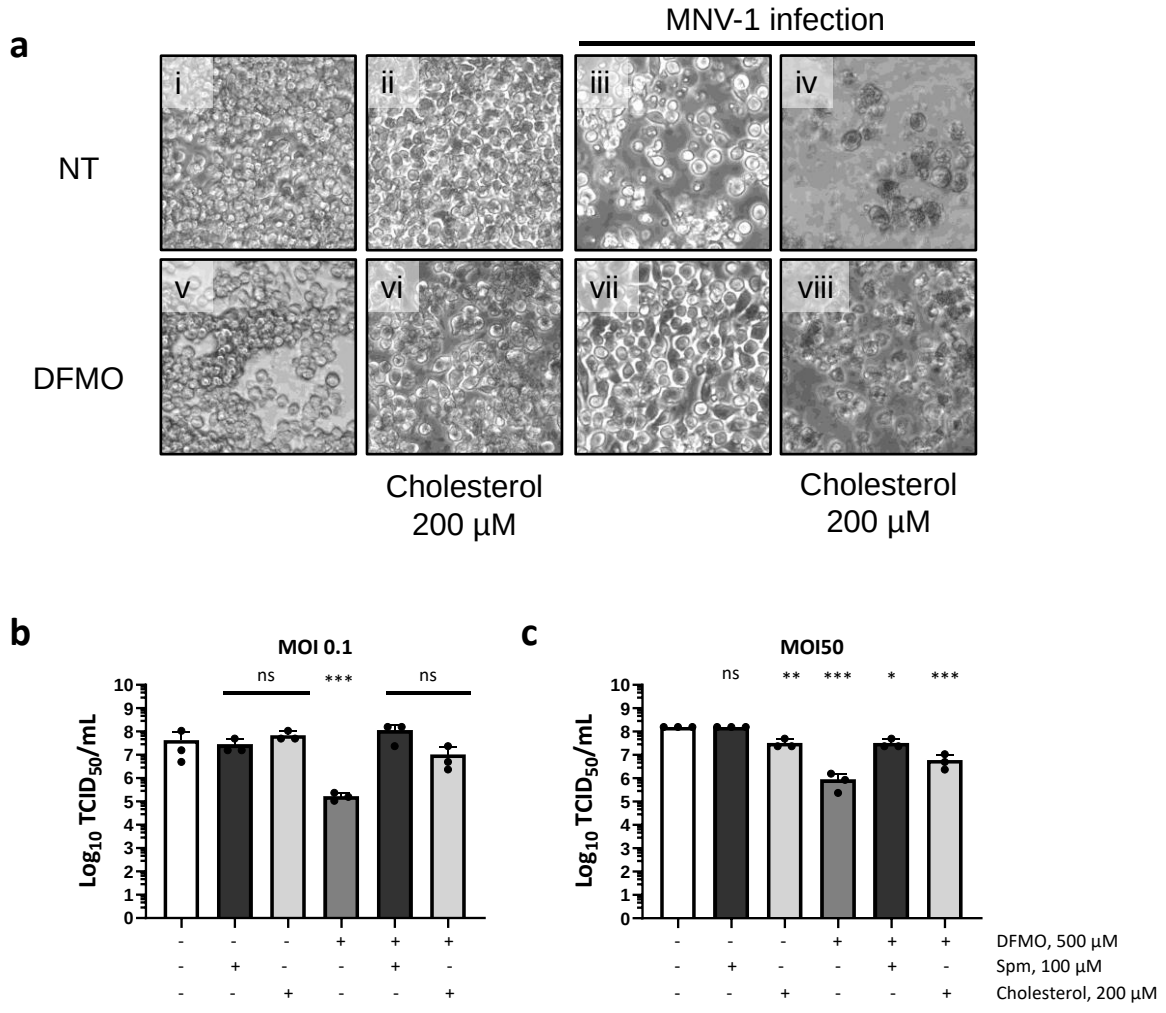

Figure 77. Cholesterol supplementation enhances MNV-1 replication in polyamine-depleted cells. RAW264.7 cells were pretreated with 500 µM DFMO for 4 days to deplete polyamines, then infected with MNV-1 at an MOI of 50. Infected cells were maintained with or without DFMO and supplemented, where indicated, with 100 µM spermine (Spm) or 200 µM cholesterol supplemented immediately after infection. (a) MNV-induced CPE was analyzed 48 hpi by bright-field microscopy. (b-c) Total cell lysate (supernatant and cells) was collected 24 hpi and virus titers were determined by $TCID_{50}$ assay. Data represent means ± standard deviation (SD) of three independent biological replicates. Statistical

*significance was assessed using a one-way ANOVA test and shown compared to non-treated (NT): ns, non-significant; * p≤0.05; ** p≤0.01; *** p≤0.001.*

In summary, the MOI of 50 MNV-1 infection model enabled us to investigate the role of polyamines in MNV capsid protein synthesis and viral release. The generation of new MNV progeny was significantly reduced in polyamine-depleted macrophages, although low-level viral release was detectable. The proportion of infected DFMO-treated cells (~11%) closely corresponded to the quantified loss of cell viability (~15%), metabolic activity (~20%), and membrane integrity (~15%), suggesting that MNV release, while significantly reduced, still exerts a mildly detrimental effect on host cell viability. Under normal conditions, viral release at titers of 10^6 infectious units per milliliter typically coincides with extensive cell death (111), however, in DFMO-treated cells, no significant reduction in cell viability was detected, indicating that virus-induced cell death is inhibited under polyamine-depleted conditions.

The constant proportion of infected cells throughout the time course indicates that MNV infection is limited to the subset of cells and does not initiate secondary rounds. This finding is particularly striking, as the release of 10^6 infectious units per milliliter would ordinarily be sufficient to establish a new infection cycle. Instead, a decline in infectious titers over time was observed, suggesting that the released virions might be less infectious.

Polyamine depletion markedly reduced VP1 synthesis and altered its intracellular localization. Collectively, these findings demonstrate that polyamine depletion inhibits MNV infection in murine macrophages by suppressing capsid protein synthesis and thereby limiting the generation of new progeny. This inhibition coincides with diminished virus release, likely through interference with virus-induced cell death that can be rescued via cholesterol supplementation. Overall, these results support the concept that the polyamine-cholesterol axis influences both replication complex formation and apoptosis induction, thereby shaping the late stages and overall outcome of MNV infection.

4.4.7. Polyamine restriction ablates HNoV GII.4 infection in HIEs

To assess whether polyamines play a broad role in norovirus infection, the impact of polyamine depletion on HNoV was investigated using two distinct HNoV GII.4 stool-isolates. To assess the impact of polyamine restriction on HNoV infection, DENSpm was used to degrade polyamines in 3D-HIEs, which resulted in full block of HNoV replication with partial titer rescue after supplementation of 100 µM spermine for both stool isolates (Figure 78a-b), suggesting that the effect is not stool dependent.

Since the HIE differentiation medium contains 150 µM putrescine, the use of DFMO, was not feasible, as putrescine supports downstream polyamine synthesis. Therefore, differentiation medium omitting the putrescine containing additives B27 and N2 (putrescine-free medium (B27-/N2-)) was used. After 7 days of differentiation, 3D-HIEs were infected with GII.4 Den Haag #1 at MOI 1. After inoculation, putrescine-free medium was reconstituted with a mix 100 µM spermine and 100 µM spermidine. HNoV titers were quantified day 2 post-infection from whole cell samples via RT-qPCR. Again, depletion of putrescine from differentiation medium resulted in full restriction of HNoV infection and partial rescue supplementing polyamines (Figure 78c). Cell viability of 3D-HIEs were not significantly affected in either treatment (Figure 78d). However, differentiation in putrescine-depleted medium led to ≤30% loss in viability, which was partially restored by supplementation of polyamine mix. Consistent with our data on murine cells, an increase in metabolic activity was also observed only in DENSpm treated spermine supplemented HIEs.

Collectively, our data show that polyamines also contribute to HNoV infection in 3D-HIEs.

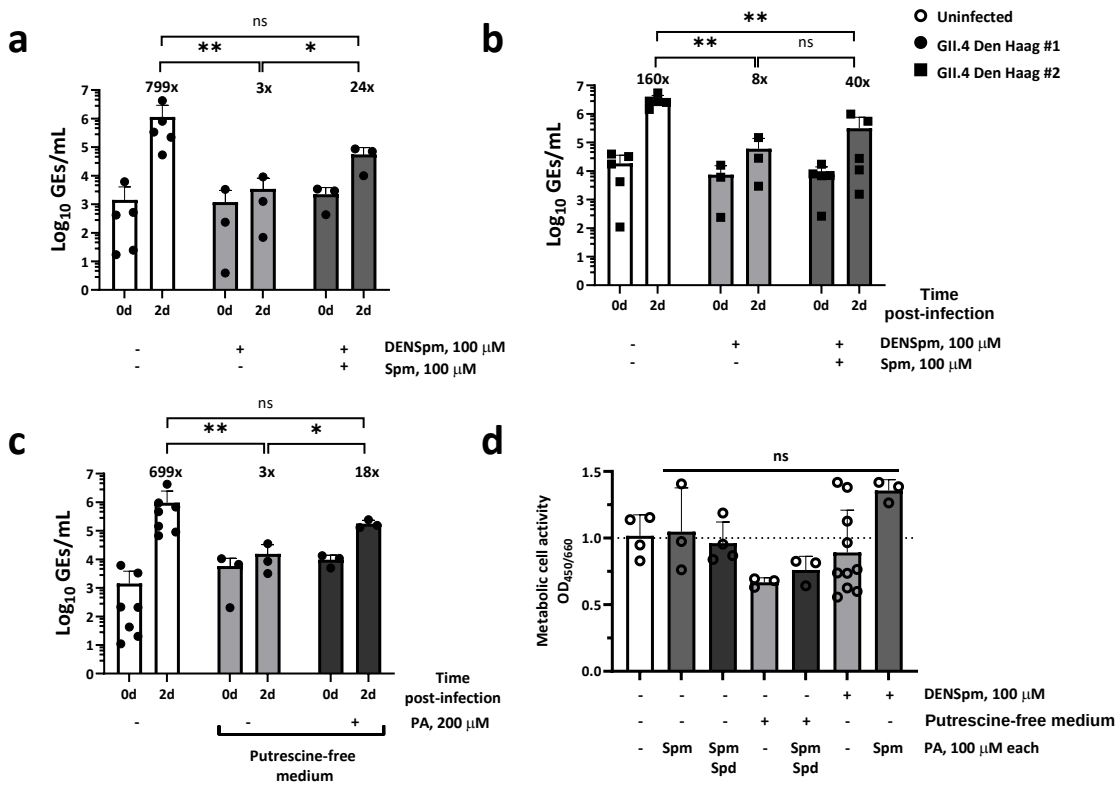

*Figure 78. Polyamine degradation inhibits HNoV GII.4 infections in 3D-HIEs. (a-b) HIEs were differentiated in standard differentiation medium with 100 µM DENSpm additionally added 2 days before infection or (c) 7 days in putrescine-free medium (B27-/N2-). HIEs were infected with (a, c) HNoV GII.4 stool isolates Den Haag #1 or (b) Den Haag, #2, at an approx. MOI of 1 for 1 h. (a-b) The inoculum was removed and replaced with standard medium with or without DENSpm and 100 µM Spm or (c) putrescine-free (B27-/N2-) medium with or without 200 µM polyamine mix (polyamine; 100 µM Spm + 100 µM Spd). HNoV GEs were determined by RT-qPCR at 48 hpi. Numbers above the bars indicate the fold-change in viral GEs at 2 days compared to 0 days. (d) Viability of uninfected, treated HIEs were assessed using the WST-1 metabolic assay. HIEs were treated as above, omitting only the viral inoculation. Data are presented as means ± standard deviation (SD) from a minimum of three independent biological assays. Individual data points are shown (a-d). Statistical significance was assessed using one-way ANOVA in comparison to (a-c) untreated/infected or (d) just untreated: ns, not significant; * p≤0.05; ** p≤0.01.*

In summary of this section:

- Both MNV and HNoV GII.4 require polyamines for efficient infection.
- The inhibitory effect of polyamine depletion on MNV infection is rescued by supplementation of
  - polyamines (spermine or spermidine)
  - inhibition of PI3K activity
  - cholesterol.
- Polyamine depletion restricts MNV-induced CPE and capsid protein accumulation in cells.

5. Discussion

HNoV disease presents a major medical and economic burden, yet specific therapeutic or preventative options remain unavailable against HNoV. This situation is largely attributed to the long-standing lack of an efficient cell culture system that supports HNoV replication. The identification of HIE as a susceptible and permissive model for HNoV infection has marked a critical breakthrough in the field (19). Building upon this advancement, the present work identified and characterized several host and environmental determinants, namely glycans, divalent cations, bile acids, and polyamines, that promote norovirus infectivity and immune escape.

5.1. The 3D-HIE model

The HIE model represents a state-of-the-art *in vitro* model for studying enteric virus-host interactions. Derived from primary intestinal stem cells, HIEs recapitulate the cellular diversity, polarity, and innate immune responses of the human intestinal epithelium (21,248), providing a physiologically relevant platform to investigate viral entry, replication, and host factor dependency. Moreover, HIEs preserve donor-specific features such as glycan expression and secretor status (149,249,250), which are critical determinants of enteric virus susceptibility. This study reports the establishment of HNoV infection in a 3D-HIE model from a diagnostic sample biobank, along with detailed maintenance and support of this cell culture system.

Screening of stool samples from a biobank of norovirus-positive patients (n=10) identified that 60% of samples were infectious (Figure 16), as defined by a >10-fold increase in GEs at day 2 post-infection. The factors determining the success of HNoV replication remain unknown, but likely involve a combination of viral and host factors, including the genetic background of the HIE donor, culture conditions, and viral fitness or concentration.

Additionally, a time-dependent decrease in infectivity of stool preparations was observed. Previous reports suggest that stool samples can remain infectious for years (153), and our with experience GII.4 Den Haag #1 strain supports this observation (Figure 17 and 18). However, several other stool samples lost infectivity within 6-18 months of the usage, presenting a significant limitation, given the persistent difficulty in generating HNoV stock in the HIE model and scarcity of diagnostic samples. While major advance in HNoV stock preparations has been made allowing the passaging and propagation of GII.3 and GII.17 variants via inhibition of cytokine CXCR3/CCR5/CCR2 receptor (151), the predominant epidemic variant GII.4, remains refractory to passaging. These observations highlight the need to identify factors that can modulate HNoV infectivity and stability in stool and cell culture samples. To the best of our knowledge, the loss of HNoV stool sample infectivity has not been discussed previously in the literature. In the present work, divalent cations and fucose were identified as enhancers of GII.4 infectivity; these findings will be discussed in detail in subsequent chapters.

To localize actively replicating cells, dsRNA immunostaining was established in HNoV-infected 3D-HIEs. The detection of a dsRNA genome intermediate was successful only at high-MOI infection, supporting the notion from other reports (154) that only a small subset of cells supports the active HNoV replication.

Further investigation into HNoV replication dynamics revealed the presence of viral GEs in culture supernatants (detected by RT-qPCR) and synthesis of the major capsid protein confirmed by Western blot. Notably, a difference in molecular size of major capsid protein between stool input and newly synthesized protein was observed (Figure 22). Such a difference was not observed in other publications

on HNoV replication in HIEs (19). However, this observation might be an explanation for the inability to passage the GII.4 variants in HIE, as it suggests differences in post-translation processing or capsid maturation between infected individuals and *in vitro* model.

While our study provides insights into the establishment of HNoV infection in 3D-HIE culture, a limited size of our biobank that lacks the relevant data for the clinical sample (including time of collection in relation to onset of symptoms, storage conditions, personal patient data, such as age and secretor status), make it difficult to define criteria for selecting samples that are infectious. While high Ct (low number of GEs) is an indicator for a non-infectious sample, each stool sample needs to be screened individually. A more comprehensive biobank study with well-annotated patient data would allow for a more systematic identification of the determinants that modulate HNoV infectivity and replication potential *in vitro*.

Although the HIE model robustly supports HNoV replication, whether it supports productive infection remains an open question. The detection of viral GEs in the supernatant (Figure 19a) cannot be unequivocally interpreted as release of viral particles, as the RT-qPCR cannot discriminate between encapsidated genomes and non-infectious RNA fragments. The absence of increase in HNoV GEs between day 2 and day 3 post-infection (Figure 19b), the synthesis of smaller size major capsid protein and inability to passage the GII.4 variants, suggests that HNoV GII.4 infection may not result in the production of infectious progeny. The observed difference in capsid protein size between stool-derived virus and *de novo* synthesized warrants further investigation, as it may provide insights into capsid processing, stability, or post-translational regulation critical for successful viral propagation and passaging *in vitro*.

In summary, this study reports the establishment of a biobank-derived HNoV infectious model in 3D-HIE for studying HNoV infection and host factor dependency. Our findings highlight the problem of infectivity loss during the storage of HNoV stool preparations. A difference in capsid protein size was also identified between the stool-derived input and the progeny capsids, which may explain the inability to successfully passage GII.4 strains in HIEs. Together, these findings provide insight into the current limitations of the 3D-HIE system and identify key directions for future optimization to achieve robust and productive HNoV culture.

5.2. Fucosylation defines HIEs susceptibility to HNoV and HRoV

Fucosyltransferases are key host factors that are associated with HNoV and HRoV susceptibility in the population. This association is supported by epidemiological data for both viruses (23,67) and for HNoV specifically, by genetic modification studies in HIEs (149). Although the importance of HBGAs in infection and disease has been well established, the contribution of specific sugar residues, such as fucose, galactose and sialic acids, remains unknown. In this study, the role of fucosylation and specific sugar moieties in HNoV and HRoV infection in 3D-HIEs was systematically investigated.

First, the presence of specific glycan on differentiated 3D-HIEs was confirmed using lectin-based profiling, including fucosylated, N-acetyl-galactosamine/glucosamine-, mannose-, and sialic acid-containing glycans on the cell surface (Figure 27). To determine whether active fucosylation occurs in 3D-HIEs, the broad-spectrum fucosyltransferase inhibitor 2-FPF was employed, and its efficacy was validated by lectin staining. Treatment with 2-FPF resulted in nearly complete loss of fucosylated glycans on HIE surface, without affecting other tested glycan types, confirming efficient and specific inhibition. Infection of 2-FPF-treated HIEs revealed complete block of HNoV and HRoV replication,

whereas influenza virus infection remained unaffected (Figure 28). To the best of our knowledge, this provides the first evidence that fucosylation is required for HRoV infection in primary human cell model. This finding, however, is consistent with prior observations from porcine intestinal enteroids, where HRoV G3.P[1] Wa strain infection also required active fucosylation (251).

It was further demonstrated that HNoV GII.4 infection could be outcompeted by lectins binding fucose and N-acetyl-galactosamine/glucosamine residues, but not by those binding mannose or sialic acids (Figure 29). The requirement for exposed fucose residues is consistent with previous reports (23).

However, several limitations of lectin assays must be acknowledged. Lectins generally have lower glycan specificity than antibodies (252). Although multiple reports describe UEA-I lectin as specific towards H type 1 and 2 antigens (253,254), discrepancies exist between UEA-I and anti-H type 1/2 antibodies recognition targets (254,255). Thus, it can only be concluded with confidence that monofucosylated glycans, irrespective of the specific H-type species, are required for HNoV infection. Future work comparing UEA-I and anti-H type 1/2 antibodies staining patterns in differentiated HIEs could help to clarify possible off-target interaction of UEA-I lectin.

The requirement of exposed N-acetylglucosamine/galactosamine residues for HNoV infection may involve a direct interaction of the viral capsid, as direct interactions of galactose and glucose have been described for HNoV GII strains (79). Alternatively, steric hindrance by WGA lectin binding may also indirectly inhibit fucose-dependent interactions, leading to reduced infection.

In contrast to HNoV, none of the tested lectins interfered with HRoV G3.P[8]eq.-like infection (Figure 30). The combined requirement for fucosyltransferase activity and the absence of UEA-I or WGA effects suggests that HRoV depends on glycans other than FUT2-dependent monofucosylated residues. Importantly, UEA-I lectin does not block difucosylated Lewis antigens (253), which corroborates that Lewis antigens may be primary ligands for HRoV [P8] strains (67). This interpretation aligns with reports showing that HRoV P[4] and P[8] strains bind difucosylated glycans and saliva from FUT2/FUT3-positive donors, where Lewis antigens are abundant (67).

While FUT2 is required for secreted HBGAs but not for cell-surface difucosylated glycans, which can be produced through FUT3 and FUT8 activity, as demonstrated in glycoproteomic analyses of FUT2-positive and -negative HIEs (250). Thus, our findings indicate that while fucosylation is essential for HRoV G3.P[8]eq-like infection, monofucosylated glycans are dispensable. This conclusion is consistent with prior studies showing FUT2 independence for culture-adapted HRoV P[8] strains (166) and highlights the need for further investigation into the specific fucosylated glycans and FUT enzymes required for HRoV infection.

Regarding the glycan requirements for IAV H1N1 infection, our results demonstrated that productive infection of 3D-HIEs depended on α2,6-linked sialic acids on the cell surface (Figure 30). The inhibitory effect of ConA lectin observed in our study aligns with previous reports showing that influenza virus hemagglutinin contains a conserved mannosylation site that must remain accessible for successful infection (256). Accordingly, blocking the viral mannose residues represents a potent antiviral strategy against IAV (257,258).

Whether fucose could act as a competitive inhibitor of HNoV infection was examined, given its essential role in viral entry. Contrary to expectations, exogenous fucose did not inhibit infection but instead modestly enhanced replication of highly infectious strains (Figure 32), rescued replication of

an aged non-replicating GII.4 Sydney preparations (Figure 33) and enabled prolonged passaging of the Sydney strain in HIEs (Figure 34). To the best of our knowledge, this represents the first report of an exogenous sugar enhancing HNoV infection. A similar effect has been described for Tulane virus (TV), a non-human primate recovirus within the *Caliciviridae* family, for which supplementation with A- and B-trisaccharides increased production of infectious particles (259,260). Subsequent work demonstrated that TV and other recoviruses require both coxsackievirus and adenovirus receptor (CAR) and HBGAs for infection, indicating that HBGAs can complement a *bona fide* proteinaceous entry receptor (261).

Enhancement of viral infection by soluble entry factors is not unique to HNoV. In hepatitis C virus (HCV) infections, soluble CD81 was shown to enhance rather than compete with cell-bound CD81, likely by priming viral glycoproteins for endosomal fusion (262). A similar effect occurs with herpes simplex virus-1 (HSV-1), where soluble nectin-1 enables infection of otherwise non-permissive cells lacking membrane-bound nectin-1 (263).

Biophysical analysis of HNoV GII.17 and GII.10 VLPs demonstrated that fucose binding can modulate viral particle size, plasticity, and stiffness (264). This suggests that fucose can act as a modulator of capsid dynamic and structural flexibility of HNoV GII variants. Taken together, these findings support the hypothesis that fucose binding promotes capsid reorganization necessary for viral entry. Although fucosylated glycans alone are not enough to permit infection in non-susceptible cell culture models, HNoV GII variants, similar to recoviruses, might require a combination of proteinaceous receptor and fucosylated HBGAs for productive entry.

Furthermore, complex fucosylated glycans, such as fucoidan and HMOs, were assessed as HNoV GII.4 inhibitors. Consistent with previous studies, 2-FL and LNFP I showed no antiviral activity in fetal HIEs (265). Fucoidan antiviral activity was observed for both HNoV GII.4 Sydney and IAV, however the heterogeneous and undefined nature of fucoidan as a polymer, together with its nonspecific effects on IAV, prevented conclusions about the specific contribution of a high-avidity fucose effect.

Collectively, our findings highlight the essential role of fucosylated glycans in determining susceptibility to HNoV GII.4 and HRoV P[8] variants. For HNoV, membrane-bound fucose-containing HBGAs are indispensable for infection, whereas exogenous fucose facilitates the infection, possibly by mediating the conformational changes in the viral capsid. In HRoV, infection is independent from monofucosylated glycans such as HBGAs and is likely to involve difucosylated Lewis antigens. Together these results expand our understanding of glycan-mediated virus-host interactions and suggest that the interplay between free and surface-bound glycans within the intestinal environment modulate infectivity.

5.3. Divalent cations and bile acid modulate norovirus infectivity and antibody escape

Recent structural studies have shown that conformational changes in the viral capsid of noroviruses, induced by environmental ligands such as divalent cations, bile acid GCDCA or acidic pH, influence mCD300lf receptor engagement and antibody binding in MNV and HNoV (101,121,125). In this study, the effect of physiologically relevant concentrations of divalent cations, specifically magnesium, and bile acid GCDCA was investigated on norovirus infection and antibody evasion.

Cations ions and the bile acid GCDCA have been shown to enhance binding of the MNV-1 P-domain to its receptor mCD300lf thereby reducing the dissociation constant tenfold (125), implicating these ligands as potent attachment enhancers. In this study, a dose-dependent increase in MNV-1 attachment to BV2 and Huh7^{mCD300lf} cells was observed upon $MgCl_2$ supplementation, whereas GCDCA had no effect (Figure 39). No enhancement was detected in Huh7^{naïve} cells, indicating that magnesium-enhanced attachment was receptor dependent. A baseline level of attachment in Huh7^{naïve} cells was still detected, likely reflecting interaction with attachment factors such as sialic acids and gangliosides (230). Magnesium-induced enhancement of attachment translated into significantly increased infectivity of MNV-1 and CR3 strains in both single- and multiple infection cycle investigations. These findings are consistent with earlier reports showing that environmental ligands, including GCDCA, acidic pH, and fetal bovine serum (estimated ~3.5 mM of calcium and ~1.8 mM of magnesium), enhance infection of multiple MNV strains (119). The responsiveness of the persistent CR3 strain further indicates that this ligand-induced enhancement mechanism is conserved across MNV variants.

The potential of environmental ligands to modulate antibody recognition of MNV was next assessed. Structural studies have shown that divalent cations, acidic pH, and GCDCA induce conformational changes in the norovirus capsid that reduce epitope accessibility and promote antibody escape (120). Escape mutations selected under antibody pressure (V338I and D348E) were further shown to adopt a contracted capsid conformation even without environmental ligands (132). Consistent with these findings, our neutralization assays demonstrated a clear dose-dependent escape of MNV-1 and CR3 from mAb A6.2 (Figure 42), restoring infectivity to levels observed in the absence of antibodies.

Because magnesium and GCDCA are encountered concurrently in the gastrointestinal tract, their cooperative effects were also examined. Biophysical studies have indicated that binding of either ligand pre-organizes the MNV P-domain to facilitate binding of the other (124,128). In our system, GCDCA alone enhanced infectivity of MNV-1 and CR3 but did not induce antibody escape (Figure 42), in contrast to some previous reports (129). However, co-supplementation with low-dose magnesium (1 mM) restored escape for both strains, consistent with a cooperative mechanism. The apparent discrepancy between our findings and earlier studies likely stems from differences in baseline divalent cation levels: prior assays were performed in DMEM or FBS-containing medium with ~2-3 mM combined of Mg^{2+} and Ca^{2+} (266,267), whereas the present work employed a divalent-cation-reduced buffer, enabling independent analysis of ligand effects. It is plausible that a presence of residual divalent cations in earlier studies may have facilitated antibody escape in the presence of GCDCA. Our data strongly supports that GCDCA alone is not sufficient to induce antibody escape of MNV-1 and CR3 (Figure 42) but supports the divalent ion effect on antibody escape.

Although the roles of bile acids, divalent cations, and acidic pH are well established for MNV, their effects on HNoV remain less defined. Structural and biophysical studies have identified three putative divalent cation-binding sites in the HNoV capsid and shown that HNoV VLPs undergo conformational changes in response to acidic pH or cation chelation, similar to MNV (101,123,128,268).

To determine whether environmental ligands modulate HNoV infectivity and antibody escape, the effects of divalent cations and bile acids were tested on four GII.4 stool isolates: two GII.4 Den Haag strains, GII.4 Yerseke, and GII.4 Sydney. Magnesium supplementation during infection enhanced viral replication 30-60-fold across all isolates (Figure 43) and fully rescued infectivity of an aged non-replicating GII.4 Sydney preparation (Figure 44). However, only the GII.4 Den Haag #1 isolate escaped neutralization by mAb A1413 under combined supplementation with GCDCA and $MgCl_2$ (Figure 45),

providing functional evidence that HNoV can also use cooperative ligand effects to evade antibody recognition, similar to MNV.

Of note, HNoV stool filtrates were prepared in Opti-MEM, which contains approx. 2 mM combined Mg^{2+} and Ca^{2+}, as such storage conditions provided longer shelf-life. However, this baseline concentration of divalent cations in Opti-MEM, even when combined with GCDCA, was insufficient to induce antibody escape in the GII.4 Den Haag #1 isolate, indicating a requirement for a higher ligand concentration to induce the phenotype.

Although this study provides the first functional evidence that HNoV GII.4 stool isolates respond to environmental ligands in terms of infectivity and immune escape, broader analyses across additional genotypes and genogroups will be required to determine how conserved these responses are. It also remains to be established which divalent cations beyond magnesium can enhance HNoV infectivity or promote immune escape. While the precise ligand-induced conformational changes in the HNoV capsid have yet to be defined, the observed phenotypes indicate that HNoV GII.4 and MNV undergo similar ligand-mediated functional modulation.

The functional responsiveness of norovirus to environmental ligands such as magnesium ions and GCDCA highlights the virus's capacity to adapt structurally to its surroundings. This structural plasticity allows noroviruses to optimize infectivity under conditions characteristic of the small intestine, where bile acids and divalent cations are abundant. Furthermore, during diarrheal episodes, the increased efflux of electrolytes into the intestinal lumen (231,232) may further support viral infectivity and transmission efficacy. In contrast, upon entry into the systemic compartments, where magnesium levels are lower and bile acids are absent, capsid relaxation may expose decoy epitopes, potentially aiding immune evasion. Whether the host produces antibodies targeting ligand-bound or collapsed capsid conformations remains to be determined; identification of such antibodies would provide important insight into norovirus immune evasion and inform therapeutic development. Overall, elucidation of environmental ligand effects on norovirus infectivity and immune response may offer key advances in understanding viral pathogenesis and support the rational design of next-generation vaccines.

5.4. Polyamines function as broad host factors supporting norovirus replication

Viruses are known to manipulate cellular signaling pathways to secure essential biomolecules and maintain conditions favorable for infection. Polyamines, which are ubiquitous cellular metabolites present at high micromolar concentrations, play key roles in numerous cellular processes (206) and are required by many RNA and DNA viruses (197). Polyamine restriction in naturally susceptible murine immune cells and in recombinant human epithelial cells was shown to significantly reduce MNV infection. Likewise, polyamine depletion in HIEs markedly inhibited HNoV GII.4 replication, indicating that noroviruses exploit host-produced polyamines to promote infection, similar to flaviviruses, coronaviruses, phleboviruses, and enteroviruses (207–209,237).

Our findings indicate that polyamines exert a multifactorial effect on norovirus infection, influencing both cellular response to infection and virus replication. On the viral side, polyamine depletion significantly inhibited capsid protein synthesis and its intracellular localization, which likely impaired production of infectious progeny and limited re-infection of the cells.

On the cellular side, polyamine depletion prevented virus-induced CPE (Figure 60 and 69) and bystander non-infected cell death. The initiation of apoptosis in bystander cells in MNV infection is evident from a full loss of anti-apoptotic PARP protein (Figure 62) and ~20% of PS externalization (Figure 64) in culture with only 5% of infected cells (at MOI 1, Figure 66). Yet polyamine depletion completely prevents PARP cleavage and PS externalization, retaining cell viability, mitochondrial activity and membrane integrity even under high-MOI infection. Interestingly, polyamine-depleted murine macrophages remained susceptible to staurosporine-induced apoptosis, indicating that virus-associated apoptosis were selectively affected by polyamine restriction.

Mechanistically, the ability of the PI3K inhibitor LY294002 to restore MNV-1 titers (Figure 65) and rescue virus-induced cell death under polyamine depletion (Figure 64), suggests that PI3K/Akt signaling pathway and its downstream effectors are involved in regulation of virus-induced cell death and capsid protein synthesis. While the PI3K/Akt molecular pathway is involved in many cellular processes, it is well established that activation of Akt protein via phosphorylation by PI3K prevents apoptosis and prolongs cell survival (201,269,270). Additionally, MNV is known to modulate Akt phosphorylation at early time-points of infection to support cell survival during virus replication and allow for optimum assembly of MNV virions (109). Thus, precise Akt protein regulation appears critical for MNV egress.

Polyamine restriction has been reported to cause sustained Akt phosphorylation (201,241), which might disrupt late stages of MNV infection and reduce apoptosis by inhibiting key events like PARP cleavage. Assessing the levels of total Akt and phosphorylated Akt protein together with cleaved PARP protein would further clarify the role of Akt in norovirus-induced cell death. However, our finding that exogenous cholesterol supplementation also rescues MNV titers and virus-induced cell death (Figure 77) provides an additional mechanistic clue. Cholesterol depletion is a known effect of intracellular polyamine restriction, however in case of MNV, its effect was evident downstream of virus attachment and entry. Of note, SREBP regulatory element is a well characterized target of PI3K/Akt pathway and Akt activation promotes lipogenesis (271,272). Therefore, it is proposed that polyamine depletion inhibits MNV replication by reducing capsid protein synthesis and lowering cellular cholesterol pools, thereby suppressing bystander cell death.

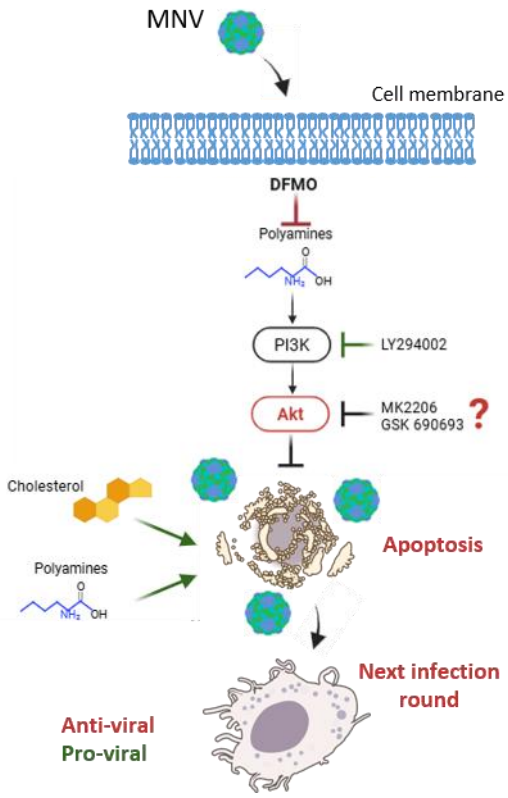

Figure 79. PI3K impact on polyamine modulated MNV-1 infection and viral release. DFMO-mediated polyamine depletion induces sustained Akt phosphorylation through PI3K activity (201,241), resulting in reduced apoptosis and inhibition of MNV-1 infection and viral dissemination. Pharmacological inhibition of PI3K using LY294002 restores virus-associated cell death and rescues MNV-1 infection. Whether direct Akt inhibitors, such as MK2206 (109) and GSK 690693 (273), similarly rescue MNV-1 infection and cytopathic effects remains to be determined. Supplementation with exogenous polyamines (spermine or spermidine) or cholesterol also restores MNV-1 infection and virus-induced cell death under polyamine-depleted conditions. MNV model is taken from PDB 7N7F.

To validate this hypothesis, future studies should employ additional PI3K/Akt modulators (e.g., Wortmannin or Akt-specific inhibitors, such as MK2206 or GSK 690693 (109,273)). Quantification of total cellular cholesterol under polyamine depletion will be essential to confirm whether pharmacological PI3K/Akt signaling modulation (i.e. using LY) under polyamine depletion restores cholesterol levels. Similar analyses should also be performed in the HIE model for HNoV to establish translational relevance.

Of note, hypusination, where spermidine becomes covalently attached to eIF5A, has been linked to the ability of the host to translate proteins from certain mRNAs, particularly those containing polyproline stretches or other ribosome-stalling motifs that are otherwise difficult to translate efficiently (274). While there are no obvious polyproline stretches in the norovirus genome, hypusination could affect the ribosomal frameshifting that leads to the translation of ORF-3, which means that this mechanism of action should be also assessed for MNV infection.

Although further investigation is needed to define the precise effect of apoptosis inhibition on MNV replication under polyamine restriction, the observed prevention of bystander cell death highlights a beneficial therapeutic aspect of polyamine depletion. Recent studies have identified apoptosis inhibitors as potent antivirals against several RNA viruses, including coronaviruses (275,276), influenza

virus (277), and closely related feline calicivirus (278), where inhibition of virus-induced apoptosis reduced tissue damage and improved survival in animal models. This highlights polyamine depletion as a promising host-directed antiviral strategy against noroviruses.

Norovirus infection in healthy individuals is typically self-limiting and resolves in 3-4 days, leaving only a narrow window for a therapeutic intervention. However, in immunocompromised patients, chronic infection can persist for months. Polyamine depletion may be a viable therapeutic strategy for chronically infected patients. Such individuals could undergo treatment for sufficient time for DFMO to exert its antiviral effects and, if needed, they could even receive long-term therapy, as DFMO has been reported to be safe and well tolerated for periods of up to three months (279). Importantly, DFMO is already approved for clinical use in both USA and Europe for the treatment of trypanosomiasis (213,214), which opens a possibility of its off-label use.

In summary, our research highlights the role of polyamines in norovirus infection. Polyamine restriction was shown to reversibly inhibit MNV and HNoV infection. For MNV, polyamine depletion was further shown to disrupt virus-induced CPE associated with PARP cleavage and apoptosis. To the best of our knowledge, this represents the first report linking polyamines to virus-induced apoptosis. Our findings identify a novel target to exploit for intervention against norovirus infection open to already licensed pharmacological approaches such as DFMO, as well as dietary and targeted microbiome modulation approaches to deplete polyamines in the gut.

6. Conclusion

A robust and reproducible HNoV and HRoV infection model in 3D-HIEs was established using clinical stool samples. This system enabled investigation of key aspects of enteric virus infection, including entry, replication, passaging and virus-host interactions.

The importance of fucosylation and surface glycan composition was examined for both HNoV and HRoV infection, showing that fucosylated glycans in 3D-HIEs are essential for HNoV GII.4 and HRoV P[8]eq.-like infection with different glycans being involved. The surface glycans involved in infection however, differed between HNoV and HRoV, as UEA-I competition only inhibited HNoV but not HRoV infection. Additionally exogenous fucose unexpectedly enhanced HNoV replication instead of outcompeting the infection, potentially impacting viral structure.

In line with recently published structural observations (101,120), a functional synergistic effect of magnesium and bile acid (GCDCA) was observed for MNV impacting both infection and antibody escape. A similar infectivity enhancement was also observed for HNoV infection for GII.4 Den Haag, Yerseke and Sydney isolates in 3D-HIEs, while magnesium-induced escape from neutralization was observed in GII.4 Den Haag #1 isolate. Of note, magnesium supplementation also restored HNoV infectivity in 3D-HIEs of stool preparations stored in solution for an extended period of time. In summary these findings highlight a broad and substantial impact for magnesium and GCDCA in modulating norovirus infection.

This work established polyamines as a broad host-dependency factors for noroviruses. Polyamine depletion by pharmacological inhibition i.e. by DFMO significantly suppressed MNV-1 and HNoV GII.4 infection Mechanistic analysis indicated the PI3K/Akt signaling pathway and cholesterol metabolism as downstream targets of polyamine modulation. Additional experiments are needed to unravel the molecular mechanism.

Collectively, this dissertation demonstrates that noroviruses exploit intrinsic host factors and environmental ligands to modulate infectivity and immune recognition. Investigation of these interactions advances our understanding of norovirus adaptation across intestinal and extraintestinal niches and informs rational vaccine design. Moreover, the identification of polyamines as host-dependency factors highlights a promising antiviral target, and since DFMO is already approved and used in patients, it opens a realistic opportunity for treating chronic HNoV infection.

7. Outlook

The findings of this dissertation provide new insights into the interplay between HNoV and HRoV, and their host and environmental factors. Understanding these relationships provides valuable foundations for the development of direct acting antiviral strategies and potentially vaccines.

A novel reverse genetics system for HNoV was recently established for a GII.17 strain allowing for site directed mutagenesis and passaging in HIEs and zebrafish embryos (280). This now opens the possibility to study the interaction with environmental factors and its functional consequences. From a structural perspective, investigation of the proposed divalent cation binding sites in the HNoV capsid protein is of particular interest to dissect the contribution of specific residues to ligand-modulated HBGA binding and antibody escape. Surrogate binding and neutralization assays using VLPs can support this approach.

Another critical direction involves dissecting the host glycosylation pathways underlying HNoV and HRoV susceptibility. A systematic analysis for HRoV could employ knockout HIE lines for key fucosyltransferases (FUT2, FUT3, FUT8 and others) to identify the minimal glycan residues required for productive infection. Integration of glycomics, proteomics, and single-cell transcriptomics within the HIE model could further clarify cell type-specific glycan expression profiles that support viral entry and replication.

Building on current findings, it would also be of interest to assess whether magnesium and exogenous fucose could improve stool biobank screening and increase the number of cultivable isolates. Supplementation with fucose may mimic the secretor phenotype by providing soluble HBGAs. Future experiments could explore supplementation with complex glycans, glycan mixtures, or even saliva as a natural glycan source to evaluate potential improvements in HNoV GII.4 replication efficiency. Overcoming the limitation of HNoV GII.4 stock preparation would greatly expand the scope of experimental work to study HNoV epidemic strains.

The identification of polyamines as broad host dependency factors for noroviruses further enhances our understanding of how enteric viruses exploit host metabolic pathways. Future research should focus on investigating where and how polyamine metabolism intersects with PI3K/Akt signaling and lipid biosynthesis during infection. Given the established safety profile of the FDA-approved ornithine decarboxylase inhibitor DFMO, testing polyamine modulation therapies in small-animal models, such as chronic MNV infection with CR3 or CR6 strains, should be considered as a feasible next step. These models, which mimic persistent human norovirus infections, offer an opportunity to evaluate whether polyamine modulation can effectively limit viral replication in the gut.

8. Bibliography

1. Chhabra P, de Graaf M, Parra GI, Chan MCW, Green K, Martella V, et al. Updated classification of norovirus genogroups and genotypes. J Gen Virol. 2019 Oct;100(10):1393–406.

2. Villabruna N, Koopmans MPG, de Graaf M. Animals as Reservoir for Human Norovirus. Viruses. 2019 May 25;11(5):478.

3. Vinjé J. Advances in Laboratory Methods for Detection and Typing of Norovirus. Journal of Clinical Microbiology. 2015 Jan 23;53(2):373–81.

4. Ahmed SM, Hall AJ, Robinson AE, Verhoef L, Premkumar P, Parashar UD, et al. Global prevalence of norovirus in cases of gastroenteritis: a systematic review and meta-analysis. The Lancet Infectious Diseases. 2014 Aug 1;14(8):725–30.

5. Calduch EN, Cattaert T, Verstraeten T. Model estimates of hospitalization discharge rates for norovirus gastroenteritis in Europe, 2004–2015. BMC Infectious Diseases. 2021 Aug 5;21(1):757.

6. Atmar RL, Opekun AR, Gilger MA, Estes MK, Crawford SE, Neill FH, et al. Norwalk Virus Shedding after Experimental Human Infection. Emerg Infect Dis. 2008 Oct;14(10):1553–7.

7. Teunis PFM, Moe CL, Liu P, E. Miller S, Lindesmith L, Baric RS, et al. Norwalk virus: How infectious is it? Journal of Medical Virology. 2008 Aug;80(8):1468–76.

8. Tung G, Macinga D, Arbogast J, Jaykus LA. Efficacy of Commonly Used Disinfectants for Inactivation of Human Noroviruses and Their Surrogates. Journal of Food Protection. 2013 July 1;76(7):1210–7.

9. Seitz SR, Leon JS, Schwab KJ, Lyon GM, Dowd M, McDaniels M, et al. Norovirus Infectivity in Humans and Persistence in Water ▿. Appl Environ Microbiol. 2011 Oct;77(19):6884–8.

10. Bányai K, Estes MK, Martella V, Parashar UD. Viral gastroenteritis. Lancet. 2018 July 14;392(10142):175–86.

11. Shah MP, Hall AJ. Norovirus Illnesses in Children and Adolescents. Infect Dis Clin North Am. 2018 Mar;32(1):103–18.

12. Tsai H, Yune P, Rao M. Norovirus disease among older adults. Ther Adv Infect Dis. 2022 Nov 14;9:20499361221136760.

13. Ye X, Van JN, Munoz FM, Revell PA, Kozinetz CA, Krance RA, et al. Noroviruses as a Cause of Diarrhea in Immunocompromised Pediatric Hematopoietic Stem Cell and Solid Organ Transplant Recipients. American Journal of Transplantation. 2015 July 1;15(7):1874–81.

14. Sukhrie FHA, Siebenga JJ, Beersma MFC, Koopmans M. Chronic Shedders as Reservoir for Nosocomial Transmission of Norovirus. J Clin Microbiol. 2010 Nov;48(11):4303–5.

15. Chaimongkol N, Kim DY, Matsushima Y, Durkee-Shock J, Barton K, Ahorrio CN, et al. A Decade of Chronic Norovirus Infection Surveillance at the National Institutes of Health Clinical Research Center: Clinical Characteristics, Molecular Epidemiology, and Replication. The Journal of Infectious Diseases. 2024 Aug 29;jiae440.

16. Karandikar UC, Crawford SE, Ajami NJ, Murakami K, Kou B, Ettayebi K, et al. Detection of human norovirus in intestinal biopsies from immunocompromised transplant patients. Journal of General Virology. 2016 Sept 1;97(9):2291–300.

17. Green KY, Kaufman SS, Nagata BM, Chaimongkol N, Kim DY, Levenson EA, et al. Human norovirus targets enteroendocrine epithelial cells in the small intestine. Nat Commun. 2020 June 2;11(1):2759.

18. Zeve D, Stas E, de Sousa Casal J, Mannam P, Qi W, Yin X, et al. Robust differentiation of human enteroendocrine cells from intestinal stem cells. Nat Commun. 2022 Jan 11;13:261.

19. Ettayebi K, Crawford SE, Murakami K, Broughman JR, Karandikar U, Tenge VR, et al. Replication of human noroviruses in stem cell–derived human enteroids. Science. 2016 Sept 23;353(6306):1387–93.

20. Jones MK, Watanabe M, Zhu S, Graves CL, Keyes LR, Grau KR, et al. Enteric bacteria promote human and mouse norovirus infection of B cells. Science. 2014 Nov 7;346(6210):755–9.

21. Mirabelli C, Santos-Ferreira N, Gillilland MG, Cieza RJ, Colacino JA, Sexton JZ, et al. Human Norovirus Efficiently Replicates in Differentiated 3D-Human Intestinal Enteroids. Journal of Virology. 2022 Nov 7;96(22):e00855-22.

22. Ghosh S, Kumar M, Santiana M, Mishra A, Zhang M, Labayo H, et al. Enteric viruses replicate in salivary glands and infect through saliva. Nature. 2022 July;607(7918):345–50.

23. Prasad BVV, Atmar RL, Ramani S, Palzkill T, Song Y, Crawford SE, et al. Norovirus replication, host interactions and vaccine advances. Nat Rev Microbiol. 2025 June;23(6):385–401.

24. Inc H. GlobeNewswire News Room. 2024 [cited 2025 Dec 15]. HilleVax Reports Topline Data from NEST-IN1 Phase 2b Clinical Study of HIL-214 in Infants. Available from: https://www.globenewswire.com/news-release/2024/07/08/2909536/0/en/HilleVax-Reports-Topline-Data-from-NEST-IN1-Phase-2b-Clinical-Study-of-HIL-214-in-Infants.html

25. Chen J, Cheng Z, Chen J, Qian L, Wang H, Liu Y. Advances in human norovirus research: Vaccines, genotype distribution and antiviral strategies. Virus Res. 2024 Oct 23;350:199486.

26. Ford-Siltz LA, Tohma K, Parra GI. Understanding the relationship between norovirus diversity and immunity. Gut Microbes. 13(1):1900994.

27. Parra GI, Tohma K, Ford-Siltz LA, Pilewski KA, Kendra JA. The saga to monitor and control norovirus: the rise of GII.17. J Gen Virol. 2025 June 6;106(6):002118.

28. Kendra JA, Tohma K, Parra GI. Global and regional circulation trends of norovirus genotypes and recombinants, 1995–2019: A comprehensive review of sequences from public databases. Rev Med Virol. 2022 Sept;32(5):e2354.

29. Siebenga JJ, Vennema H, Zheng DP, Vinjé J, Lee BE, Pang XL, et al. Norovirus Illness Is a Global Problem: Emergence and Spread of Norovirus GII.4 Variants, 2001–2007. J Infect Dis. 2009 Sept 1;200(5):802–12.

30. Beek J van, Graaf M de, Al-Hello H, Allen DJ, Ambert-Balay K, Botteldoorn N, et al. Molecular surveillance of norovirus, 2005–16: an epidemiological analysis of data collected from the NoroNet network. The Lancet Infectious Diseases. 2018 May 1;18(5):545–53.

31. Cannon JL, Bonifacio J, Bucardo F, Buesa J, Bruggink L, Chan MCW, et al. Global Trends in Norovirus Genotype Distribution among Children with Acute Gastroenteritis. Emerg Infect Dis. 2021 May;27(5):1438–45.

32. Arias A, Thorne L, Ghurburrun E, Bailey D, Goodfellow I. Norovirus Polymerase Fidelity Contributes to Viral Transmission In Vivo. mSphere. 2016 Oct 19;1(5):10.1128/msphere.00279-16.

33. Mahar JE, Bok K, Green KY, Kirkwood CD. The Importance of Intergenic Recombination in Norovirus GII.3 Evolution. Journal of Virology. 2013 Apr;87(7):3687–98.

34. Bull RA, Eden JS, Rawlinson WD, White PA. Rapid Evolution of Pandemic Noroviruses of the GII.4 Lineage. PLOS Pathogens. 2010 Mar 26;6(3):e1000831.

35. Parra GI, Squires RB, Karangwa CK, Johnson JA, Lepore CJ, Sosnovtsev SV, et al. Static and Evolving Norovirus Genotypes: Implications for Epidemiology and Immunity. PLoS Pathog. 2017 Jan 19;13(1):e1006136.

36. Chhabra P, Tully DC, Mans J, Niendorf S, Barclay L, Cannon JL, et al. Emergence of Novel Norovirus GII.4 Variant. Emerg Infect Dis. 2024 Jan;30(1):163–7.

37. Parra GI. Emergence of norovirus strains: A tale of two genes. Virus Evol. 2019 July;5(2):vez048.

38. Cannon JL, Barclay L, Collins NR, Wikswo ME, Castro CJ, Magaña LC, et al. Genetic and Epidemiologic Trends of Norovirus Outbreaks in the United States from 2013 to 2016 Demonstrated Emergence of Novel GII.4 Recombinant Viruses. J Clin Microbiol. 2017 July;55(7):2208–21.

39. Karst SM, Wobus CE, Lay M, Davidson J, Virgin HW. STAT1-Dependent Innate Immunity to a Norwalk-Like Virus. Science. 2003 Mar 7;299(5612):1575–8.

40. Thackray LB, Wobus CE, Chachu KA, Liu B, Alegre ER, Henderson KS, et al. Murine Noroviruses Comprising a Single Genogroup Exhibit Biological Diversity despite Limited Sequence Divergence. J Virol. 2007 Oct;81(19):10460–73.

41. Gonzalez-Hernandez MB, Liu T, Payne HC, Stencel-Baerenwald JE, Ikizler M, Yagita H, et al. Efficient norovirus and reovirus replication in the mouse intestine requires microfold (M) cells. J Virol. 2014 June;88(12):6934–43.

42. Wobus CE, Thackray LB, Virgin HW. Murine Norovirus: a Model System To Study Norovirus Biology and Pathogenesis. Journal of Virology. 2006 June;80(11):5104–12.

43. Niendorf S, Klemm U, Marques AM, Bock CT, Höhne M. Infection with the Persistent Murine Norovirus Strain MNV-S99 Suppresses IFN-Beta Release and Activation of Stat1 In Vitro. PLOS ONE. 2016 June 13;11(6):e0156898.

44. Wobus CE, Karst SM, Thackray LB, Chang KO, Sosnovtsev SV, Belliot G, et al. Replication of Norovirus in Cell Culture Reveals a Tropism for Dendritic Cells and Macrophages. PLOS Biology. 2004 Nov 30;2(12):e432.

45. Lee S, Liu H, Wilen CB, Sychev ZE, Desai C, Hykes BL, et al. A Secreted Viral Nonstructural Protein Determines Intestinal Norovirus Pathogenesis. Cell Host & Microbe. 2019 June 12;25(6):845-857.e5.

46. Lee S, Wilen CB, Orvedahl A, McCune BT, Kim KW, Orchard RC, et al. Norovirus Cell Tropism Is Determined by Combinatorial Action of a Viral Non-structural Protein and Host Cytokine. Cell Host & Microbe. 2017 Oct 11;22(4):449-459.e4.

47. Wilen CB, Lee S, Hsieh LY, Orchard RC, Desai C, Hykes BL, et al. Tropism for tuft cells determines immune promotion of norovirus pathogenesis. Science. 2018 Apr 13;360(6385):204–8.

48. Strine MS, Alfajaro MM, Graziano VR, Song J, Hsieh LL, Hill R, et al. Tuft-cell-intrinsic and -extrinsic mediators of norovirus tropism regulate viral immunity. Cell Rep. 2022 Nov 8;41(6):111593.

49. Strine MS, Fagerberg E, Darcy PW, Barrón GM, Filler RB, Alfajaro MM, et al. Intestinal tuft cell immune privilege enables norovirus persistence. Sci Immunol. 2024 Mar 22;9(93):eadi7038.

50. Cox C, Cao S, Lu Y. Enhanced detection and study of murine norovirus-1 using a more efficient microglial cell line. Virol J. 2009 Nov 10;6:196.

51. Haga K, Fujimoto A, Takai-Todaka R, Miki M, Doan YH, Murakami K, et al. Functional receptor molecules CD300lf and CD300ld within the CD300 family enable murine noroviruses to infect cells. Proceedings of the National Academy of Sciences. 2016 Oct 11;113(41):E6248–55.

52. Orchard RC, Wilen CB, Doench JG, Baldridge MT, McCune BT, Lee YCJ, et al. Discovery of a proteinaceous cellular receptor for a norovirus. Science. 2016 Aug 26;353(6302):933–6.

53. Graziano VR, Walker FC, Kennedy EA, Wei J, Ettayebi K, Strine MS, et al. CD300lf is the primary physiologic receptor of murine norovirus but not human norovirus. PLoS Pathog. 2020 Apr 6;16(4):e1008242.

54. Thorne LG, Goodfellow IG. Norovirus gene expression and replication. Journal of General Virology. 2014 Feb 1;95(2):278–91.

55. Mirabelli C, Jones MK, Young VL, Kolawole AO, Owusu I, Shan M, et al. Human Norovirus Triggers Primary B Cell Immune Activation In Vitro. mBio. 2022 Apr 11;13(2):e00175-22.

56. Lin Y, Fengling L, Lianzhu W, Yuxiu Z, Yanhua J. Function of VP2 protein in the stability of the secondary structure of virus-like particles of genogroup II norovirus at different pH levels: Function of VP2 protein in the stability of NoV VLPs. J Microbiol. 2014 Nov;52(11):970–5.

57. Ishiyama R, Yoshida K, Oikawa K, Takai-Todaka R, Kato A, Kanamori K, et al. Production of Infectious Reporter Murine Norovirus by VP2 trans-Complementation [Internet]. Microbiology; 2023 July [cited 2023 Oct 31]. Available from: http://biorxiv.org/lookup/doi/10.1101/2023.07.27.550866

58. McFadden N, Bailey D, Carrara G, Benson A, Chaudhry Y, Shortland A, et al. Norovirus Regulation of the Innate Immune Response and Apoptosis Occurs via the Product of the Alternative Open Reading Frame 4. PLOS Pathogens. 2011 Dec 8;7(12):e1002413.

59. Borg C, Jahun AS, Thorne L, Sorgeloos F, Bailey D, Goodfellow IG. Murine norovirus virulence factor 1 (VF1) protein contributes to viral fitness during persistent infection. Journal of General Virology [Internet]. 2021 Sept 23 [cited 2024 Jan 11];102(9). Available from: https://www.microbiologyresearch.org/content/journal/jgv/10.1099/jgv.0.001651

60. Matsushima Y, Levenson EA, Chaimongkol N, Harris L, Zhao Y, Turan S, et al. Single-cell transcriptional analysis of murine norovirus infection in a human intestinal cell line. J Virol. 2024;98(11):e01617-24.

61. Stewart BM, Pierce LR, Olson MC, Ji C, Orchard RC. Membrane asymmetry facilitates murine norovirus entry and persistent enteric infection. PLOS Biology. 2025 Apr 17;23(4):e3003147.

62. Perry JW, Wobus CE. Endocytosis of Murine Norovirus 1 into Murine Macrophages Is Dependent on Dynamin II and Cholesterol. J Virol. 2010 June 15;84(12):6163–76.

63. Gerondopoulos A, Jackson T, Monaghan P, Doyle N, Roberts LO. Murine norovirus-1 cell entry is mediated through a non-clathrin-, non-caveolae-, dynamin- and cholesterol-dependent pathway. Journal of General Virology. 2010 June 1;91(6):1428–38.

64. Lindesmith L, Moe C, Marionneau S, Ruvoen N, Jiang X, Lindblad L, et al. Human susceptibility and resistance to Norwalk virus infection. Nat Med. 2003 May;9(5):548–53.

65. Oriol R. Genetic control of the fucosylation of ABH precursor chains. Evidence for new epistatic interactions in different cells and tissues. J Immunogenet. 1990;17(4–5):235–45.

66. Mollicone R, Bara J, Le Pendu J, Oriol R. Immunohistologic pattern of type 1 (Lea, Leb) and type 2 (X, Y, H) blood group-related antigens in the human pyloric and duodenal mucosae. Lab Invest. 1985 Aug;53(2):219–27.

67. Barbé L, Le Moullac-Vaidye B, Echasserieau K, Bernardeau K, Carton T, Bovin N, et al. Histo-blood group antigen-binding specificities of human rotaviruses are associated with gastroenteritis but not with in vitro infection. Sci Rep. 2018 Aug 28;8(1):12961.

68. Currier RL, Payne DC, Staat MA, Selvarangan R, Shirley SH, Halasa N, et al. Innate Susceptibility to Norovirus Infections Influenced by FUT2 Genotype in a United States Pediatric Population. Clin Infect Dis. 2015 June 1;60(11):1631–8.

69. Tu LT, Liu FP, Huang YC, Huang CG, Yang S, Tsao KC, et al. Genetic Susceptibility to Norovirus GII.4 Sydney Strain Infections in Taiwanese Children. The Pediatric Infectious Disease Journal. 2017 Apr;36(4):353.

70. Carlsson B, Kindberg E, Buesa J, Rydell GE, Lidón MF, Montava R, et al. The G428A nonsense mutation in FUT2 provides strong but not absolute protection against symptomatic GII.4 Norovirus infection. PLoS One. 2009;4(5):e5593.

71. Jin M, He Y, Li H, Huang P, Zhong W, Yang H, et al. Two Gastroenteritis Outbreaks Caused by GII Noroviruses: Host Susceptibility and HBGA Phenotypes. PLOS ONE. 2013 Mar 5;8(3):e58605.

72. Sharma S, Hagbom M, Carlsson B, Nederby Öhd J, Insulander M, Eriksson R, et al. Secretor Status is Associated with Susceptibility to Disease in a Large GII.6 Norovirus Foodborne Outbreak. Food Environ Virol. 2020 Mar 1;12(1):28–34.

73. Rouphael N, Beck A, Kirby AE, Liu P, Natrajan MS, Lai L, et al. Dose-Response of a Norovirus GII.2 Controlled Human Challenge Model Inoculum. J Infect Dis. 2022 Feb 8;226(10):1771–80.

74. Shirato H, Ogawa S, Ito H, Sato T, Kameyama A, Narimatsu H, et al. Noroviruses Distinguish between Type 1 and Type 2 Histo-Blood Group Antigens for Binding. Journal of Virology. 2008 Nov;82(21):10756–67.

75. De Rougemont A, Ruvoen-Clouet N, Simon B, Estienney M, Elie-Caille C, Aho S, et al. Qualitative and Quantitative Analysis of the Binding of GII.4 Norovirus Variants onto Human Blood Group Antigens. J Virol. 2011 May;85(9):4057–70.

76. Wegener H, Mallagaray Á, Schöne T, Peters T, Lockhauserbäumer J, Yan H, et al. Human norovirus GII.4(MI001) P dimer binds fucosylated and sialylated carbohydrates. Glycobiology. 2017 Nov 1;27(11):1027–37.

77. Liang Y, Wang WB, Zhang J, Hou JW, Tang F, Zhang XF, et al. Evolution of the interactions between GII.4 noroviruses and histo-blood group antigens: Insights from experimental and computational studies. PLOS Pathogens. 2021 July 12;17(7):e1009745.

78. Hong X, Xue L, Cao Y, Xu R, Wang J, Gao J, et al. The variation of antigenic and histo-blood group binding sites synergistically drive the evolution among chronologically emerging GII.4 noroviruses. Heliyon. 2024 Mar 15;10(5):e26567.

79. Fiege B, Leuthold M, Parra F, Dalton KP, Meloncelli PJ, Lowary TL, et al. Epitope mapping of histo blood group antigens bound to norovirus VLPs using STD NMR experiments reveals fine details of molecular recognition. Glycoconj J. 2017 Oct 1;34(5):679–89.

80. Choi JM, Hutson AM, Estes MK, Prasad BVV. Atomic resolution structural characterization of recognition of histo-blood group antigens by Norwalk virus. Proceedings of the National Academy of Sciences. 2008 July 8;105(27):9175–80.

81. Singh BK, Leuthold MM, Hansman GS. Human Noroviruses' Fondness for Histo-Blood Group Antigens. Journal of Virology. 2015 Jan 26;89(4):2024–40.

82. Hao N, Chen Y, Xia M, Tan M, Liu W, Guan X, et al. Crystal structures of GI.8 Boxer virus P dimers in complex with HBGAs, a novel evolutionary path selected by the Lewis epitope. Protein Cell. 2015 Feb 1;6(2):101–16.

83. Qian Y, Song M, Jiang X, Xia M, Meller J, Tan M, et al. Structural Adaptations of Norovirus GII.17/13/21 Lineage through Two Distinct Evolutionary Paths. Journal of Virology. 2018 Dec 10;93(1):10.1128/jvi.01655-18.

84. Wang C, Kang H, Tan M, Cong J, Su D, Li X, et al. Structural Insight into Terminal Galactose Recognition by Two Non-HBGA Binding GI.3 Noroviruses. Journal of Virology. 2022 June 6;96(13):e00420-22.

85. Shanker S, Choi JM, Sankaran B, Atmar RL, Estes MK, Prasad BVV. Structural Analysis of Histo-Blood Group Antigen Binding Specificity in a Norovirus GII.4 Epidemic Variant: Implications for Epochal Evolution. Journal of Virology. 2011 Sept;85(17):8635–45.

86. Tan M, Xia M, Chen Y, Bu W, Hegde RS, Meller J, et al. Conservation of Carbohydrate Binding Interfaces — Evidence of Human HBGA Selection in Norovirus Evolution. PLOS ONE. 2009 Apr 1;4(4):e5058.

87. Guix S, Asanaka M, Katayama K, Crawford SE, Neill FH, Atmar RL, et al. Norwalk Virus RNA Is Infectious in Mammalian Cells. Journal of Virology. 2007 Nov 15;81(22):12238–48.

88. Straub TM, Bartholomew RA, Valdez CO, Valentine NB, Dohnalkova A, Ozanich RM, et al. Human norovirus infection of Caco-2 cells grown as a three-dimensional tissue structure. Journal of Water and Health. 2011 June 1;9(2):225–40.

89. Herbst-Kralovetz MM, Radtke AL, Lay MK, Hjelm BE, Bolick AN, Sarker SS, et al. Lack of Norovirus Replication and Histo-Blood Group Antigen Expression in 3-Dimensional Intestinal Epithelial Cells - Volume 19, Number 3—March 2013 - Emerging Infectious Diseases journal - CDC. [cited 2025 Sept 4]; Available from: https://wwwnc.cdc.gov/eid/article/19/3/12-1029_article

90. Todd KV, Tripp RA. Vero Cells as a Mammalian Cell Substrate for Human Norovirus. Viruses. 2020 Apr;12(4):439.

91. Pohl C, Szczepankiewicz G, Liebert UG. Analysis and optimization of a Caco-2 cell culture model for infection with human norovirus. Arch Virol. 2022 June 1;167(6):1421–31.

92. Ayyar BV, Ettayebi K, Salmen W, Karandikar UC, Neill FH, Tenge VR, et al. CLIC and membrane wound repair pathways enable pandemic norovirus entry and infection. Nat Commun. 2023 Feb 28;14(1):1148.

93. Ayyar BV, Apostol CV, Dave JJ, Kaundal S, Kendra JA, Neill FH, et al. Functional diversity in GII.4 norovirus entry: HBGA binding and capsid clustering dynamics. Proc Natl Acad Sci U S A. 2025 Oct 7;122(40):e2517493122.

94. Sun W, Wang M, Shi Z, Wang P, Wang J, Du B, et al. VP2 mediates the release of the feline calicivirus RNA genome by puncturing the endosome membrane of infected cells. J Virol. 2024;98(5):e00350-24.

95. Hyde JL, Sosnovtsev SV, Green KY, Wobus C, Virgin HW, Mackenzie JM. Mouse Norovirus Replication Is Associated with Virus-Induced Vesicle Clusters Originating from Membranes Derived from the Secretory Pathway. Journal of Virology. 2009 Oct;83(19):9709–19.

96. Doerflinger SY, Cortese M, Romero-Brey I, Menne Z, Tubiana T, Schenk C, et al. Membrane alterations induced by nonstructural proteins of human norovirus. PLoS Pathog. 2017 Oct 27;13(10):e1006705.

97. Royet A, Ruedas R, Gargowitsch L, Gervais V, Habersetzer J, Pieri L, et al. Nonstructural protein 4 of human norovirus self-assembles into various membrane-bridging multimers. J Biol Chem. 2024 Aug 28;300(9):107724.

98. Kaundal S, Anish R, Ayyar BV, Shanker S, Kaur G, Crawford SE, et al. RNA-dependent RNA polymerase of predominant human norovirus forms liquid-liquid phase condensates as viral replication factories. Science Advances. 2024 Dec 20;10(51):eadp9333.

99. Simmonds P, Karakasiliotis I, Bailey D, Chaudhry Y, Evans DJ, Goodfellow IG. Bioinformatic and functional analysis of RNA secondary structure elements among different genera of human and animal caliciviruses. Nucleic Acids Res. 2008 May;36(8):2530–46.

100. Morales M. Synthesis in Vitro of Rabbit Hemorrhagic Disease Virus Subgenomic RNA by Internal Initiation on (–)Sense Genomic RNA - Journal of Biological Chemistry [Internet]. 2004 [cited 2025 Sept 9]. Available from: https://www.jbc.org/article/S0021-9258(19)75519-7/fulltext

101. Hu L, Salmen W, Chen R, Zhou Y, Neill F, Crowe JE, et al. Atomic structure of the predominant GII.4 human norovirus capsid reveals novel stability and plasticity. Nat Commun. 2022 Mar 10;13:1241.

102. Taube S, Kurth A, Schreier E. Generation of recombinant Norovirus-like particles (VLP) in the human endothelial kidney cell line 293T. Arch Virol. 2005 July 1;150(7):1425–31.

103. Vongpunsawad S, Venkataram Prasad BV, Estes MK. Norwalk Virus Minor Capsid Protein VP2 Associates within the VP1 Shell Domain. J Virol. 2013 May;87(9):4818–25.

104. Dave JJ, Crawford SE, Atmar RL, Ettayebi K, Prasad BVV, Estes MK. Mutational Analysis of Human Norovirus VP2 Elucidates Critical Molecular Interactions for Virus Assembly. bioRxiv. 2025 Aug 23;2025.08.23.671901.

105. Bok K, Prikhodko VG, Green KY, Sosnovtsev SV. Apoptosis in Murine Norovirus-Infected RAW264.7 Cells Is Associated with Downregulation of Survivin. Journal of Virology. 2009 Apr 15;83(8):3647–56.

106. Deerain JM, Aktepe TE, Trenerry AM, Ebert G, Hyde JL, Charry K, et al. Murine norovirus infection of macrophages induces intrinsic apoptosis as the major form of programmed cell death. Virology. 2024 Jan 1;589:109921.

107. Newton K, Strasser A, Kayagaki N, Dixit VM. Cell death. Cell. 2024 Jan;187(2):235–56.

108. Verburg SG, Lelievre RM, Westerveld MJ, Inkol JM, Sun YL, Workenhe ST. Viral-mediated activation and inhibition of programmed cell death. PLoS Pathog. 2022 Aug 11;18(8):e1010718.

109. Owusu IA, Passalacqua KD, Mirabelli C, Lu J, Young VL, Hosmillo M, et al. Akt Plays Differential Roles during the Life Cycles of Acute and Persistent Murine Norovirus Strains in Macrophages. López S, editor. J Virol. 2022 Feb 9;96(3):e01923-21.

110. Furman LM, Maaty WS, Petersen LK, Ettayebi K, Hardy ME, Bothner B. Cysteine protease activation and apoptosis in Murine norovirus infection. Virology Journal. 2009 Sept 10;6(1):139.

111. Aktepe TE, Deerain JM, Hyde JL, Fritzlar S, Pearson J, White PA, et al. Norovirus NS3 protein induces apoptosis through translation repression and dysregulation of BCL-2 pro-survival proteins [Internet]. Microbiology; 2023 Apr [cited 2024 Jan 11]. Available from: http://biorxiv.org/lookup/doi/10.1101/2023.04.23.537759

112. Herod MR, Salim O, Skilton RJ, Prince CA, Ward VK, Lambden PR, et al. Expression of the Murine Norovirus (MNV) ORF1 Polyprotein Is Sufficient to Induce Apoptosis in a Virus-Free Cell Model. PLOS ONE. 2014 Mar 5;9(3):e90679.

113. Yen JB, Wei LH, Chen LW, Chen LY, Hung CH, Wang SS, et al. Subcellular Localization and Functional Characterization of GII.4 Norovirus-Encoded NTPase. Journal of Virology. 2018 Feb 12;92(5):10.1128/jvi.01824-17.

114. Rozman B, Fisher T, Stern-Ginossar N. Translation—A tug of war during viral infection. Molecular Cell. 2023 Feb;83(3):481–95.

115. Wang G, Zhang D, Orchard R, Hancks DC, Reese TA. Norovirus MLKL-like pore forming protein initiates programed cell death for viral egress [Internet]. Microbiology; 2023 Mar [cited 2024 Jan 11]. Available from: http://biorxiv.org/lookup/doi/10.1101/2023.03.17.533118

116. Jahun AS, Sorgeloos F, Chaudhry Y, Arthur SE, Hosmillo M, Georgana I, et al. Leaked genomic and mitochondrial DNA contribute to the host response to noroviruses in a STING-dependent manner. Cell Reports. 2023 Mar 28;42(3):112179.

117. Robinson BA, Winkle JAV, McCune BT, Peters AM, Nice TJ. Caspase-mediated cleavage of murine norovirus NS1/2 potentiates apoptosis and is required for persistent infection of intestinal epithelial cells. PLOS Pathogens. 2019 July 22;15(7):e1007940.

118. Santiana M, Ghosh S, Ho BA, Rajasekaran V, Du WL, Mutsafi Y, et al. Vesicle-cloaked virus clusters are optimal units for inter-organismal viral transmission. Cell Host Microbe. 2018 Aug 8;24(2):208-220.e8.

119. Helm EW, Peiper AM, Phillips M, Williams CG, Sherman MB, Kelley T, et al. Environmentally-triggered contraction of the norovirus virion determines diarrheagenic potential. Frontiers in Immunology [Internet]. 2022 [cited 2024 Jan 24];13. Available from: https://www.frontiersin.org/articles/10.3389/fimmu.2022.1043746

120. Williams AN, Sherman MB, Smith HQ, Taube S, Pettitt BM, Wobus CE, et al. Multiple Signals in the Gut Contract the Mouse Norovirus Capsid To Block Antibody Binding While Enhancing Receptor Affinity. J Virol. 2023;95(22):e01471-21.

121. Sherman MB, Williams AN, Smith HQ, Pettitt BM, Wobus CE, Smith TJ. Structural Studies on the Shapeshifting Murine Norovirus. Viruses. 2021 Oct 26;13(11):2162.

122. Devant JM, Hofhaus G, Bhella D, Hansman GS. Heterologous expression of human norovirus GII.4 VP1 leads to assembly of T=4 virus-like particles. Antiviral Res. 2019 Aug;168:175–82.

123. Jung J, Grant T, Thomas DR, Diehnelt CW, Grigorieff N, Joshua-Tor L. High-resolution cryo-EM structures of outbreak strain human norovirus shells reveal size variations. Proc Natl Acad Sci U S A. 2019 June 25;116(26):12828–32.

124. Sherman M, Cox F, Smith H, Habib MH, Karst S, Wobus CE, et al. The reversible activation of norovirus by metal ions. Dutch RE, editor. J Virol. 2024 Feb 20;98(2):e01735-23.

125. Nelson CA, Wilen CB, Dai YN, Orchard RC, Kim AS, Stegeman RA, et al. Structural basis for murine norovirus engagement of bile acids and the CD300lf receptor. Proc Natl Acad Sci U S A. 2018 Sept 25;115(39):E9201–10.

126. Lewis CB, Sherry L, Conley MJ, Nakashima M, Akbar S, Govindan N, et al. Conformational Flexibility in Capsids Encoded by the Caliciviridae. Viruses. 2024 Nov 26;16(12):1835.

127. Kolawole AO, Xia C, Li M, Gamez M, Yu C, Rippinger CM, et al. Newly isolated mAbs broaden the neutralizing epitope in murine norovirus. Journal of General Virology. 2014 Sept 1;95(9):1958–68.

128. Maass T, Westermann LT, Sharotri L, Blankenhorn L, Lane MS, Chaika M, et al. NMR Reveals the Synergistic Roles of Bivalent Metal Ions in Norovirus Infections [Internet]. bioRxiv; 2024 [cited 2025 Jan 17]. p. 2024.07.10.602906. Available from: https://www.biorxiv.org/content/10.1101/2024.07.10.602906v1

129. Creutznacher R, Maaß T, Dülfer J, Feldmann C, Hartmann V, Knickmann J, et al. Murine norovirus capsid plasticity – Glycochenodeoxycholic acid stabilizes P-domain dimers and triggers escape from antibody recognition [Internet]. bioRxiv; 2021 [cited 2025 June 4]. p. 2021.02.27.433148. Available from: https://www.biorxiv.org/content/10.1101/2021.02.27.433148v1

130. Creutznacher R, Schulze E, Wallmann G, Peters T, Stein M, Mallagaray A. Chemical-Shift Perturbations Reflect Bile Acid Binding to Norovirus Coat Protein: Recognition Comes in Different Flavors. ChemBioChem. 2020;21(7):1007–21.

131. Lindesmith LC, McDaniel JR, Changela A, Verardi R, Kerr SA, Costantini V, et al. Sera Antibody Repertoire Analyses Reveal Mechanisms of Broad and Pandemic Strain Neutralizing Responses after Human Norovirus Vaccination. Immunity. 2019 June 18;50(6):1530-1541.e8.

132. Sherman MB, Smith HQ, Cox F, Wobus CE, Lynch GC, Pettitt BM, et al. Murine norovirus allosteric escape mutants mimic gut activation. J Virol. 2025 June 17;99(6):e0021925.

133. Hayashi T, Kobayashi S, Hirano J, Murakami K. Human norovirus cultivation systems and their use in antiviral research. Journal of Virology. 2024 Mar 12;98(4):e01663-23.

134. Taube S, Kolawole AO, Höhne M, Wilkinson JE, Handley SA, Perry JW, et al. A mouse model for human norovirus. mBio. 2013 July 16;4(4):e00450-13.

135. Cheetham S, Souza M, Meulia T, Grimes S, Han MG, Saif LJ. Pathogenesis of a Genogroup II Human Norovirus in Gnotobiotic Pigs. Journal of Virology. 2006 Nov;80(21):10372–81.

136. Cuvry A, Gozalbo-Rovira R, Strubbe D, Neyts J, de Witte P, Rodríguez-Díaz J, et al. The Role of Histo-Blood Group Antigens and Microbiota in Human Norovirus Replication in Zebrafish Larvae. Microbiology Spectrum. 2022 Oct 31;0(0):e03157-22.

137. Kolawole AO, Rocha-Pereira J, Elftman MD, Neyts J, Wobus CE. Inhibition of human norovirus by a viral polymerase inhibitor in the B cell culture system and in the mouse model. Antiviral Res. 2016 Aug;132:46–9.

138. Lei S, Ryu J, Wen K, Twitchell E, Bui T, Ramesh A, et al. Increased and prolonged human norovirus infection in RAG2/IL2RG deficient gnotobiotic pigs with severe combined immunodeficiency. Sci Rep. 2016 Apr 27;6(1):25222.

139. Park BJ, Jung ST, Choi CS, Myoung J, Ahn HS, Han SH, et al. Pathogenesis of human norovirus genogroup II genotype 4 in post-weaning gnotobiotic pigs. 2018 Dec 28;28(12):2133–40.

140. Lei S, Twitchell EL, Ramesh AK, Bui T, Majette E, Tin CM, et al. Enhanced GII.4 human norovirus infection in gnotobiotic pigs transplanted with a human gut microbiota. J Gen Virol. 2019 Nov;100(11):1530–40.

141. Subekti D s., Tjaniadi P, Lesmana M, McArdle J, Iskandriati D, Budiarsa I n., et al. Experimental infection of Macaca nemestrina with a Toronto Norwalk-like virus of epidemic viral gastroenteritis. Journal of Medical Virology. 2002;66(3):400–6.

142. Rockx B h. g., Bogers W m. j. m., Heeney J l., van Amerongen G, Koopmans M p. g. Experimental norovirus infections in non-human primates. Journal of Medical Virology. 2005;75(2):313–20.

143. Rimkute I, Chaimongkol N, Woods KD, Nagata BM, Darko S, Gudbole S, et al. A non-human primate model for human norovirus infection. Nat Microbiol. 2024 Mar;9(3):776–86.

144. Dycke JV, Ny A, Conceição-Neto N, Maes J, Hosmillo M, Cuvry A, et al. A robust human norovirus replication model in zebrafish larvae. PLOS Pathogens. 2019 Sept 19;15(9):e1008009.

145. Van Dycke J, Rymenants J, Neyts J, Rocha-Pereira J. Assessment of the anti-norovirus activity in cell culture using the mouse norovirus: Identification of active compounds. Antivir Chem Chemother. 2021 Jan 1;29:20402066211026852.

146. Roux E, Willms RJ, Van Dycke J, Cortes Calabuig Á, Van Espen L, Schoofs G, et al. Transcriptional profiling of zebrafish intestines identifies macrophages as host cells for human norovirus infection. Gut Microbes. 2024;16(1):2431167.

147. Tan MTH, Gong Z, Li D. Use of Zebrafish Embryos To Reproduce Human Norovirus and To Evaluate Human Norovirus Infectivity Decay after UV Treatment. Applied and Environmental Microbiology. 2023 Mar 21;89(4):e00115-23.

148. Zhang D, Tan M, Zhong W, Xia M, Huang P, Jiang X. Human intestinal organoids express histo-blood group antigens, bind norovirus VLPs, and support limited norovirus replication. Sci Rep. 2017 Oct 3;7:12621.

149. Haga K, Ettayebi K, Tenge VR, Karandikar UC, Lewis MA, Lin SC, et al. Genetic Manipulation of Human Intestinal Enteroids Demonstrates the Necessity of a Functional Fucosyltransferase 2 Gene for Secretor-Dependent Human Norovirus Infection. mBio. 2020 Mar 17;11(2):e00251-20.

150. Sato S, Hisaie K, Kurokawa S, Suzuki A, Sakon N, Uchida Y, et al. Human Norovirus Propagation in Human Induced Pluripotent Stem Cell–Derived Intestinal Epithelial Cells. Cellular and Molecular Gastroenterology and Hepatology. 2019 Jan 1;7(3):686-688.e5.

151. Kaur G, Crawford S, Ramani S, Ayyar BV, Boussattach A, Zeng XL, et al. Overcoming host restrictions to enable continuous passaging of human noroviruses in human intestinal enteroids [Internet]. bioRxiv; 2025 [cited 2025 Sept 5]. p. 2025.05.22.655571. Available from: https://www.biorxiv.org/content/10.1101/2025.05.22.655571v1

152. Lewis MA, Cortés-Penfield NW, Ettayebi K, Patil K, Kaur G, Neill FH, et al. Standardization of an antiviral pipeline for human norovirus in human intestinal enteroids demonstrates nitazoxanide has no to weak antiviral activity. Antimicrobial Agents and Chemotherapy. 2023 Oct 3;67(10):e00636-23.

153. Ettayebi K, Kaur G, Patil K, Dave J, Ayyar BV, Tenge VR, et al. Insights into human norovirus cultivation in human intestinal enteroids. mSphere. 2024 Oct 15;9(11):e00448-24.

154. Santos-Ferreira N, Van Dycke J, Chiu W, Neyts J, Matthijnssens J, Rocha-Pereira J. Molnupiravir inhibits human norovirus and rotavirus replication in 3D human intestinal enteroids. Antiviral Research. 2024 Mar 1;223:105839.

155. Crawford SE, Ramani S, Tate JE, Parashar UD, Svensson L, Hagbom M, et al. Rotavirus infection. Nat Rev Dis Primers. 2017 Nov 9;3(1):1–16.

156. Tate. 2008 estimate of worldwide rotavirus-associated mortality in children younger than 5 years before the introduction of universal rotavirus vaccination programmes: a systematic review and meta-analysis - The Lancet Infectious Diseases [Internet]. 2012 [cited 2025 Sept 12]. Available from: https://www.thelancet.com/journals/laninf/article/PIIS1473-3099(11)70253-5/abstract

157. Tate JE, Burton AH, Boschi-Pinto C, Parashar UD, for the World Health Organization–Coordinated Global Rotavirus Surveillance Network, Agocs M, et al. Global, Regional, and National Estimates of Rotavirus Mortality in Children <5 Years of Age, 2000–2013. Clin Infect Dis. 2016 May 1;62(suppl_2):S96–105.

158. Santos N, Hoshino Y. Global distribution of rotavirus serotypes/genotypes and its implication for the development and implementation of an effective rotavirus vaccine. Reviews in Medical Virology. 2005;15(1):29–56.

159. Matthijnssens J, Bilcke J, Ciarlet M, Martella V, Bányai K, Rahman M, et al. Rotavirus disease and vaccination: Impact on genotype diversity. Future Microbiology. 2009 Dec 1;4(10):1303–16.

160. Patton JT. Rotavirus Diversity and Evolution in the Post-Vaccine World. Discovery Medicine. 2012 Jan 26;13(68):85–97.

161. Pérez-Ortín R, Vila-Vicent S, Carmona-Vicente N, Santiso-Bellón C, Rodríguez-Díaz J, Buesa J. Histo-Blood Group Antigens in Children with Symptomatic Rotavirus Infection. Viruses. 2019 Apr 10;11(4):339.

162. Willame C. EuroRotaNet: Annual report 2019.

163. Karatas M, Bloemen M, Cuypers L, Wollants E, Ranst MV, Matthijnssens J. 14-year experience of National Reference Center for Rotavirus A in Belgium: unusual dominance of equine-like G3P[8] genotype after the pandemic [Internet]. In Review; 2024 [cited 2025 Sept 12]. Available from: https://www.researchsquare.com/article/rs-4320299/v1

164. Pietsch C, Liebert UG. Molecular characterization of different equine-like G3 rotavirus strains from Germany. Infection, Genetics and Evolution. 2018 Jan 1;57:46–50.

165. Goldstein SA, Elde NC. Recurrent viral capture of cellular phosphodiesterases that antagonize OAS-RNase L. Proc Natl Acad Sci USA. 2024 Jan 30;121(5):e2312691121.

166. Saxena K, Blutt SE, Ettayebi K, Zeng XL, Broughman JR, Crawford SE, et al. Human Intestinal Enteroids: a New Model To Study Human Rotavirus Infection, Host Restriction, and Pathophysiology. J Virol. 2015 Dec 17;90(1):43–56.

167. Finkbeiner SR, Zeng XL, Utama B, Atmar RL, Shroyer NF, Estes MK. Stem Cell-Derived Human Intestinal Organoids as an Infection Model for Rotaviruses. mBio. 2012 July 3;3(4):10.1128/mbio.00159-12.

168. Ramani S, Hu L, Venkataram Prasad BV, Estes MK. Diversity in Rotavirus–Host Glycan Interactions: A “Sweet” Spectrum. Cellular and Molecular Gastroenterology and Hepatology. 2016 May 1;2(3):263–73.

169. Sun X, Guo N, Li D, Jin M, Zhou Y, Xie G, et al. Binding specificity of P[8] VP8* proteins of rotavirus vaccine strains with histo-blood group antigens. Virology. 2016 Aug 1;495:129–35.

170. Huang P, Xia M, Tan M, Zhong W, Wei C, Wang L, et al. Spike Protein VP8* of Human Rotavirus Recognizes Histo-Blood Group Antigens in a Type-Specific Manner. Journal of Virology. 2012 May;86(9):4833–43.

171. Böhm R, Fleming FE, Maggioni A, Dang VT, Holloway G, Coulson BS, et al. Revisiting the role of histo-blood group antigens in rotavirus host-cell invasion. Nat Commun. 2015 Jan 5;6(1):5907.

172. Gozalbo-Rovira R, Ciges-Tomas JR, Vila-Vicent S, Buesa J, Santiso-Bellón C, Monedero V, et al. Unraveling the role of the secretor antigen in human rotavirus attachment to histo-blood group antigens. PLOS Pathogens. 2019 June 21;15(6):e1007865.

173. Hu L, Sankaran B, Laucirica DR, Patil K, Salmen W, Ferreon ACM, et al. Glycan recognition in globally dominant human rotaviruses. Nat Commun. 2018 July 6;9(1):2631.

174. Ma X, Li D di, Sun X man, Guo Y qing, Xiang J yao, Wang W huan, et al. Binding Patterns of Rotavirus Genotypes P[4], P[6], and P[8] in China with Histo-Blood Group Antigens. PLOS ONE. 2015 Aug 14;10(8):e0134584.

175. Papa G, Borodavka A, Desselberger U. Viroplasms: Assembly and Functions of Rotavirus Replication Factories. Viruses. 2021 July 12;13(7):1349.

176. Nichols SL, Haller C, Borodavka A, Esstman SM. Rotavirus NSP2: A Master Orchestrator of Early Viral Particle Assembly. Viruses. 2024 June;16(6):814.

177. Zhang XF, Long Y, Tan M, Zhang T, Huang Q, Jiang X, et al. P[8] and P[4] Rotavirus Infection Associated with Secretor Phenotypes Among Children in South China. Sci Rep. 2016 Oct 6;6(1):34591.

178. Rodríguez-Díaz J, García-Mantrana I, Vila-Vicent S, Gozalbo-Rovira R, Buesa J, Monedero V, et al. Relevance of secretor status genotype and microbiota composition in susceptibility to rotavirus and norovirus infections in humans. Sci Rep. 2017 Mar 30;7(1):45559.

179. Günaydın G, Nordgren J, Sharma S, Hammarström L. Association of elevated rotavirus-specific antibody titers with HBGA secretor status in Swedish individuals: The FUT2 gene as a putative susceptibility determinant for infection. Virus Research. 2016 Jan 4;211:64–8.

180. Corvelo TC de O, Loiola R do SP de, Aguiar DCF, Matos G de CB de, Brito DC de. The Lewis Histo-Blood Group System: Molecular Analysis of the 59T>G, 508G>A, and 1067T>A Polymorphisms in an Amazonian Population. PLOS ONE. 2013 July 29;8(7):e69908.

181. Nordgren J, Svensson L. Genetic Susceptibility to Human Norovirus Infection: An Update. Viruses. 2019 Mar;11(3):226.

182. Krammer F, Smith GJD, Fouchier RAM, Peiris M, Kedzierska K, Doherty PC, et al. Influenza. Nat Rev Dis Primers. 2018 June 28;4(1):3.

183. Janssens Y, Joye J, Waerlop G, Clement F, Leroux-Roels G, Leroux-Roels I. The role of cell-mediated immunity against influenza and its implications for vaccine evaluation. Frontiers in Immunology. 2022 Aug 16;13.

184. Uyeki TM, Hui DS, Zambon M, Wentworth DE, Monto AS. Influenza. The Lancet. 2022 Aug 27;400(10353):693–706.

185. Carter T, Iqbal M. The Influenza A Virus Replication Cycle: A Comprehensive Review. Viruses. 2024 Feb;16(2):316.

186. Bullock TA, Pappas C, Uyeki TM, Brock N, Kieran TJ, Olsen SJ, et al. The (digestive) path less traveled: influenza A virus and the gastrointestinal tract. mBio. 2025 Aug 12;0(0):e01017-25.

187. Gu J, Xie Z, Gao Z, Liu J, Korteweg C, Ye J, et al. H5N1 infection of the respiratory tract and beyond: a molecular pathology study. Lancet. 2007 Sept 29;370(9593):1137–45.

188. Shu Y, Li CK fai, Li Z, Gao R, Liang Q, Zhang Y, et al. Avian influenza A(H5N1) viruses can directly infect and replicate in human gut tissues. J Infect Dis. 2010 Apr 15;201(8):1173–7.

189. Jahangir A, Ruenphet S, Hara K, Shoham D, Sultana N, Okamura M, et al. Evaluation of human intestinal epithelial differentiated cells (Caco-2) for replication, plaque formation and isolation of avian influenza viruses. Journal of Virological Methods. 2010 Oct 1;169(1):232–8.

190. Qu B, Li X, Gao W, Sun W, Jin Y, Cardona CJ, et al. Human intestinal epithelial cells are susceptible to influenza virus subtype H9N2. Virus Research. 2012 Jan 1;163(1):151–9.

191. Aleandri M, Conte MP, Simonetti G, Panella S, Celestino I, Checconi P, et al. Influenza A Virus Infection of Intestinal Epithelial Cells Enhances the Adhesion Ability of Crohn's Disease Associated Escherichia coli Strains. PLoS One. 2015 Feb 23;10(2):e0117005.

192. Al Khatib HA, Coyle PV, Al Maslamani MA, Al Thani AA, Pathan SA, Yassine HM. Molecular and biological characterization of influenza A viruses isolated from human fecal samples. Infection, Genetics and Evolution. 2021 Sept 1;93:104972.

193. Basarab O, Smith H. Growth patterns of influenza virus in cultures of ferret organs. Br J Exp Pathol. 1970 Feb;51(1):1–6.

194. Kawaoka Y, Bordwell E, Webster RG. Intestinal replication of influenza A viruses in two mammalian species. Brief report. Arch Virol. 1987;93(3–4):303–8.

195. Chua SCJH, Tan HQ, Engelberg D, Lim LHK. Alternative Experimental Models for Studying Influenza Proteins, Host–Virus Interactions and Anti-Influenza Drugs. Pharmaceuticals. 2019 Dec;12(4):147.

196. Gibeaud A, Pizzorno A, Terrier O. *In vitro* modeling of influenza infection in the respiratory epithelium: advanced cellular models to better understand complex host–virus interactions. Current Opinion in Virology. 2025 Feb 1;70:101452.

197. Firpo MR, Mounce BC. Diverse Functions of Polyamines in Virus Infection. Biomolecules. 2020 Apr 18;10(4):628.

198. Bae DH, Lane DJR, Jansson PJ, Richardson DR. The old and new biochemistry of polyamines. Biochimica et Biophysica Acta (BBA) - General Subjects. 2018 Sept 1;1862(9):2053–68.

199. Zhao C, Ma Y, Zhang M, Gao X, Liang W, Qin Y, et al. Polyamine metabolism controls B-to-Z DNA transition to orchestrate DNA sensor cGAS activity. Immunity. 2023 Nov;56(11):2508-2522.e6.

200. Firpo MR, LoMascolo NJ, Petit MJ, Shah PS, Mounce BC. Polyamines and eIF5A hypusination facilitate SREBP2 synthesis and cholesterol production leading to enhanced enterovirus attachment and infection. PLOS Pathogens. 2023 Apr 18;19(4):e1011317.

201. Zhang HM, Rao JN, Guo X, Liu L, Zou T, Turner DJ, et al. Akt Kinase Activation Blocks Apoptosis in Intestinal Epithelial Cells by Inhibiting Caspase-3 after Polyamine Depletion *. Journal of Biological Chemistry. 2004 May 21;279(21):22539–47.

202. Muscari C, Bonafé F, Stanic I, Flamigni F, Stefanelli C, Farruggia G, et al. Polyamine Depletion Reduces TNFα/MG132-Induced Apoptosis in Bone Marrow Stromal Cells. STEM CELLS. 2005;23(7):983–91.

203. Stanic I, Facchini A, Borzì RM, Vitellozzi R, Stefanelli C, Goldring MB, et al. Polyamine depletion inhibits apoptosis following blocking of survival pathways in human chondrocytes stimulated by tumor necrosis factor-α. Journal of Cellular Physiology. 2006;206(1):138–46.

204. Bratton DL, Fadok VA, Richter DA, Kailey JM, Frasch SC, Nakamura T, et al. Polyamine Regulation of Plasma Membrane Phospholipid Flip-Flop during Apoptosis*. Journal of Biological Chemistry. 1999 Oct 1;274(40):28113–20.

205. Zou T, Rao JN, Guo X, Liu L, Zhang HM, Strauch ED, et al. NF-κB-mediated IAP expression induces resistance of intestinal epithelial cells to apoptosis after polyamine depletion. American Journal of Physiology-Cell Physiology. 2004 May;286(5):C1009–18.

206. Mounce BC, Olsen ME, Vignuzzi M, Connor JH. Polyamines and Their Role in Virus Infection. Microbiology and Molecular Biology Reviews. 2017 Sept 13;81(4):e00029-17.

207. Firpo MR, Mastrodomenico V, Hawkins GM, Prot M, Levillayer L, Gallagher T, et al. Targeting Polyamines Inhibits Coronavirus Infection by Reducing Cellular Attachment and Entry. ACS Infect Dis. 2021 June 11;7(6):1423–32.

208. Mounce BC, Poirier EZ, Passoni G, Simon-Loriere E, Cesaro T, Prot M, et al. Interferon-Induced Spermidine-Spermine Acetyltransferase and Polyamine Depletion Restrict Zika and Chikungunya Viruses. Cell Host & Microbe. 2016 Aug 10;20(2):167–77.

209. Mastrodomenico V, Esin JJ, Qazi S, Omoba OS, Fung BL, Khomutov MA, et al. Virion-associated spermidine transmits with Rift Valley fever virus particles to maintain infectivity [Internet]. bioRxiv; 2020 [cited 2022 Nov 9]. p. 2020.01.23.915900. Available from: https://www.biorxiv.org/content/10.1101/2020.01.23.915900v1

210. Mastrodomenico V, LoMascolo NJ, Cruz-Pulido YE, Cunha CR, Mounce BC. Polyamine-Linked Cholesterol Incorporation in Rift Valley Fever Virus Particles Promotes Infectivity. ACS Infect Dis. 2022 Aug 12;8(8):1439–48.

211. Olsen ME, Filone CM, Rozelle D, Mire CE, Agans KN, Hensley L, et al. Polyamines and Hypusination Are Required for Ebolavirus Gene Expression and Replication. mBio. 2016 July 26;7(4):e00882-16.

212. Mao B, Wang Z, Pi S, Long Q, Chen K, Cui J, et al. Difluoromethylornithine, a Decarboxylase 1 Inhibitor, Suppresses Hepatitis B Virus Replication by Reducing HBc Protein Levels. Frontiers in Cellular and Infection Microbiology [Internet]. 2020 [cited 2024 Jan 8];10. Available from: https://www.frontiersin.org/articles/10.3389/fcimb.2020.00158

213. Nightingale SL. From the Food and Drug Administration. JAMA. 1991 Mar 13;265(10):1229.

214. Steverding D. The development of drugs for treatment of sleeping sickness: a historical review. Parasites & Vectors. 2010 Mar 10;3(1):15.

215. Kuemmerle A, Schmid C, Bernhard S, Kande V, Mutombo W, Ilunga M, et al. Effectiveness of Nifurtimox Eflornithine Combination Therapy (NECT) in T. b. gambiense second stage sleeping sickness patients in the Democratic Republic of Congo: Report from a field study. PLOS Neglected Tropical Diseases. 2021 Nov 8;15(11):e0009903.

216. Kroneman A, Vennema H, Deforche K, v d Avoort H, Peñaranda S, Oberste MS, et al. An automated genotyping tool for enteroviruses and noroviruses. J Clin Virol. 2011 June;51(2):121–5.

217. Crawford SE, Mukherjee SK, Estes MK, Lawton JA, Shaw AL, Ramig RF, et al. Trypsin Cleavage Stabilizes the Rotavirus VP4 Spike. J Virol. 2001 July;75(13):6052–61.

218. Almeida JD, Hall T, Banatvala JE, Totterdell BM, Chrystie IL. The Effect of Trypsin on the Growth of Rotavirus. Journal of General Virology. 1978;40(1):213–8.

219. Klenk HD, Rott R, Orlich M, Blödorn J. Activation of influenza A viruses by trypsin treatment. Virology. 1975 Dec 1;68(2):426–39.

220. Hamilton BS, Chung C, Cyphers SY, Rinaldi VD, Marcano VC, Whittaker GR. Inhibition of influenza virus infection and hemagglutinin cleavage by the protease inhibitor HAI-2. Biochem Biophys Res Commun. 2014 July 25;450(2):1070–5.

221. Rocha-Pereira J, Jochmans D, Debing Y, Verbeken E, Nascimento MSJ, Neyts J. The viral polymerase inhibitor 2'-C-methylcytidine inhibits Norwalk virus replication and protects against norovirus-induced diarrhea and mortality in a mouse model. J Virol. 2013 Nov;87(21):11798–805.

222. Peña-Gil N, Randazzo W, Carmona-Vicente N, Santiso-Bellón C, Cárcamo-Cálvo R, Navarro-Lleó N, et al. Culture of Human Rotaviruses in Relevant Models Shows Differences in Culture-Adapted and Nonculture-Adapted Strains. Int J Mol Sci. 2023 Dec 11;24(24):17362.

223. Rillahan CD, Antonopoulos A, Lefort CT, Sonon R, Azadi P, Ley K, et al. Global metabolic inhibitors of sialyl- and fucosyltransferases remodel the glycome. Nat Chem Biol. 2012 July;8(7):661–8.

224. Koromyslova AD, Leuthold MM, Bowler MW, Hansman GS. The sweet quartet: Binding of fucose to the norovirus capsid. Virology. 2015 Sept 1;483:203–8.

225. Weichert S, Koromyslova A, Singh BK, Hansman S, Jennewein S, Schroten H, et al. Structural Basis for Norovirus Inhibition by Human Milk Oligosaccharides. J Virol. 2016 Apr 14;90(9):4843–8.

226. Kim H, Lim CY, Lee DB, Seok JH, Kim KH, Chung MS. Inhibitory Effects of Laminaria japonica Fucoidans Against Noroviruses. Viruses. 2020 Sept;12(9):997.

227. Tan MTH, Eshaghi Gorji M, Toh JYL, Park AY, Li Y, Gong Z, et al. Fucoidan from *Fucus vesiculosus* can inhibit human norovirus replication by enhancing the host innate immune response. Journal of Functional Foods. 2022 Aug 1;95:105149.

228. Tan MTH, Li Y, Eshaghi Gorji M, Gong Z, Li D. Fucoidan But Not 2'-Fucosyllactose Inhibits Human Norovirus Replication in Zebrafish Larvae. Viruses. 2021 Mar;13(3):461.

229. König P. Zur Bindung von Glykanen an Calicivirus P-Domänen. Dissertation. University of Lübeck. 2023.

230. Taube S, Perry JW, Yetming K, Patel SP, Auble H, Shu L, et al. Ganglioside-Linked Terminal Sialic Acid Moieties on Murine Macrophages Function as Attachment Receptors for Murine Noroviruses. Journal of Virology. 2009 May;83(9):4092–101.

231. Kandil H, Opper F, Switzer B, Heizer W. Marked resistance of normal subjects to tube-feeding-induced diarrhea: the role of magnesium. The American Journal of Clinical Nutrition. 1993 Jan;57(1):73–80.

232. Phillips S, Donaldson L, Geisler K, Pera A, Kochar R. Stool Composition in Factitial Diarrhea: A 6-Year Experience with Stool Analysis. Ann Intern Med. 1995 July 15;123(2):97–100.

233. Santos LGAA, Musther H, Bala N, Deferm N, Patel G, Brouwers J, et al. Gastrointestinal Bile Salt Concentrations in Healthy Adults Under Fasted and Fed Conditions: A Systematic Review and Meta-Analysis for Mechanistic Physiologically-Based Pharmacokinetic (PBPK) Modelling. AAPS J. 2025 Jan 22;27(1):31.

234. Mastrodomenico V, Esin JJ, Graham ML, Tate PM, Hawkins GM, Sandler ZJ, et al. Polyamine Depletion Inhibits Bunyavirus Infection via Generation of Noninfectious Interfering Virions. J Virol. 2019 July 15;93(14):e00530-19.

235. Pekelis M. Polyamine dependency in murine norovirus (MNV-1) infection is functionally linked to an epitope in the NS4 protein. Master Thesis. University of Lübeck. 2025.

236. Wang L, Liu Y, Qi C, Shen L, Wang J, Liu X, et al. Oxidative degradation of polyamines by serum supplement causes cytotoxicity on cultured cells. Sci Rep. 2018 July 10;8(1):10384.

237. Kicmal TM, Tate PM, Dial CN, Esin JJ, Mounce BC. Polyamine Depletion Abrogates Enterovirus Cellular Attachment. Pfeiffer JK, editor. J Virol. 2019 Oct 15;93(20):e01054-19.

238. Jahun AS, Goodfellow IG. Interferon responses to norovirus infections: current and future perspectives. J Gen Virol. 2021 Oct 26;102(10):001660.

239. Laschin HM. Role of Polyamines and Apoptosis in Norovirus Infection. Master Thesis. University of Lübeck. 2024.

240. Kato H, Takeuchi O, Sato S, Yoneyama M, Yamamoto M, Matsui K, et al. Differential roles of MDA5 and RIG-I helicases in the recognition of RNA viruses. Nature. 2006 May 4;441(7089):101–5.

241. Kucharzewska P, Welch JE, Svensson KJ, Belting M. The polyamines regulate endothelial cell survival during hypoxic stress through PI3K/AKT and MCL-1. Biochemical and Biophysical Research Communications. 2009 Mar 6;380(2):413–8.

242. Müller A. Impact of Polyamine Depletion on Norovirus Infection and Cell Survival. Master Thesis. University of Lübeck. 2025.

243. Passalacqua. Glycolysis Is an Intrinsic Factor for Optimal Replication of a Norovirus | mBio [Internet]. 2019 [cited 2025 Nov 10]. Available from: https://journals.asm.org/doi/10.1128/mbio.02175-18

244. Hyde JL, Gillespie LK, Mackenzie JM. Mouse Norovirus 1 Utilizes the Cytoskeleton Network To Establish Localization of the Replication Complex Proximal to the Microtubule Organizing Center. Journal of Virology. 2012 Apr 15;86(8):4110–22.

245. Branche E, Wang YT, Viramontes KM, Valls Cuevas JM, Xie J, Ana-Sosa-Batiz F, et al. SREBP2-dependent lipid gene transcription enhances the infection of human dendritic cells by Zika virus. Nat Commun. 2022 Sept 12;13(1):5341.

246. Naveed A, Naveed MA, Akram L, Sharif M, Kang MI, Park SI. Rotavirus exploits SREBP pathway for hyper lipid biogenesis during replication. Journal of General Virology. 2022;103(5):001757.

247. Cruz-Pulido YE, LoMascolo NJ, May D, Hatahet J, Thomas CE, Chu AKW, et al. Polyamines mediate cellular energetics and lipid metabolism through mitochondrial respiration to facilitate virus replication. PLOS Pathogens. 2024 Nov 18;20(11):e1012711.

248. Kolawole AO, Mirabelli C, Hill DR, Svoboda SA, Janowski AB, Passalacqua KD, et al. Astrovirus replication in human intestinal enteroids reveals multi-cellular tropism and an intricate host innate immune landscape. PLOS Pathogens. 2019 Oct 31;15(10):e1008057.

249. Adeniyi-Ipadeola GO, Hankins JD, Kambal A, Zeng XL, Patil K, Poplaski V, et al. Infant and Adult Human Intestinal Enteroids are Morphologically and Functionally Distinct [Internet]. Microbiology; 2023 May [cited 2023 July 6]. Available from: http://biorxiv.org/lookup/doi/10.1101/2023.05.19.541350

250. Nilsson J, Rimkute I, Sihlbom C, Tenge VR, Lin SC, Atmar RL, et al. N-glycoproteomic analyses of human intestinal enteroids, varying in histo-blood group geno- and phenotypes, reveal a wide repertoire of fucosylated glycoproteins. Glycobiology. 2024 June 1;34(6):cwae029.

251. Guo Y, Candelero-Rueda RA, Saif LJ, Vlasova AN. Infection of porcine small intestinal enteroids with human and pig rotavirus A strains reveals contrasting roles for histo-blood group antigens and terminal sialic acids. Arias CF, editor. PLoS Pathog. 2021 Jan 29;17(1):e1009237.

252. Cummings RD, Etzler ME. Antibodies and Lectins in Glycan Analysis. In: Varki A, Cummings RD, Esko JD, Freeze HH, Stanley P, Bertozzi CR, et al., editors. Essentials of Glycobiology [Internet]. 2nd ed. Cold Spring Harbor (NY): Cold Spring Harbor Laboratory Press; 2009 [cited 2025 Nov 3]. Available from: http://www.ncbi.nlm.nih.gov/books/NBK1919/

253. Bojar D, Meche L, Meng G, Eng W, Smith DF, Cummings RD, et al. A Useful Guide to Lectin Binding: Machine-Learning Directed Annotation of 57 Unique Lectin Specificities. ACS Chem Biol. 2022 Nov 18;17(11):2993–3012.

254. Baldus SE, Thiele J, Park YO, Hanisch FG, Bara J, Fischer R. Characterization of the binding specificity of Anguilla anguilla agglutinin (AAA) in comparison to Ulex europaeus agglutinin I (UEA-I). Glycoconj J. 1996 Aug;13(4):585–90.

255. Tulin EKC, Muerner L, McKitrick TR, Tilton CA, Pepi LE, Jia T, et al. Blood group O expression in normal tissues and tumors. The FEBS Journal [Internet]. 2025 [cited 2025 Nov 3];n/a(n/a). Available from: https://onlinelibrary.wiley.com/doi/abs/10.1111/febs.70172

256. Thompson AJ, Cao L, Ma Y, Wang X, Diedrich JK, Kikuchi C, et al. Human Influenza Virus Hemagglutinins Contain Conserved Oligomannose N-Linked Glycans Allowing Potent Neutralization by Lectins. Cell Host & Microbe. 2020 May 13;27(5):725-735.e5.

257. Kase T, Suzuki Y, Kawai T, Sakamoto T, Ohtani K, Eda S, et al. Human mannan-binding lectin inhibits the infection of influenza A virus without complement. Immunology. 1999 July;97(3):385–92.

258. Sato Y, Morimoto K, Kubo T, Sakaguchi T, Nishizono A, Hirayama M, et al. Entry Inhibition of Influenza Viruses with High Mannose Binding Lectin ESA-2 from the Red Alga Eucheuma serra through the Recognition of Viral Hemagglutinin. Marine Drugs. 2015 June;13(6):3454–65.

259. Farkas T, Cross RW, Hargitt E, Lerche NW, Morrow AL, Sestak K. Genetic Diversity and Histo-Blood Group Antigen Interactions of Rhesus Enteric Caliciviruses. Journal of Virology. 2010 Sept;84(17):8617–25.

260. Farkas T. Rhesus enteric calicivirus surrogate model for human norovirus gastroenteritis. Journal of General Virology. 2015;96(7):1504–14.

261. Farkas T, Srivastava V. Strain-specific requirements of susceptibility to rhesus enteric calicivirus infection. Journal of Virology. 2024 Feb 14;98(3):e01851-23.

262. Sharma NR, Mateu G, Dreux M, Grakoui A, Cosset FL, Melikyan GB. Hepatitis C Virus Is Primed by CD81 Protein for Low pH-dependent Fusion. J Biol Chem. 2011 Sept 2;286(35):30361–76.

263. Kwon H, Bai Q, Baek HJ, Felmet K, Burton EA, Goins WF, et al. Soluble V Domain of Nectin-1/HveC Enables Entry of Herpes Simplex Virus Type 1 (HSV-1) into HSV-Resistant Cells by Binding to Viral Glycoprotein D. J Virol. 2006 Jan;80(1):138–48.

264. Feng Y, Pogan R, Thiede L, Müller-Guhl J, Uetrecht C, Roos WH. Fucose Binding Cancels out Mechanical Differences between Distinct Human Noroviruses. Viruses. 2023 June 30;15(7):1482.

265. Patil K, Ayyar BV, Hayes NM, Neill FH, Bode L, Estes MK, et al. 2'-Fucosyllactose inhibits human norovirus replication in human intestinal enteroids. Journal of Virology. 2025 Jan 10;99(2):e00938-24.

266. Stival ACS, da Silva ACG, Valadares MC. Qualitative and quantitative evaluation of Fetal Bovine Serum composition: toward ethical and best quality *in vitro* science. NAM Journal. 2025 Jan 1;1:100047.

267. 11965 - DMEM, high glucose - DE [Internet]. [cited 2025 Dec 16]. Available from: https://www.thermofisher.com/de/de/home/technical-resources/media-formulation.8.html

268. Song C, Takai-Todaka R, Miki M, Haga K, Fujimoto A, Ishiyama R, et al. Dynamic rotation of the protruding domain enhances the infectivity of norovirus. PLoS Pathog. 2020 July 2;16(7):e1008619.

269. Zhou H, Li XM, Meinkoth J, Pittman RN. Akt Regulates Cell Survival and Apoptosis at a Postmitochondrial Level. J Cell Biol. 2000 Oct 30;151(3):483–94.

270. Luo HR, Hattori H, Hossain MA, Hester L, Huang Y, Lee-Kwon W, et al. Akt as a mediator of cell death. Proceedings of the National Academy of Sciences. 2003 Sept 30;100(20):11712–7.

271. Calvisi DF, Wang C, Ho C, Ladu S, Lee SA, Mattu S, et al. Increased lipogenesis, induced by AKT-mTORC1-RPS6 signaling, promotes development of human hepatocellular carcinoma. Gastroenterology. 2011 Mar;140(3):1071-1083.e5.

272. Porstmann T, Santos CR, Griffiths B, Cully M, Wu M, Leevers S, et al. SREBP Activity Is Regulated by mTORC1 and Contributes to Akt-Dependent Cell Growth. Cell Metab. 2008 Sept 3;8(3–3):224–36.

273. Definition of pan-AKT kinase inhibitor GSK690693 - NCI Drug Dictionary - NCI [Internet]. 2011 [cited 2025 Dec 15]. Available from: https://www.cancer.gov/publications/dictionaries/cancer-drug/def/pan-akt-kinase-inhibitor-gsk690693

274. Gutierrez E, Shin BS, Woolstenhulme CJ, Kim JR, Saini P, Buskirk AR, et al. eIF5A Promotes Translation of Polyproline Motifs. Mol Cell. 2013 July 11;51(1):35–45.

275. Chu H, Hou Y, Yang D, Wen L, Shuai H, Yoon C, et al. Coronaviruses exploit a host cysteine-aspartic protease for replication. Nature. 2022 Sept;609(7928):785–92.

276. Chu H, Shuai H, Hou Y, Zhang X, Wen L, Huang X, et al. Targeting highly pathogenic coronavirus-induced apoptosis reduces viral pathogenesis and disease severity. Science Advances. 2021 June 16;7(25):eabf8577.

277. Soni S, Walton-Filipczak S, Nho RS, Tesfaigzi Y, Mebratu YA. Independent role of caspases and Bik in augmenting influenza A virus replication in airway epithelial cells and mice. Virology Journal. 2023 Apr 24;20(1):78.

278. Yan Y, Yang M, Liu Z, Li L, Fu Z, Jiao Y, et al. Sclareol can effectively ameliorate Feline calicivirus induced lung injury via the inhibition of inflammation and apoptosis. International Immunopharmacology. 2025 Oct 30;164:115342.

279. Meyskens FL, Emerson SS, Pelot D, Meshkinpour H, Shassetz LR, Einspahr J, et al. Dose de-escalation chemoprevention trial of alpha-difluoromethylornithine in patients with colon polyps. J Natl Cancer Inst. 1994 Aug 3;86(15):1122–30.

280. Kotaki T, Akieda Y, Chen Z, Onishi M, Komatsu S, Motooka D, et al. Recovery of infectious recombinant human norovirus using zebrafish embryos. Proc Natl Acad Sci USA. 2025 Dec 9;122(49):e2526726122.

9. Acknowledgement

I acknowledge the use of AI-assisted language editing tools to improve style, grammar, and readability, as well as translation of the abstract into German. AI was not used to generate scientific content.

I am grateful to the group of Dr. Peter König at the Institute of Anatomy, University of Lübeck, and in particular to Dr. Mario Pieper, for their support with two-photon microscopy and for providing access to the instrumentation and expertise required to perform the imaging experiments.

I further thank Dr. Sandra Niendorf at the Robert Koch Institute for sequencing and genotyping the HNoV samples, and Dr. Sonja Jacobsen for kindly providing the HRoV material, performing GE titrations, and offering valuable expertise and consultation on rotavirus-related work.

I would like to thank Dr. Carmen Mirabelli for her support and mentorship at the beginning of my PhD, and for trusting me with the polyamine project. I also thank the students who contributed to this project during their internships or Master's theses, in particular Nina Eichler M.Sc., Heike Laschin M.Sc., Marina Pekelis M.Sc., and Alexander Müller M.Sc., whose enthusiasm, commitment, and hard work greatly helped to move this part of the project forward.

I am also grateful to my PhD colleagues, Miranda Lane M.Sc., and Iqra Kashif M.Sc., for their support, friendship, and all the good moments we shared both in and outside the lab.

My gratitude also goes to Katja Thiele-Bössel for her tireless support, including continuous assistance with cell culture and numerous plaque assays, and the day-to-day organization of laboratory work.

Finally, my deepest gratitude goes to Stefan Taube for giving me the opportunity to pursue my PhD in his lab, for the many discussions and debates that pushed the science forward, for trusting me with the enteroid system, and for his continuous support throughout my PhD.

Part of this thesis was published:

Chaika, M. et.al. Polyamine depletion inhibits norovirus infection by blocking virus-induced apoptosis 2025.09.14.676151 Preprint at https://www.biorxiv.org/content/10.1101/2025.09.14.676151v1 (2025).

Parts of this thesis were presented:

Schöntal, Germany, 2022, 20th Workshop "Cell Biology of Viral Infections"
Chaika, M., Lane, M. S., Mirabelli, C., & Taube, S.
Establishing a reverse genetics platform using human intestinal enteroids to generate recombinant human noroviruses.

Ulm, Germany, 2023, Annual Meeting of the Society for Virology (GfV)
Chaika, M., Mirabelli, C., & Taube, S.
Polyamine depletion reduces murine norovirus replication.

Rotterdam, Netherlands, 2023, Calicivirus Conference
Chaika, M., Lane, M. S., Gresens, L., Wobus, C. E., Smith, T., & Taube, S.
Impact of ions on murine norovirus infection and escape from antibody neutralization.

Kyiv, Ukraine, 2023, IX International Conference "BioResources and Viruses"
Chaika, M., Mirabelli, C., Wobus, C. E., & Taube, S.
Human intestinal enteroids as a model system for human norovirus infection.

Vienna, Austria, 2024, GfV
Laschin., H., **Chaika, M.**, & Taube, S.
Murine norovirus inhibits interferon-β production in murine microglial cells (BV-2) but not in murine macrophages (RAW264.7).

Vienna, Austria, 2024, GfV
Chaika, M. Wobus, C. E., Taube, S
Norovirus infection is dependent on polyamines produced by the host and microbiome.

Smögen, Sweden, 2024, 21st Smögen Summer Symposium on Virology
Chaika, M., Mirabelli, C., Wobus, C. E., & Taube, S.
Human intestinal enteroids, a versatile tool to study human norovirus biology.

Hamburg, Germany, 2025, GfV
Chaika, M., Müller, A., Jacobsen, S., Niendorf, S., Mirabelli, C., Wobus, C. E., & Taube, S.
Surface Glycans as Therapeutic Targets to Prevent Human Norovirus and Rotavirus Infections in a Human Intestinal Enteroid Model.

Hamburg, Germany, 2025, GfV
Chaika, M., Laschin, H., Pekelis, M., Müller, A., Mirabelli, C., Niendorf, S., Wobus, C., & Taube, S.,
Polyamine depletion inhibits norovirus infection by blocking virus-induced apoptosis.